INVESTIGATION OF DISSOLVED CARBON DIOXIDE INJECTION INTO PALEOZOIC AGED GEOTHERMAL RESERVOIR ROCK

A THESIS SUBMITTED TO
THE GRADUATE SCHOOL OF NATURAL AND APPLIED SCIENCES
OF
MIDDLE EAST TECHNICAL UNIVERSITY

BY

HAKKI AYDIN

IN PARTIAL FULFILLMENT OF THE REQUIREMENTS
FOR
THE DEGREE OF DOCTOR OF PHILOSOPHY
IN
PETROLEUM AND NATURAL GAS ENGINEERING

OCTOBER 2023

Approval of the thesis:

INVESTIGATION OF DISSOLVED CARBON DIOXIDE INJECTION INTO PALEOZOIC AGED GEOTHERMAL RESERVOIR ROCK

submitted by **HAKKI AYDIN** in partial fulfillment of the requirements for the degree of **Doctor of Philosophy** in **Petroleum and Natural Gas Engineering, Middle East Technical University** by,

Prof. Dr. Halil Kalıpçılar
Dean, Graduate School of **Natural and Applied Sciences** _____

Assoc. Prof. Dr. İsmail Durgut
Head of the Department, **Petroleum and Natural Gas Engineering** _____

Prof. Dr. Serhat Akın
Supervisor, **Petroleum and Natural Gas Eng. Dept., METU** _____

Examining Committee Members:

Assoc. Prof. Dr. Çağlar Sınayuç
Petroleum and Natural Gas Engineering Dept., METU _____

Prof. Dr. Serhat Akın
Petroleum and Natural Gas Eng. Dept., METU _____

Prof. Dr. Ömer İnanç Türeyen
Petroleum and Natural Gas Eng. Dept., ITU _____

Assoc. Prof. Dr. Ali Bülbül
Geological Engineering Dept., PAÜ _____

Asst. Prof. Dr. Selçuk Erol
Energy Systems Engineering, IZTECH _____

Date: 30.10.2023

I hereby declare that all information in this document has been obtained and presented in accordance with academic rules and ethical conduct. I also declare that, as required by these rules and conduct, I have fully cited and referenced all material and results that are not original to this work.

Name Last name: Hakkı Aydın

Signature:

ABSTRACT

INVESTIGATION OF DISSOLVED CARBON DIOXIDE INJECTION INTO PALEOZOIC AGED GEOTHERMAL RESERVOIR ROCK

Aydin, Hakki
Doctor of Philosophy, Petroleum and Natural Gas Engineering
Supervisor: Prof. Dr. Serhat Akin

October 2023, 167 pages

The scientific consensus is that greenhouse gas emissions are causing global climate change. Carbon dioxide (CO_2) is the main greenhouse gas, and it is produced by a variety of chemical reactions and combustion processes. One potential method for CO_2 disposal is reinjection into water-bearing reservoirs. Geothermal reservoirs have been identified as promising candidates for this purpose. A number of studies have been conducted on CO_2 sequestration in different types of formations. However, more research is needed to understand the changes that CO_2 injection can cause to geothermal fluid chemistry and reservoir rock properties. Several small-scale experiments were conducted to investigate the effects of CO_2-dissolved brine injection using core samples from the Kızıldere geothermal reservoir at depths of 1900 m and 3000 m. The batch reactor experiments were conducted at different temperatures and pressures. The interaction between CO_2-dissolved brine and reservoir rock was simulated using the PHREEQC and TOUGHREACT, which are based on equilibrium and kinetic modeling. Mineral precipitations and dissolutions were determined using X-ray fluorescence (XRF), X-ray diffraction (XRD), and

scanning electron microscopy (SEM) measurements. Major anions and cations were measured using ion chromatography (IC) and inductively coupled plasma (ICP) spectroscopy. The results of the batch reactor experiments showed that CO_2-dissolved brine injection can cause significant changes to geothermal fluid chemistry and reservoir rock properties. These changes include mineral precipitation, dissolution, and alteration such as magnesite, kaolinite, feldspar, biotite, siderite, and dolomite. This study provides valuable insights into the effects of CO_2 injection on geothermal fluid chemistry and reservoir rock properties. The findings of this study can be used to design and operation field-scale CO_2 sequestration projects in geothermal reservoirs.

Keywords: Noncondensable Gases, Geothermal Energy, Reactive Transport, Carbon Dioxide, Sequestration

ÖZ

ÇÖZÜNMÜŞ KARBONDİOKSİTİN PALEOZOİK JEOTERMAL REZERVUAR KAYACINDA ENJEKSİYONUNUN ARAŞTIRILMASI

Aydın, Hakkı
Doktora, Petrol ve Doğal Gaz Mühendisliği
Tez Yöneticisi: Prof. Dr. Serhat Akın

Ekim 2023, 167 sayfa

Sera gazı emisyonunun dünyadaki iklim değişikliğine neden olduğu ve üzerindeki olumsuz etkileri bilimsel fikir birliği ile sabittir. Karbondioksit (CO_2) temel sera gazıdır ve çeşitli kimyasal reaksiyonlar ve yanma süreçleri ile üretilir. Karbondioksit'in bertaraf edilmesi için potansiyel bir yöntem akifer rezervuarlara geri basımıdır. Jeotermal rezervuarlar, bu amaç için umut verici aday rezervuarlar olarak belirlenmiştir. Çeşitli formasyonlarda CO_2 depolaması ile ilgili çok sayıda çalışma yapılmıştır. Ancak, CO_2 enjeksiyonunun jeotermal akışkan kimyası ve rezervuar kaya özellikleri üzerinde olabilecek değişiklikleri anlamak için daha fazla araştırmaya ihtiyaç vardır. Kızıldere jeotermal rezervuarından 1900 m ve 3000 m derinliklerden alınan karot örnekleri kullanılarak CO_2'de çözünmüş tuzlu su enjeksiyonunun etkilerini araştırmak için küçük ölçekli deneyler yapıldı. CO_2'de çözünmüş tuzlu su ile rezervuar kayacı arasındaki etkileşim, denge ve kinetik modellemeye dayanan PHREEQC ve TOUGHREACT kullanılarak simüle edildi. Mineral çökelmeleri ve çözünmeleri, X-ışını floresansı (XRF), X-ışını kırınımı (XRD) ve taramalı elektron mikroskobu (SEM) ölçümleri kullanılarak belirlendi. Ana anyonlar ve katyonlar, iyon kromatografisi (IC) ve indüktif olarak eşleşmiş plazma (ICP) spektroskopisi kullanılarak ölçüldü. Kesikli reaktör deneylerinin

sonuçları, CO_2'de çözünmüş tuzlu su enjeksiyonunun, jeotermal akışkan kimyasında ve rezervuar kaya özelliklerinde önemli değişikliklere neden olabileceğini gösterdi. Bu değişiklikler arasında manyezit, kaolinit, feldispat, biyotit, siderit ve dolomit gibi minerallerin çökelmesi, çözünmesi ve alterasyonu yer alır. Bu çalışma, CO_2 enjeksiyonunun jeotermal akışkan kimyası ve rezervuar kaya özellikleri üzerindeki etkilerine dair değerli bilgiler sunmaktadır. Bu çalışmanın bulguları, jeotermal rezervuarlarda saha ölçeğinde CO_2 tutma projelerinin tasarlanması ve işletilmesi için kullanılabilir.

Anahtar Kelimeler: Kondense Olmayan Gazlar, Jeotermal Enerji, Reaktif Taşınım, Karbon Dioksit Depolama

To My Beloved Family

ACKNOWLEDGMENTS

I would like to express my deepest gratitude to my thesis supervisor Prof. Dr. Serhat Akın, for his guidance, advice, criticism, encouragements, and insight throughout the research.

Prof. Dr. Ömer İnanç Türeyen, and Assoc. Prof. Dr. Çağlar Sınayuç are gratefully acknowledged for their valuable suggestions and comments in shaping my thesis studies. I would also like to thank Asst. Prof. Dr. Selçuk Erol for his suggestions, helps, and comments throughout the thesis. I would also like to thank Assoc. Prof. Dr. Ali Bülbül who served as my PhD committee members, for their valuable comments and suggestions.

Special thanks to Dr. Taylan Akın for his valuable discussions and suggestions about my thesis.

I would like to express my deep gratitude to Ex-Deputy General Manager of Zorlu Energy, Bahadır Erdoğan for his supports.

This dissertation would not be existed without funding of Zorlu Enerji. Zorlu Enerji always support and encouraged me for the scientific works.

Last but not least I would like to thank my dear wife Seher Yüksel Aydın for her patience, supports, and love throughout stressful times.

TABLE OF CONTENTS

ABSTRACT v

ÖZ vii

ACKNOWLEDGMENTS x

TABLE OF CONTENTS xi

LIST OF TABLES xiv

LIST OF FIGURES xvi

NOMENCLATURE xxiii

CHAPTERS

1 INTRODUCTION 1

2 LITERATURE REVIEW 5

2.1 Carbon Capture Technology 6

2.2 Carbon Storage Technology 7

2.2.1 CO_2 Injection for Enhanced Coal Bed Methane (CBM) 8

2.2.2 Gas hydrate production by injecting CO_2 9

2.2.3 EGR and EOR Methods in Shale Gas Reservoirs 10

2.2.4 CO_2 Sequestration in Deep Saline Aquifers 12

2.2.5 CO_2 Dissolution and Sequestration into Geothermal Reservoirs 14

2.3 Worldwide Carbon Capture and Storage (CCS) Field Applications 20

2.4 Non-Condensable Gases in Geothermal Energy 24

2.5 Mineral Trapping of CO_2 in Geothermal Reservoirs 28

2.5.1 Potassic alteration 29
2.5.2 Propylitic alteration 29
2.5.3 Phyllic (sericitic) alteration 30
2.5.4 Argillic alteration 30
2.5.5 Silicification 30
2.5.6 Carbonatization 31
2.5.7 Greisenization 32
2.6 Previous Studies about CO_2 Sequestration in Geothermal Reservoirs 34
3 STATEMENT OF THE PROBLEM 39
4 MATERIALS AND METHODS 41
4.1 Methodology of CO_2 Dissolution Experiment 41
4.2 Batch and Core-flood Experiments 45
4.3 Methodology of Simulation Approaches 49
4.3.1 Simulation of Batch Experiments using PHREEQC 49
4.3.2 3D Reactive-Transport Modeling 50
4.3.3 Geological Structure of the Reservoir 54
4.3.4 Gridding of the Model 59
4.3.5 Physical and Geochemical Boundary Conditions of the Model 61
5 RESULTS AND DISCUSSIONS 73
5.1 CO_2 Dissolution in Geothermal Brine 73
5.2 Water-Rock Interaction with Batch Experiments 90
5.3 Water-Rock Interaction Core-flood Experiments 106
5.4 Results of 3D Numerical Reservoir Model for Heterogeneous System 112
5.5 Results of 3D Numerical Reservoir Model for Homogeneous System 120

5.6 Effect of CO_2 on the Production Performance using Wellbore Simulation 129

6 CONCLUSION 133

REFERENCES 137

APPENDICES

A. Water Rock Interaction Experiments 151

B. 3D Reactive Transport Simulation 154

CURRICULUM VITAE 163

LIST OF TABLES

TABLES

Table 2.1 Studies about CO_2 solubility in water. 15
Table 2.2 Database of large-scale CCS projects operated or identified in recent years (Raza et al. 2016; Kelemen et al. 2019). 20
Table 2.3 Composition of NCG in Kızıldere field. 27
Table 2.4 Diagnostic minerals in hydrothermally altered volcanogenic massive sulfide deposits at different metamorphic grade (Shanks III, 2012; Alt et al., 2012). 33
Table 2.5 Hydrothermal alterations in West Anatolia geothermal systems 33
Table 2.6 Mineralogy of the caprock (Dalkhaa and Okandan, 2013). 35
Table 2.7 Saturation index of minerals as the result of water-rock interaction Waldmann et al. (2014). 36
Table 4.1 Examples for acid and base mechanisms (Palandri and Kharaka, 2004). 53
Table 4.2 Grid size distribution of the model. 60
Table 4.3 Initial and boundary of water chemistry at reservoir. 64
Table 4.4 Injection brine chemistry. 65
Table 4.5 Aqueous complexes. 65
Table 4.6 Mineral composition. 67
Table 4.7 Porosity and permeability values of the formations. 68
Table 4.8 Characteristic of rock properties (Küçük, 2018) 68
Table 5.1 Exponential behavior of NCG dissolution in the geothermal brine at different gas ratio (x represents time (seconds) and y is NCG dissolution rate (kg/L/second)). 75
Table 5.2 The amount of CO_2 that remained in the geothermal brine based on alkalinity tests. 76

Table 5.3 The amount of CO_2 that remained in the geothermal brine based on alkalinity tests. 77
Table 5.4 Typical composition of Geothermal Gas (Fridriksson et al. 2016). 84
Table 5.5 Gas mixtures to account for gas purity affecting CO_2 dissolution..... 84
Table 5.6 Surface area and mole number of mineral assemblies for rock sample taken from 1900 m depth. 97
Table 5.7 Surface area and mole number of mineral assemblies for rock sample taken from 3000 m depth. 97
Table 5.8 Activation energy and kinetic rate constant for matching PHREEQC model with experiment results and USGS values. 98
Table 5.9 Solubility of kaolinite with respect to pH (Created from Rao et al. 2011). 100
Table 5.10 Solubility of siderite with respect to pH (Silve et al. 2002)..... 100
Table 5.11 Wellbore simulation parameters. 131
Table 6.1 Chemistry of minerals found in EDX SEM of rock sample from 1900 m depth..... 151
Table 6.2 Chemistry of minerals found in EDX SEM of rock sample from 3000 m depth..... 153

LIST OF FIGURES

FIGURES

Figure 2.1 Carbon capture, transportation, utilization, and storage (Dziejarski et al., 2023). 5
Figure 2.2 Schematic view of a CCS system (Rubin et al. 2012). 6
Figure 2.3 Schematic representation of Enhanced CBM process (Mazzotti et al. 2009). 9
Figure 2.4 Schematic diagram of natural gas exploitation and CO_2 isolation process (Phale et al. 2006). 10
Figure 2.5 Simplified Huff and Puff cyclic gas injection (Pankaj et al., 2018). 11
Figure 2.6 CO_2 injection for enhanced oil recovery (Shevalier et al. 2009). 11
Figure 2.7 Injection of carbon dioxide into depleted oil and gas reservoir (Scottish Centre for Carbon Storage, 2023). 13
Figure 2.8 Sedimentary basins showing suitability as sequestration sites (Benson and Cole, 2008). 13
Figure 2.9 Henry's constant (KH) calculated for the H_2O-CO_2 using five different empirical correlations. 14
Figure 2.10 CO_2 injection as a dissolved gas in water (a) and supercritical condition (b) (Snæbjörnsdóttiret al. 2020). 18
Figure 2.11 Phase diagram of CO_2 (Saeedi, 2012). 19
Figure 2.12 CO_2 injection by using a dual string system in Iceland (CarbFix project, 2018). 19
Figure 2.13 Map of CO_2 sequestration facilities, pilot projects, and long-term storage potential in geologic formations (Kelemen et al. 2019). 21
Figure 2.14 The Frio-I injection experiments (Kampman et al. 2014). 22
Figure 2.15 CO_2 injection site in Iceland (Matter et al., 2009). 23
Figure 2.16 Gas emission from different energy sources (revised from Amponsah et al., 2014). 25

Figure 2.17 NCG decline of Alaşehir and Kızıldere geothermal reservoirs (Aydin et al. 2020). 25
Figure 2.18 Kızıldere geothermal field and location of the studied well (Modified from Haklıdır et al. 2021). 26
Figure 2.19 NCG releasing to atmosphere in Kızıldere geothermal power plant. 27
Figure 2.20 Typical flash cycle power plant (Richardson et al. 2015). 28
Figure 2.21 Centimeter-scale view of comb-textured quartz crystals within wall rock (sericitized, kaolinized and silicic) (Kumral et al. 2016). 31
Figure 2.22 Photo of the sandstone sample and thin section image observed by electron (Liu et al. 2018). 38
Figure 4.1 A view of batch experiment setup in the field. 42
Figure 4.2 A view of gas measurement system consisting of a condenser and a gas flowmeter. 42
Figure 4.3 Transferring NCG from a geothermal well to a high-pressure tube.... 43
Figure 4.4 Illustration of batch reactor. 44
Figure 4.5 Workflow of the water-rock interaction experiments. 45
Figure 4.6 Core samples taken from 3000 m depth (a) and 1900 m depth (b). 46
Figure 4.7 Crushing core samples into small particles (Screener (a), shaking screeners (b), sorted particles (c). 46
Figure 4.8 A view of core-flood experiment setup. 47
Figure 4.9 Sythetically fractured core sample and core holder used in the experiments. 48
Figure 4.10 A general geological columnar section of Kızıldere field and alteration types (Haklıdır et al. 2021). 56
Figure 4.11 The geological conceptual model of the Kızıldere Geothermal Field (Haklıdır et al. 2021). 57
Figure 4.12 Stratigraphic columns and distribution of formations of the studied area in Kızıldere field. 58
Figure 4.13 Faults used in the numerical model representing Kızıldere field: Fault-1, fault-1A and Gebeler fault. 59

Figure 4.14 A top view of grids of 3D model. 60
Figure 4.15 a) Constant pressure boundary b) No flow boundary (Küçük, 2018). 61
Figure 4.16 Heat source from the bottom of model. 62
Figure 4.17 Fixed state of top layer of the model..... 63
Figure 4.18 Permeability factor and porosity factor assigned to formations. 69
Figure 4.19 Permeability and porosity factors assigned to fault-cut grids. 69
Figure 4.20 Matching with static pressure profile of reinjection well. 70
Figure 4.21 Matching with static temperature profile of reinjection well..... 70
Figure 4.22 Matching with static pressure profile of production well. 71
Figure 4.23 Matching with static temperature profile of production well. 71
Figure 5.1 CO_2 dissolution experiments for dissolution reaction kinetics. 74
Figure 5.2 Dissolution kinetics of NCG in geothermal brine for different gas/(gas+brine) volumetric ratio..... 75
Figure 5.3 Comparison of gas dissolution experiments with empirical formulas available in the literature. 79
Figure 5.4 Comparison of gas dissolution experiments with empirical formulas a) Cramer, 1982 b) Fournier, 1989. 79
Figure 5.5 Comparison of gas dissolution experiments against PHREEQC. 80
Figure 5.6 CO_2 solubility under high temperature and pressure. 81
Figure 5.7 CO_2 solubility in the geothermal brine with varying NaCI concentration at 100 ^oC using PHREEEQC. 82
Figure 5.8 CO_2 dissolution results for mixtures of gases at 20 barg. 84
Figure 5.9 Distribution of species at pH=9. 86
Figure 5.10 pH value of geothermal brine under dissolving CO_2 at varying pressure and temperature values. 88
Figure 5.11 Saturation Index of saturated minerals before and after CO_2 dissolution at 8 Bar and 95 ^oC. 88
Figure 5.12 Distribution of species at 0.4 % by wt of CO_2 dissolution at 8 Bar and 95 ^oC. 89

Figure 5.13 Set scale for image process. 91
Figure 5.14 Statistical information about mineral surface area. 91
Figure 5.15 a) Macroscopic view of core sample taken from 1900 m depth b) In thin-section scans, Quartz filled lenses and bands were identified c) Lepidoblastic biotite and granoblastic quartz and albite minerals, and the alteration products magnesite (Mgs) and siderite (Sd) and kaolinites. 93
Figure 5.16 a) Macroscopic view core sample taken from 3000 m depth (b) In thin-section scans Calcite-filled lenses and quartz-filled bands, (c) Granoblastic textured calcites and quartz, albite, muscovite and Optical microscope views of the levels containing the opaque mineral (pyrite). 94
Figure 5.17 XRD measurements of the core sample taken from 1900 m depth before (a) and after (b) batch experiments. 95
Figure 5.18 Core samples taken from 3000 m depth a) before water-rock interaction in the batch experiments b) after water-rock interactions in the batch experiments. 95
Figure 5.19 Experiment and simulation results for rock samples taken from 1900 m a) Antimony b) Aluminum c) Iron d) Calcium. 102
Figure 5.20 Experiment and simulation results for rock samples taken from 1900 m a) Silica b) Magnesium c) Chloride d) pH. 103
Figure 5.21 Experiment and simulation results for rock samples taken from 3000 m a) Magnesium b) Aluminum c) Calcium d) pH. 105
Figure 5.22 Experiment and simulation results for rock samples taken from 3000 m a) Silica b) Iron. 106
Figure 5.23 a) Front-side of fracture surface where water-rock interaction occurred b) backside of the fracture surface where no water-rock interaction occurred for core sample taken from 1900m depth. 107
Figure 5.24 CT scan of the core sample (right hand image shows the slice location and lateral view of the core plug). 108
Figure 5.25 SEM analysis of fracture surface area at different magnification magnitudes for 1900m depth core sample. 109

Figure 5.26 XRD analysis of the core sample with 1 cm thickness (analysis of two side of the sample). 110
Figure 5.27 Pressure recordings and injection rate during core-flood experiment. 111
Figure 5.28 Silica concentration of brine during core flood experiment. 111
Figure 5.29 Pressure distribution of the studied field area. 112
Figure 5.30 Temperature distribution of the studied field area. 113
Figure 5.31 Pressure history of reinjection well. 114
Figure 5.32 Temperature history of reinjection well. 114
Figure 5.33 Density history of reinjection well. 115
Figure 5.34 Reservoir pressure of production well. 115
Figure 5.35 Water density of production well. 116
Figure 5.36 Permeability changes as the result of CO_2 injection in the reinjection well. 117
Figure 5.37 Porosity changes as the result of CO_2 injection in the reinjection well. 118
Figure 5.38 Sensitivity analysis for effects of mineral assembly on the permeability. 118
Figure 5.39 Changes in the secondary minerals during 0.03 wt CO_2 injection... 119
Figure 5.40 Changes in the primary minerals' volume fraction during 0.03 wt CO_2 injection (normalized values). 119
Figure 5.41 Changes in the CO_2 content of production well. 120
Figure 5.42 Gridding and stratigraphic units of homogeneous model. 121
Figure 5.43 Initial temperature (left) and pressure (right) distribution of homogeneous model. 121
Figure 5.44 Temperature variation along the grid cells between injection and production wells. 122
Figure 5.45 CO_2 distribution at gas-free brine injection. 123
Figure 5.46 CO_2 distribution after gas injection at 5 % by weight. 123

Figure 5.47 CO_2 variation along the grid cells between injection and production wells. 124
Figure 5.48 Changes in the CO_2 content of production well in homogeneous model. 124
Figure 5.49 Changes in the permeability of reinjection well in homogeneous model. 125
Figure 5.50 Changes in the porosity of reinjection well in homogeneous model. 126
Figure 5.51 Changes in the secondary minerals' volume fraction during 0.05 wt CO_2 injection. 126
Figure 5.52 Changes in the primary minerals' volume fraction during 0.05 wt CO_2 injection (normalized values). 127
Figure 5.53 Bromide distribution after CO_2 injection. 128
Figure 5.54 Aluminum distribution after CO_2 injection. 129
Figure 5.55 Calibrated wellbore simulation for a geothermal well in Kızıldere field. 131
Figure 5.56 Effect of CO_2 on the performance of production well. 132
Figure 6.1 Images of EDX SEM analysis of rock samples from 1900 m depth. 151
Figure 6.2 Images of EDX SEM analysis of rock samples from 3000 m depth. 152
Figure 6.3 Dissolved CO_2 injection history in reinjection well. 154
Figure 6.4 Changes in the calcium concentration of reinjection well in heterogeneous model. 154
Figure 6.5 Changes in the magnesium concentration of reinjection well in heterogeneous model. 155
Figure 6.6 Changes in the aluminum concentration of reinjection well in heterogeneous model. 155
Figure 6.7 Changes in the silica concentration of reinjection well in heterogeneous model. 156
Figure 6.8 Spatial distribution of temperature before (a) and after reinjection (b) in heterogeneous model. 156

Figure 6.9 Spatial distribution of dissolved CO_2 before (a) and after reinjection (b) in heterogeneous model. 157
Figure 6.10 Spatial distribution of silica before (a) and after reinjection (b) in heterogeneous model. 157
Figure 6.11 Spatial distribution of magnesium before (a) and after reinjection (b) in heterogeneous model. 158
Figure 6.12 Spatial distribution of iron before (a) and after reinjection (b) in heterogeneous model. 158
Figure 6.13 Spatial distribution of calcium before (a) and after reinjection (b) in heterogeneous model. 159
Figure 6.14 Spatial distribution of aluminum before (a) and after reinjection (b) in heterogeneous model. 159
Figure 6.15 Changes in the aluminum concentration of reinjection well for homogenous model. 160
Figure 6.16 Changes in the calcium concentration of reinjection well for homogenous model. 160
Figure 6.17 Changes in the silica concentration of reinjection well for homogenous model. 161
Figure 6.18 Changes in the Albite faction of reinjection well for homogenous model. 161
Figure 6.19 Changes in the Dolomite faction of reinjection well for homogenous model. 162

NOMENCLATURE

A_0: Mineral surface area, m^2

a_{fmr}: A factor representing reduction for water and surface area contact

α_H: Acid mechanism

α_{OH}: Base mechanism

A_m: Mineral surface area, m^2

A_n : Specific reactive surface area, $m^2_{mineral}$ / kg^{-1}_{water}

A_r: Reactive surface area, m^2/m^3

E_a: Activation energy, J $mole^{-1}$

k: Permeability, m^2

k_0: initial permeability, m^2

k: kinetic rate constant, mol/m2/s

k_{25}: kinetic rate constant at 25 ^oC, mol/m2/s

K_n : Equilibrium constant for the mineral–water reaction written for the destruction of one mole of mineral n

k_n : Rate constant, n denotes kinetic mineral index

m: Current moles of the kinetic reactant, moles

m_0 : Initial moles of the kinetic reactant, moles

MW: Molecul weight

nu: Neutral

η: Power term

Θ: Power term

R: Gas constant, J mole-1 $^{o}C^{-1}$

SI: Saturation index

SR: Saturation ratio, fraction

S_w : Water saturation

T_K: Temperature in Kelvin

V: Solution volume in contact with mineral, L

ρ_w : Water density

ϕ_f : Fracture porosity

ϕ_0 : initial porosity

CHAPTER 1

INTRODUCTION

Carbon capture and storage (CCS) in deep geological formations has emerged as one of the most effective methods to reduce greenhouse gas emissions from the combustion of hydrocarbon fuels such as coal, oil, and natural gas (Gunnarsson et al., 2018; DiPippo, 2016; Snæbjörnsdóttir et al. 2018). Other significant sources of gas emissions include volcanic eruptions and meteoric gases such as hydrogen sulfide (H_2S), and carbon dioxide (CO_2) (Arnórsson, 1986; Pfeiffer et al. 2018).

Sequestration of CO_2 in geological formations is a well-studied topic. CO_2 storage relies on variety of trapping mechanisms, including: physical trapping where CO_2 is trapped in a gaseous, liquid, or critical state in a subsurface formation. Geochemical trapping of CO_2 as dissolution within brine, hydrocarbon, or other formation fluids, and mineralization (Shukla et al. 2010; André et al. 2012; Jin et al. 2016). It is generally not cost-effective to consider gas injection in oil and gas projects without enhanced gas and oil recovery. Possible CO_2 underground storage applications are enhanced coal bed methane recovery, gas hydrate production by injecting CO_2, enhanced gas recovery and oil recovery, CO_2 storage in deep saline depleted oil and gas reservoirs, and CO_2 sequestration into geothermal reservoirs.

CO_2 sequestration into geothermal reservoirs is attractive for a number of reasons. To illustrate, CO_2 can be permanently stored in the reservoir as dissolved gas or converted into rocks through mineralization. In addition to reducing greenhouse gas emissions, CO_2 injection can also have a positive impact on production wells. CO_2

content can significantly impact the performance of geothermal wells, so reinjecting CO_2 into the reservoir can help to compensate pressure depletion due to production wells by creating a partial pressure in the wellbore. Prior to the implementation of a large-scale CO_2 sequestration project, it is essential to assess the potential water-rock interactions. Key considerations are water-rock interactions, reactive-transport simulations, and deciding on the gas injection method: supercritical or dissolved gas, The potential problems that may arise from long-term CO_2 reinjection are ground deformation, gas leakage along the faults, mineral precipitation causing a decline in reinjection capacity, and two-phase fluid flow in the reservoir causing production decline (Hou et al. 2012). A limited number of studies are available about these topics.

This dissertation investigates CO_2 sequestration in Paleozoic-aged geothermal reservoirs in western Anatolia, Turkey. The study begins with CO_2 dissolution experiments using a novel experimental setup. Real reservoir gas and geothermal brine were used in the experiments, and validated with empirical and geochemical models using PHREEQC. The calibrated PHREEQC model was then employed to understand the effects of salting-out and gas impurity at higher reservoir temperatures and pressure values representing reservoir conditions.

Following the CO_2 dissolution experiments, water-rock interaction experiments were conducted in a batch experimental setup. The experiments involved a continuous CO_2 supply at constant pressure and using crushed rock samples from 1900 m and 3000 m depth reservoir rock in Kızıldere geothermal field. The batch experiments were then simulated using PHREEQC codes to obtain mineral kinetic rates and activation energy of minerals. Once the model was calibrated, the matched data were used to perform a 3D reactive transport simulations in TOUGHREACT. This revealed the long-term effects of CO_2 injection in both reinjection and production wells in the Kızıldere geothermal reservoir.

The dissertation is organized as follows:

Chapter 2 provides an overview of recent carbon capture and storage (CCS) technologies and worldwide field applications, including enhanced oil recovery (EOR), enhanced gas recovery (EGR), coal bed methane recovery, in gas hydrate production, deep saline water, and geothermal reservoirs. It also discusses NCG capture in geothermal power plants and mineral trapping of CO_2 in geothermal reservoirs, with a detailed description of typical rock alterations.

Chapter 3 identifies the main research questions to be addressed in this dissertation.

Chapter 4 decribes the materials and methods used in this study. This includes a detailed description of the experimental setup and procedure for CO_2 dissolution, batch experiments and core-flood experiments. The methodology of the modeling approaches used for the batch experiments and 3D reactive transport simulation is also discussed.

Chapter 5 presents results obtained from CO_2 dissolution, batch and core-flood experiments. The results of the experiments are discussed and compared to the simulations. The parameters obtained from the batch model calibration are then used in the 3D reactive transport model to estimate the long-term effects of CO_2 injection in the Kızıldere geothermal reservoir. The effects of CO_2 sequestration on the reinjection well and the performance of production wells are delineated.

Chapter 6 summarizes the findings of the study and presents the key conclusions in bullet poin

CHAPTER 2

LITERATURE REVIEW

This chapter provides a general overview of carbon carbon capture, transportation, utilization, and storage methodology as shown in Figure 2.1. The study focuses on CO_2 sequestration in geothermal reservoirs.

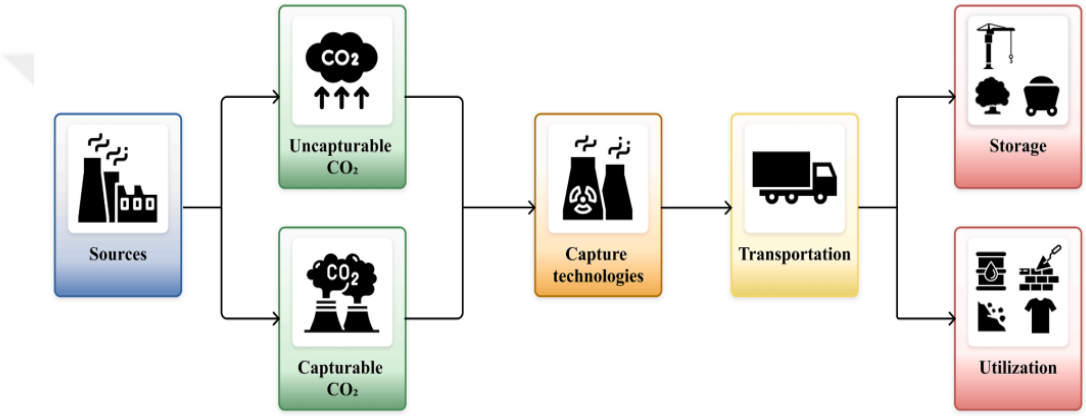

Figure 2.1 Carbon capture, transportation, utilization, and storage (Dziejarski et al., 2023).

A comprehensive literature review was conducted to provide a deeper understanding of CO_2 injection into geothermal formations and water-rock interaction experiments to date. CO_2 can be reinjected into the reservoir as dissolved gas or in a supercritical state. In both reinjection methods, CO_2 mixes with brine in the reservoir, and CO_2 saturation increases rapidly. The acidic brine reacts with carbonate minerals within days to weeks. These reactions buffer fluid pH and alkalinity, and the dissolution of carbonate minerals results in carbonate precipitation. In some cases, caprock is exposed to CO_2-rich brine in the experiments.

2.1 Carbon Capture Technology

The three critical steps of CCS are capture, transportation, and storage. Carbon capture is the most expensive step in CCS projects. The operational and investment costs of CCS projects are still not competitive with carbon taxes and trading prices. Therefore, carbon capture technology is still under development. The costs of carbon capture technology have been reported to range from US$35/t carbon to US$264/ton carbon and from 24 to 52 EUR/ton of carbon (Bode and Jung, 2006).

Carbon capture technology can be classified into three categories: post-combustion, pre-combustion, and oxyfuel combustion (Figure 2.2). Application of the Pre-combustion system has started in the last few years. Oxyfuel has no field-scale application. The number of post-combustion capture cases has doubled since 2006.

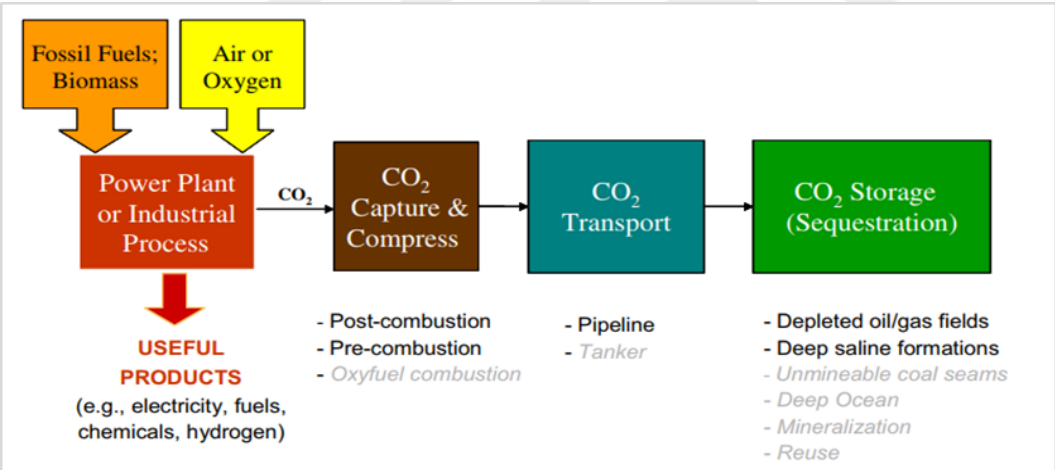

Figure 2.2 Schematic view of a CCS system (Rubin et al. 2012).

Post-combustion process involves the separation of CO_2 from the flue gas. It is typically implemented in steam turbine power plants. It is a highly mature technology applied at full-scale commercial plants. The products of gas combustion, flue gases, are released into the atmosphere via the stack. CO_2 is captured with different systems, such as adsorption, absorption, and membrane separation. The

method is compatible with the existing power plants. Large equipment sizes create high capital and operational costs. The capital cost of post-combustion is around 900 USD/kW for gas-fired plants and about 2000 USD/kW for coal-fired plants (Theo et al. 2016).

In the pre-combustion, CO_2 is eliminated before the combustion process. A partially combusted fuel produces CO_2/CO and H_2, which is then eliminated from CO_2 through chemical and physical processes. Pre-combustion carbon capture is favorable at high pressures and low-temperature conditions. It is a less-energy-intensive CO_2 separation process. As a result of pre-combustion, hydrogen gas is obtained as an alternative fuel. One of the disadvantages of the method is significant energy loss due to sorbent regeneration, which is still less than post-combustion capture. The high capital cost of the Integrated Gasification Combined Cycle (IGCC) makes the pre-combustion method unfavorable. The capital cost is around USD1200 per kW for gas-fired and USD 1900 per kW for coal-fired plants (Theo et al. 2016).

The oxyfuel method uses oxygen instead of air for combustion. The oxyfuel technology has not been fully developed yet. The application is limited to pilot-scale operations. It is compatible with a variety of coal fuels. The method is easy to apply and has high carbon capture efficiency. However, it requires developed air separation technology. Energy-intensive air separation units reduce the net power output. The typical two issues in this method are possible corrosion problems and leakage problems due to overpressure. The capital cost is around USD1600 per kW for gas-fired and USD2300 per kW for coal-fired plants (Theo et al. 2016).

2.2 Carbon Storage Technology

Carbon storage in geological formations is a mature technology that has been under development for over 40 years. This research has improved our understanding of subsurface storage mechanisms, working principles, and monitoring methods. The geological carbon storage can be achieved through a physical trapping or

mineralization. Possible storage systems include deep saline aquifers, depleted oil and gas reservoirs, and geothermal reservoirs. CO_2 can also be stored in the form of hydrate at the seafloor, but this may have significant negative consequences for marine life. Therefore, geological storage is considered as the most suitable option. Long-term carbon storage projects involve risks, such as leakage through conductive faults, cement failure, and surface deformation. It is critical to select the appropriate field and reservoir storage application. A comprehensive characterization study is required to understand CO_2 storage, including seismic surveys, geological analysis, reservoir simulation, and monitoring systems.

Critical reservoir parameters that influence geological carbon storage include porosity, permeability, mineral content of the reservoir rock, fluid geochemistry, reservoir pressure, and temperature. Screening these reservoir parameters can be useful for selecting suitable sites for CCS applications. Ramirez et al. (2010) used the Multi-Criteria Analysis (MCA) method to screen reservoir parameters for long-term CO_2 storage.

2.2.1 CO_2 Injection for Enhanced Coal Bed Methane (CBM)

Carbon dioxide (CO_2) can be used to displace methane (CH_4) from coal seams due to their different adsorption-desorption properties. This process, known as carbon dioxide enhanced methane recovery (CO_2-ECBM), can enhance CH_4 recovery while also permanently storing CO_2 underground. Figure 2.3 shows the schematic representation of CO_2 sequestration in CBM reservoirs. Vishal et al. (2012) conducted a field-scale study of CO_2-ECBM in a coal block. They showed that it is possible to inject 427.5 million m^3 of CO_2 into the coal block and recover 141.6 m^3 of CH_4.

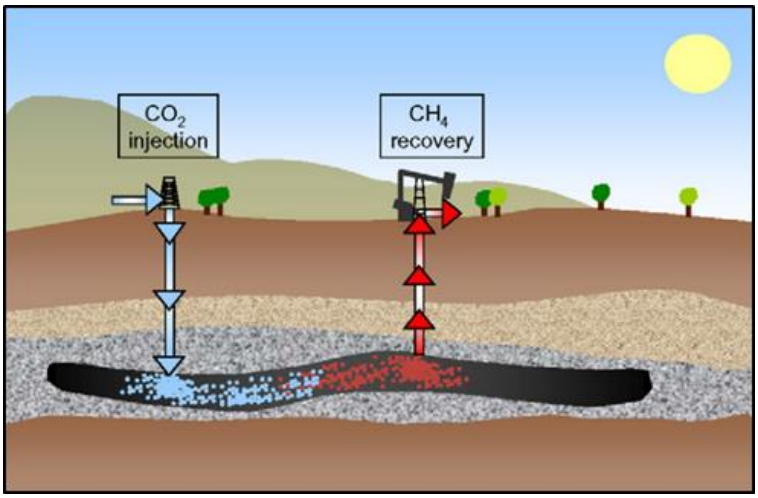

Figure 2.3 Schematic representation of Enhanced CBM process (Mazzotti et al. 2009).

Sınayuç and Gümrah (2009) proposed CO_2 injection into the Amasra coalbed in Zonguldak, Turkey to enhance coalbed methane production. They used the Computer Modeling Group's (CMG) GEM module to simulate the effects of coal density, adsorption capacity, permeability, porosity, and anisotropy on CBM production.

2.2.2 Gas hydrate production by injecting CO_2

Gas hydrates are a type of unconventional natural gas reservoir in which methane is trapped within water molecules at low temperatures and high pressures in sand pores. One hydrate production technique is to replace methane (CH_4) with CO_2 in the hydrate formation. CO_2 is injected and stored in the hydrate formation, while CH_4 is released as a gas production technique. This process can help to maintain formation stability during methane production, which is one of the main challenges in gas hydrate production (Figure 2.4). White et al. (2005) overviewed this process with a wide literature searching. Ors and Sinayuc (2014) demonstrated this process in CO_2

-CH_4 swap experiments, suggesting that replacing CO_2 with CH_4 can increase the stabilization of unconsolidated sand packs.

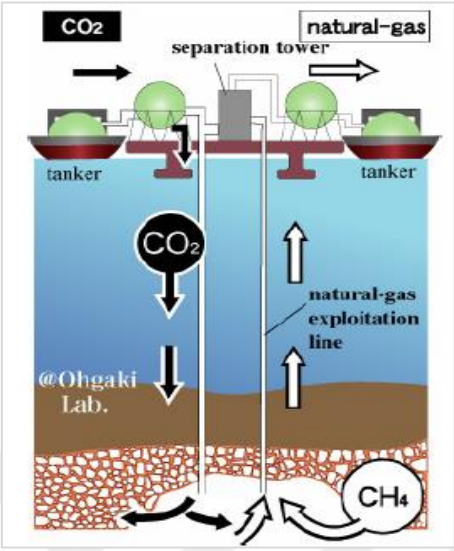

Figure 2.4 Schematic diagram of natural gas exploitation and CO_2 isolation process (Phale et al. 2006).

2.2.3 EGR and EOR Methods in Shale Gas Reservoirs

The huff-n-puff method has been effectively applied in shale oil reservoirs. Gas is injected into low permeability shale formations in a cyclic manner, where it diffuses into the oil during the soaking period. After soaking, the well is produced for a while, during the puff period. CO_2 is one of the most widely used gases in huff-n-puff processes (Figure 2.5). During these processes, a significant portion of CO_2 is stored as clay minerals in the shale rocks. Sun et al. 2016 investigated the impact of molecular diffusion of CO_2 on the performance of huff-n-puff. The huff-n-puff method is more effective when the reservoir pressure is below the bubble point pressure. CO_2 flooding is another crucial CO_2 trapping application in enhanced oil

recovery projects (Figure 2.6). It is a common method used in heavy oil reservoirs to reduce the viscosity of the oil.

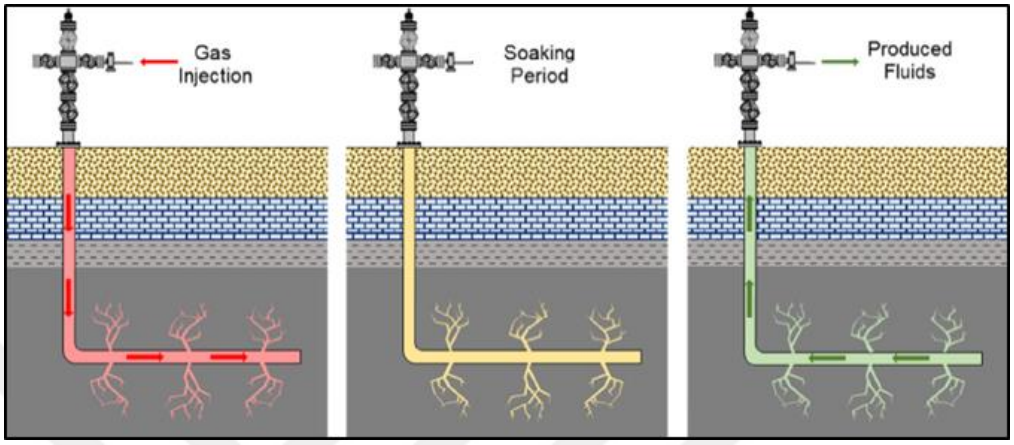

Figure 2.5 Simplified Huff and Puff cyclic gas injection (Pankaj et al., 2018).

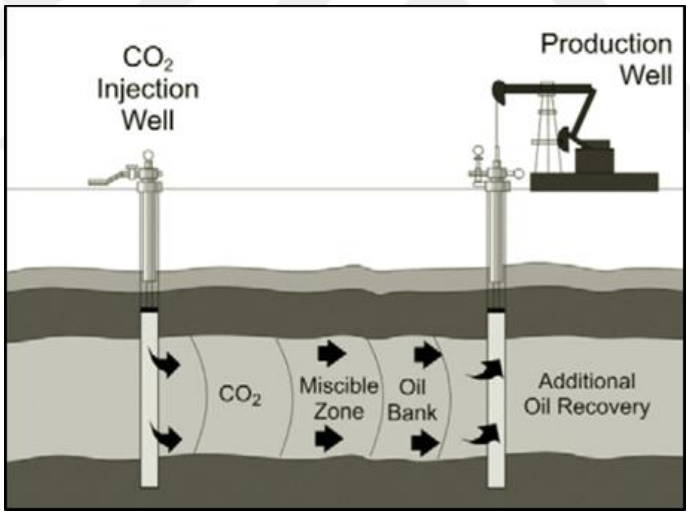

Figure 2.6 CO_2 injection for enhanced oil recovery (Shevalier et al. 2009).

Comprehensive understanding of the operational mechanism of enhanced gas recovery (EGR) with CO_2 injection is essential for large-scale field applications. Nuttal et al. (2005) used drill cuttings from the Kentucky Geological Survey Well Sample to investigate CO_2 displacement methane. Similarly, Merey and Sinayuc

(2016) used experimental adsorption measurements to investigate CO_2 sequestration in the Dadas shale reservoir. Their findings suggest that CO_2 injection into shale reservoirs is a promising option for both enhancing gas production performance and permanently sequestering CO_2.

2.2.4 CO_2 Sequestration in Deep Saline Aquifers

Depleted oil and gas reservoirs are geological formations that have the potential to be used for carbon storage (Figure 2.7). The black oil simulator is a numerical model that can be used to simulate CO_2 storage in saline aquifers. Bachu and Adams (2003) estimated the ultimate CO_2 sequestration capacity in the Viking aquifer in the Alberta basin in western Canada. They used empirical corrections to the CO_2 content at saturation in pure water to determine CO_2 content in the reservoir brine. The CO_2 storage capacity of the Alberta basin at depths greater than 1000 m was reported to be 4000 Gt CO_2. Ampomah et al. (2015) used a compositional simulator to simulate CO_2 storage in depleted oil reservoirs. Their simulations showed that over 25 years of water alternating gas (WAG) injection, 75 % of the CO_2 was sequestered within the Murrow formation. In Salah project is a large-scale carbon capture and storage project that is being developed by a joint venture of Statoil, BP, and Sonatrach. The project has successfully injected CO_2 into a deep saline formation near Algeria's producing gas field. Morris et al. (2010) studied the mechanical deformation caused by CO_2 injection in the Salah field. Zhang et al. (2014) investigated the potential of CO2 storage in the Jilin oilfield. They showed that 60.2 % of CO_2 is trapped in a supercritical state, and the remaining CO_2 is dissolved in residual oil and water. The North Sea has significant potential for CO_2 storage. Chamwudhiprecha and Blunt (2012) studied CO_2 injection into a large aquifer in the North Sea.

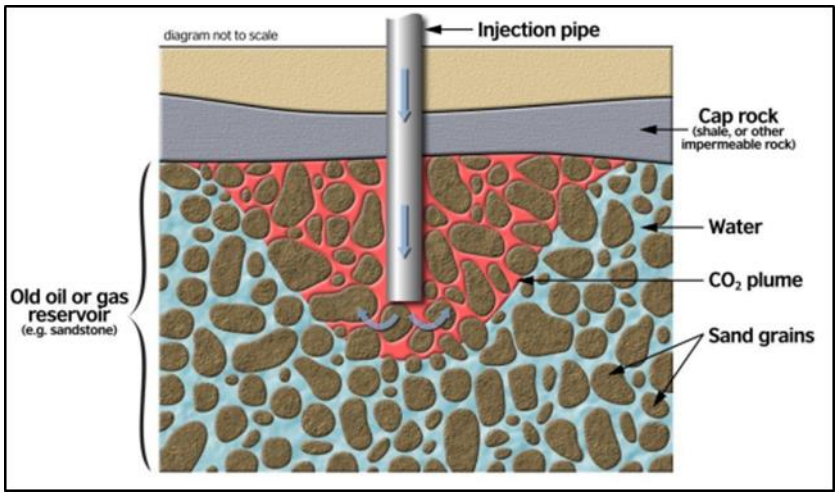

Figure 2.7 Injection of carbon dioxide into depleted oil and gas reservoir (Scottish Centre for Carbon Storage, 2023).

Sedimentary rocks are potential formations for CO_2 storage because of their high capacity. Benson and Cole (2008) presented a map of sedimentary basins in the world that might be suitable for CO_2 storage (Figure 2.8). They estimated the gas storage capacity of the deep saline reservoirs changing between 1000 and 10000 Giga tons.

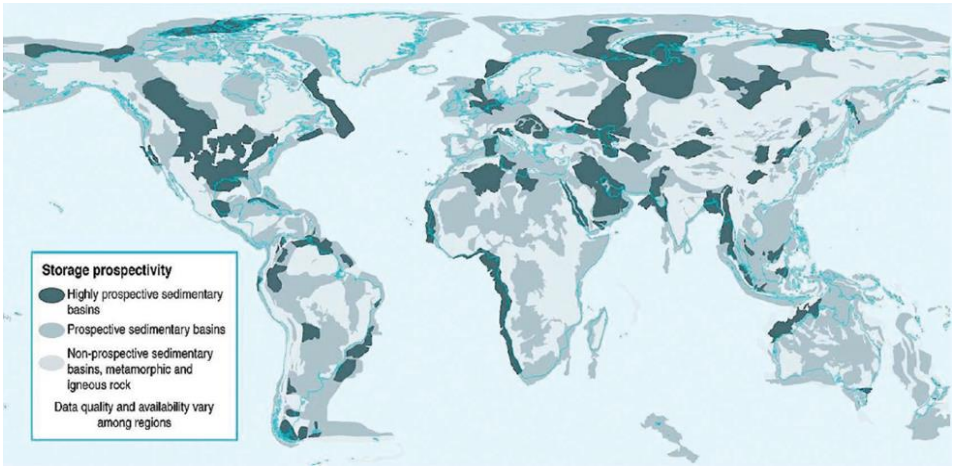

Figure 2.8 Sedimentary basins showing suitability as sequestration sites (Benson and Cole, 2008).

2.2.5 CO_2 Dissolution and Sequestration into Geothermal Reservoirs

Experimental studies, empirical correlations, and statistical analyses have been used to estimate the solubility of CO_2 in water over a range of temperature and pressure intervals. Most of these studies have focused on the dissolution of pure CO_2 in fresh water. Malinin (1959) published one of the first methodologies for CO_2 solubility in water, based on experimental results. His study proposed a modified version of Henry's law that uses an exponential correction factor. Experimental-based correlations proposed in different studies are shown in Figure 2.9 (Malinin, 1975; Fournier, 1989; Crovetto, 1991; Moya and Iglesias, 1992; Battistelli et al., 1997). The empirical correlations begin to diverge at temperatures above 75 ^{o}C. However, all correlations agree well on the values of CO_2 solubility at low temperatures.

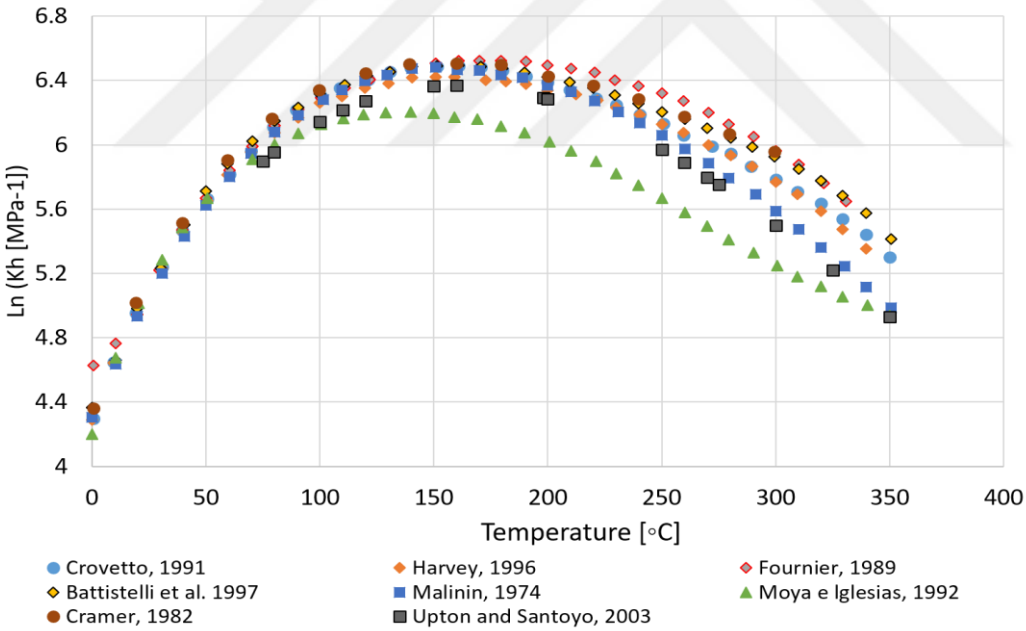

Figure 2.9 Henry's constant (KH) calculated for the H_2O-CO_2 using five different empirical correlations.

The solubility of CO_2 in the geothermal brine is a function of temperature, pressure, and brine salinity. Gas dissolution experiments are essential prior to large-scale CO_2

sequestration projects. Researchers have investigated CO_2 solubility in pure water and saline water at various temperatures, pressures, and salt types (NaCI) (Table 2.1). Henry's law constant (KH) is one of the most widely used methods for estimating CO_2 solubility in water. However, the lack of the experimental data and the use of different equations have led to significant discrepancies. Additionally, most studies have focused on CO_2 solubility alone and have not considered other gases such as H_2S. In this study, we investigate CO_2 solubility in geothermal brine, instead of fresh water using actual field gas and brine samples. A novel experimental setup continuously heated with geothermal brine was used to measure the gas phase and brine separately and to conduct alkalinity tests. The results of this study will provide valuable insights for CO_2 injection projects in the geothermal industry.

Table 2.1 Studies about CO_2 solubility in water.

Solution	Temperature (^oK)	Pressure (Bar)	Reference
Water	323-373	25-710	(Wiebe and Gaddy, 1939)
Water	286-348	1.02-1.40	(Morrison and Billett, 1952)
Water	383-623	100-1500	(Takenouchi and Kennedy, 1964)
0-2 m NaCl	445-610	15-200	(Ellis and Golding, 1963)
0-6 m NaCl	298-423	47.92	(Malinin and Kurorskaya, 1975)
1-4.3 m NaCl	408-800	30-2800	(Gehrig, 1980)
0-0.17 m NaCl	353-473	20-100	(Nighswander et al. 1989)
4-6 m NaCl	313-433	1-100	(Rumpf et al. 1994)
0-4.3 m NaCl	273-533	0-2000	(Duan and Sun, 2003)
Water	298-623	29.42-98.1	(Upton and Santoyo, 2003)
0-4.5 m NaCl	273-533	0-2000	(Duan et al. 2006)

Table 2.1 (cont'd)

0-5 m NaCl	323-413	5-40	(Yan et al. 2011)
2m NaCl	120	0-35	(Savary et al. 2012)
Water	338-373	3-200	(Caumon et al. 2016)
1.81- 2.53 m K_2CO_3	353-393	0-1	(Grimekis et al. 2019)

Upton and Santoyo (2003) proposed an empirical correlation for CO_2 dissolution that can be coupled with a geothermal wellbore simulator to study vertical two-phase flow in the wellbore. They performed statistical analysis on experimental data obtained from previous studies to develop CO_2 solubility curve. The salting-out effect is another critical parameter that determines the amount of CO_2 dissolved in water. Liu et al. (2011) studied the solubility of CO_2 in aqueous solutions with NaCl, KCl, and $CaCl_2$. They found that the solubility of CO_2 is directly proportional to pressure and inversely proportional to temperature. The addition of salt to the mixture is unfavorable for CO_2 dissolution due to the salting-out effect. The salting-out effect of KCl was reported to be relatively smaller than those of NaCl and $CaCl_2$. Yan et al. (2011) simulated CO_2 solubility in NaCl brine using experimental data and EOS models.

There are suitable geothermal reservoirs that contain anhydrite ($CaSO_4$) as a matrix mineral and plagioclase that supplies alkalinity. The CO_2 storage capacity depends on reservoir characteristic properties, such as porosity, area, thickness, and chemical and mineralogical composition of the brine and reservoir rock. Mass balance calculations show that the storage capacity can be estimated from the abundance of anhydrite in the reservoir. Due to the decreased solubility of anhydrite with temperature, injecting cold water dissolves the mineral in a region expanding around the well. The concentrations of calcium and sulfate increase in the water with the dissolution of anhydrite as given in Equation (2.1):

$$CaSO_4 <=> Ca^{++} + SO_4O_4^{--} \quad (2.1)$$

Before re-injection, the produced and cooled brines will be enriched with carbon dioxide generating; as a result, carbonic acid is formed as shown in Equation (2.2).

$$CO_2 + H_2O \ <=> H_2CO_3 <=> H^+ \ HCO_3^- \quad (2.2)$$

The overall reaction, the transfer of anhydrite into calcite, describes the favored reaction path described in Equation (2.3):

$$CaSO_4 + \ H_2CO_3 \ <=> CaCO_3 + 2H^+ + SO_4^{--} \quad (2.3)$$

Equation (2.3) shows that there is an excess of acid, which generally inhibits calcite precipitation. However, if the increase in Ca is large enough as given in Equation (2.1) or if alkalinity is available to buffer the reaction, the solubility product of calcite is exceeded, and CO_2 will be trapped as calcite. Alkalinity can be provided by surface water treatment with fly ashes or in situ by weathering feldspars.

CO_2 can be dissolved in the brine in the form of carbonic acid ($H_2CO_3^-$), which then dissociates into bicarbonate (HCO_3^-), and carbonate (CO_3^{2-}) ions that are more stable species at the first step of the transformation of CO_2. The equilibrium equations given below, Equations (2.4), (2.5), (2.6) show the transformation of CO_2 during the injection (Thomas et al., 2015). The release of H+ during the equilibria lowers the pH of the aqueous solution.

$$CO_{2(g)} <=> CO_{2(aq)} \quad (2.4)$$

$$CO_{2(aq)} + \ H_2O <=> H^+ + HCO_3^- \quad (2.5)$$

$$HCO_3^- \ <=> H^+ + CO_3^{2-} \quad (2.6)$$

CO_2 injection can be carried out in two ways: as a dissolved gas in the brine or as a pure gas injected into the well at supercritical conditions (Figure 2.10). Injecting CO_2 at supercritical conditions is more challenging due to the need for high gas compression and sophisticated infrastructure (Figure 2.11). Therefore, injecting CO_2 as dissolved gas in the brine is more practical and cost-effective. CO_2 dissolution can be achieved by mixing CO_2 and brine along the surface lines or in the wellbore using single or dual string systems (Figure 2.12). The appropriate pressure, temperature, and mixing ratio must be used to achieve efficient CO_2 dissolution. The main advantage of CO_2 dissolution in the brine (mixing on the surface) is that low pressure is required to dissolve the gas at a relatively low brine injection temperature. In this study, we focus on the experiments and simulations involving gas dissolution in geothermal brine.

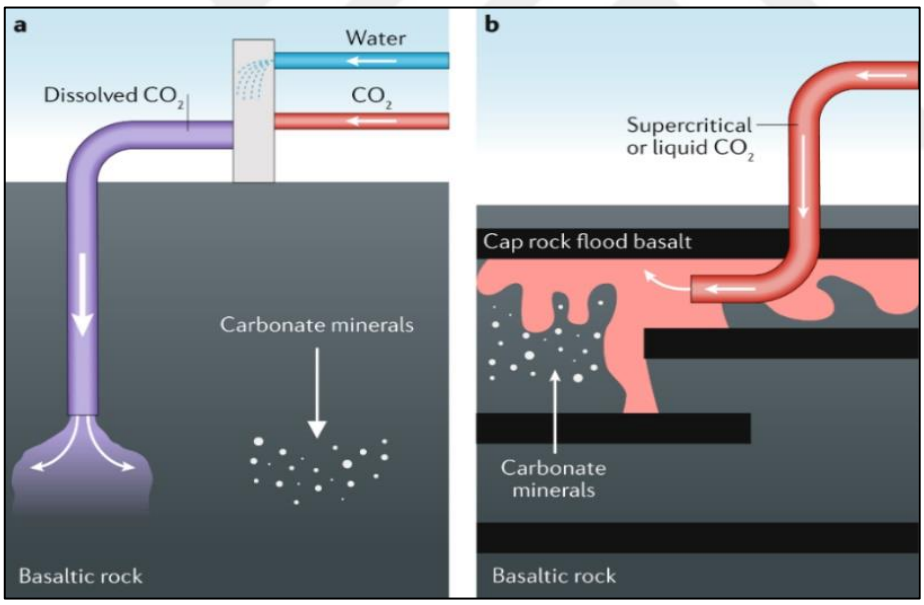

Figure 2.10 CO_2 injection as a dissolved gas in water (a) and supercritical condition (b) (Snæbjörnsdóttiret al. 2020).

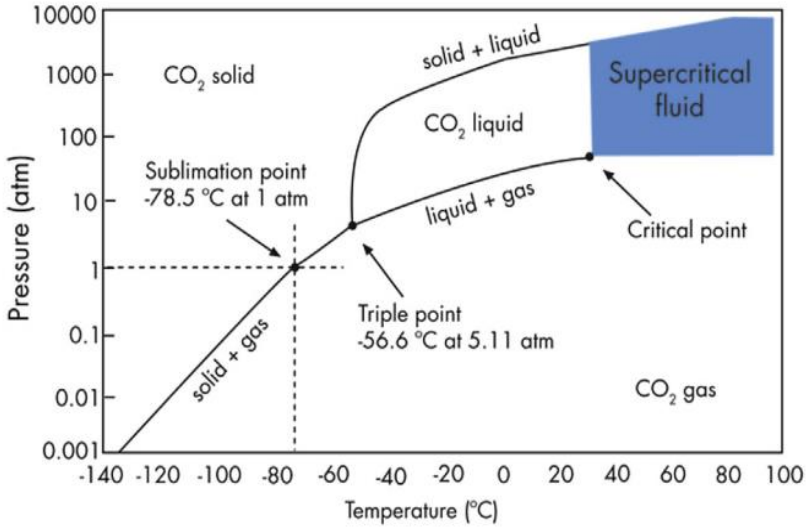

Figure 2.11 Phase diagram of CO_2 (Saeedi, 2012).

Figure 2.12 CO_2 injection by using a dual string system in Iceland (CarbFix project, 2018).

2.3 Worldwide Carbon Capture and Storage (CCS) Field Applications

CCS is a costly process typically implemented as complementary to EOR and EGR projects. Some important CO_2 sequestration projects are listed in Table 2.2 and shown in map Figure 2.13

Table 2.2 Database of large-scale CCS projects operated or identified in recent years (Raza et al. 2016; Kelemen et al. 2019).

Location	**Operation date**	**Primary storage type/formation**
Sleipner, Norway	1996- Present	Saline formation/ sandstone/
Weyburn, Canada	2000- Present	EOR/carbonates
ORC (K12-B) phase 2, Netherlands	2004- Present	Depleted gas field Rotliegend (sandstone)
In Salah, Algeria	2004- Present	Producing gas field Krechba (carbonate)
Frio Project, USA Gulf Coast	2004-Present	Deep Saline Aquifer in sandstone
Snøhvit Offshore Norway	2008–Present	Sandstone
CarbFix, Iceland	2007-Present	Basalt geothermal reservoir
Quest Alberta, Canada	2015- Present	Basal Cambrian Sands

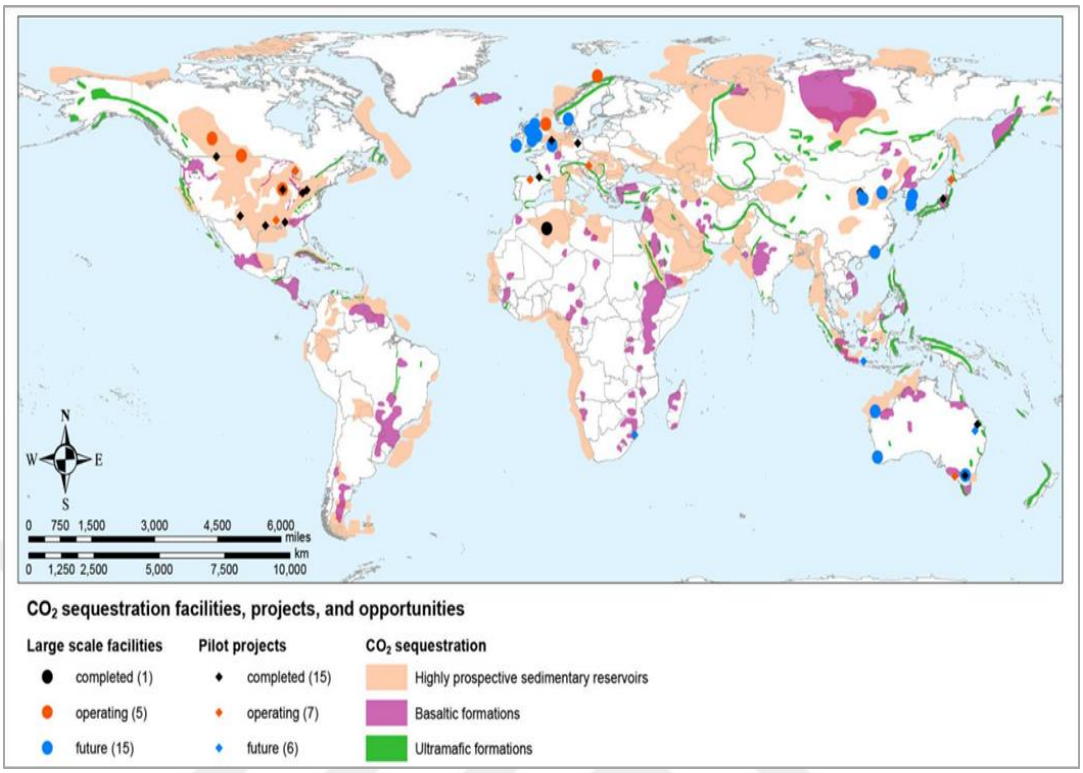

Figure 2.13 Map of CO_2 sequestration facilities, pilot projects, and long-term storage potential in geologic formations (Kelemen et al. 2019).

The Frio-I project tested the injection of 1600 tons of CO_2 into the Upper Frio Formation at a depth of 1500 m over 11 days (Figure 2.14). The results showed that the flow rates of CO_2 and brine significantly influenced CO_2 dissolution in the brine and the interaction between the CO_2 and the rock minerals. Carbon dissolution moved to carbonate precipitation in days to weeks with the alkalinity of pH. Silicate mineral dissolution reactions were initially fast in low pH fluids surrounding the CO_2 plume; but the reaction rate decreased by 2-5 orders of magnitude as the system approached the thermodynamic equilibrium.

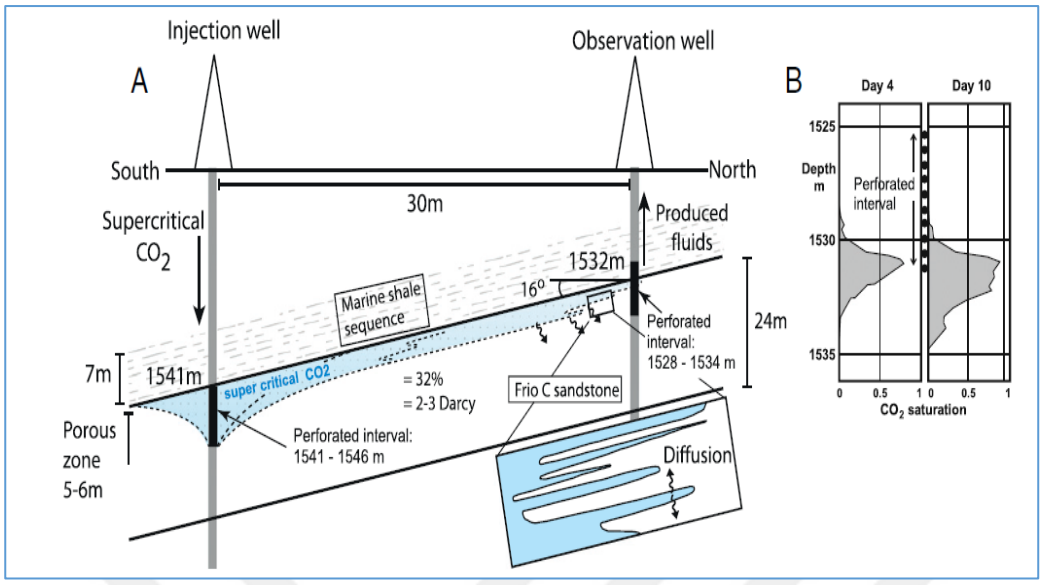

Figure 2.14 The Frio-I injection experiments (Kampman et al. 2014).

EnCana Corporation conducted a large-scale CO_2 injection project as part of Enhanced Oil Recovery in the Weyburn oil field. The injection rate was approximately 5000 tonnes per day. Emberley et al. (2004) monitored changes in the fluid chemistry and isotope composition for a year. The fluid compositions suggested 100 million tons of CO_2 storing potential in the injection area. Zhang et al. (2009) presented a long-term case study of CO_2 trapped in deep saline formations in Songliao Basin, China. They reported the CO_2 storage capacity of 10 kg/m^3 for mineral trapping.

The Sleipner CCS project was started in 1996, located 200 km from shore, injecting CO_2 into the Utsira sandstone reservoir at a depth of 1012 m. A 50 m thick shale formation acts as caprock for the Sleipner project (Zhang et al. 2022). The latest CO_2 injection rate was reported as 1Mtpa (Eiken, 2019). The project will terminate when the average reservoir pressure approaches shale fracturing pressure (Shukla et al., 2010).

In Salah CO_2 storage project has been in operation since 2004 (Mathieson et al. 2011). CO_2 is injected into a fractured Carboniferous sandstone reservoir with a 20

m thickness at around 1850 m depth. The seal rock is mudstone overlain by sandstone with 900 m thickness. The injectors were drilled horizontally (1500-1800 m) by using geosteering technologies to keep the well in the formation and perpendicular to the dominant fracture orientation to achieve maximum injection capacity (Mathieson et al. 2011). The total CO_2 injection rate reached up to 50 mmscfd and is planned to store 17 million tons of CO_2 over the project's life (Mathieson et al. 2011).

CarbFix project involves CO_2 sequestration into a basaltic geothermal reservoir in Iceland. The project was officially established in 2007 (Matter et al., 2009). The field is located at SE Iceland, near the Hellisheidi geothermal power plant, which produces 30,000 tons of CO_2 per year (Figure 2.15). The major gases in the NCG were mainly CO_2 (83 %) and H_2S (16 %). The NCG was mixed and re-injected with geothermal water into the basalt aquifer. Prior to CO_2 injection, which began in 2009, reservoir characterization studies such as tracer tests, geophysical measurements, and soil CO_2 flux measurements were carried out. The CO_2 injection zone is located at a depth of 400 to 800 m. CO_2 was injected at 25 bar and at a rate of 0.5 kg/sec to 0.7 kg/sec accompanied by 20-25 l/sec of water. This injection method is expected to result in faster CO_2 mineralization than injection in supercritical gas form.

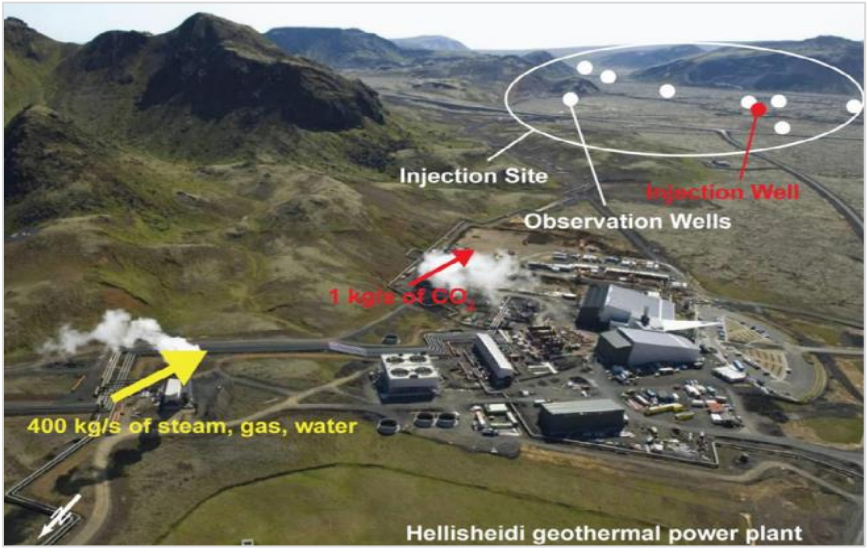

Figure 2.15 CO_2 injection site in Iceland (Matter et al., 2009).

2.4 Non-Condensable Gases in Geothermal Energy

Geothermal energy is a renewable, sustainable, and environmentally friendly energy resource. The average greenhouse gas emission from geothermal resources is lower than that of fossil fuel-based power plants (Figure 2.16). Geothermal energy can be used for different applications, depending on the resource temperature. Resource with a temperature of more than 150 ^{o}C can be used for electricity generation, while low-temperature resources can be used for direct-use applications such as heating greenhouses, thermal hotels, food drying, etc. Geothermal energy is generally abundant in tectonically active areas such as Indonesia, Turkey, the United States, the Philippines, New Zealand, El Salvador, Iceland, and Japan. Faults and fault-associated fractures are the primary fluid conduits in geothermal reservoirs. Porous sedimentary rocks can also serve as reservoir rocks for a geothermal system. The main parameters that influence geothermal systems are the depth of heat source, the stratigraphic sequence of formations, the tectonic mechanisms, and the convective and conductive heat flow mechanisms. In addition to conventional geothermal systems, new technologies such as Enhanced Geothermal Systems (EGS) are being developed. EGS is a technology that uses hydraulic fracturing to create artificial reservoirs for geothermal fluids. EGS is still in the pilot stage, but it has the potential to increase the amount of geothermal energy that can be extracted.

Geothermal reservoirs may contain a certain amount CO_2, which can have different origins, such as magmatic rock, meteoric water, and sedimentary rock. Meteoric-origin CO_2 is found in most of the geothermal reservoirs in western Turkey (Haizlip et al., 2016). Aydin et al. (2020) reported that Paleozoic-aged Menderes metamorphic host liquid dominated geothermal fluid in the Kızıldere, with a CO_2 content higher than the average value of the world's geothermal reservoirs. The CO_2 content of the Kızıldere field ranged from 1 % to 2 % for the intermediate reservoir rock, which is Igdecik formation, and the deep metamorphic contains CO_2 ranging from 3 % to 4 % (Satman et al. 2017). However, a significant decline in CO_2 production has been reported as the fields have been put into production and

injection. To illustrate, Aydin et al. (2020) presented a sharp decline in CO_2 production for Alaşehir and Kızıldere geothermal reservoirs (

Figure 2.17). More than 98 % of NCG in the Kızıldere field consists of CO_2, remaining less than 2 % of NCG consists of hydrogen sulfide, ammonia, argon, nitrogen, methane, and hydrogen. Therefore, it would not be an exaggeration to consider NCG as CO_2 for the Kızıldere field. This study focuses on the Kızıldere geothermal field, which is in the Denizli province of Turkey (Figure 2.18).

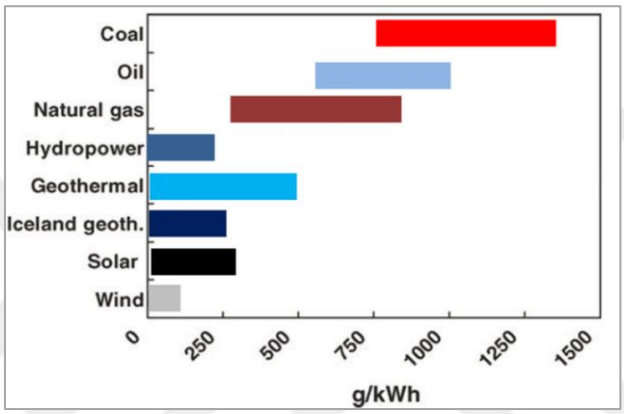

Figure 2.16 Gas emission from different energy sources (revised from Amponsah et al., 2014).

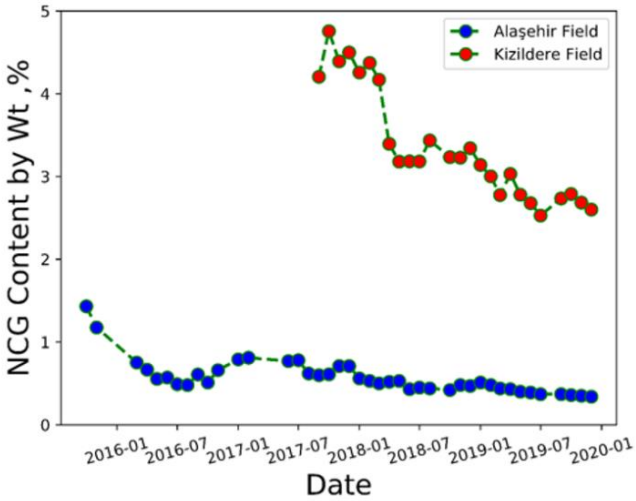

Figure 2.17 NCG decline of Alaşehir and Kızıldere geothermal reservoirs (Aydin et al. 2020).

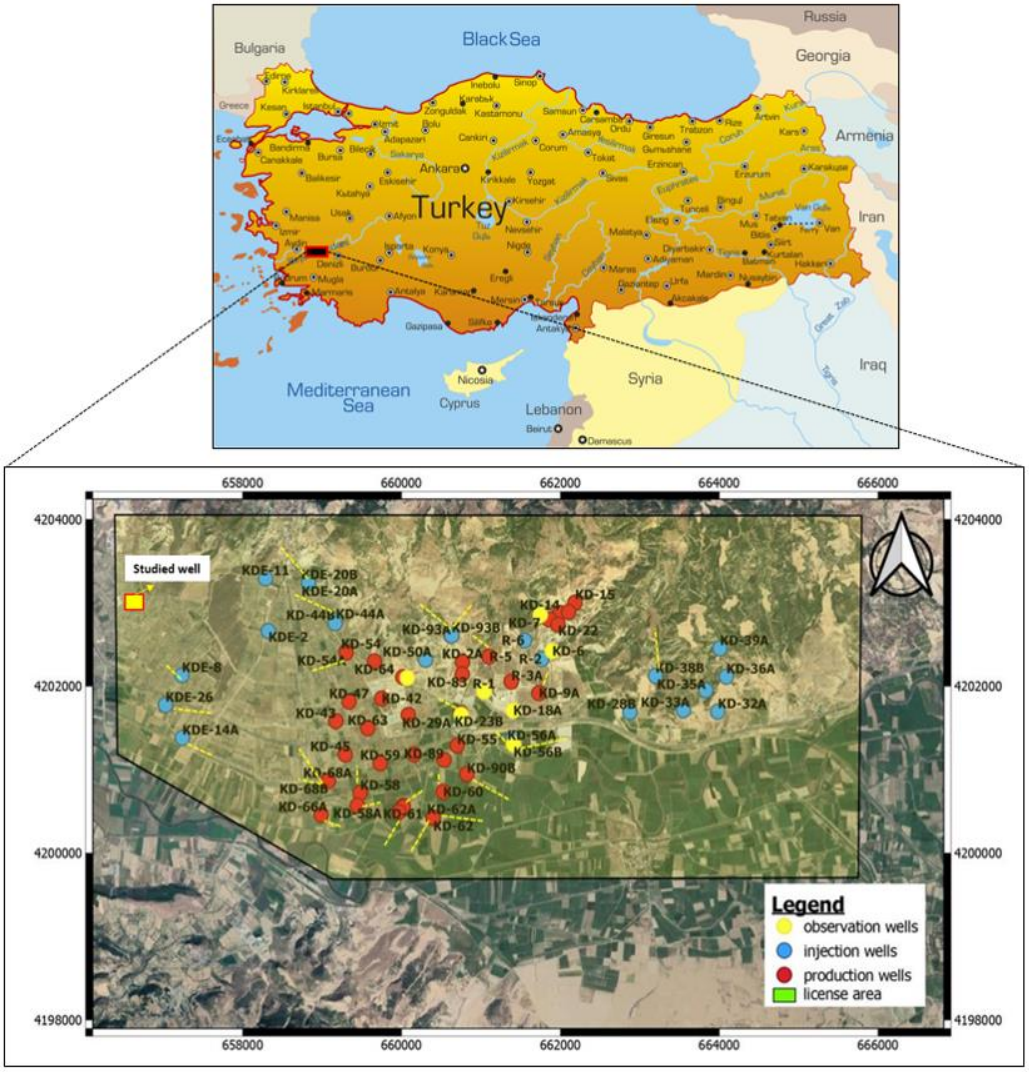

Figure 2.18 Kızıldere geothermal field and location of the studied well (Modified from Haklıdır et al. 2021).

The Kızıldere geothermal field hosts three geothermal power plants (GPPs). GPP-I has been in operation for over 40 years and has a single flash system with an installed capacity of 20 MW. GPP-II was commissioned in 2013 and has a maximum capacity of 80 MW, with a triple flash and a binary (combined) system. The third plant was commissioned in 2017 and 2018 in two units, with a total capacity of 165 MW. This plant also uses a triple flashing system and a binary unit (combined) system. All of the units have a wet cooling tower, which release non-condensable gases (NCGs)

with waste steam to the atmosphere (Figure 2.19). NCG content of the Kızıldere field is given in Table 2.3. CO_2 constitutes more than 98 % of the dry gas volume.

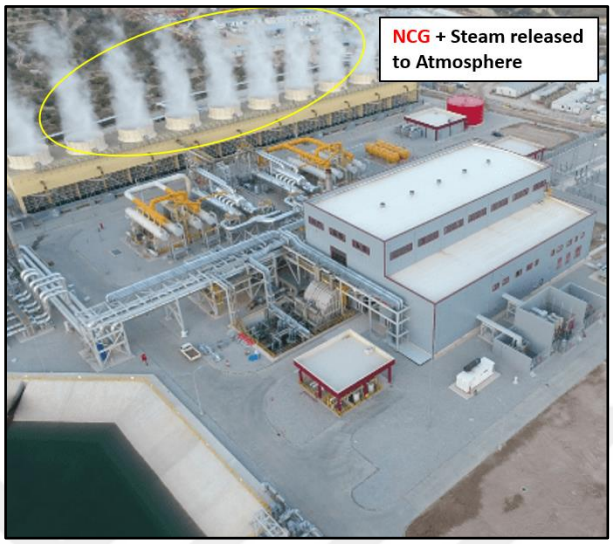

Figure 2.19 NCG releasing to atmosphere in Kızıldere geothermal power plant.

Table 2.3 Composition of NCG in Kızıldere field.

Gas Composition	Volume % in dry gas
Carbon Dioxide (CO_2)	98.9
Nitrogen	0.577
Methane	0.426
Hydrogen Sulfide (H_2S)	0.052
Ammonia	0.0494
Argon	0.00129
Hydrogen	0.000693

The NCG removal system is used to separate NCG from the geothermal power plant. A schematic illustration of the NCG removal system in a flashing-type geothermal power plant is shown in Figure 2.20. The condenser of flashing-type plants has

significant parasitic load effects on the overall power generation of the geothermal plants. Therefore, the condenser should be operated under vacuum to reduce the backpressure on the turbine. The CO_2 and H_2S are withdrawn from the condenser by the vacuum system and released into the atmosphere. To increase the turbine working efficiency, vacuum systems consisting of liquid ring vacuum pumps, steam jet ejectors, and a combination of vacuum pumps and ejector systems are effectively employed.

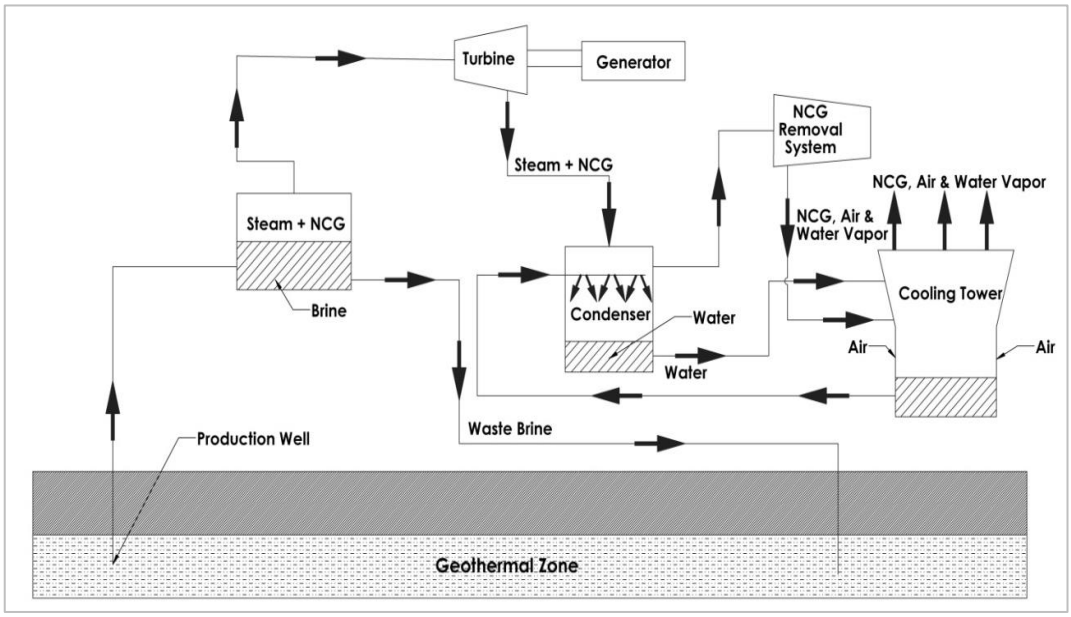

Figure 2.20 Typical flash cycle power plant (Richardson et al. 2015).

2.5 Mineral Trapping of CO_2 in Geothermal Reservoirs

Hydrothermal alteration is a complex process that involves chemical, textural, and mineralogical changes considered as evidence for fluid circulation patterns in the formations. This indication is useful in mineral exploration and understanding of geothermal systems. Hydrothermal alteration occurs with fluid-rock interaction processes such as recharge, upflow, and burial metamorphism. The types of hydrothermal alteration that occur can vary depending on a number of factors,

including the deposit type, environment temperature, pressure, fluid/rock ratio, and fluid content. The extent of the alteration zone can vary, from a few centimeters to kilometers.

There are two main alteration divisions: hypogene alteration and supergene alteration. Hypogene alteration is typically caused by temperature increase, while supergene alteration is associated with meteoric water reactions at low-temperature environments (Brimhall and Ghiorso,1983). Important mineral alterations are potassic alteration, phyllic alteration, propylitic alteration, argillic alteration, silicification, carbonization, greisenization, and hematitization (Wallace and Maher, 2019; Seki, 1973; Parry et al. 2002; Di Tommaso and Rubinstein, 2007).

2.5.1 Potassic alteration

Potassic alteration occurs by replacement of plagioclase and mafic silicate at a temperature between 450 and 600 ^{o}C (Battles and Barton, 1995). K-Silicate is characterized with K-feldspar, biotite, minor quartz, and chlorite. Anhydrite is also an associated mineral in potassic alteration. Glazner (1988) studied potassic alteration of Miocene volcanic rocks in the Sleeping Beauty area in California. The K_2O contents in Peach Springs Tuff was reported as high as 13.3 wt %. Duan et al. (2021) showed that Na-rich fluids can trigger potassic alteration.

2.5.2 Propylitic alteration

Propylitic alteration occurs by adding H_2O, CO_2, and local S, with no appreciable H^+ metamorphism (Binglin et al. 2014). Chlorite and epidote mainly exist with less calcite, albite, and zoisite in a propylitic alteration environment. It is found in low to intermediate temperatures (200-350 ^{o}C) and low fluid-rock ratios. Gallardo et al. (2018) reported an intense propylitic alteration at 320 m depth in Nevados de Chillan geothermal system.

2.5.3 Phyllic (sericitic) alteration

Destabilization of feldspars causes sericitic alteration by hydrolysis in the presence of K, S, OH to form quartz, chlorite, pyrite, and sericite (Meunier and Velde, 1976). The process involves leaching out of Mg, Fe, Na, Ti, and K. Wallace et al. (2019) noted the presence of CO_2-rich, carbonate, and pH neutral as the responsible for alteration.

2.5.4 Argillic alteration

The argillic alteration is categorized into intermediate and advanced argillic depending on the intensity of the clay mineral. Intermediate argillic alteration is characterized by smectite and kaolinite group formation at a temperature below 250 ^{o}C (Hikov, 2004). Advanced argillic alteration is active in high fluid/rock ratio environments. Alteration minerals are mainly kaolinite and alunite, with less quartz.

2.5.5 Silicification

Silicification involves the formation of new quartz or amorphous silica minerals as the result of isochemical hydrolysis reactions in the local presence of Silica. Quartz precipitation occurs in fractures where hydrothermal fluids travel through (Kumar and Ghassemi, 2005). High level epithermal precious metal ore deposits influence silicification alteration. Geothermal water includes a cocktail of species (cations and anions) at equilibrium temperature in the reservoir. As hot water is utilized, dissolved species like silica can precipitate. The silica precipitation can cause pipe-plug and turbine damage in geothermal production systems. Silica precipitation is more problematic in flashing-type systems where silica concentration in the brine becomes supersaturated with steam generation. To illustrate, approximately 25% of flashing in the Kızıldere geothermal field causes an increase in silica concentration from 381 ppm in the reservoir to 500 ppm in the reinjection brine (Haklıdır et al. 2021). Ueda

et al. (2022) investigated the recovery of silica from geothermal brine at the Yamagawa power plant by using batch and circulation tests. They used reagents and cationic flocculant to change retention time and decrease silica concentration.

Watanabe et al. (2021) investigated the effect of the formation of amorphous silica particles on the fractured granite reservoir at various temperatures (430-500 ^{o}C) and pressures (20-30 MPa). The study reported a slight reduction of permeability.

Kumral et al. (2016) studied hydrothermal alteration in the Miocene magmatic intrusion in Tavşanlızone of the Kütahya-Bolkardağ Belt, northwestern of Turkey. They noted silicified/iron carbonatized alteration and argillic-silicic alterations (Figure 2.21).

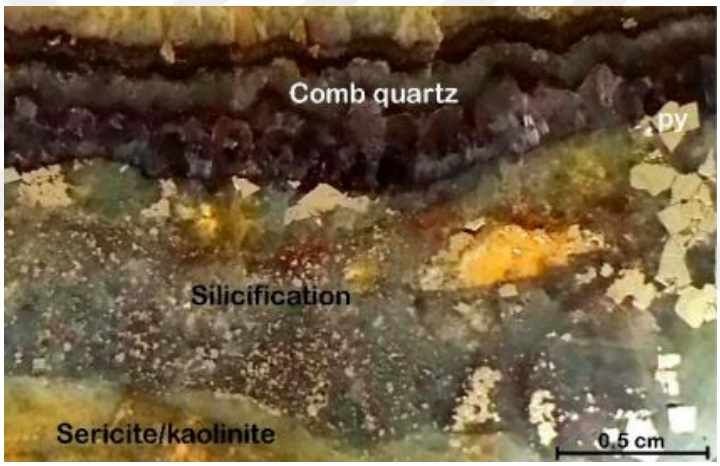

Figure 2.21 Centimeter-scale view of comb-textured quartz crystals within wall rock (sericitized, kaolinized and silicic) (Kumral et al. 2016).

2.5.6 Carbonatization

Carbonatization means the formation of carbonate minerals such as dolomite, calcite, siderite, and magnesite during rock alteration. Mineral carbonation requires metallic cations such as Mg^{2+}, Ca^{2+}, and Fe^{2+} (Equation (2.7)). The high partial pressure of carbon dioxide and neutral to alkaline pH promote carbonatization alteration. The carbonization process is typically found in CO_2 reinjection to store carbon gases in

the geological formations permanently. Erol et al. (2022) evaluated the dynamic fluid-rock interactions during long-term CO_2-charged fluid injection. They identified secondary minerals developed as the results of the mineralization process in the metamorphic reservoir consisting of quartzite, marble, and schist. The calcite dissolution mechanism was reported because of the acidic property of CO_2-saturated brine. Liu et al. (2019) studied reactive transport modeling of CO_2 sequestration in basalts. They reported mineral carbonation in the serpentinite basalt. Matter et al. (2009) reported carbon dioxide storage in basalt in the Carbfix pilot project in Iceland.

$$(Ca^{2+}, Mg^{2+}) + CO_2 + H_2O = (Ca, Mg)CO_3 + 2H^+ \quad (2.7)$$

2.5.7 Greisenization

Greisenization represents the alteration of muscovite, quartz, and lesser fluorite (Witt, 1988). It is a post-magmatic alteration changing the composition of granites with several sequential stages. It is a metasomatic process related to high silica leucocratic granitoids (Stemprok, 1987). Zhang et al. (2018) characterized hydrothermal alteration at the Dahutang tungsten deposit in South China as phyllic, biotite, greisenization, and silicification. The weak greisenization showed mass gains in SiO_2, Fe_2O_3, K_2O, P_2O_5 , and W and reduced Na_2O, MgO, and CaO, whereas Al_2O_3 and MnO remained unchanged. Peterková and Dolejš (2019) studied the evolution of magmatic-hydrothermal alteration in the granite-pegmatite-greisen system of Eastern Krusne hory. The greisenization stage was reported at temperatures between 600 and 500 ^oC. Shanks III (2012) presented the primary alteration assemblages of alteration types in Table 2.4. Hydrothermal alterations observed in West of Anatolia are shown in Table 2.5.

Table 2.4 Diagnostic minerals in hydrothermally altered volcanogenic massive sulfide deposits at different metamorphic grade (Shanks III, 2012; Alt et al., 2012).

Alteration type	**Diagnostics minerals: unmetamorphosed deposits**	**Diagnostic minerals: greenschist facies**
Advanced argillic	Kaolinite, alunite, opal, smectite	Kaolinite,pyrophyllite, andalusite,corundum, topaz
Argillic	Sericite, illite, smectite, pyrophyllite, opal	Sericite,illite, pyrophyllite
Sericitic	Sericite,illite, pyrophyllite	Sericite, illite, quartz
Chloritic	Chlorite, quartz, sericite	Chlorite, quartz, sericite
Carbonate propylitic	Carbonate (Fe, Mg), epidote, chlorite, sericite, feldspar	Carbonate (Fe, Mg), epidote, chlorite, sericite, feldspar

Table 2.5 Hydrothermal alterations in West Anatolia geothermal systems

Field ID	**Reservoir rock type**	**Hydrothermal Alterations**	**References**
Aydın-Salavatlı Geothermal Field	Menderes metamorphic reservoir rock (calc-schist, mica-schist, quartzite, gneiss, marble)	Kaolinite, illite, montmorillonite, calcite, pyrite, dolomite, and hydro biotite	(Karamanderesi and Helvaci, 2003)
Alaşehir Geothermal Field	Menderes metamorphic reservoir rock (calc-schist, mica-schist, quartzite, marble)	Chrolitization, sericitization, silicification, carbonification	(İlhan and Kabak, 2018)
Kızıldere Geothermal Field	Menderes metamorphic reservoir rock (calc-schist, mica-schist, quartzite, marble)	Phyllic, argillic, silicic, hematitized, and carbonatized alteration zones	(Özgür, 2010)

2.6 Previous Studies about CO_2 Sequestration in Geothermal Reservoirs

Geological storage of carbon dioxide is a slow process that can take years to complete. The reaction time is influenced by several critical parameters, including the mineral surface area, mineral types, thermodynamic conditions, and CO_2 saturation. Laboratory tests are typically applied to provid insights about the initiation of CO_2 storage process. Batch experiments, which involve mixing CO_2 with rock particles, can be completed in weeks due to the high mineral surface area of crushed samples. However, flow-through experiments, which involve continuously flowing CO_2 through a rock sample, can take months to years to reach equilibrium due to the limited contact surface area. Reactive transport simulations are generally applied to understand the effects of CO_2 reinjection on the reservoir rock and fluid.

Secure storage of CO_2 requires an impermeable caprock to trap the CO_2 underground. However, permeable faults along the caprock could cause gas to escape to the atmosphere. Stress variation associated with injection may create fractures along the caprock. Therefore, it is crucial to understand the working mechanisms and evaluate possible risks before long-term injection. Dalkhaa and Okandan (2013) studied CO_2-water-caprock interactions for potential CO_2 storage in Turkey. They used TOUGHREACT program to investigate the influence of CO_2-dissolved water on the Sayındere formation (caprock) for 1000 years of post-injection in a 2D radial modeling. The mineralogy of the caprock and geochemical analysis of the reservoir water are shown in Table 2.6. The study reported the dissolution of calcite in the reservoir rock and caprock. The variation of the porosity and permeability was found to be negligible. As an example of CO_2 escape from the reservoir, many researchers have reported the travel of CO_2-charged fluids through Navajo sandstone to the surface (Assayag et al., 2009a and Han et al., 2013).

Table 2.6 Mineralogy of the caprock (Dalkhaa and Okandan, 2013).

	Primary Minerals	**Mass fraction**
Sayındere caprock	Calcite	0.76
	Quartz	0.227
	Kaolinite	0.013
Karaboğaz reservoir	Calcite	1.0
	Secondary Minerals	**Mass fraction**
	Magnesite	0.0
	Siderite	0.0
	Dolomite	0.0
	Hematite	0.0

Kinetic reaction rates and mineral surface area have a significant impact on fluid-rock interactions. However, it is difficult to estimate the reservoir mineral surface area in heterogeneous systems. Therefore, sensitivity analyses are typically used to understand the effect of mineral surface area on the results. Reaction rates determined from laboratory tests may not be accurate representations of the reaction rates in natural field settings (White and Brantley, 2003). Kampman et al. (2014) noted that the limited sample size complicates direct sampling of CO_2-rich fluids, which can lead to CO_2 degassing during sampling. Waldmann et al. (2014) investigated the importance of mineral surface area on CO_2-water-rock interactions. They studied the effects of specific mineral surface area, mineral distribution, and whole rock surface areas separately. The study showed that the initial amount of K-feldspar, hematite, kaolinite, and carbonate controls the clay mineral precipitation during CO_2 storage in Rotliegend sandstones. They employed PHREEQC geochemical modeling software to show that the aqueous phase was supersaturated with respect to some carbonate and sulfide minerals (Table 2.7).

Table 2.7 Saturation index of minerals as the result of water-rock interaction Waldmann et al. (2014).

Mineral	Formula	Initial SI	Precipitation (mol/kgw)	SI (after mineral precipitation)
Ankerite	$CaMg_{0.3}Fe_{0.7}(CO_3)_2$	4.07	0	-0.56
Aragonite	$CaCO_3$	1.79	0	-0.50
Barite	$BaSO_4$	0.05	0	-1.70
Calcite	$CaCO_3$	1.94	0	-0.36
Dolomite	$CaMg(CO_3)_2$	4.60	0.0046	0
Galena	PbS	3.17	0.0001	0
Hematite	Fe_2O_3	4.03	0	-1.81
Magnesite	$MgCO_3$	1.40	0	-0.91
Pyrite	FeS_2	2.23	0.0010	0
Siderite	$FeCO_3$	1.39	0	-0.96
Sphalerite	ZnS	2.73	0.0001	0
Strontianite	$SrCO_3$	1.40	0	-0.90

Although the major component of NCGs in gas sequestration projects is CO_2, impurities such as SO_2, O_2, and NO_x may also be present. The impurity of gases may cause different reactions with various kinetic rates. Pearce et al. (2015) performed an experimental and simulation-based study to reveal the impacts of SO_2 on CO_2-water-rock interactions. They showed that SO_2 gas in the water generated sulphuric acid, increasing silicate and carbonate dissolution. The amount of mineral dissolution was changed with the rock composition. The study showed that the more cation concentrations in the solution, the higher potential for CO_2 trapping. Wang et al. (2016) performed an experimental study investigating CO_2-brine-rock interaction

for CO_2 sequestration in deep coal seams. The experiments included powdered rock samples representing caprock in the batch system at 160 ^oC and 15 MPa. Changes in the mineralogical compositions were determined with XRD and SEM measurements. It was reported that the content of quartz, illite, chlorite, and plagioclase were increased while the content of biotite, kaolinite, and smectite decreased.

Experiments are a cost-effective way to understand the reactions between CO_2-saturated brine and reservoir rock under reservoir conditions. Steel et al. (2018) conducted hydrothermal experiments over 6 months to investigate the potential for mineral carbonation by buffering brine with calcite. The experiments were then simulated with PHREEQC to determine the equilibrium state. The study found that calcite was insufficient to enhance mineral carbonation. Liu et al. (2012) reviewed reactive experiments between CO_2-brine-caprock, using the Eau Claire formation as a case study. A batch experiment was conducted at 200 ^oC and 300 bars. Stable isotope tests suggested that CO_2 exists in the caprock's free and dissolved phases. The study reported the precipitation of clay and carbonate minerals and the dissolution of feldspars and carbonate minerals. Liu et al. (2018) investigated CO_2-brine-rock interactions for CO_2 sequestration in a deep saline aquifer. They performed experiments on the minerals taken from the upper layer of the Shahejie formation in China (Figure 2.22). The experiments observed changes in ion concentration after 72 h of reaction. The concentrations of HCO_3^- and Ca^{2+} were significantly increased. They used TOUGHREACT and PHREEQC to simulate the long-term geochemical behavior of the solution.

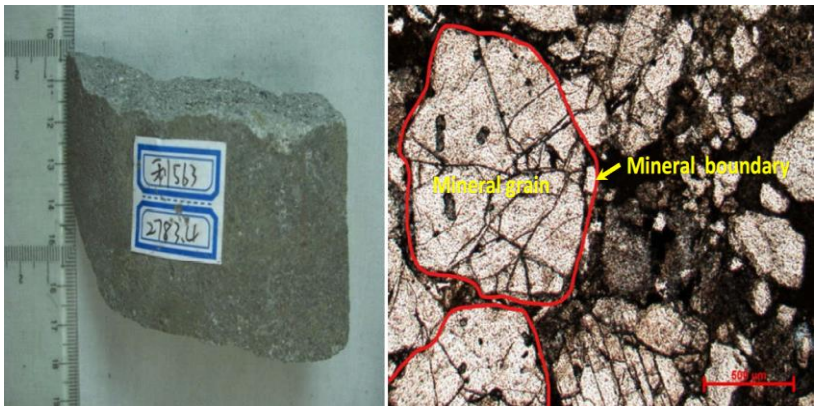

Figure 2.22 Photo of the sandstone sample and thin section image observed by electron (Liu et al. 2018).

CHAPTER 3

STATEMENT OF THE PROBLEM

Global warming is a major threat to the planet, with potentially catastrophic consequences such as floods, sea-level rise, and widespread species loss. One of the main causes of global warming is the increasing concentration of greenhouse gases (GHGs) in the atmosphere, such as CO_2, H_2S, and CH_4. Sequestration of GHGs into geological formations is a promising method to mitigate climate change. CO_2 reinjection has been successfully performed in many depleted oil and gas reservoirs, and deep saline water reservoirs are also good candidates for CO_2 storage. Geothermal reservoirs could be one of the most promising geological formations for CO_2 storage.

Turkey has a significant geothermal potential, and the total installed capacity of the Turkish geothermal industry has increased by ten folds in the last two decades. However, the gas emission of geothermal reservoirs in Turkey exceeded the world's average value. For example, the CO_2 content of the Alaşehir, Kızıldere, and Germencik geothermal fields was higher than 3 % during production startup and short-term flow tests. CO_2 capture and reinjection into the reservoir could generate more environmentally friendly electricity.

The reinjection of CO_2 into Paleozoic-aged geothermal reservoirs is a promising method to mitigate climate change and improve the efficiency of geothermal power plants. However, it is important to understand the CO_2 trapping mechanism in the reservoirs for permanent and safe storage. Otherwise, critical problems such as gas leakage, ground deformation, and injectivity decline might occur.

This study investigates the reinjection of CO_2 into Paleozoic-aged geothermal reservoirs using experimental and simulation-based approaches. Most of the previous studies on CO_2 storage in geothermal reservoirs are based on assumptions

and simulations. This study includes batch and core-flood experiments using real reservoir fluids and reservoir core samples. It was aimed to reveal water-rock interactions during long-term CO_2 injection. Gas dissolution kinetics in the reservoir brine was also investigated with real reservoir gases and brine. The experiments were simulated by using PHREEQC geochemical modeling tool. The secondary minerals that might develop during long-term gas reinjection were found by using experiments and simulations. Kinetic reaction rates and activation energy of primary and secondary minerals were obtained during matching simulation results with experiments. Finally, the study was upscaled to a field application using TOUGHREACT for 3D reactive transport simulation.

The results of this study provide a better understanding of the CO_2 trapping mechanism in geothermal reservoirs and can be used to design and optimize CO_2 storage projects. This study also provides a basis for injecting dissolved CO_2 into the Kızıldere geothermal reservoir before long-term CO_2 injection.

CHAPTER 4

MATERIALS AND METHODS

4.1 Methodology of CO_2 Dissolution Experiment

Understanding of gas dissolution mechanism in geothermal brine is crucial for carbon dioxide injection projects and two-phase flow calculations in geothermal systems. Gas dissolution experiments are reliable methods for mimicking the dissolution mechanism in reservoir conditions. This section investigates the dissolution experiments of CO_2 in geothermal brine at various temperatures (20 ^oC to 142 ^oC) and pressures (1 barg to 13 barg). The NCG, with more than 98 % carbon dioxide was captured from a geothermal well in Western Anatolia. The gas dissolution experiments were conducted in a novel experimental setup that included a batch reactor, mini-separator, brine sampling, and gas measurement system. The total dissolved gas at various temperatures and pressure was calculated by individually measuring free gas flow, brine volume, and alkalinity tests. Unlike typical gas dissolution studies that consider only sodium chloride (NaCI) in the brine, this study considered the major anions and cations in the brine during calculations. The goodness of the experimental results was tested against the calculations of an aqueous geochemical software, PHREEQC, and empirical correlations available in the literature. To understand the kinetics of gas dissolution, the batch system was continuously mixed while the gas injection was kept at constant pressure. The pressure behavior of the gas-brine mixture showed the importance of complete mixing to reach the maximum gas dissolution in the brine.

The batch experiment setup, (see Figure 4.1) was transported to different well locations to obtain different temperatures. Figure 4.2 shows the system of gas flowmeter used in the experiments.

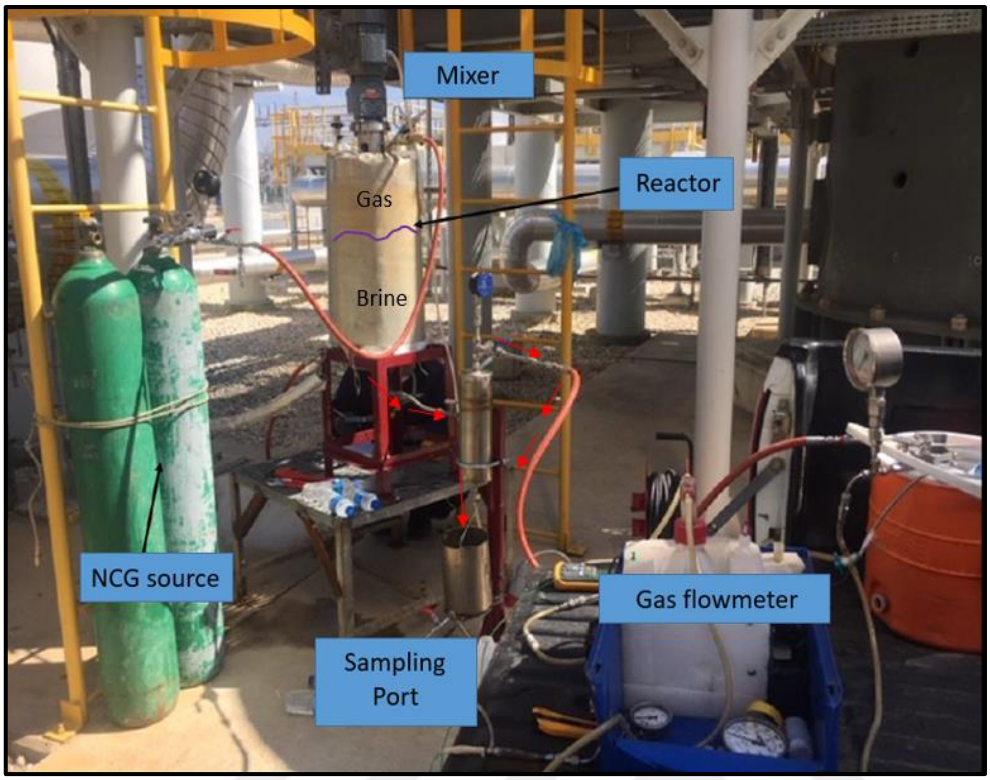

Figure 4.1 A view of batch experiment setup in the field.

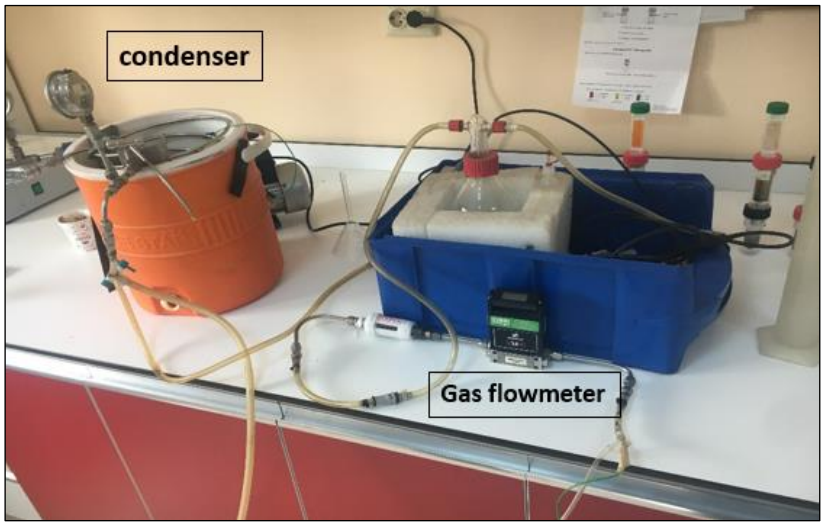

Figure 4.2 A view of gas measurement system consisting of a condenser and a gas flowmeter.

The NCG used in the experiments were the original gases transferred from a geothermal well at static conditions with a wellhead pressure of 89 barg (Figure 4.3). CO_2 was the major gas, accounting for more than 98 % of total dry gas volume. The NCG accumulated at the wellhead due to density differences after being in static condition in the geothermal well for more than 16 months.

Figure 4.3 Transferring NCG from a geothermal well to a high-pressure tube.

The study used two types of experimental setups: a batch reactor and a core-flood setup. Stainless steel components were used to eliminate reactions that could change the composition of the geothermal brine. The batch reactor consisted of a mixer with a power of 0.75 kW, a 300 rpm reducer, Teflon packing, and a special sealing system

that allowed for continuous mixing under high temperature and pressure. ¼ inch injection ports were located at the top of the reactor, to allow for the injection of gas and brine. A pressure relief valve released any uncontrolled pressure buildup in the reactor. The temperature and pressure of the system were continuously recorded using a thermocouple and a pressure transmitter located at the bottom of the reactor. The temperature and pressure conditions of the experiments were kept constant using insulation materials and a double-stage gas regulator. The reactor was heated using geothermal brine continously flowing from the production line. Brine samples were collected from the sampling port at the bottom of the reactor. The sampling line was connected to a mini separator at atmospheric conditions. The flashed brine sample was decomposed into gas and liquid phases. The gas phase flowed into a steam condenser to remove steam from the CO_2 . The pure and dry CO_2 was measured using a gas flow meter. The illustration of the experiment setup is shown in Figure 4.4.

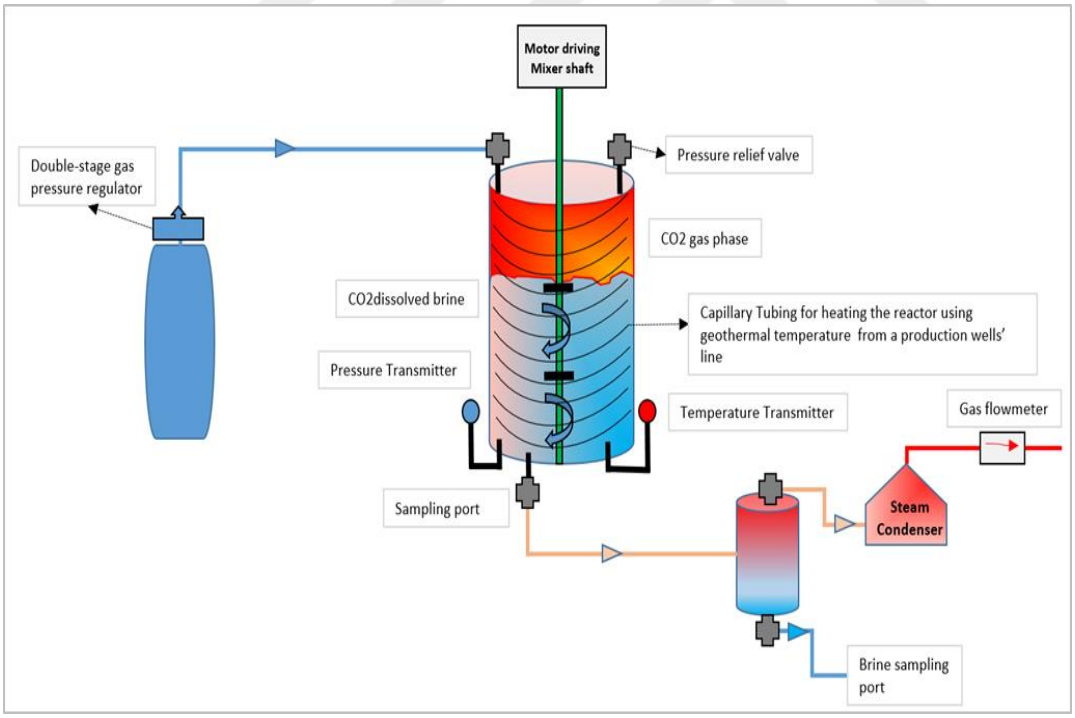

Figure 4.4 Illustration of batch reactor.

4.2 Batch and Core-flood Experiments

The workflow of the study is shown in Figure 4.5. The study started with CO_2 dissolution experiments using real reservoir gas and geothermal brine collected from injection line of the power plant. Core samples taken from the deep geothermal reservoir in Kızıldere were crushed and analyzed before water-rock interactions. Then, batch and core-flood experiments were conducted to understand the mechanisms of CO_2 injection in large-scale field applications. Batch experiments were simulated with PHREEQC to obtain mineral kinetic reaction rates and activation energy of minerals. The data obtained from batch experiments were then used to simulate a 3D reactive transport model of the field under CO_2 injection using TOUGHREACT. Thus, the effects of CO_2 injection on the reinjection and production wells were revealed through this workflow.

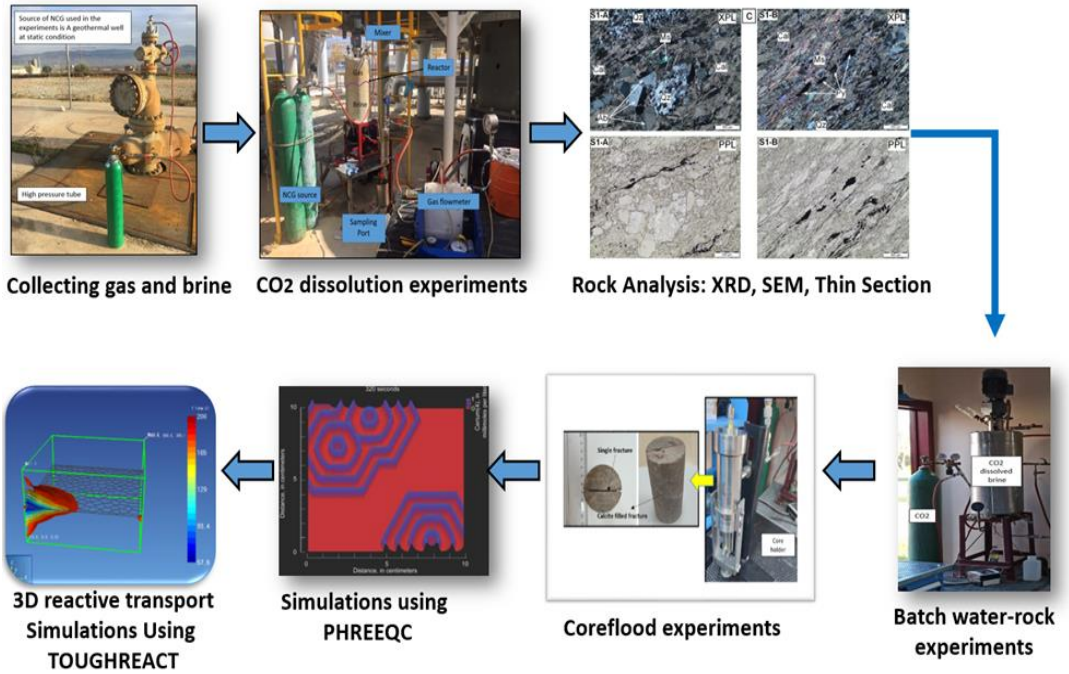

Figure 4.5 Workflow of the water-rock interaction experiments.

The batch experiments started with the preparation of rock samples. Two core samples were taken from 1900-m and 3000-m depths of the studied well, located in the western region of the Kızıldere field, Turkey (Figure 4.6). The core samples were crushed into small pieces and sorted with sidderent sized screeners, resulting in particles with diameters ranging from 0.6 to 0.7 mm (Figure 4.7).

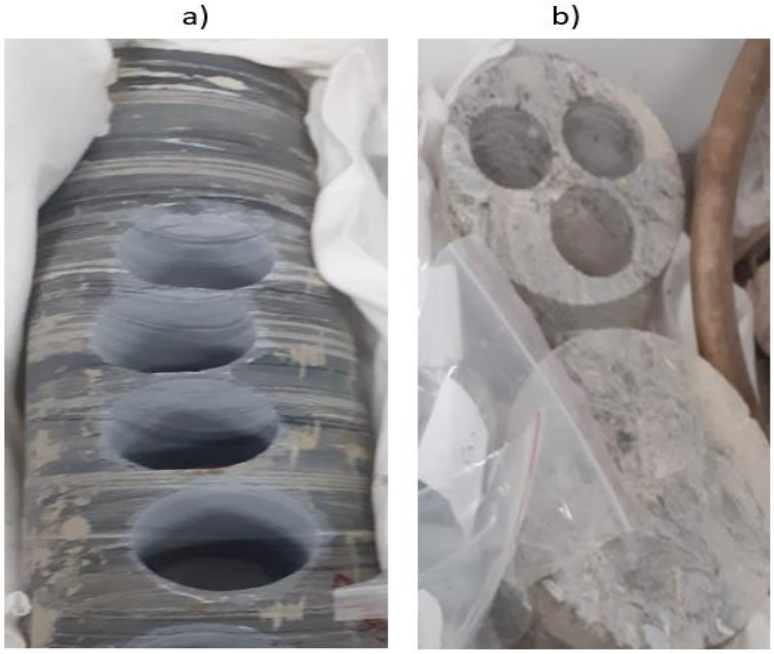

Figure 4.6 Core samples taken from 3000 m depth (a) and 1900 m depth (b).

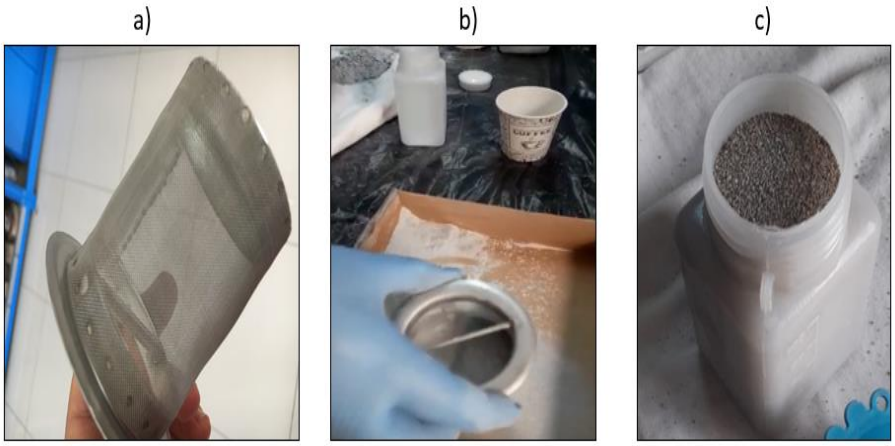

Figure 4.7 Crushing core samples into small particles (Screener (a), shaking screeners (b), sorted particles (c).

The experimental setup is shown in Figure 4.8. Geothermal brine collected from the reinjection line of the power plant was placed in the batch reactor. CO_2 collected from a geothermal well were stored in a high-pressure tube. CO_2 was continuously supplied to the geothermal brine at a constant pressure. The reactor was continuously mixed to ensure that the gas and brine were fully mixed. The CO_2-dissolved brine was then transferred to a transfer cell, that could withstand high pressure. The batch reactor and transfer cell were then disconnected, and the transfer cell was connected to high-pressure CO_2 tube. A double-stage gas regulator was used to provide a constant pressure displacement of brine. The exit pressure of the core holder was also kept constant using a back-pressure valve (Figure 4.8).

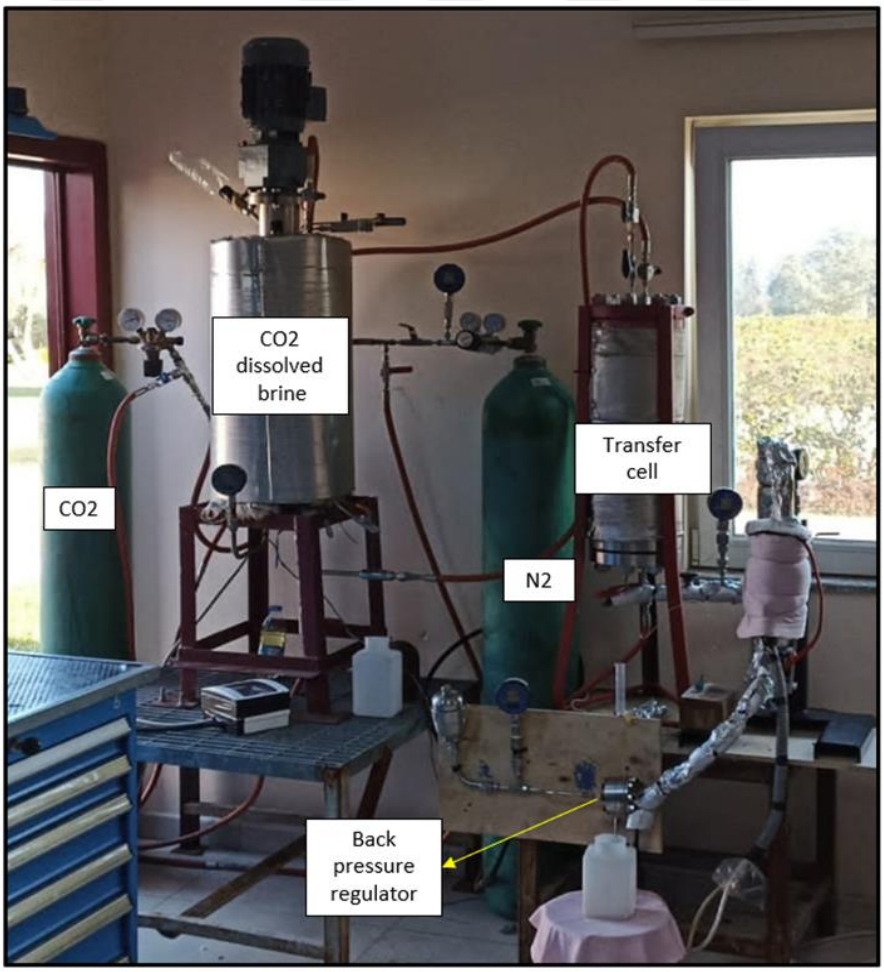

Figure 4.8 A view of core-flood experiment setup.

The core holder could withstand a pressure of 70 bar and was surrounded by heat tapes to provide a temperature of 95 ^{o}C, which is the reservoir temperature in the vicinity of reinjection wells. The core sample was 60 mm in diameter and was split to create a smooth and single fracture with an aperture of 2 mm (Figure 4.9). The core sample was very tight, and small fractures were identified with carbonate fillings. Therefore, it was assumed that the main fluid flow occurred through the synthetic fracture, and there is no flow in the matrix.

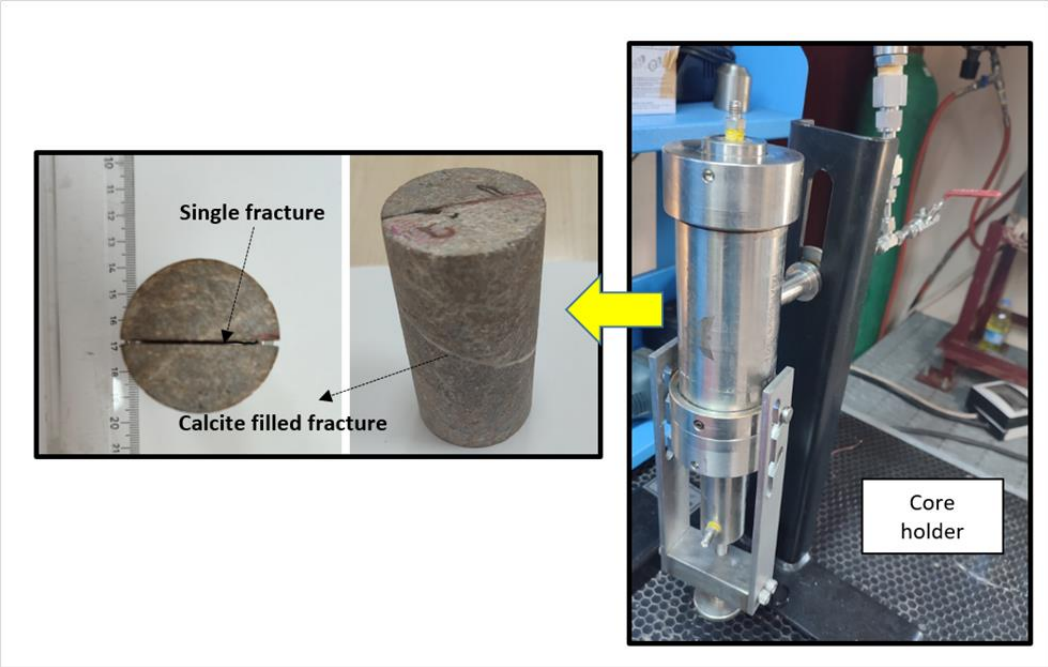

Figure 4.9 Sythetically fractured core sample and core holder used in the experiments.

4.3 Methodology of Simulation Approaches

Batch experiments were simulated using PHREEQC, and experiments' results were then used to enlarge the results to field scale with TOUGHREACT.

4.3.1 Simulation of Batch Experiments using PHREEQC

PHREEQC is a geochemical simulation software that can perform a wide variety of calculations, including speciation and saturation index calculation, advective-transport simulation, inverse modeling, multicomponent diffusion transport, and surface complexation reactions (Parkhurst and Appelo, 1999). One of the most critical advantages is that it can handle a wide range of thermodynamic data, including data for aqueous species, minerals, gases, and solid solutions (Parkhurst and Appelo, 2013).

This study used a PHREEQC code to simulate the reactions between CO_2-saturated geothermal brine and reservoir rock in the batch experiments. The critical parameters that influence the interactions are mineral surface area, kinetic reaction rate and mineral activation energy. The mineral surface area was obtained using SEM, and XRD analysis and image processing of mineral particles. The kinetic reaction rate and activation energy of minerals were the tuning parameters during simulation. The governing equations are given in the Equations (4.1), (4.2), (4.3) and (4.4)

$$k = \mathrm{k}_{25} \times \exp\left(\frac{E_a}{\mathrm{R}} \times \left(\frac{1}{\mathrm{T_K}} - \frac{1}{298.15}\right)\right) \tag{4.1}$$

$$\mathrm{Rate} = \left(\frac{\mathrm{A_0}}{\mathrm{V}}\right) \times \left(\frac{\mathrm{m}}{\mathrm{m_0}}\right)^{0.67} \times \mathrm{k_2} \times (1 - \mathrm{SR(Mineral)}) \tag{4.2}$$

$$\mathrm{Moles} = \mathrm{rate} \times \mathrm{time} \tag{4.3}$$

$$\text{Concentration} = \text{moles} \times \text{MW} \times 1000 \quad (4.4)$$

4.3.2 3D Reactive-Transport Modeling

Numerical reservoir simulation is a strong tool that mimic the flow system of actual porous and permeable reservoirs. Numerical models typically use a top-down modeling approach, in which the overall system is divided into smaller and smaller parts until the desired level of detail is reached. In other words, the overall system is refined into more detail such that, a 3D model is divided into grid blocks, and each grid block is assigned rock-characteristic properties such as porosity and permeability. Grid blocks intersecting with faults' planes are populated with higher porosity and permeability values, while impermeable formations are represented with extremely low permeability factors. This approach allows for the heterogeneity of geothermal reservoirs to be implemented in the 3D model.

In this study, we performed a 3D reactive transport modeling of the studied area using TOUGHREACT, a reactive transport module of TOUGH2. TOUGHREACT is a widely used simulation program for reactive transport problems in non-isothermal, fractured, and porous media. It was developed in FORTRAN77 and embedded into TOUGH2 to handle thermo-physical-chemical processes under a variety of conditions of temperature, pressure, pH, ionic strength, and salinity (Xu et al., 2006). Fluid flow equations were solved for each grid block by considering mass balance, momentum balance, and energy balance concepts. The equivalent continuum method (ECM) was used to simulate fluid flow in fractured and porous media of the Kızıldere field. ECM considers the primary and secondary porosity as a single pore space for simplicity.

TOUGHREACT can calculate the variation of permeability and porosity due to reactions such as precipitation and dissolution. This requires significant

computational resources. The software allows users to model species in the form of gas, liquid, and solid. The interaction between flowing phases is handled using relative permeability and capillary pressure. Convective and conductive heat flow and diffusion of non-condensable gases are also considered in the simulations. Aqueous complexation, cation exchange, and redox processes are assumed to be at local equilibrium. Mineral dissolution and precipitation can be modeled under kinetic conditions, but they can also be determined by assuming local equilibrium. The program uses a sequential iteration approach, in which the chemical transport equations are solved after the flow equations have been evaluated. The chemical reaction equations are solved using Newton-Raphson iteration on grid blocks. The dissolution and precipitation of minerals occur under kinetic conditions. These processes result in temporal variations in reservoir porosity and permeability. Porosity changes are calculated based on variations in mineral volume fractions. Permeability changes are calculated using the cubic law, which considers porosity.

Reactive transport models are typically used as preliminary studies for field-scale CO_2 storage projects. These models can help experts to understand the potential problems that may arise during long-term gas injection. For example, André et al. (2007) used TOUGHREACT to simulate CO_2 injection in a carbonate reservoir in Paris, France. The model considered two CO_2 injection scenarios: CO_2-saturated water and pure supercritical CO_2 injection. The results of the model confirmed that CO_2-saturated water is highly reactive, which could lead to a significant decline in injectivity. On the other hand, supercritical CO_2 injection showed weakly reactive behavior. In another study, Maskell et al. (2015) investigated the chemical evolution of groundwater flowing through a basalt aquifer in Soda Springs, Idaho. They determined the kinetics of CO_2-fluid-rock reactions in this system. The primary fluid minerals in the aquifer were plagioclase, gypsum, pyroxene, and orthoclase. The developed secondary minerals were silica, kaolinite, zeolite, calcite, and albite. The kinetic rates obtained from the study were found to be similar to those observed in other natural CO_2-charged groundwater systems.

TOUGHREACT is a non-isothermal reactive fluid flow and geochemical transport program that includes comprehensive chemical interactions between different phases such as liquid, solid, and gas phases. Different forms of process may develop during carbon sequestration based on the existence of ions, minerals, and thermodynamic conditions. Mineral precipitation and dissolution occur at different rates and are typically controlled by kinetic rate constant and mineral surface area. Kinetic rate constant changes with specific parameters such as species, absolute temperature, and activation energy. The general rate expression used in TOUGHREACT is given in Equation (4.5).

$$k = \pm k_n A_n \left(1 - (\frac{Q_n}{K_n})^{\theta}\right)^{\eta} \tag{4.5}$$

Where ŋ represents the kinetic mineral index, the positive value of r_n means dissolution, and the negative values precipitation, k_n is the rate constant which depends on temperature. A_n is the specific reactive surface area, and K_n is the equilibrium constant. The parameters of ŋ and Θ are determined from experiments. However, their values are typically considered as one.

For different minerals, the kinetic rate constant can be obtained from Equation (4.6) (Palandri and Kharaka, 2004).

$$\begin{aligned} k = k_{25}^{nu} \exp\left[\frac{-E_a^{nu}}{R}\left(\frac{1}{T} - \frac{1}{298.15}\right)\right] \\ + k_{25}^{H} \exp\left[\frac{-E_a^{H}}{R}\left(\frac{1}{T} - \frac{1}{298.15}\right)\right] {a_H}^{n_H} \\ + k_{25}^{OH} \exp\left[\frac{-E_a^{OH}}{R}\left(\frac{1}{T} - \frac{1}{298.15}\right)\right] {a_{OH}}^{n_{OH}} \end{aligned} \tag{4.6}$$

Where OH, H, and nu are subscripts that indicates base, acid, and neutral mechanisms, respectively. E_a represents activation energy, k_{25} is the constant rate at

25 ^{o}C, R is as constant, T is absolute temperature, a is activity of the species, and n is power term.

Mineral dissolution and precipitation cause changes in the porosity and permeability, affecting fluid flow path characteristics. Variations in the mineral volume fractions are used to calculate changes in the porosity. Equation (4.7), used in the TOUGHREACT, was proposed by Kozeny-Carman

$$\frac{k}{k_o} = \left(\frac{\phi}{\phi_0}\right)^3 \left(\frac{1-\phi_0}{1-\phi}\right)^2 \tag{4.7}$$

Where ϕ represents the porosity, k is the permeability, and "0" denotes the initial values of variables.

Palandri and Kharaka (2004) calculated the reaction constant of acid and base mechanism for different minerals (Table 4.1).

Table 4.1 Examples for acid and base mechanisms (Palandri and Kharaka, 2004).

	Acid mechanism			Neutral		Base mechanism		
	Log k	E	n	Log k	E	Log k	E	n
Kaolinite	-11.31	65.9	0.777	-13.18	22.2	-17.05	17.9	-0.472
Montmorillonite	-12.71	48	0.220	-14.41	48.0	-14.41	48.0	-0.130
Smectite	-10.98	23.6	0.340	-12.78	35.0	-16.52	58.9	-0.40

Reactive mineral surface area is a critical parameter influencing reaction rates between fluid-CO_2-rock. Walls of fractures are considered surfaces filled with

mineral grains. The fracture surface area is calculated based on fracture porosity and interface ratio. TOUGHREACT uses Equation (4.8) for each mineral. TOUGHREACT treats mineral grains as a plate.

$$A_m = \frac{A_r a_{fmr}}{\rho_w \Theta_f S_w} \tag{4.8}$$

The other software used for geochemical modeling is PHREEQC, written in C++ programming language. It can be used to perform a wide variety of geochemical calculations in aqueous systems (Parkhurst et al. 2013), including:

- Saturation index calculations
- Speciation
- Ion exchange equilibria
- Surface complexation
- Mixing of solutions
- Inverse modeling
- Gas solubility calculations using the Peng-Robinson equation of state
- One-dimensional transport calculations with reversible and irreversible reactions

PHREEQC uses the Peng-Robinson equation of state and fugacity to model CO_2 solubility in water (Peng & Robinson, 1976).

4.3.3 Geological Structure of the Reservoir

Numerical reservoir models typically start with the construction of a conceptual model, which is a simplified representation of the reservoir based on data from different disciplines. The conceptual model for the Kızıldere geothermal field was built using data from geology, geophysics, reservoir engineering, drilling,

geochemistry, and well logging. The Kızıldere geothermal field is a mature field that has been producing geothermal energy for over 40 years. More than 100 existing wells provide a wealth of data that can be used to construct a conceptual model of the field. Haklıdır et al. (2021) presented the general geology columns of the Kızıldere field by analyzing the geology of the existing wells and alteration types observed from cuttings during drilling (Figure 4.10).

The geological formations can be listed from the top layer to deep reservoir sections observed in existing wells as follow (Figure 4.10):

- Tosunlar formation
- Kolonkaya formation
- Sazak formation (Reservoir-I)
- Kızılburun formation (Caprock)
- İğdecik formation (Reservoir-II)
- Menderes Metamorphics (Reservoir-III)

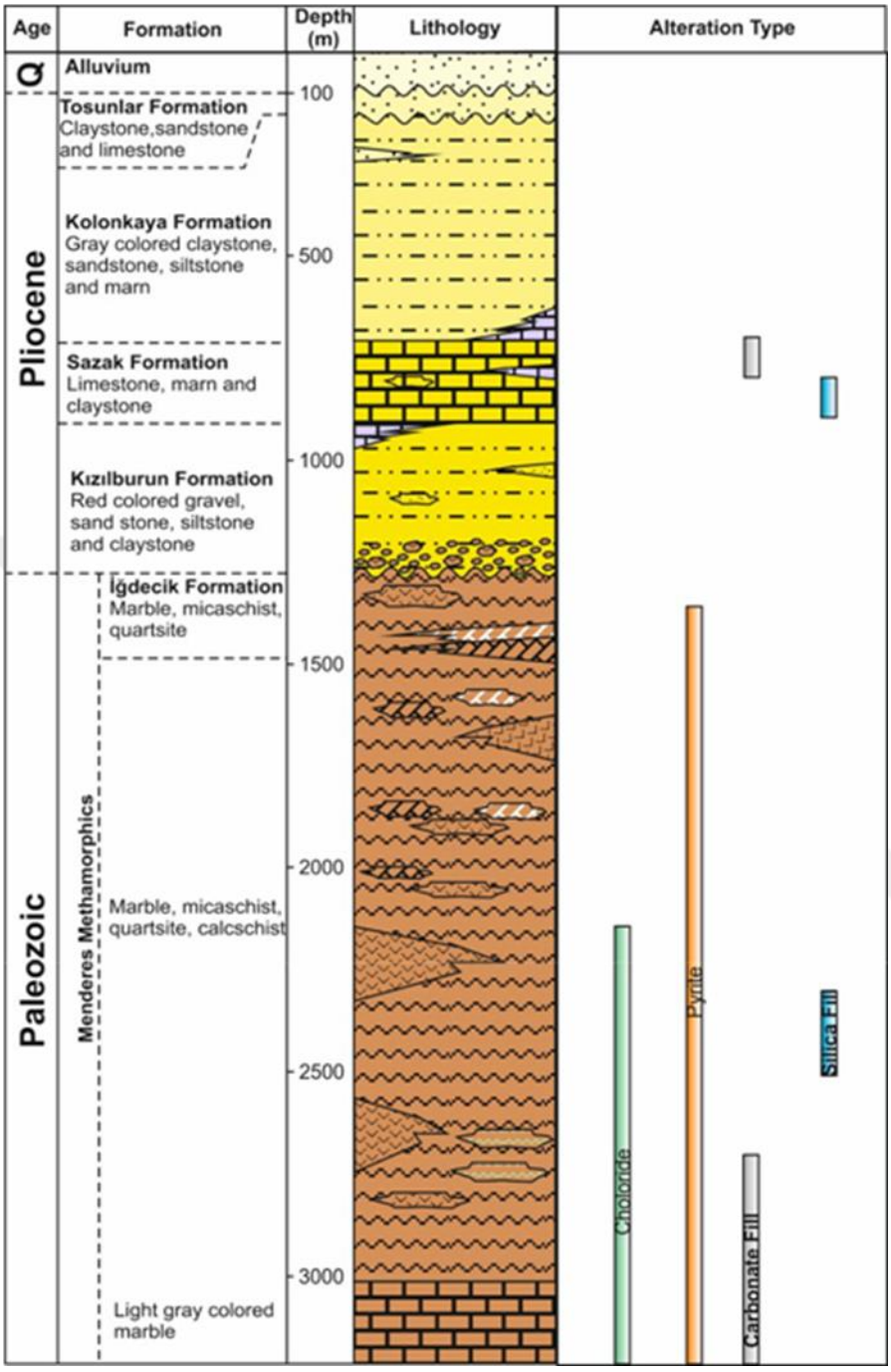

Figure 4.10 A general geological columnar section of Kızıldere field and alteration types (Haklıdır et al. 2021).

A conceptual model of a geothermal field can be constructed by incorporating information from pre-drilled wells, seismic data, outcrop analyses, and field observations. Haklıdır et al. (2021) revised the conceptual model of the Kızıldere field by including new information obtained from deep geothermal wells (Figure 4.11).

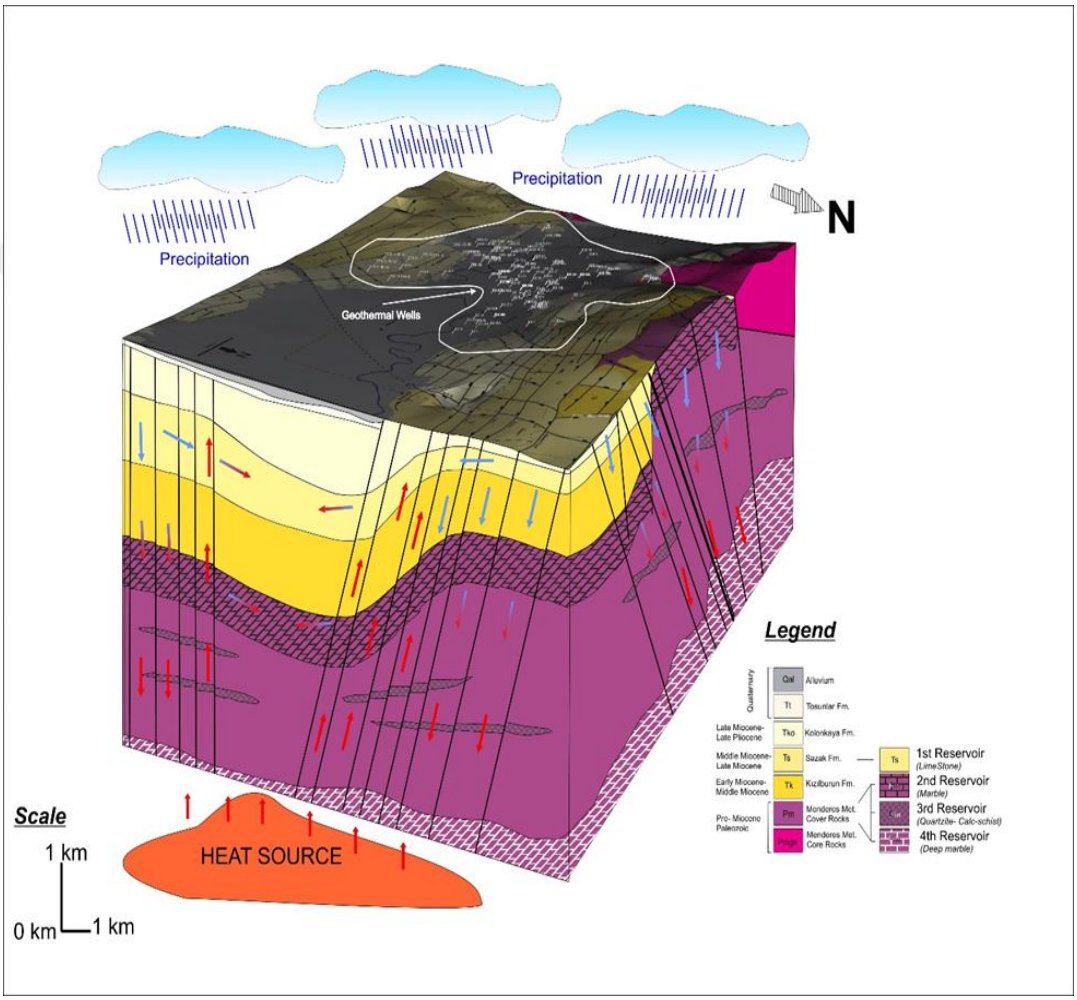

Figure 4.11 The geological conceptual model of the Kızıldere Geothermal Field (Haklıdır et al. 2021).

In this study, we constructed a simplified 3D model of the studied area in Kızıldere field, including a production and an injection well. The spatial distribution of

geological formations was based on the observed data in existing wells (Figure 4.12). The studied area is 3.78 km^2, with a depth of 5 km. For simplicity, we considered İğdecik and metamorphic rocks as a single reservoir, which we named Menderes metamorphic reservoir.

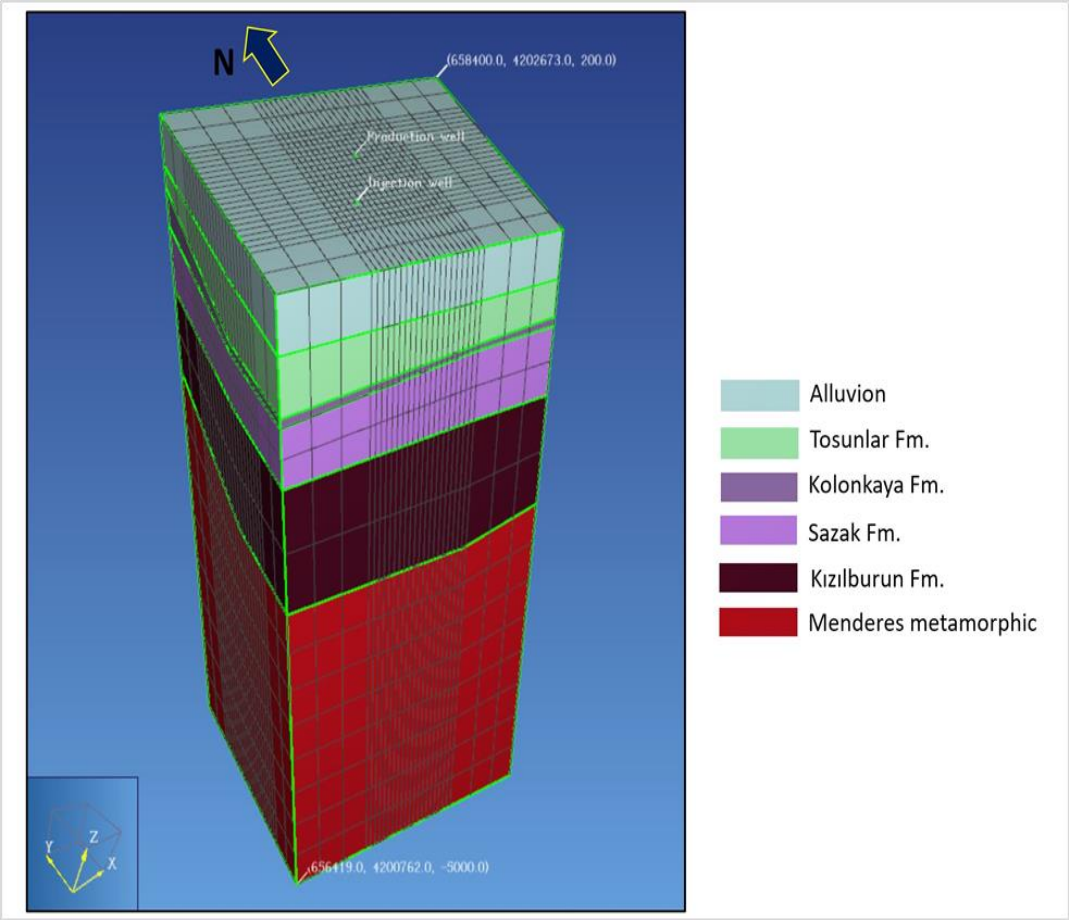

Figure 4.12 Stratigraphic columns and distribution of formations of the studied area in Kızıldere field.

The Kızıldere geothermal field produces geothermal fluids from three different sections: the Sazak formation, the İğdecik formation, and the Paleozoic metamorphic rocks. The Paleozoic metamorphic rocks have different compositions depending on

their depth. These formations are mainly produced from fault-associated fractures. The dominant faults in the field are described in (Bayraktar, 2022). In this study, we only considered fault-1, fault-1A, and the Gebeler fault, which cut the two geothermal wells in the field. Fault-1 and fault-1A are E-W trending and south-dipping normal faults with a dip angle up to 75°. The Gebeler fault is a NE-SW trending strike-slip fault that dominates the main fluid flow in the field. (Figure 4.13).

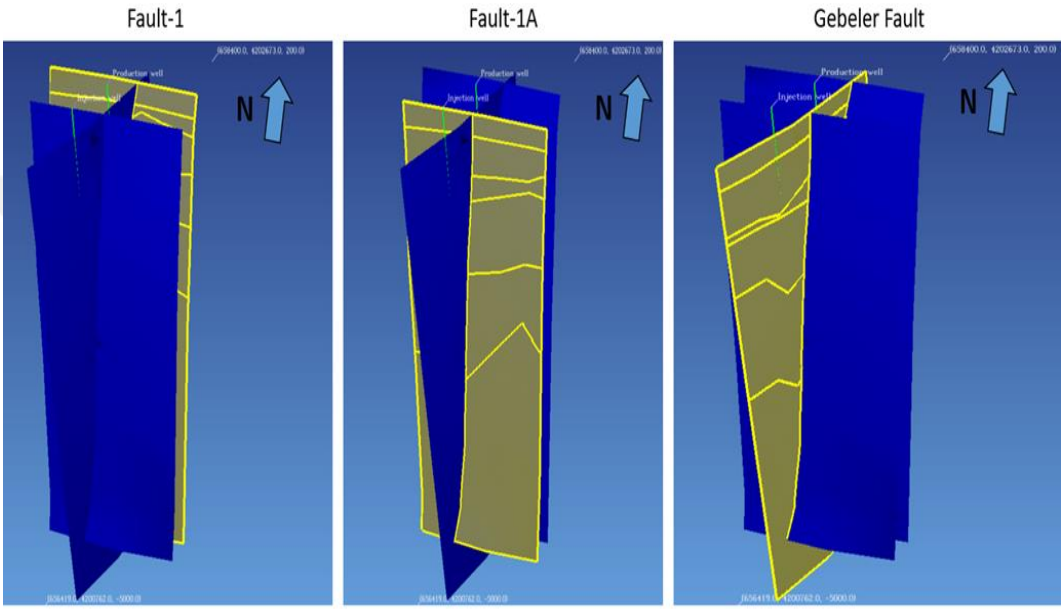

Figure 4.13 Faults used in the numerical model representing Kızıldere field: Fault-1, fault-1A and Gebeler fault.

4.3.4 Gridding of the Model

A total of 9360 three-dimensional rectangular grids with varying sizes were used to subdivide the sector doublet model into smaller parts (Figure 4.14). During the gridding operation, smaller grid blocks were used near well locations for more accurate and precise results, while relatively large grid blocks were used at the model extends for simulation run-time optimization (Table 4.2). The grid block size was selected as 39 m in the well regions, which enables to accurately capture pressure

and temperature transients near wellbore and it was increased to 200 m, which is still less than the well-spacing in Kızıldere (500 m).

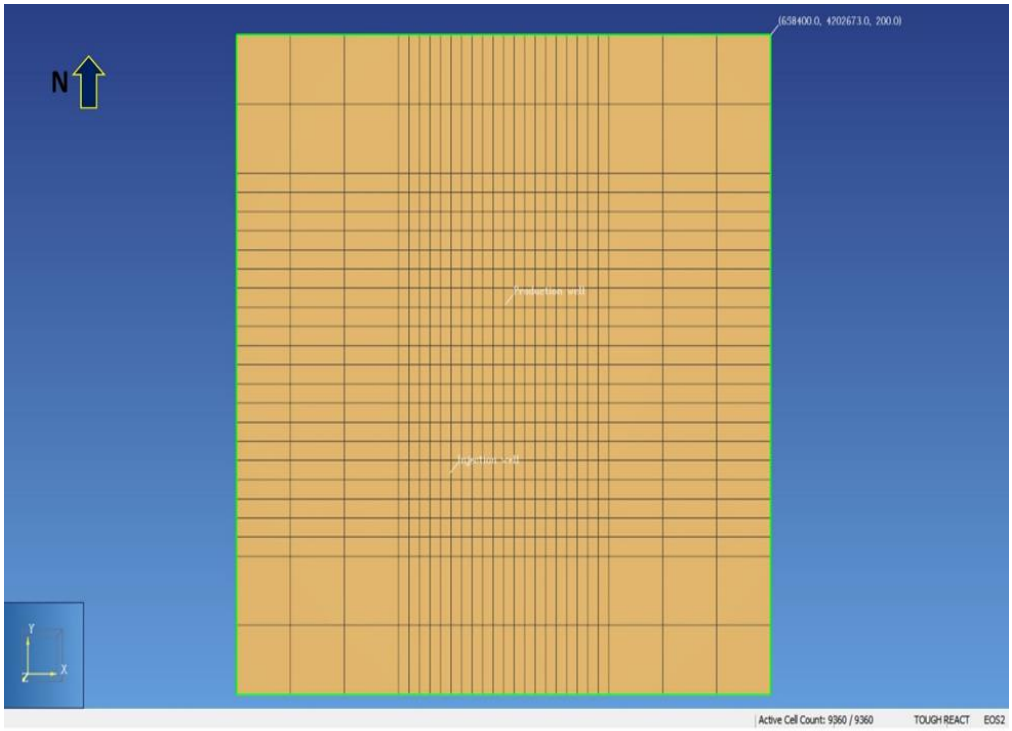

Figure 4.14 A top view of grids of 3D model.

Table 4.2 Grid size distribution of the model.

X		Y	
Number of Grids	Grid Sizes, meter	Number of Grids	Grid Sizes, meter
6	200	4	200
20	39	20	55.5
Total: 1980 meter		1910 meter	

4.3.5 Physical and Geochemical Boundary Conditions of the Model

The two most important steps in a numerical reservoir simulation are the definition of boundary conditions and initial reservoir conditions. The reservoir extension can be limited by no-flow boundaries, which are caused by impermeable lithologies or sealing faults. A constant pressure can also be supplied by a strong water influx from the bottom and outer of the system. Production and reinjection wells are considered internal boundaries (Figure 4.15).

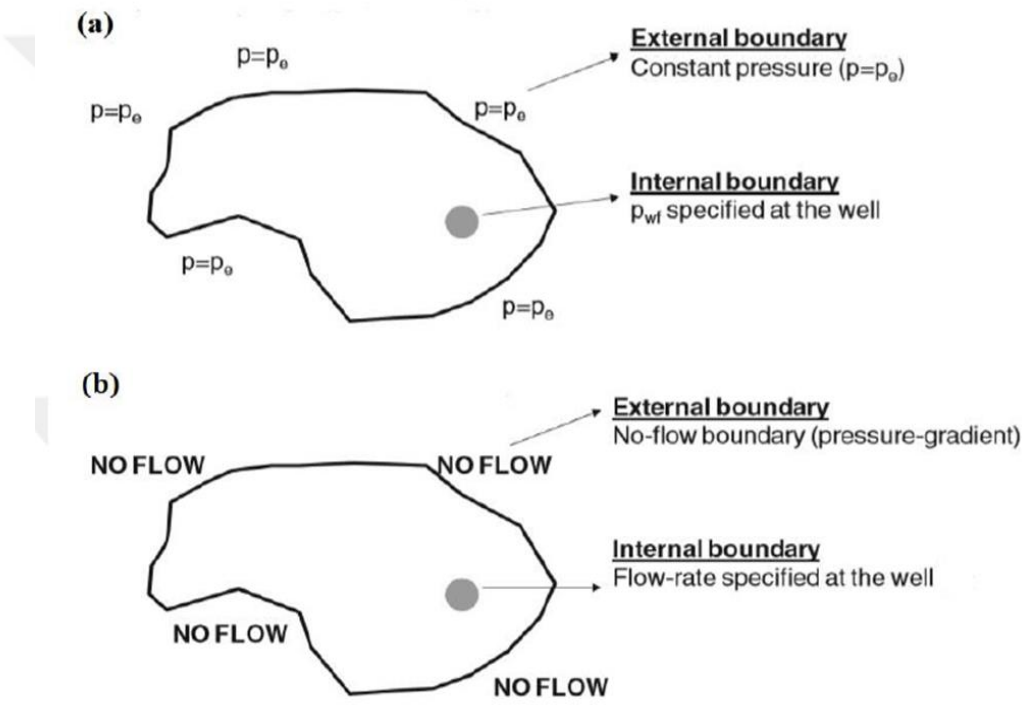

Figure 4.15 a) Constant pressure boundary b) No flow boundary (Küçük, 2018).

We set no-flow boundaries from the bottom layer, top, outer layers of the model. The model has a heat source at the bottom (-5000 m depth), covering approximately 0.1 km^2, with a water flux of 1 kg/s at an enthalpy of 1000 kj/kg, and a CO_2 content 4.5 % by weight. The conductive heat flux was 0.1 $J/s/m^2$ (Figure 4.16). The outer and bottom layers have no flow boundaries in terms of pressure, except for the grid blocks representing the heat source. A production and a reinjection well was

constucted at a depth of 3200-m and 2900 m. Production rate, and reinjection rate of the wells were 100 kg/s and 70 kg/s.

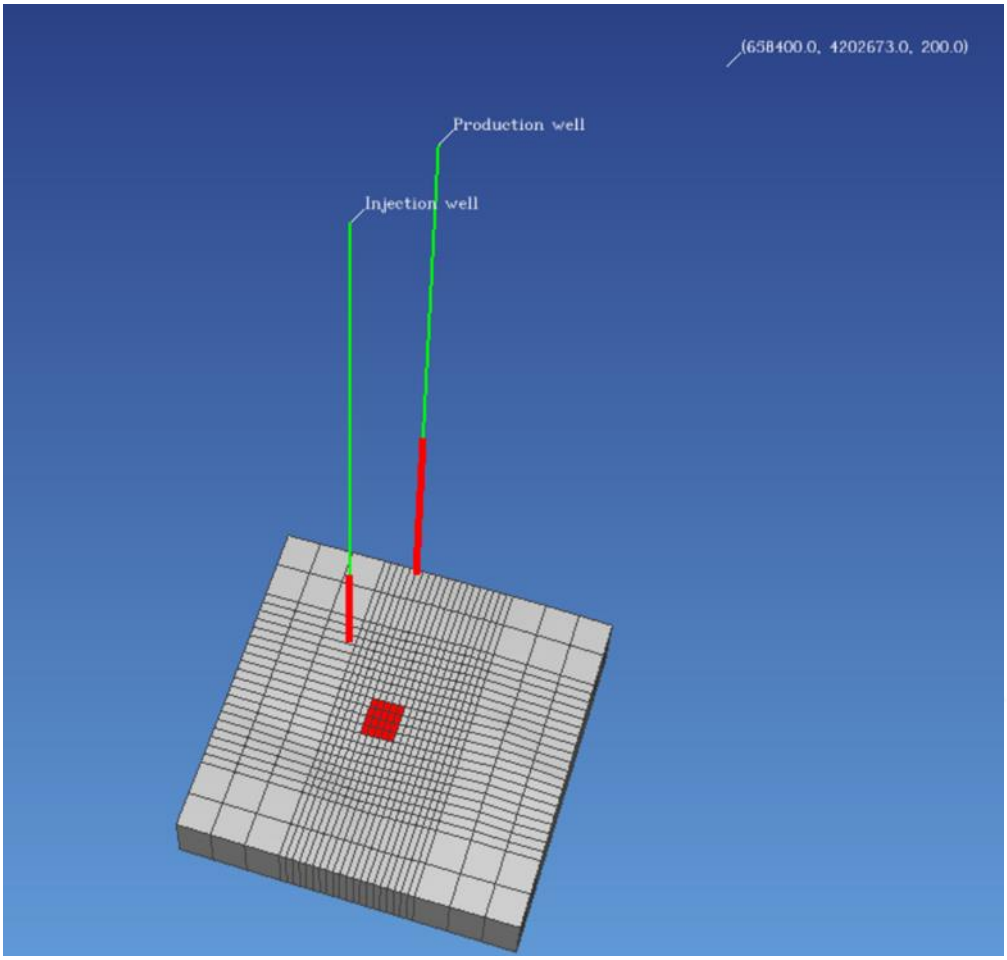

Figure 4.16 Heat source from the bottom of model.

The top layer of the model (-100 meter depth) was set as constant pressure and temperature boundary condition with a 10 barg pressure and a temperature of 45 ^{o}C, which represents static temperature gradient of the region (Figure 4.17). This layer was set as a fixed state, which means that there will be no changes throughout simulations at this layer.

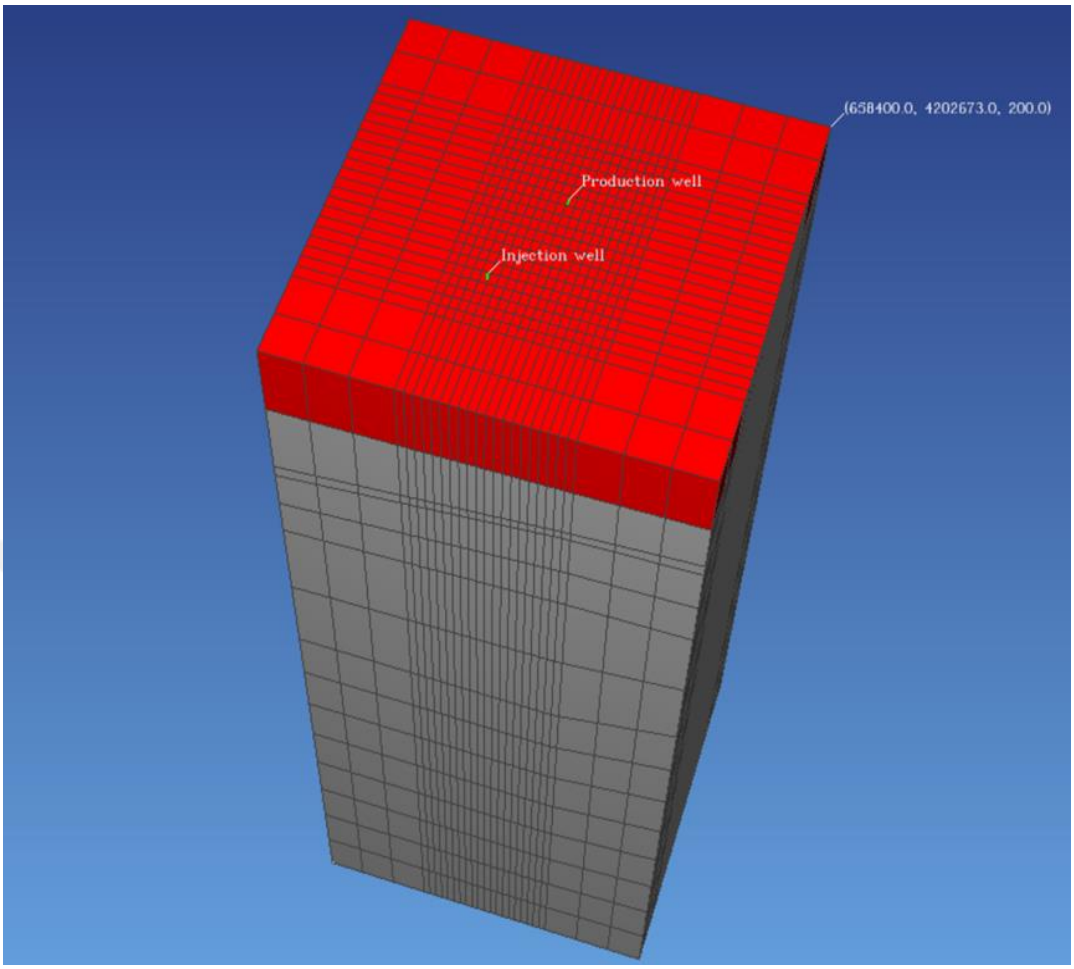

Figure 4.17 Fixed state of top layer of the model.

It is essential to state geochemical boundaries in TOUGHREACT, specifying chemical species and complexes that the program will use for reactions. Chemical species and complexes were found by using PHREEQC and were introduced TOUGHREACT, as shown in (Table 4.3, Table 4.4, and Table 4.5).

Table 4.3 Initial and boundary of water chemistry at reservoir.

Primary Species	CGUESS (molality)	CTOTAL (molality)
$Alo2^{-}$	$1.71x10^{-5}$	$8.4x10^{-4}$
Br^{-}	$5.538x10^{-6}$	$5.738x10^{-6}$
Ca^{+2}	$1.33x10^{-4}$	$3.33x10^{-4}$
Cl^{-}	0.002892	0.003892
F^{-}	0.001175	0.003175
Fe^{+2}	$2.639x10^{-8}$	$6.64x10^{-7}$
H^{+}	$7.948x10^{-6}$	$7.948x10^{-4}$
H_2O	55.51	55.51
HCO_3^{-}	0.06136	0.06636
K^{+}	0.004627	0.005627
Mg^{+2}	$2.482x10^{-6}$	$4.482x10^{-6}$
Na^{+}	0.05166	0.05266
SiO_2 (aq)	0.007445	0.009629
SO_4^{-2}	0.00616	0.00816

Table 4.4 Injection brine chemistry.

Primary Species	CGUESS (molality)	CTOTAL (molality)
$Alo2^{-}$	$1.0x10^{-5}$	$3.28x10^{-5}$
Br^{-}	$3.0x10^{-6}$	$7.8x10^{-6}$
Ca^{+2}	$1.56x10^{-4}$	$2.56x10^{-4}$
Cl^{-}	0.003377	0.003177
F^{-}	0.001388	0.001988
Fe^{+2}	$4.0x10^{-7}$	$4.56x10^{-7}$
H^{+}	$1.29x10^{-9}$	$1.29x10^{-9}$
H_2O	55.51	55.51
HCO_3^{-}	0.07136	0.08136
K^{+}	0.005429	0.005929
Mg^{+2}	$2.48x10^{-6}$	$2.98x10^{-6}$
Na^{+}	0.06083	0.06183
SiO_2 (aq)	0.008775	0.009775
SO_4^{-2}	0.007226	0.008226

Table 4.5 Aqueous complexes.

$Al(OH)_2^{+}$	$AI(OH)_3$(aq)	$AI(OH)_4^{-}$
$AI(SO_4)_2^{-}$	Al^{+3}	$Al_{13}O_4(OH)_{24}^{+7}$
$Al_2(OH)_2^{+4}$	$Al_3(OH)_4^{+5}$	AIF^{+2}
AlF_2^{+}	AlF_3(aq)	AlF_4^{-}
$AlOH^{+2}$	$AlSO_4^{+}$	$CaCl^{+}$

Table 4.5 (cont'd)

$CaCl_2(aq)$	$CaCO_3(aq)$	CaF^+
$CaH_2SiO_4(aq)$	$CaH_3SiO_4^+$	$CaHCO_3^+$
$CaOH^+$	$CO_2(aq)$	CO_3^{-2}
$Fe(OH)_2(aq)$	FeF^+	$FeHCO_3^+$
$FeO(aq)$	$FeOH^+$	$FeSO_4(aq)$
$H_2SO_4(aq)$	$H_3SiO_4^-$	$HAlO_2(aq)$
$HCl(aq)$	$HF(aq)$	HF_2^-
$HFeO_2^-$	$HSiO_3^-$	HSO_4^-
$KCl(aq)$	$KHSO_4(aq)$	$KOH(aq)$
$Mg_4(OH)_4^{+4}$	$MgCl^+$	$MgCO_3(aq)$
MgF^+	$MgHCO_3^+$	$MgOH^+$
$MgSO_4(aq)$	$NaAlO_2(aq)$	$NaCl(aq)$
$NaCO_3^-$	$NaF(aq)$	$NaH_3SiO_4(aq)$
$NaHCO_3(aq)$	$NaSO_4^-$	OH^-
SiF_6^{-2}		

The mineral composition of a rock must be specified in TOUGHREACT to prevent unbalanced chemical reactions. The software requires the user to define the primary minerals and their product minerals, also known as secondary minerals. Primary minerals and their product minerals, called secondary minerals, are introduced to the software, leading reaction types and possible product occurrences. The secondary mineral is a product of the reaction between CO_2-charged water and primary mineral. It can form as a result of mineral precipitation or dissolution. If the mineral composition is not defined in TOUGHREACT appropriately, the program will prematurely terminate with an error due to a chemical reaction. Therefore, it is

essential to define the primary and secondary minerals correctly. Rock mineral analysis, such as XRD and SEM, can be used to identify the primary and secondary minerals. In this case, the primary minerals were calcite and quartzite, while the secondary minerals were dolomite, magnesite, kaolinite, and albite (Table 4.6). In TOUGHREACT, the secondary minerals are defined by assigning them a volume fraction as “0”. This means that they are not initially present in the rock sample, but they can form as a result of the chemical reactions. It is important to note that the rock sample was taken from a core in the field. This means that there was already a certain amount of secondary mineral content in the mineral assembly. However, this content was not included in the TOUGHREACT model.

Table 4.6 Mineral composition.

	Grain Radius (cm)	Volume Fraction	Surface area (cm^2/gr
Calcite	0.001	0.01	10
Quartzite	0.001	0.01	10
Kaolinite	0.001	0.01	10
Albite	0.001	0.4	10
Dolomite	0.001	0.01	10
Siderite	0.001	0.01	10
Magnesite	0.001	0.0	10

Rock properties of the model were modified from (Küçük, 2018), based on the pressure transient analysis of the existing wells (Table 4.7). The thermal and physical rock properties were taken from Küçük, 2018 (Table 4.8).

Table 4.7 Porosity and permeability values of the formations.

Formation Name	Porosity	Permeability in x Direction (mD)	Permeability in y direction (mD)	Permeability in z direction (mD)
Sazak	0.1	10	10	2
İğdecik	0.05	10	10	2
Metamorphics	0.02	1	1	0.5

Table 4.8 Characteristic of rock properties (Küçük, 2018)

Formation Name	Rock Density (kg/m^3)	Rock Specific Heat (J/kg^oC)	Wet Heat Conductivity (W/m^oC)
Sazak	2600	1000	1.0
İğdecik	2600	1000	1.0
Metamorphics	2600	1000	1.0

Permeability and porosity factors were assigned to grid blocks to represent fault, fracture, and caprock properties (Figure 4.18) and (Figure 4.19). During the natural state calibration of the model, the tuning parameters were porosity, permeability factors, and the source rate heating the system with a convective and conductive heat flow. The natural state model calibration was validated with static pressure and temperature wells' profiles, as shown in Figure 4.20, Figure 4.21, Figure 4.22, and Figure 4.23. There is a good match between simulated and actual field data for natural state condition.

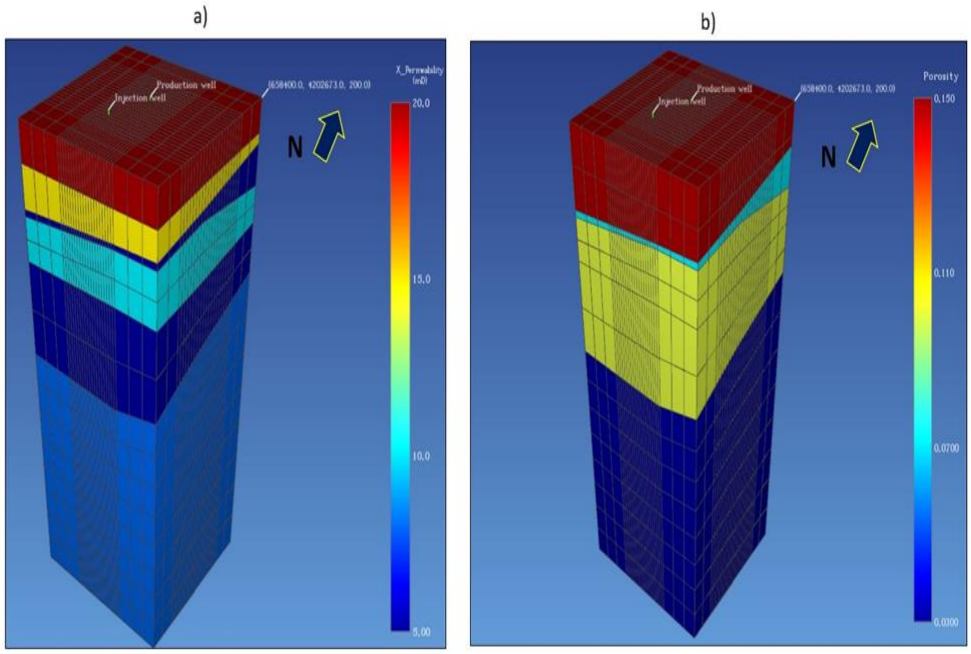

Figure 4.18 Permeability factor and porosity factor assigned to formations.

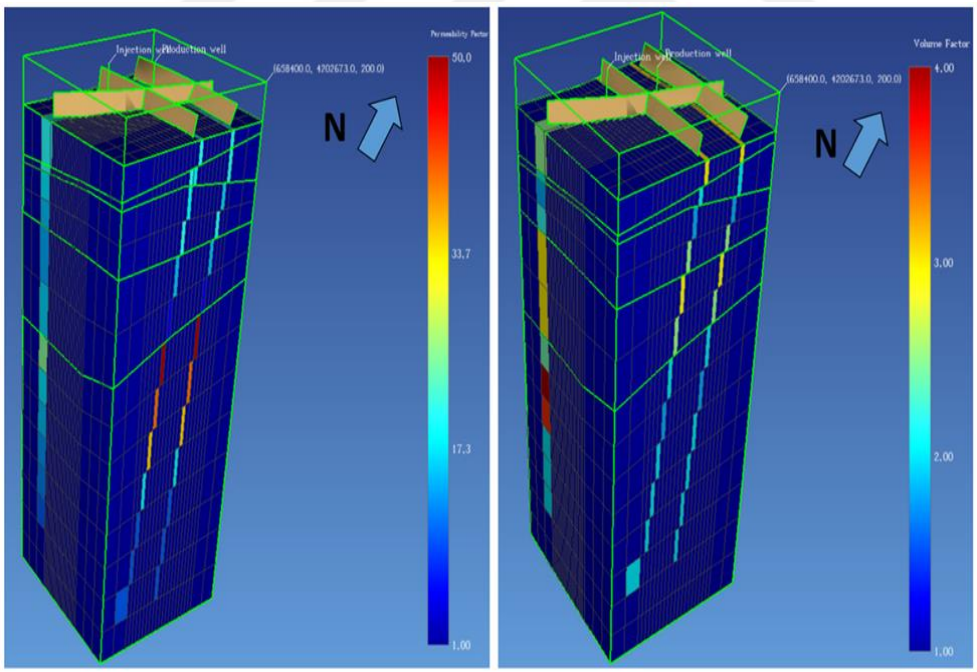

Figure 4.19 Permeability and porosity factors assigned to fault-cut grids.

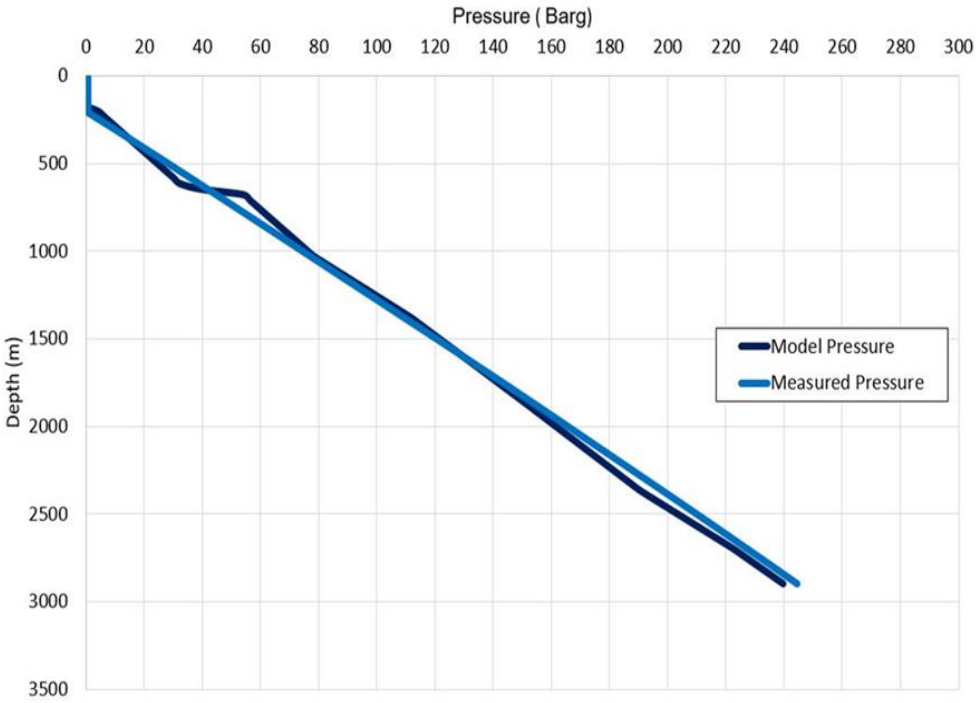

Figure 4.20 Matching with static pressure profile of reinjection well.

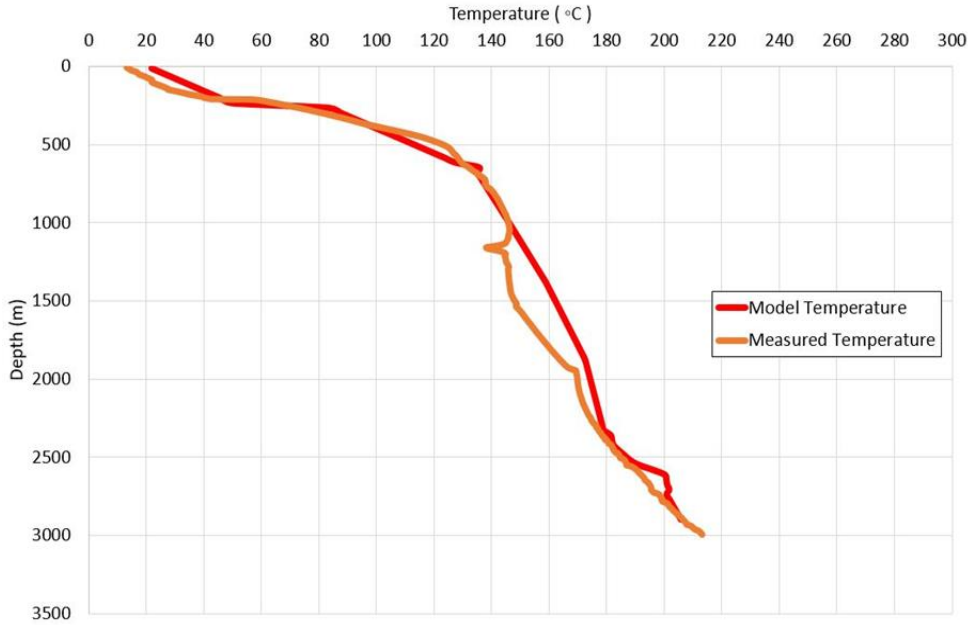

Figure 4.21 Matching with static temperature profile of reinjection well.

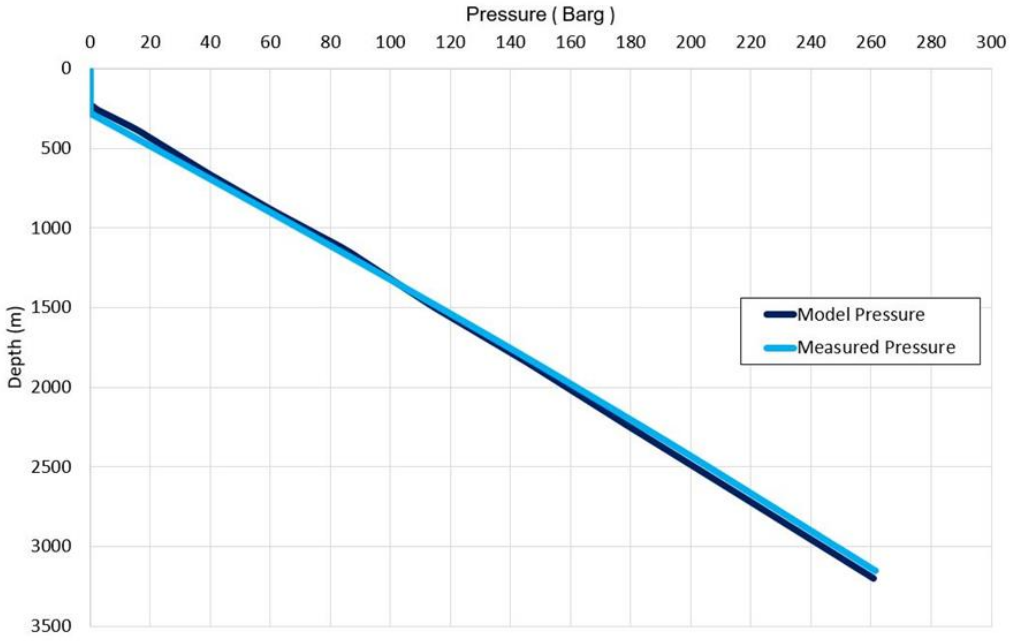

Figure 4.22 Matching with static pressure profile of production well.

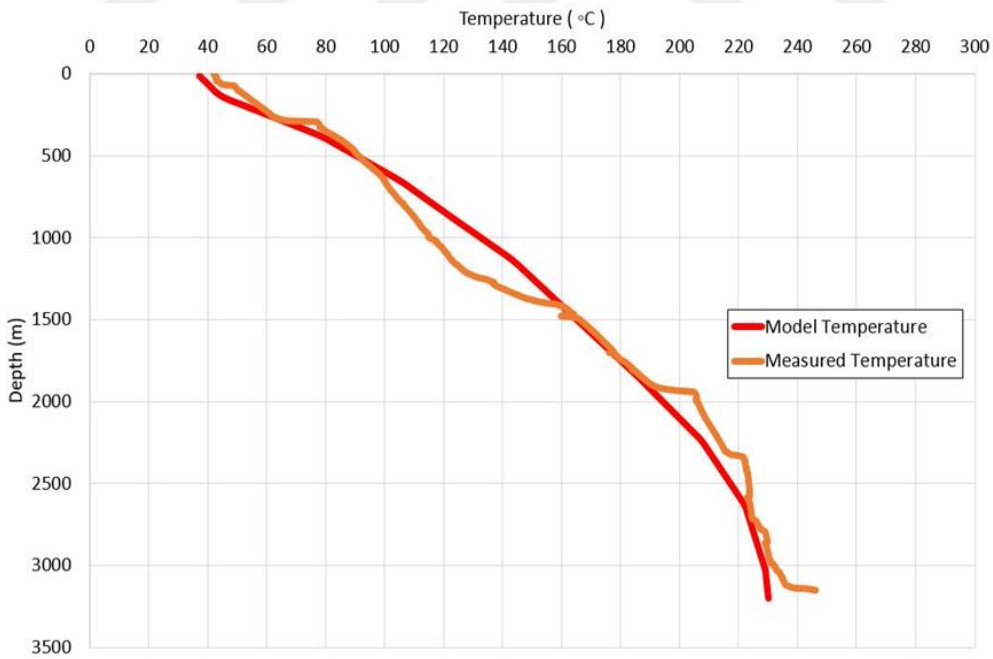

Figure 4.23 Matching with static temperature profile of production well.

CHAPTER 5

RESULTS AND DISCUSSIONS

5.1 CO_2 Dissolution in Geothermal Brine

This study presents a novel experimental setup for gas dissolution tests in geothermal brine at varying temperatures, pressures, and mineral concentrations. The setup consists of a 12-liter reactor with geothermal heating, a mixer, a gas flow meter, a gas source, a two-stage regulator, sampling ports, and a mini separator. Geothermal brine (9 liters) was collected from an injection well in the Alaşehir field and placed in the reactor. NCG was also collected from a geothermal well at static conditions with a gas pressure of 40 barg at the wellhead. More than 98% of the NCG was CO_2, thus the process can be considered as CO_2 dissolution in the brine. The brine sample was placed in the reactor and heated using the temperature of an actively producing geothermal well. The high-temperature geothermal brine was directed into a capillary tubing surrounding the reactor. The reactor was then isolated from the atmosphere with insulating materials. The setup was transferred to different well locations for different temperatures. Once the temperature stabilized, CO_2 was supplied to the reactor at a constant pressure while the system was continuously mixed. The continuous mixing of the fluids in the reactor maximized the contact surface area between the geothermal brine and the CO_2.

A batch reactor system was filled with 9 liters of brine and 3 liters of CO_2 at 8 barg pressure. To investigate the dissolution behavior of CO_2 in geothermal brine, the batch system was continuously mixed for 3.15 minutes while the gas supply was maintained at a constant pressure of 8.4 barg. The mixer was then stopped until the initial pressure condition of 8 barg was reached (Figure 5.1). The reactor pressure decreased slightly, indicating CO_2 dissolution. After the mixing process was stopped, a pressure buildup was observed due to the pressure supply from the pressure vessel.

The stabilization pressure increased with increasing mixing times during mixing because the brine approached its maximum gas dissolution capacity. Experiments were conducted at different gas-to-brine (G/B) ratios to investigate the effect of volumetric ratio on gas dissolution kinetics. As the G/B ratio increased, the given amount of brine reached its maximum gas dissolution capacity more quickly (Figure 5.2). This suggests that it is critical to have a large surface contact area between brine and NCG for complete mixing and solubility. The gas dissolution rates showed an exponential decline with time for all G/B ratios (Figure 5.4). The empirical equations showing exponential decline are shown in Table 5.1 for each volumetric ratio.

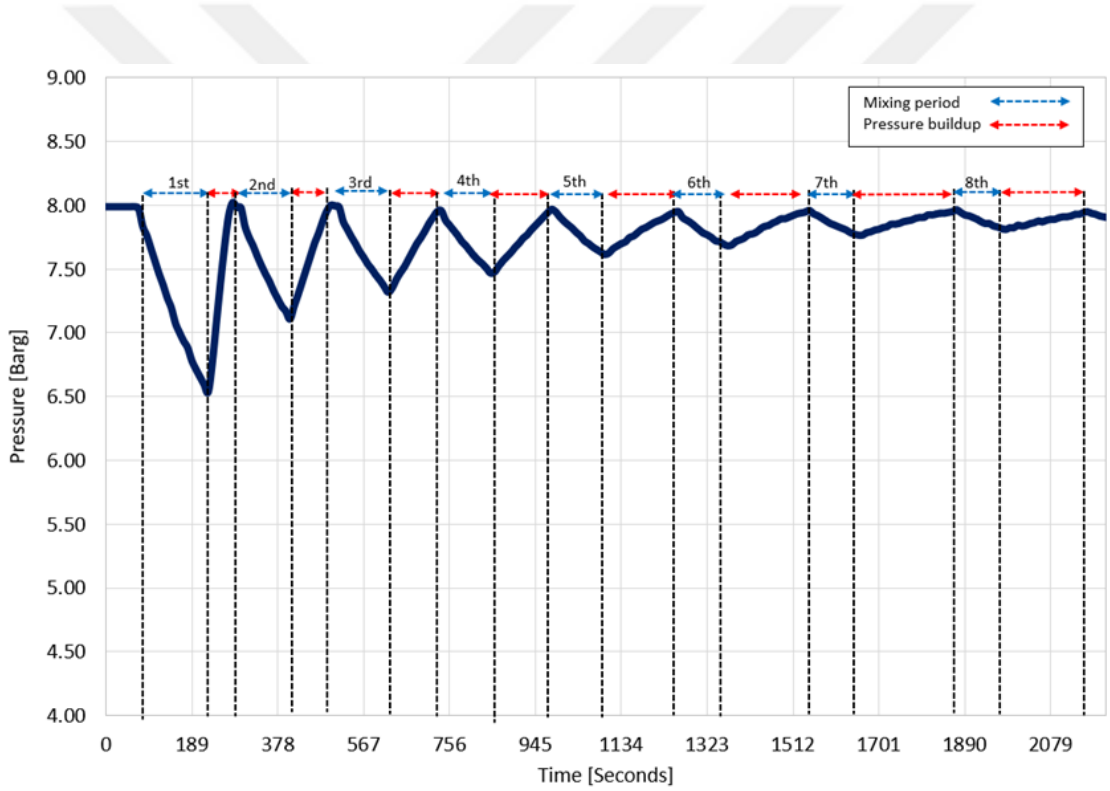

Figure 5.1 CO_2 dissolution experiments for dissolution reaction kinetics.

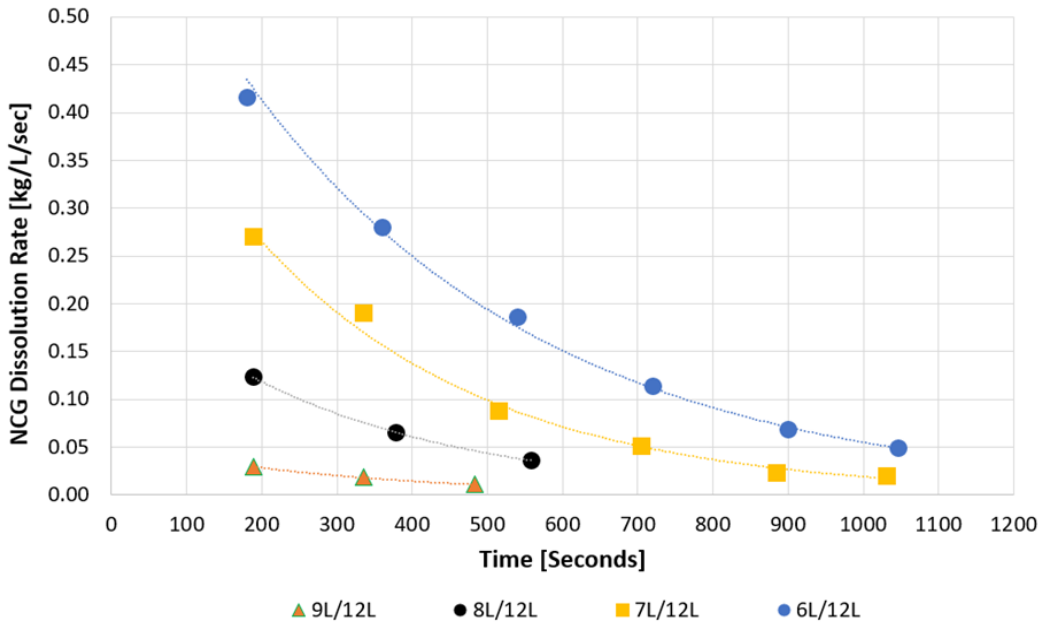

Figure 5.2 Dissolution kinetics of NCG in geothermal brine for different gas/(gas+brine) volumetric ratio.

Table 5.1 Exponential behavior of NCG dissolution in the geothermal brine at different gas ratio (x represents time (seconds) and y is NCG dissolution rate (kg/L/second)).

Volumetric ratio of Gas/(Gas+Brine)	Exponential Decline
9/12	$y = 0.0556e^{-0.003x}$
8/12	$y = 0.2301e^{-0.003x}$
7/12	$y = 0.5108e^{-0.003x}$
6/12	$y = 0.6834e^{-0.003x}$

Gas dissolution experiments were conducted at various temperatures and pressures using the above procedure. The amount of CO_2 that remained dissolved in the brine and flashed out of the solution was explicitly measured (Table 5.2 and Table 5.3).

As shown in Table 5.2, a large fraction of CO_2 is present as bicarbonate (HCO_3^-). However, the majority of the CO2 was flashed out when the system was opened to atmospheric pressure in the brine sampling separator. The flashed-out free gas was measured using a gas flow meter connected to the separator, as shown in Figure 4.2 and Figure 4.4. The calculated gas content by weight was compared with popular empirical formulas from the literature (Cramer, 1982; Fournier, 1989) (Figure 5.3). The experimental results are in agreement with empirical formulas for a wide range of pressures (Figure 5.4).

Table 5.2 The amount of CO_2 that remained in the geothermal brine based on alkalinity tests.

HCI volume (4.3) ml	HCI volume (8.2) ml	NaOH volume (8.2) ml	CO_2 from HCO_3^- (mg)	CO_2 from CO_3^- (mg)	CO_2 from H_2CO_3 (mg)	CO_2 (mg)
10.60	3.70		14.08	16.28		30.36
13.10		4.20	57.64		18.48	76.12
13.10		5.00	57.64		22.00	79.64
14.80		6.00	65.12		26.40	91.52
13.00		3.80	57.20		16.72	73.92
13.10		4.00	57.64		17.60	75.24
14.20		4.80	62.48		21.12	83.60
15.30		6.00	67.32		26.40	93.72
15.50		6.00	68.20		26.40	94.60
13.10		3.60	57.64		15.84	73.48
13.70		4.00	60.28		17.60	77.88
12.80		3.60	56.32		15.84	72.16

Table 5.2 (cont'd)

13.10		4.20	57.64		18.48	76.12
13.10		5.00	57.64		22.00	79.64
14.80		6.00	65.12		26.40	91.52
14.70		6.00	64.68		26.40	91.08
15.20		6.40	66.88		28.16	95.04
16.00		7.00	70.40		30.80	101.20
16.80		8.00	73.92		35.20	109.12
17.80		9.00	78.32		39.60	117.92
16.10		7.20	70.84		31.68	102.52
16.20		7.50	71.28		33.00	104.28
16.70		8.00	73.48		35.20	108.68
19.10		10.00	84.04		44.00	128.04

Table 5.3 The amount of CO_2 that remained in the geothermal brine based on alkalinity tests.

CO_2 (L)	Gas Temperature (^oC)	Condensate (ml)	CO_2 (mol)	CO_2 in Brine (mg)	CO_2 Free Gas (mg)	Total CO_2 (g)	CO_2 % wt
0.20	26.70	266.00	0.008	76.12	355.84	0.43	0.16
0.28	28.00	326.00	0.011	79.64	491.04	0.57	0.17
0.58	29.00	831.00	0.023	91.52	1022.73	1.11	0.13
0.82	17.80	458.00	0.034	73.92	1507.53	1.58	0.34

Table 5.3 (cont'd)

0.55	17.90	363.00	0.023	75.24	1014.51	1.09	0.30
0.66	18.50	403.00	0.028	83.60	1214.91	1.30	0.32
0.78	18.80	458.00	0.033	93.72	1434.33	1.53	0.33
0.60	18.60	433.00	0.025	94.60	1098.56	1.19	0.27
0.38	13.20	353.00	0.016	73.48	704.95	0.78	0.22
0.40	14.00	323.00	0.017	77.88	753.46	0.83	0.26
0.54	14.50	378.00	0.023	72.16	998.52	1.07	0.28
0.20	26.70	243.00	0.008	76.12	355.75	0.43	0.18
0.28	28.00	303.00	0.011	79.64	490.95	0.57	0.19
0.58	29.00	808.00	0.023	91.52	1021.64	1.11	0.14
0.16	11.90	263.00	0.007	91.08	303.23	0.39	0.15
0.18	11.43	253.00	0.008	95.04	336.93	0.43	0.17
0.18	11.54	243.00	0.008	101.20	343.22	0.44	0.18
0.10	12.00	208.00	0.004	109.12	188.28	0.30	0.14
0.26	13.10	218.00	0.011	117.92	494.39	0.61	0.28
0.39	13.29	238.00	0.017	102.52	732.28	0.83	0.35
0.15	13.37	180.00	0.006	104.28	276.57	0.38	0.21
0.30	13.45	165.00	0.013	108.68	565.53	0.67	0.41
0.34	14.41	213.00	0.014	128.04	626.74	0.75	0.35

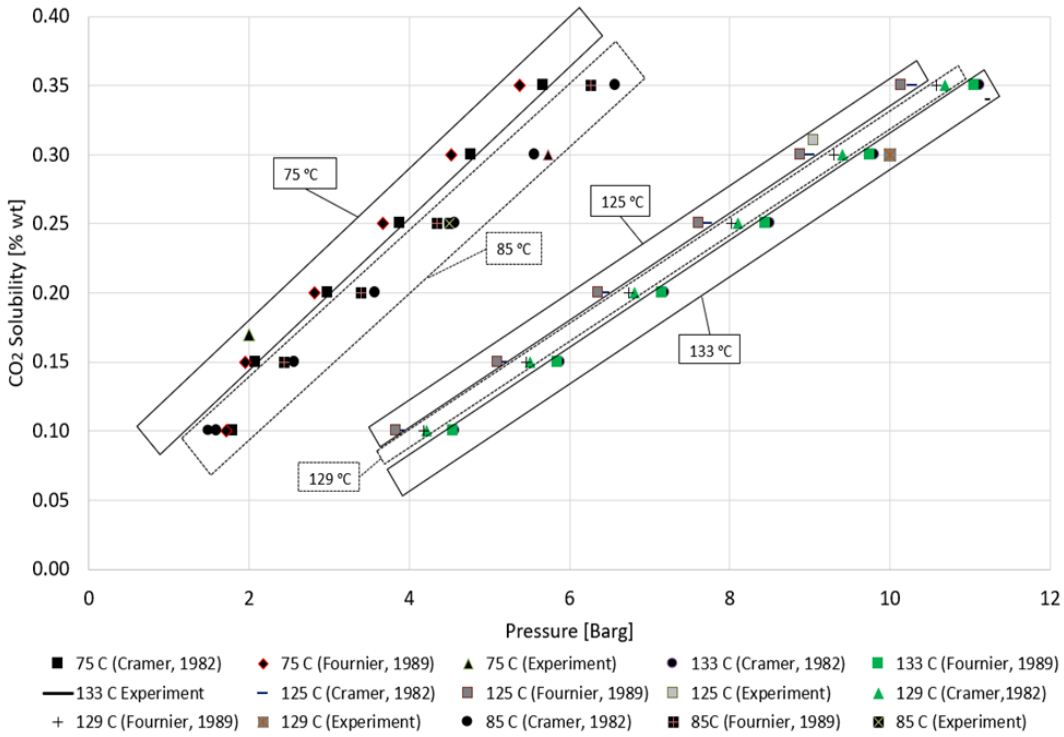

Figure 5.3 Comparison of gas dissolution experiments with empirical formulas available in the literature.

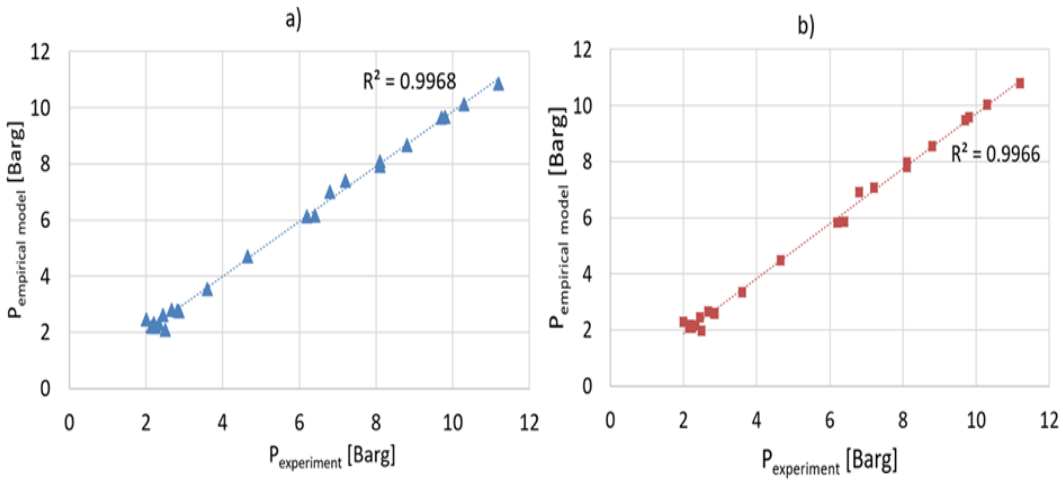

Figure 5.4 Comparison of gas dissolution experiments with empirical formulas a) Cramer, 1982 b) Fournier, 1989.

Experimental results were also compared with simulated results obtained from PHREEQC. Akin & Kargı (2019) used PHREEQC to simulate the geochemical evolution of fluids in geothermal wells west of Turkey. They compared the results of two databases, PHREEQC.dat and LLNL.dat, against actual field data and found that LLNL.dat provided a better match. Therefore, we used LLNL.dat as the reference database for our simulation of CO_2 dissolution in geothermal fluids, which have similar compositions.

PHREEQC predicted a somewhat higher gas content than was observed experimentally (Figure 5.5). This discrepancy may be attributed to the assumption of complete mixing of NCG and brine under ideal conditions. It is possible that complete mixing is not achieved in all experiments, regardless of duration.

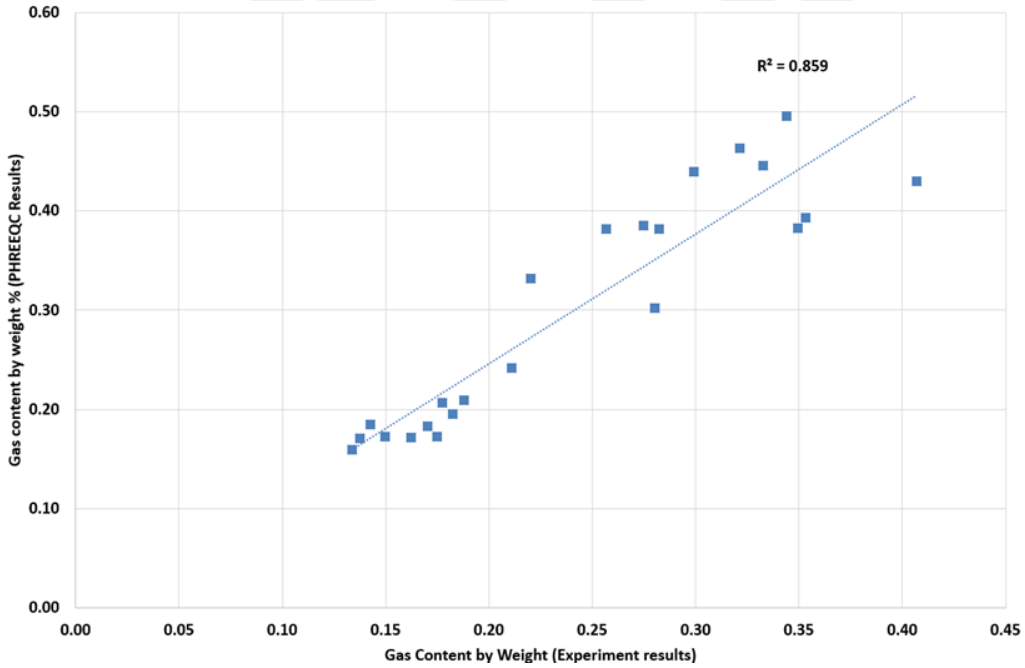

Figure 5.5 Comparison of gas dissolution experiments against PHREEQC.

Due to the limitations of the experimental setup, it is challenging to conduct continuous mixing batch experiments under high temperatures and pressures. The

main limitation is the sealing of the mixing system, which requires a special design for operation under high pressure and temperature. The mechanical sealing method used in pumps, which uses a carbon graphite bearing system to seal the batch reactor, is limited to a working pressure of 15 barg. Therefore, we used a calibrated PHREEQC model to estimate CO_2 dissolution at temperatures and pressures, representive of reservoir conditions. As shown in Figure 5.6, dissolved CO_2 increases linearly with pressure at low pressures (1-30 barg). However, deviation from linearity begins at pressures higher than 30 barg. Upton and Santoyo (2022) found the Henry constant by plotting solubility data at constant temperatures on a straight line.

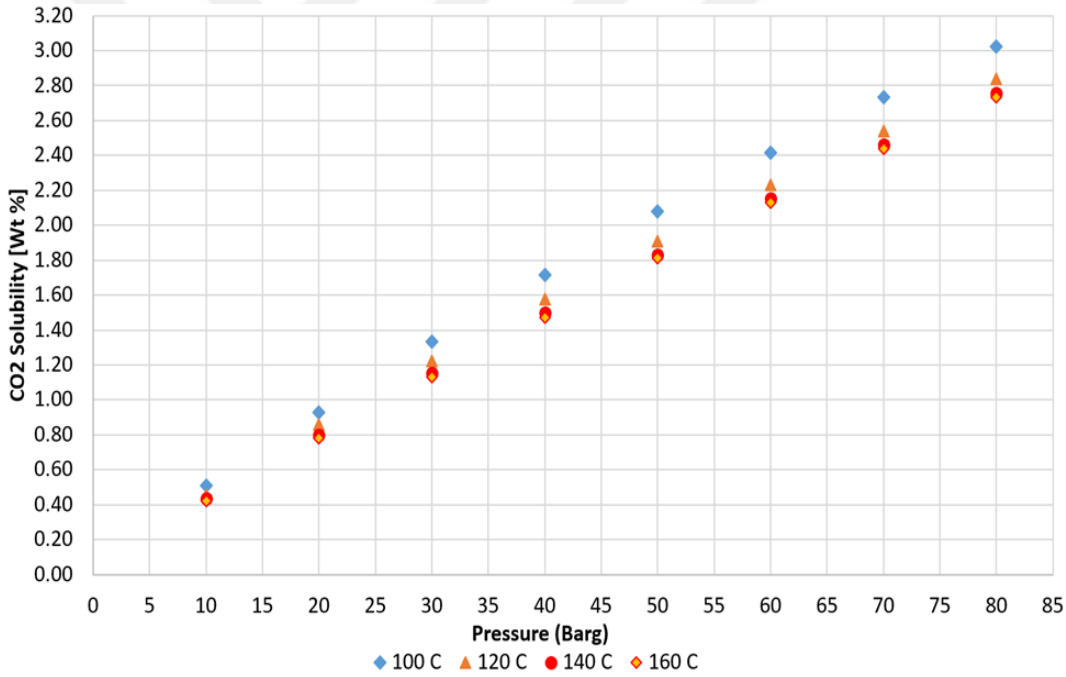

Figure 5.6 CO_2 solubility under high temperature and pressure.

The solubility of CO_2 in brine is also affected a phenomenon known as the salting-out effect. CO_2 solubility decreases with increasing salt content. NaCI is the most abundant salt in geothermal fluids. Therefore, we investigated the effect of NaCI on CO_2 solubility at salt concentrations ranging from 0.05 and 2 mol/kg (Figure 5.7).

We found that increasing the salt concentration from 0.05 M to 2 M, reduces brine's CO_2 solubility capacity by more than 30 %. Therefore, it is important to consider the salt content of geothermal brine when determining CO_2 injection parameters. To illustrate, Figure 5.7 shows that injecting CO_2 at 50 bar pressure and a rate greater than 1.8 ton/hr (tph) with 100 tph of brine containing 1 M NaCI will result in the presence of free gas that remains undissolved in the mixture. The presence of free can lead to gas escape and mechanical problems during injection in the wellbore.

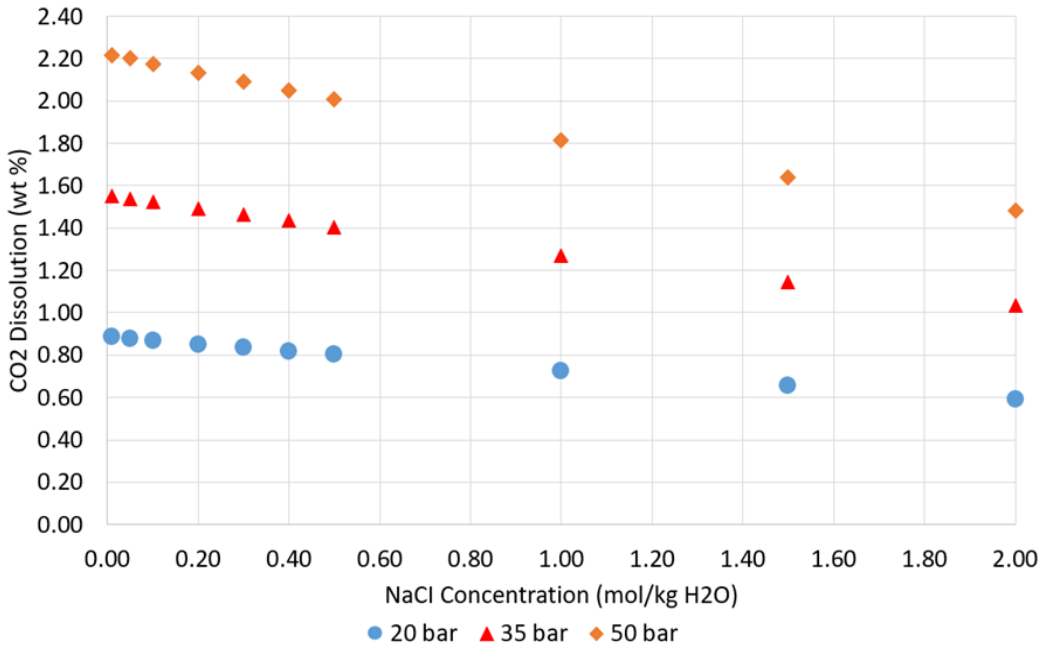

Figure 5.7 CO_2 solubility in the geothermal brine with varying NaCI concentration at 100 ^{o}C using PHREEEQC.

Geothermal gases dissolve in the liquid phase in the reservoir if reservoir pressure is greater than the flashing pressure. In two-phase reservoirs, gases may be present in both the liquid and steam phases. Captured CO_2 streams from power plants typically contain a certain amount of NCGs species. The separation of CO_2 from the captured stream is the major cost of carbon capture, and storage, and impure CO_2 injection is

often used to reduce the overall cost of CCS (Li et al. 2018). Impure CO_2 injection has specific impacts on CO_2 dissolution in the brine, migration, and sequestration in the formation. Fridriksson et al. (2016) presented a range of gas compositions from 15 representative high-temperature geothermal systems in Europe, North America, Central America, Africa, Asia, and Oceania (Table 5.4). Based on Table 5.4, we created three hypothetical mixtures of NCG to investigate the effects of gas impurity on CO_2 dissolution (Table 5.5). It is clear from Table 5.5 that CO_2 is the major gas in all three mixtures, followed by hydrogen sulfide (H_2S) and nitrogen (N_2). The presence of non-CO_2 species in a limited volume reduces the amount of CO_2, which decreases the contact surface area between CO_2 and brine. This leads a lower CO_2 dissolution capacity. As shown in Figure 5.8, mixture-3 has the highest CO_2 dissolution capacity at varying temperatures and 20 barg. This indicates that increasing the CO_2 content of NCG enhances the CO_2 dissolution capability of brine due to the increased contact surface area between CO_2 and brine. Mahmoodpour et al. (2020) showed that the presence of NCG impurities and inert impurities such as N_2, Ar, O_2, and CH_4 would decrease the structural trapping capacity of CO_2. N_2 has lower solubility and viscosity than CO_2, which may cause leakage problems during NCG injection in poorly cemented wellbores. However, N_2 is not corrosive, and does not damage wellbore integrity. N_2 also reduces the dew point of the gas mixture, requiring higher compression power during the injection. H_2S is corrosive and can damage wellbore integrity over the long term. Mahmoodpour et al. (2023) showed N_2 enhances CO_2 solubility at reservoir conditions because of its lower viscosity than CO_2. This causes N_2 to move ahead of the injected gas, spreading the geothermal fluid over a wider area in the reservoir and increasing the CO_2-brine contact surface area. This is acceptable at reservoir conditions, but in experiments, where the overall reactor volume is the same, increasing non-CO_2 impurity reduces the number of CO_2 molecules in the tank, and eventually, decreases CO_2 solubility.

Table 5.4 Typical composition of Geothermal Gas (Fridriksson et al. 2016).

	CO_2	H_2S	H_2	CH_4	NH_3	N_2	AR
Median	95.4	3	0.012	0.15	0.29	0.84	0.02
Maximum	99.8	21.2	2.2	1.7	1.8	3.0	0.04
Minimum	75.7	0.1	0.001	0.0045	0.005	0.17	0.004

Table 5.5 Gas mixtures to account for gas purity affecting CO_2 dissolution.

Gas Composition	Mixture-1	Mixture-2	Mixture-3
CO_2	76	90	98
N_2	0.11	0.3	0.167
CH_4	1	0.2	0.15
H_2S	21	8.5	1.529
H_2	1.885	0.5	0.15
NH_3	0.005	0.5	0.004

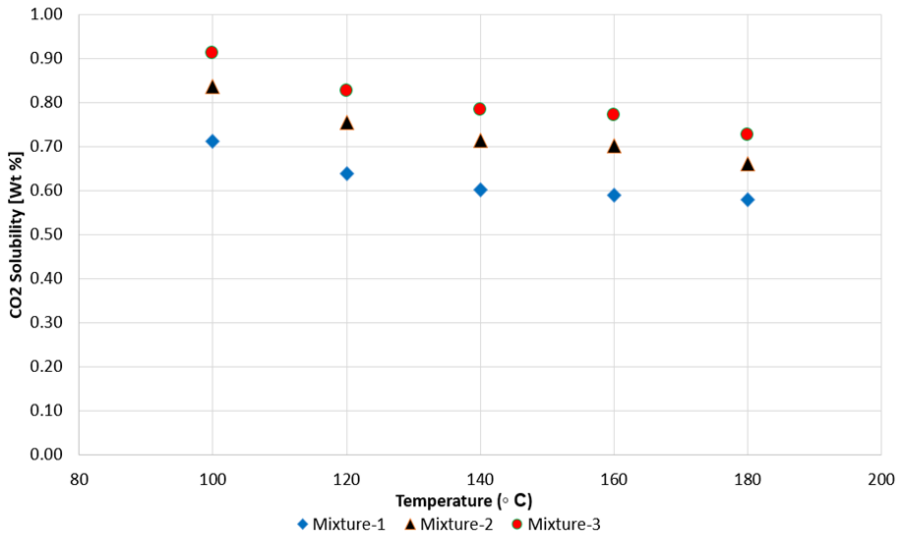

Figure 5.8 CO_2 dissolution results for mixtures of gases at 20 barg.

Geothermal brine has a specific geochemical equilibrium under reservoir conditions. However, due to thermodynamic and physicochemical changes, some minerals tend to precipitate during production. For example, steam and (NCG) flashing in the wellbore increases the pH and element concentrations. Calcium carbonate and silicate are typically precipitated minerals in high and low temperatures, respectively. Since reinjected brine has a low temperature, it is expected to experience silica precipitation, which can significantly reduce well injection capacity. CO_2 dissolution can be considered for inhibiting mineral precipitation by adjusting the pH of brine. Topcu et al. (2019) investigated the effect of CO_2 injection on metal silicates in the Tuzla geothermal field in Turkey. We used PHREEQC to simulate the effects of CO_2 dissolution on the mineral precipitation for the geothermal brine sample shown in Figure 5.9. The distribution of species before CO_2 dissolution is shown in Figure 5.9. Free ions of Ca^{2+}, SO_4^{2-}, F^-, K^+, Mg^{2+}, and Na^+ are the dominant species before CO_2 dissolution. Dissolved silicon is completely composed of SiO_2 uncharged complex.

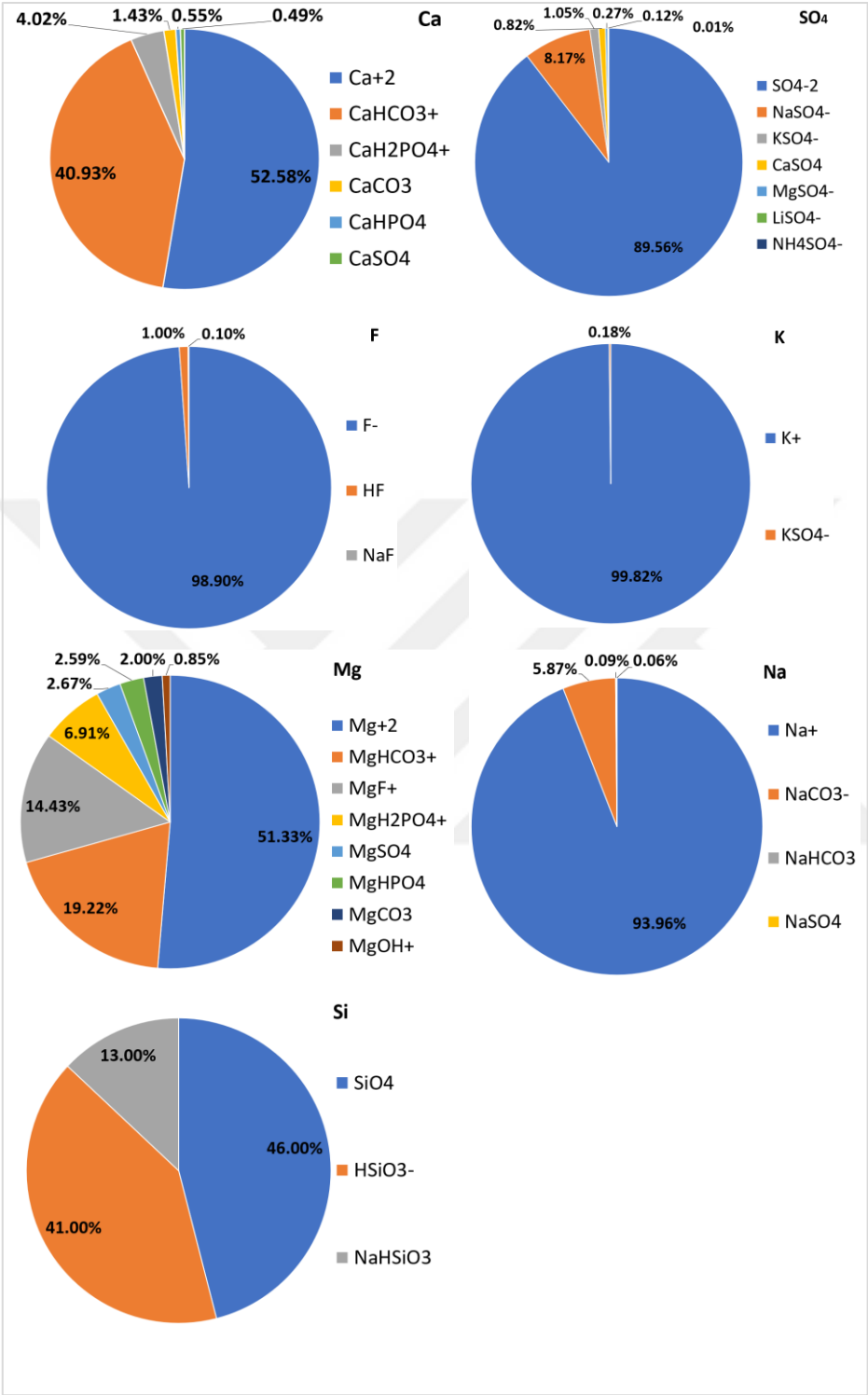

Figure 5.9 Distribution of species at pH=9.

Dissolution of CO_2 in brine at varying temperatures and pressure resulted in a decrease in pH value from 9 (basic) to the range of of 4.8 - 6 (acidic) (Figure 5.10). This is because the solubility of CO_2 increases with decreasing temperature and increasing pressure, leads to a decrease in pH. Dissolution of CO_2 created a new equilibrium in the brine Figure 5.12, with a decrease in the number and bulk mass of complexes and a significant increase in the bulk mass of free ions. This redistribution of bulk mass between related species of ions and complexes altered the saturation indices of minerals. The LLNL database of PHREEQC contains over 150 dissolution reactions of mineral and gas phases (Akin and Kargi, 2019). PHREEQC model showed that the saturation indices of calcite, dolomite, sepiolite, aragonite, and chalcedony shifted from precipitation to the dissolution after CO_2 dissolution (Figure 5.11). However, the precipitation tendency of quartzite and amorphous silica slightly increased. This is because the solubility of amorphous silica increases above a pH of 9 and below a pH of 5. The initial pH value of the brine was 9, so amorphous silica was in a dissolution state. However, the pH decreased to 5.5 after CO_2 dissolution, increasing the precipitation tendency of amorphous silica. Utami et al. (2014) and Bush et al. (2018) found similar effects of pH on the precipitation of amorphous silica. This suggests that ,for the given brine concentration, keeping the pH value below 5 is essential to prevent the formation of amorphous silica. If the reinjection temperature is assumed to be 100 ^{o}C, then the injecting pressure must be at least 30 bar to keep the pH below 5, corresponding to CO_2 dissolution of 1.33 % by weight. Otherwise, it is expected that the injection well capacity will be reduced due to silica scaling.

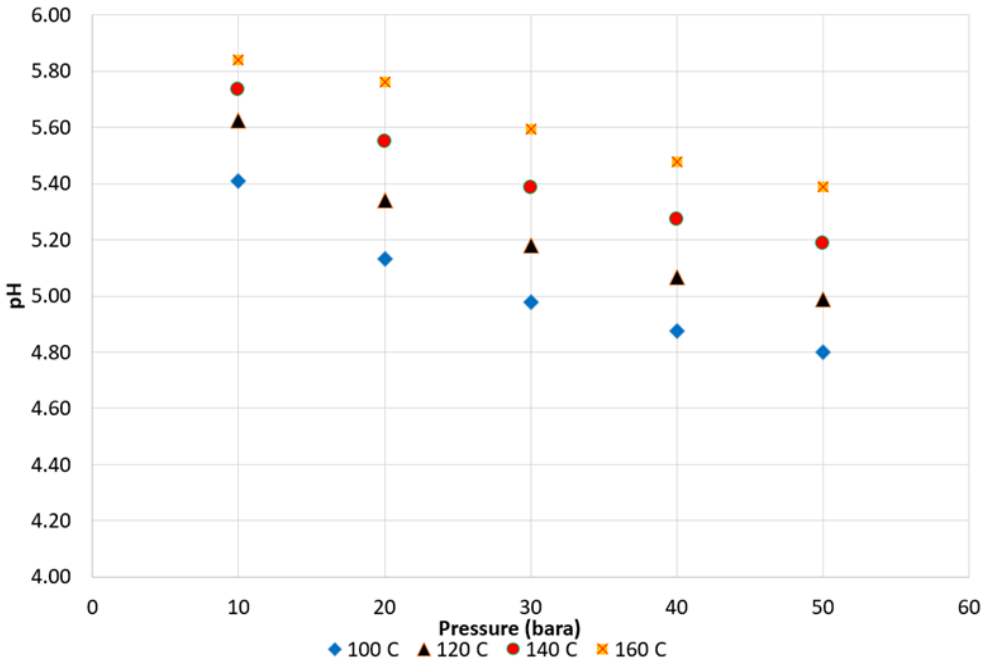

Figure 5.10 pH value of geothermal brine under dissolving CO_2 at varying pressure and temperature values.

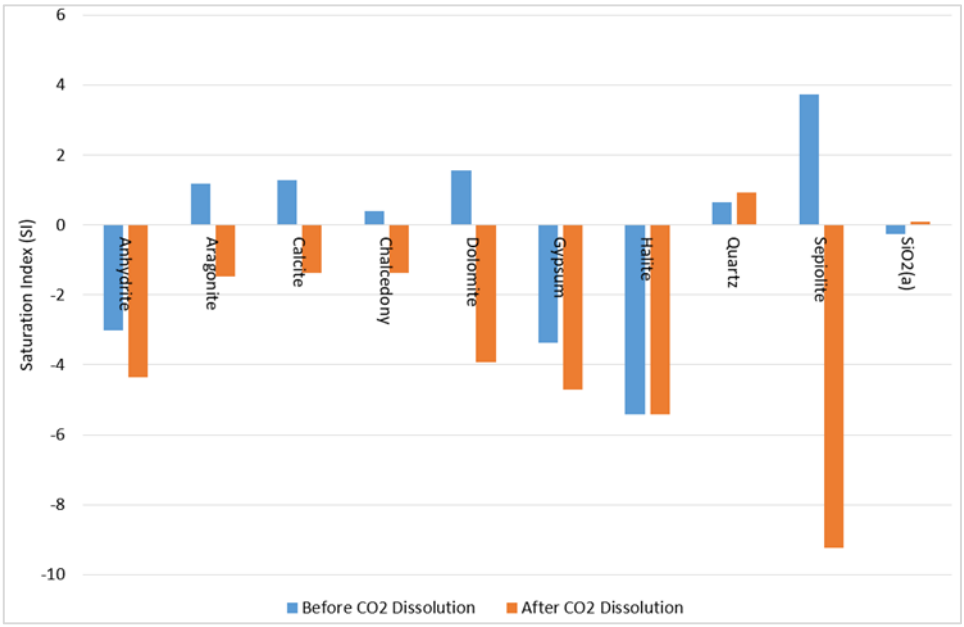

Figure 5.11 Saturation Index of saturated minerals before and after CO_2 dissolution at 8 Bar and 95 ^{o}C.

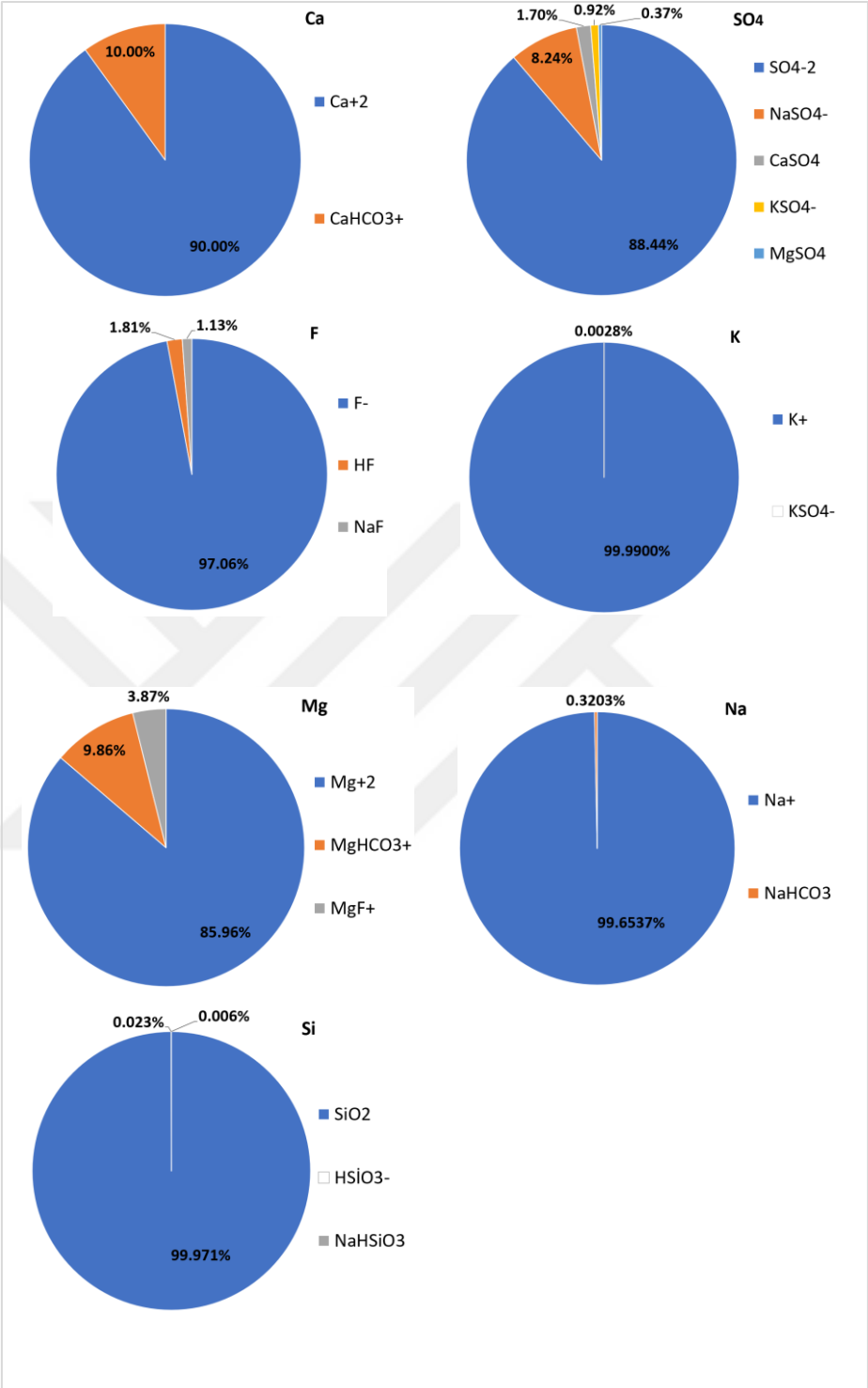

Figure 5.12 Distribution of species at 0.4 % by wt of CO_2 dissolution at 8 Bar and 95 ^{o}C.

5.2 Water-Rock Interaction with Batch Experiments

Understanding the mechanisms of water-rock interaction is essential for CO_2 sequestration projects. Experiments using representative reservoir rock and fluid samples are an effective way to mimic CO_2 injection into an actual reservoir. However, experimental conditions are typically limited to short time periods and cannot replicate reservoir conditions exactly. Therefore, simulation of reactions using robust software programs is a powerful tool for estimating long-term CO_2 sequestration in geothermal reservoirs. This study used PHREEQC code to simulate a batch experiment, considering rock surface area, the initial moles of minerals, kinetic reaction rates, and activation energy. The secondary minerals formed from water-rock interaction were validated with XRD results. In simulating experiments, the important variable parameters are the activation energy of minerals, mineral kinetic reaction rate, and mineral surface area. The key variable parameters in simulating experiments are the activation energy of minerals, mineral kinetic reaction rate, and mineral surface area. Mineral surface area is a critical unknown parameter in reservoir-scale reactive transport simulations. However, it is possible to determine mineral surface area in experiments using rock analysis and image processing.

The geometry of the selected rock particles was analyzed using the ImageJ software, which is a Java-based program solving image process and analysis problems. A high-resolution photograph of the rock particles was imported into ImageJ for particle analyses. Figure 5.13 shows the image scale setting process in ImageJ prior particle analysis.

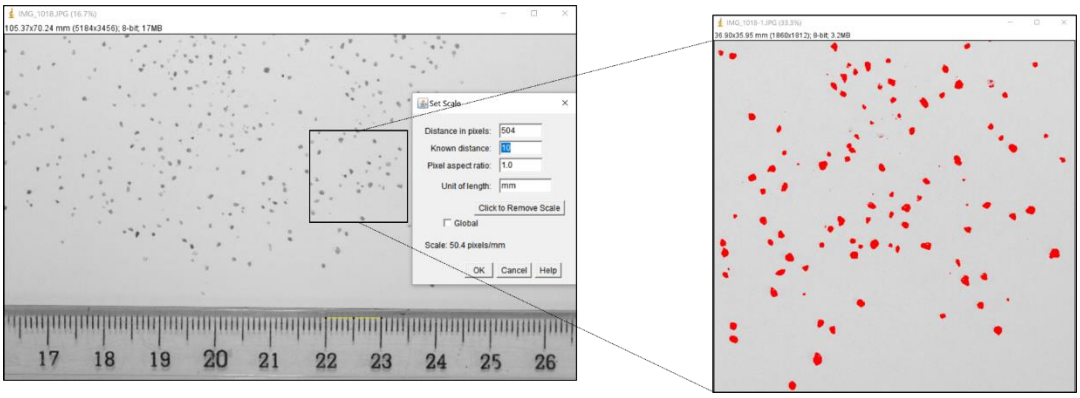

Figure 5.13 Set scale for image process.

Figure 5.14 shows the statistical results of the image processing of the rock particles. The mean surface area was 0.398 mm^2 with a standard deviation of 0.167 mm^2. Mineral surface area is a critical parameter that determines the reaction rate during fluid-rock interaction. By crushing the rock body into small particles, the total surface area of the rock samples was increased, which increased the chances of water-rock interaction between the mineral and geothermal brine.

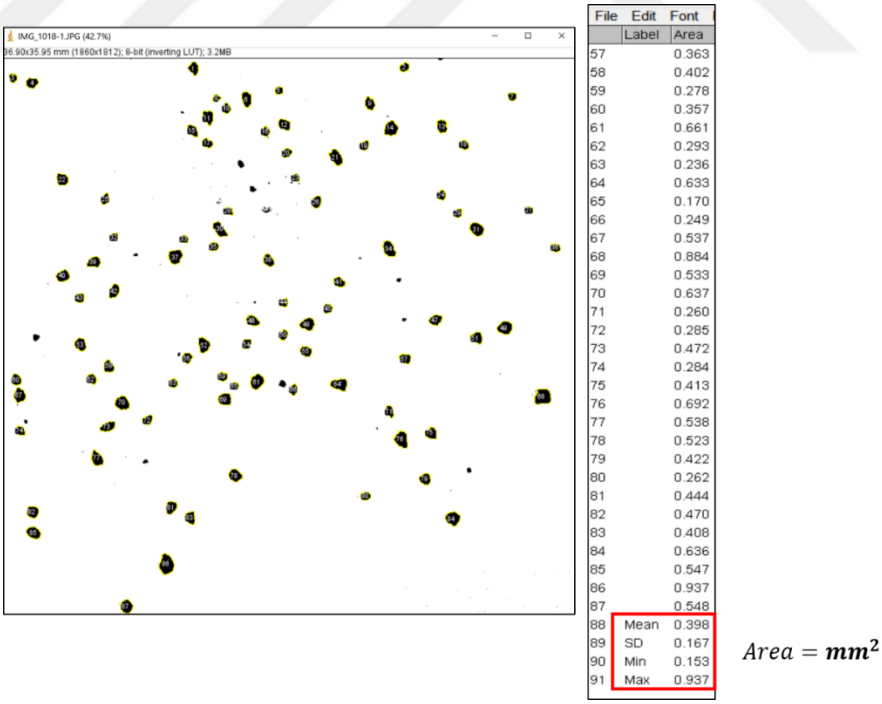

Figure 5.14 Statistical information about mineral surface area.

XRD analyses of core samples from 3000 m and 1900 m depth were conducted using GNR APD 2000PRO brand X-ray diffractometer at Pamukkale University Research Center. The samples were crushed to powder and placed on plates for XRD analysis. XRD patterns were interpreted to identify the mineral content, and mineral contents were calculated by matching peak measurements to the ICSD (Inorganic Crystal Structure Database) 12++ dataset. Figure 5.16 shows the XRD results of mineral analysis before and after batch experiments for the 1900-m depth core sample. The CO_2-charged geothermal water reacted with rock minerals in two ways. First, it consumes hydrogen ions that neutralizing the acidic gas-charged water. This increases the tendency of carbonate mineral precipitation with increasing pH. Second, the cations reacts with the dissolved CO_2 form stable carbonate minerals. The representative reaction for this process is shown in Equation (5.1) (Delerce et al., 2023). These cations promoted the mineralization of CO_2(g) as biotite, calcite, and kaolinite.

The 1900-m depth core sample was also exposed to CO_2-dissolved water in the batch experiments. Figure 5.17 shows the XRD results of mineral analysis before and after batch experiments. The content of feldspar (albite) increased from 35% to 38.4%, quartzite mineral content decreased from 19.4% to 15.3%, magnesite mineral content remained the same, kaolinite mineral content increased from 13.2% to 15.7%, biotite mineral content increased from 3.6% to 4.3%, dolomite mineral content decreased by half of its initial value, and siderite content decreased from 1.5% to 0.4%. The batch experiments showed that the mineral composition of the samples remained the same while the content of the mineral was slightly changed.

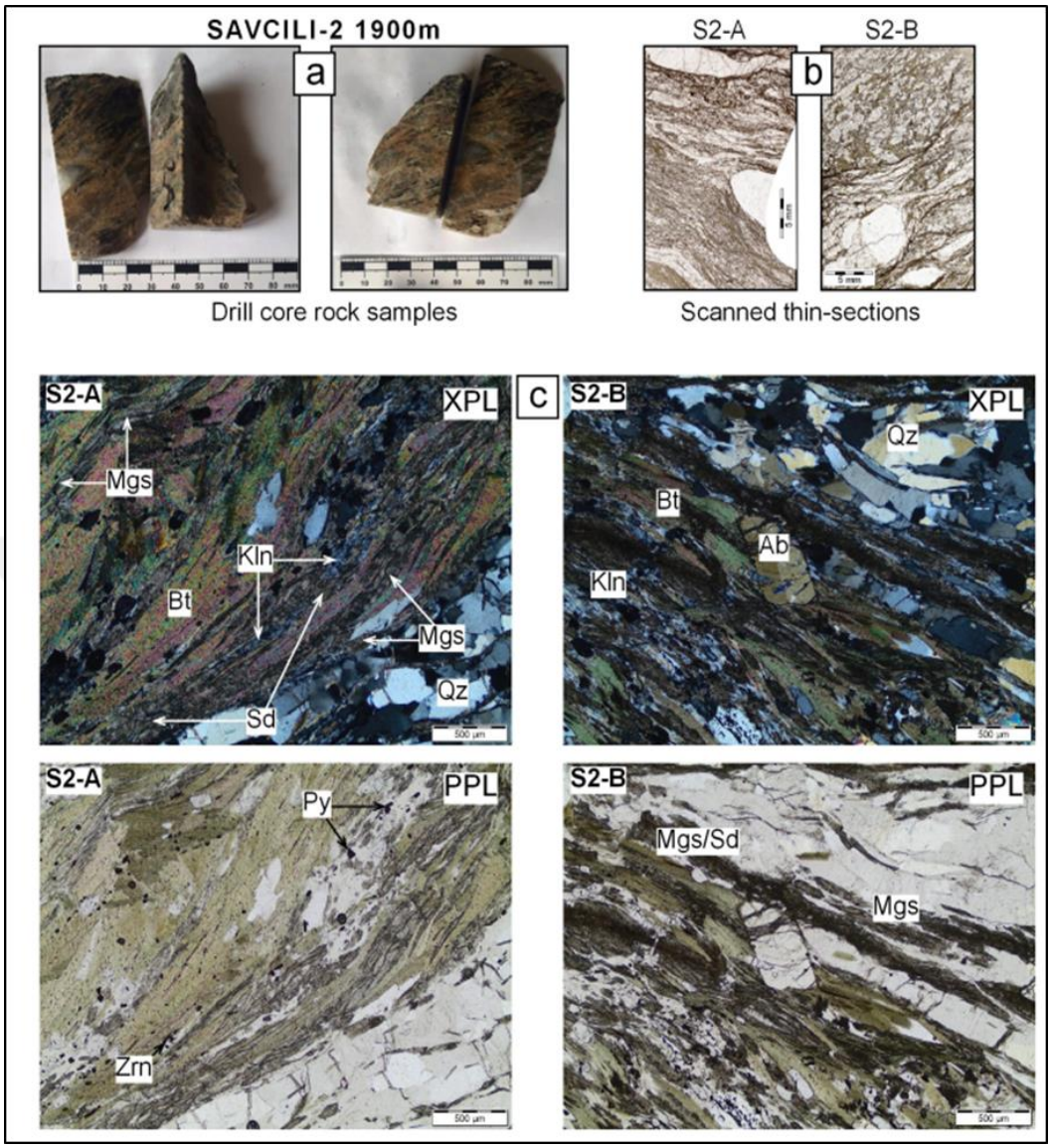

Figure 5.15 a) Macroscopic view of core sample taken from 1900 m depth b) In thin-section scans, Quartz filled lenses and bands were identified c) Lepidoblastic biotite and granoblastic quartz and albite minerals, and the alteration products magnesite (Mgs) and siderite (Sd) and kaolinites.

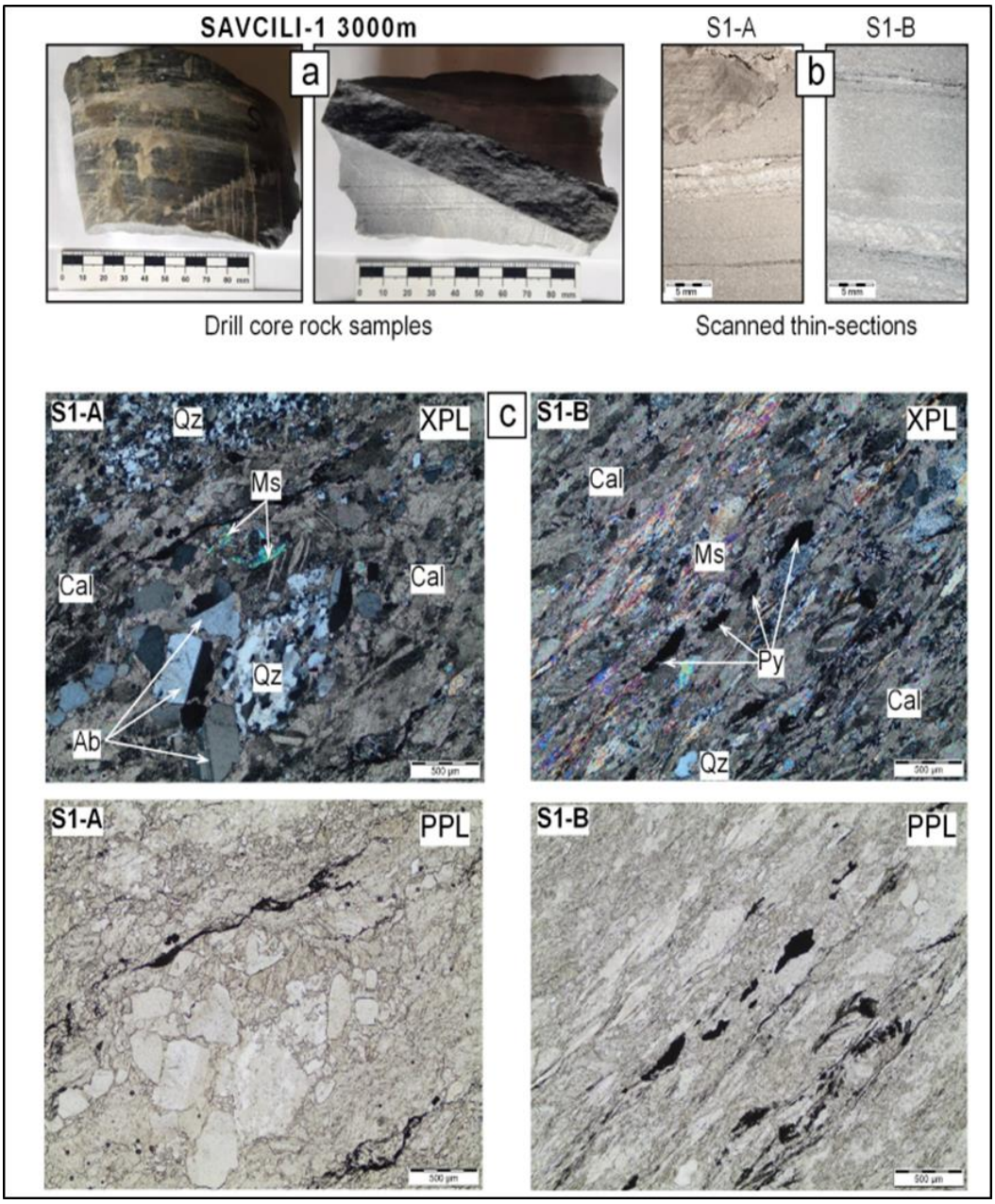

Figure 5.16 a) Macroscopic view core sample taken from 3000 m depth (b) In thin-section scans Calcite-filled lenses and quartz-filled bands, (c) Granoblastic textured calcites and quartz, albite, muscovite and Optical microscope views of the levels containing the opaque mineral (pyrite).

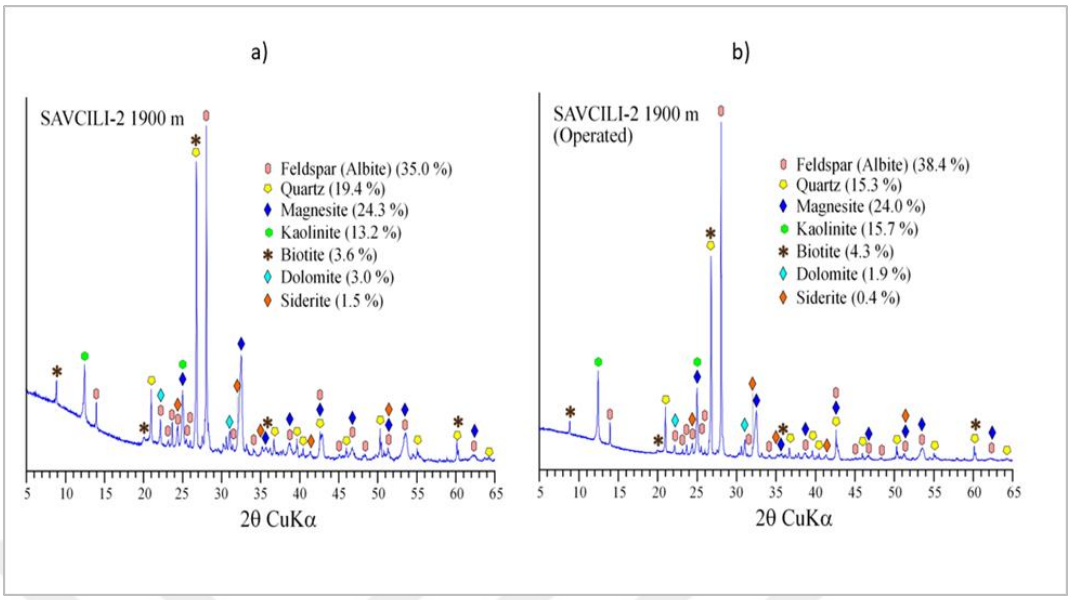

Figure 5.17 XRD measurements of the core sample taken from 1900 m depth before (a) and after (b) batch experiments.

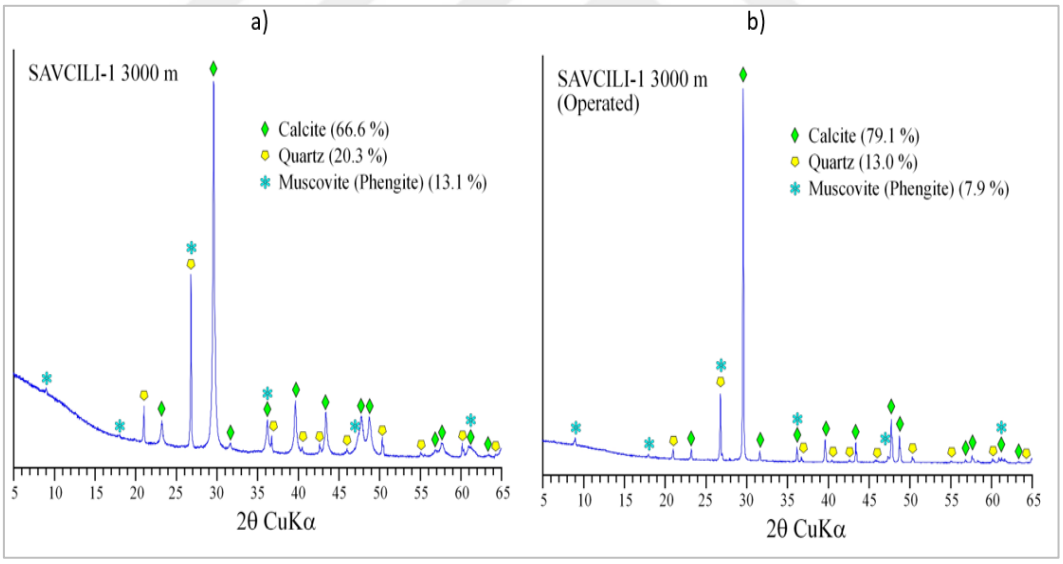

Figure 5.18 Core samples taken from 3000 m depth a) before water-rock interaction in the batch experiments b) after water-rock interactions in the batch experiments.

Equations (5.2) and (5.3) describe the carbonation of the siderite mineral (Mendoza et al. 2019), and Equation (5.4) shows the reaction of pyrite with water and oxygen to produce sulphuric acid. Equations (5.5) and (5.6) describe the carbonation of magnesite. Metals in minerals can be exchanged with H^+ , releasing metal cations (K^+, Ca^{2+}, Na+, etc) and forming new clay minerals such as smectite, and kaolinite from retained ions (AI^{3+}, O^{2-}, Si^{4+}). Equations (5.7) and (5.8) describe the hydrolysis of calcium plagioclase feldspar and potassium feldspar, respectively. Equation (5.9) shows alteration of albite into muscovite.

$$2H^+ + H_2O + (Ca, Mg, Fe, Al)\ SiO_3 \rightarrow Ca^{2+}, Mg^{2+}, Fe^{2+}, Al^{3+} + H_4SiO_4 \quad (5.1)$$

$$Fe_3O_4(s) + Fe(s) + 4CO_2(g) \rightarrow 4FeCO_3\ (s) \quad (5.2)$$

$$Fe_2O_3(s) + Fe(s) + 3CO_2(g) \rightarrow 3FeCO_3\ (s) \quad (5.3)$$

$$2FeS_2(s) + 7O_2 + 2H_2O \rightarrow 2Fe^{2+} + H_2SO_4 + 2H^+ \quad (5.4)$$

$$Mg^{2+}\ (aq) + 2HCO_3^-\ (aq) \Rightarrow MgCO_3\ (s) + CO_2\ (g) + H_2O \quad (5.5)$$

$$Mg\ (OH)_2 + 2CO_2 \rightarrow Mg\ (HCO_3)_2 \quad (5.6)$$

$$KAISi_3O_8 + H^+ + 4.5H_2O \rightarrow 0.5\ Al_2Si_2O_5(OH)_4 + K^+ + 2H_4SiO_4(aq) \quad (5.7)$$

$$CaAl_2Si_2O_8 + H_2CO_3 + 0.5O_2 \rightarrow Al_2Si_2O_5(OH)_4 + Ca^{2+} + CO_3^{2-} \quad (5.8)$$

$$3NaAlSi_3O_8 + K^+ + 2H^+ \rightarrow KAl_3Si_3O_{10}(OH)_2 + 3Na^+ + 6SiO_2 \quad (5.9)$$

The PHREEQC code was used to simulate the batch experiment, considering rock surface area, initial moles of minerals, kinetic reaction rates, and activation energy of the minerals. Moles and rock surface area for each mineral were calculated using an image process using ImageJ and XRD results (Table 5.6 and Table 5.7). By tuning the kinetic rates and activation energy of the minerals, ion concentrations (silica, calcium, aluminum, chloride, and iron) were matched with experiment results (Table 5.8). Major elements concentrations were also matched with experimental

results (Figure 5.19, Figure 5.20, Figure 5.21, and Figure 5.22). The tuning parameters for matching were kinetic reaction rates and activation energy of minerals. These tuning parameters were consistent with USGS data (Table 5.10).

Table 5.6 Surface area and mole number of mineral assemblies for rock sample taken from 1900 m depth.

Minerals	**Mole number**	**Mineral surface area (cm^2)**
Feldspar	0.226	1451.9
Quartzite	0.581	804.8
Magnesite	0.518	1008.0
Kaolinite	0.092	547.6
Biotite	0.0149	149.3
Dolomite	0.029	124.5
Siderite	0.023	62.2

Table 5.7 Surface area and mole number of mineral assemblies for rock sample taken from 3000 m depth.

Minerals	**Mole number**	**Mineral surface area (cm^2)**
Calcite	1.118	2578.5
Quartzite	0.570	786.0
Muscovite	0.068	507.2

Table 5.8 Activation energy and kinetic rate constant for matching PHREEQC model with experiment results and USGS values.

	Activation Energy (kj/mol)		**Kinetic Rate (mol/m^2/s)**	
	PHREEQC Model	USGS (Palandri and Kharaka, 2004)	PHREEQC Model	USGS (Palandri and Kharaka, 2004)
Quartzite	77	87.7	9×10^{-14}	1.023×10^{-14}
Muscovite	22	22	1.404×10^{-13}	2.81×10^{-14}
Pyrite	57	56	8.81×10^{-6}	2.8×10^{-5}
Albite	69	69	2.75×10^{-10}	2.754×10^{-13}
Kaolinite	22	38	6×10^{-11}	1.1×10^{-14}
Dolomite	36	52	6.45×10^{-9}	2.95×10^{-8}
Magnesite	20	23.5	4×10^{-10}	4.5×10^{-10}
Siderite	63	62.7	9×10^{-8}	1.26×10^{-9}
Calcite	20	23.5	$9x10^{-9}$	$1.55x10^{-9}$

In the first batch experiment, a mineral assembly consisting of rock powder from a core sample at 1900 m depth, was exposed to CO_2-saturated geothermal fluid for 3 weeks at 95 ^oC and 10 barg. The concentration of major elements were matched with simulations by tuning the activation energy and kinetic reaction rate of minerals. As shown in Figure 5.19a, the antimony concentration increased from 0.3 ppm to 1.1 ppm. Antimony is a constituent of hydrothermally formed mineral assemblages, often in the trivalent state as stibnite (Sb_2S_3) (Krupp, 1988). Stibnite (Sb_2S_3) is the most abundant antimony mineral and the primary control on the concentration of

antimony in hydrothermal fluids (Olsen vd., 2012). Antimony sulfur solubility is highly sensitive to temperature and pH changes (Erten et al. 2021). In general, stibnite is more soluble in acidic solutions than in basic solutions. This is because the sulfide ion (S^{2-}) is more stable in acidic solutions. In basic solutions, the sulfide ion can react with hydroxide ions (OH^-) to form insoluble hydroxides. The following reaction, Equation (5.10) shows the oxidation of stibnite in acidic solution:

$$Sb_2S_3 + 3H_2O + 3O_2 \rightarrow 2Sb(OH)_3 + 3H_2S \qquad (5.10)$$

The dissolution of CO_2 in the geofluid decreased the pH from 9.5 to 7.2. This shifted the reaction in Equation (5.10) to right and resulting in an increase in antimony concentration.

Aluminum concentration decreased from 0.43 ppm to 0.15 ppm (Figure 5.19b). The source of Aluminum was the kaolinite mineral in the rock sample. Precipitation of kaolinite (increasing mineral content from 13.1 % to 15.7 %) caused the aluminum concentration to decline (Figure 5.17). Kaolinite is a clay mineral that is relatively insoluble in water, but its solubility increases with decreasing pH. This is because the negative charges on the surface of the kaolinite particles are more easily balanced by hydrogen ions (H^+) in acidic solutions (Rao et al. 2011). Kaolinite is also more reactive to acid at lower pH values. This is because the acid can break down the bonds between the silicon and oxygen atoms in the kaolinite structure. In the experiment, pH value was Alkaline property, which is unfavorable for the solubility of kaolinite. Therefore, the precipitation of kaolinite was favored.

Table 5.9 Solubility of kaolinite with respect to pH (Created from Rao et al. 2011).

pH	Solubility	Reactivity	Stability
Acidic (<4)	High	High	Low
Neutral (4-7)	Low	Low	High
Alkaline (>7)	Very low	Very low	High

Iron concentration decreased from 0.1 ppm to 0.02 ppm and stabilized at this value (Figure 5.19c). The source of iron in this experiment was siderite and biotite minerals in the rock sample. XRD results showed that siderite was dissolving and biotite was in a precipitating (Figure 5.17). The solubility of siderite ($FeCO_3$) in water decreases with increasing pH. This is because siderite is a slightly acidic compound, and its solubility is favored by acidic conditions (Silva et al. 2002). The Equation (5.11) shows the dissolution of siderite in water:

$$FeCO_3\ (s) + H_2O\ (l) + CO_2\ (g) \rightleftharpoons Fe^{2+}\ (aq) + HCO_3^-\ (aq) \qquad (5.11)$$

The solubility of siderite is also affected by the temperature and the ionic strength of the solution (Bénézeth et al. 2009). The solubility of siderite decreases with increasing temperature and increasing ionic strength (Table 5.10).

Table 5.10 Solubility of siderite with respect to pH (Silve et al. 2002).

pH	Temperature (^oC)	Solubility (mgL^{-1})
5	25	100
6	25	50
7	25	10
8	25	0.1

Biotite is a phyllosilicate mineral that is common in igneous, metamorphic, and sedimentary rocks. Its structure consists of alternating layers of silicon dioxide (SiO_2) and aluminum, iron, magnesium, and potassium (Samadi et al. 2021). Biotite dissolves more rapidly in acidic solutions than in basic solutions because the acidic solutions can more easily break down the bonds that hold the mineral together (Bray et al., 2015). The solubility of biotite in water decreases with increasing temperature because the increased temperature provides more energy for water molecules to break down these bonds (Malmström and Banwart, 1997). In the experiment, the initial temperature was 25 ^{o}C, and increased to 95 ^{o}C before stabilizing. This increase in temperature decreased the solubility of biotite, resulting in its precipitation. The precipitation of biotite caused the iron concentration to decrease, because iron is a major constituent of biotite.

Calcium concentration decreased during the experiment (Figure 5.19d). The solubility of calcium carbonate ($CaCO_3$) in water increases as the pH decreases, meaning that more $CaCO_3$ will dissolve in acidic solutions (Hart et al. 2013). This is because the carbonate ion (CO_3^{2-}) is more stable in acidic solutions. The solubility Ca^{2+} in water decreases with increasing temperature (Straub, 1932). This means that less Ca^{2+} will dissolve in hot water than in cold water. The source of Ca^{2+} in the experiment was dolomite. As seen in Figure 5.17, the dolomite content decreased from 3.0 % to 1.9 %. Dolomite solubility is affected by several factors, including temperature, pH, and the presence of other ions. However, temperature is the most significant factor. The solubility of dolomite in water increases with increasing pH, meaning that more dolomites will dissolve in basic solutions. This is because the carbonate ion (CO_3^{2-}) which is the main form of dissolved dolomite in water, is more stable in basic solutions. The solubility of dolomite in water decreases with increasing temperature. This means that less dolomite will dissolve in hot water than in cold water. The pH of the experiment decreased from 9.5 to 7.2 (Figure 5.19d). Therefore, it was expected that Ca^{2+} would increase. However, temperature of the system was increased from 25 ^{o}C to 95 ^{o}C, which caused Ca^{2+} to decrease.

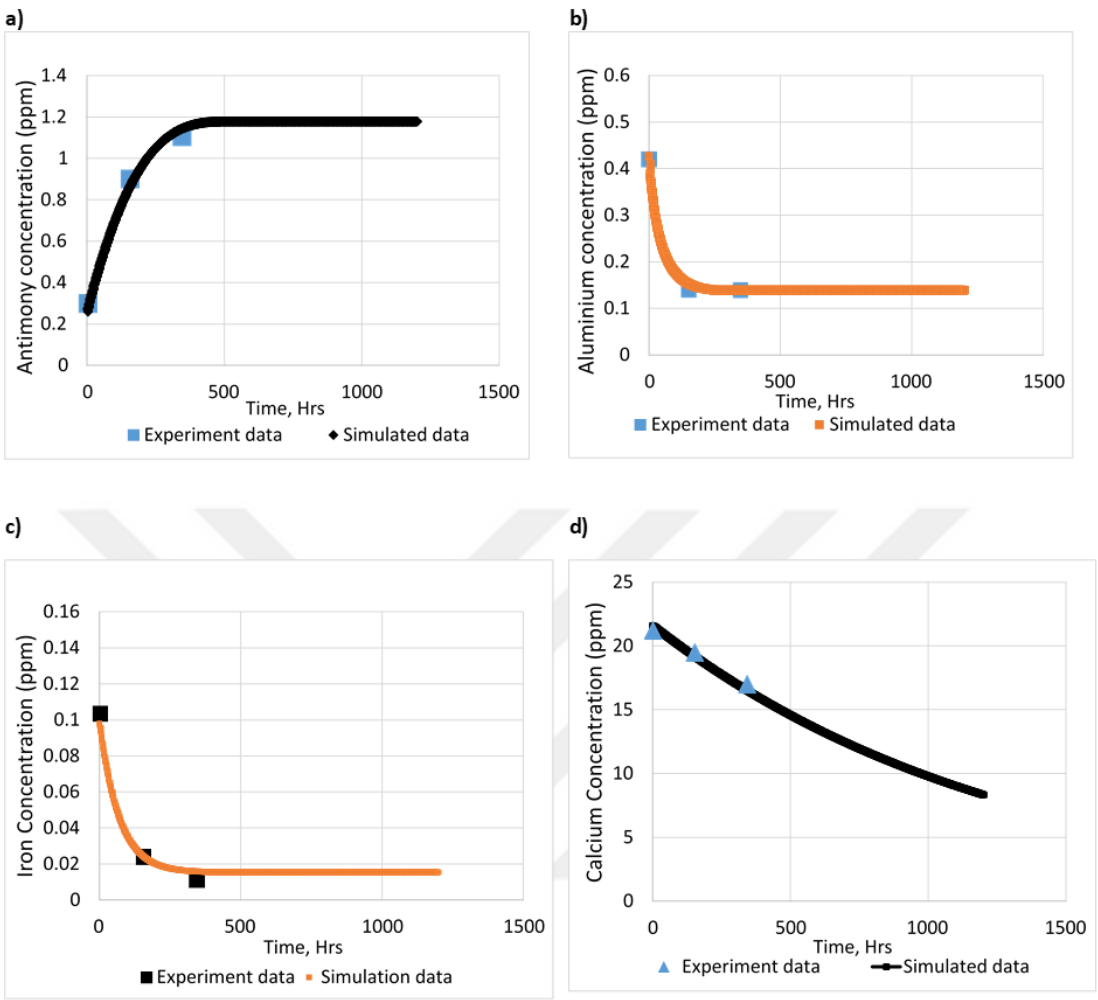

Figure 5.19 Experiment and simulation results for rock samples taken from 1900 m a) Antimony b) Aluminum c) Iron d) Calcium.

Silica concentration decreased from 120 ppm to 85 ppm (Figure 5.20a). The solubility of silica increases with increasing temperature (Krauskopf, 1956). This is because the water molecules can more easily break apart the silica molecules at higher temperatures. The solubility of silica is also affected by the presence of other ions in the water. For example, the presence of calcium ions can reduce the solubility of silica. This is because the calcium ions can form complexes with the silica molecules, making them less soluble in water (Szymanek et al. 2021).

Magnesium concentration increased from 0.8 ppm to 5 ppm (Figure 5.20b). The source of magnesium was magnesite and dolomite minerals in the experiment. Magnesite mineral content decreased from 24.3% to 24 % and dolomite mineral content decreased from 3.0% to 1.9 % (Figure 5.17).

Chloride concentration remained unchanged and stabilized around 145 ppm (Figure 5.20c). The solubility of chloride ions in water is independent of pH, as Cl^- are negatively charged ions (Musa and Hamoshi, 2012). Negatively charged ions are not affected by the electrical charge of the water molecules, and therefore their solubility is not affected by pH.

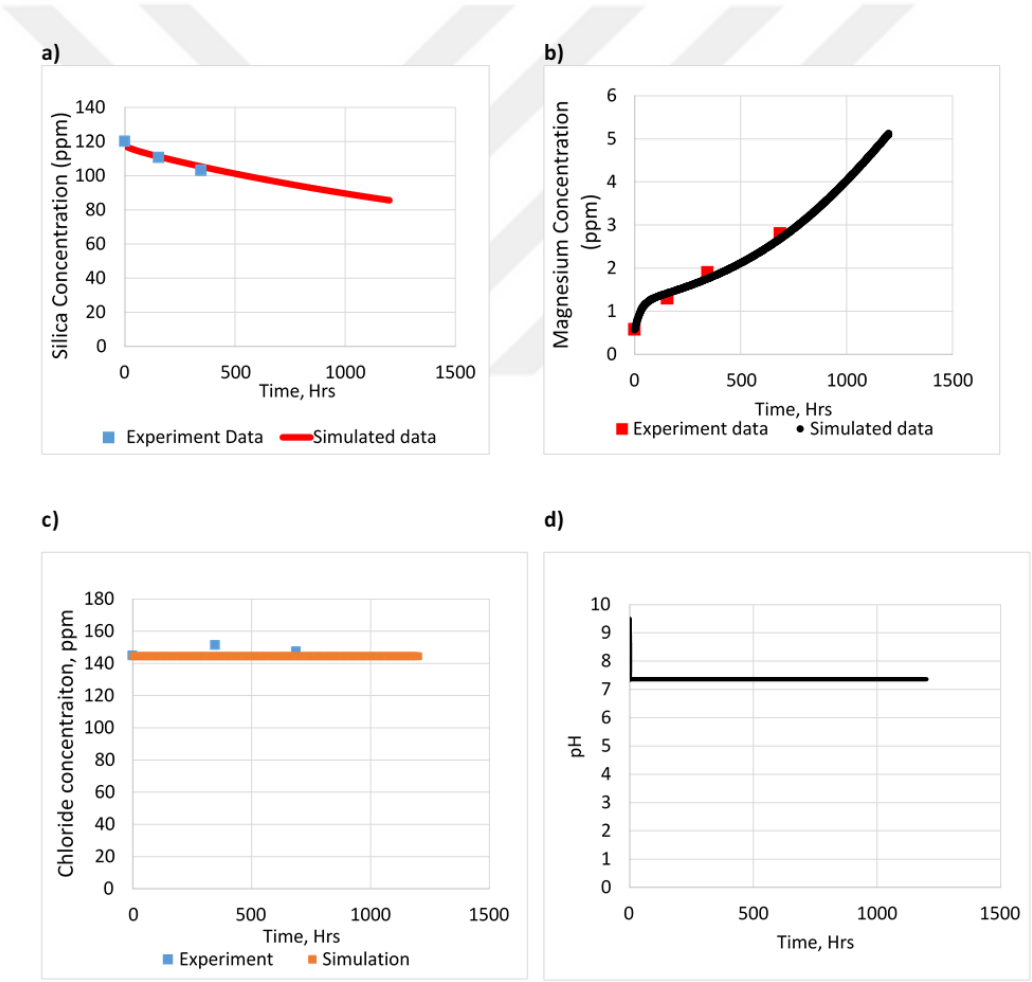

Figure 5.20 Experiment and simulation results for rock samples taken from 1900 m a) Silica b) Magnesium c) Chloride d) pH.

In the second batch experiment, a mineral assemblage consisting of rock powder from a core sample at 3000 m depth was exposed to CO_2-saturated geothermal fluid at 95 ^oC and 10 barg for 3 weeks. The mineral content of the rock sample is shown in Figure 5.18.

Mg^{2+} showed an increase behavior (Figure 5.21a). The solubility of Mg^{2+} increases with increasing pH because the hydroxide ion (OH^-), which is the main form of Mg^{2+} in water, is more stable in basic solutions (Nishiki et al. 2023). As shown in Figure 5.21d, the pH decreased from 9.5 to 7.1 due to CO_2 dissolution, and then slightly increased to 7.5 slightly. This increase in pH resulted in an increase in Mg^{2+} concentration.

Al^{3+} concentration showed a decline behavior (Figure 5.21b). The solubility of aluminum hydroxide decreases with increasing temperature and increasing ionic strength (Feng et al. 2008). The temperature of the system was increased from 25 ^oC to 95 ^oC and the lack of the kaolinite in the system also contributed to the decrease in aluminum concentration.

The solubility of calcium carbonate ($CaCO_3$) in water increases with decreasing pH because the carbonate ion (CO_3^{2-}) is more stable in acidic solutions. The solubility of Ca^{2+} in water decreases with increasing temperature (Straub, 1932). In the experiment, Ca^{2+} concentration increased significantly (Figure 5.21c). This is because of increasing acidity of the brine (Figure 5.21d). Based on the solubility relationships, it was expected that the calcite mineral content of the assembly would decrease at the end of the experiment. However, XRD results show an increase in calcite mineral content (Figure 5.18). This is most likely due to the flashing process that occurred when the system pressure was opened to the atmosphere to collect mineral samples. During flashing process, $CaCO_3$ precipitation occurred which, increased the abundance $CaCO_3$.

SiO_2 concentration decreased from 105 ppm to 67 ppm (Figure 5.22a). The solubility of silica increases with increasing temperature (Krauskopf, 1956). This is because the water molecules can more easily break apart the silica molecules at higher

temperatures. The solubility of SiO_2 is also affected by the presence of other ions in the water. For example, the presence of Ca^{2+} ions can reduce the solubility of silica. This is because the Ca^{2+} can form complexes with the SiO_2 molecules, making them less soluble in water (Szymanek et al. 2021). A significant increase in the Ca^{2+} concentration probably, decreased silica solubility.

Iron solubility depends on pH. In acidic solutions, iron is more soluble than in neutral or alkaline solutions. This is because iron atoms in acidic solutions are more likely to lose electrons and form positively charged ions (Fe^{2+} or Fe^{3+}). These ions are more soluble in water than the neutral or negatively charged iron atoms (Liu and Millero, 2002). In this experiment, the pH decreased from 9.5 to 7.1, which increased iron solubility from 0.165ppm to 0.205 ppm (Figure 5.22b).

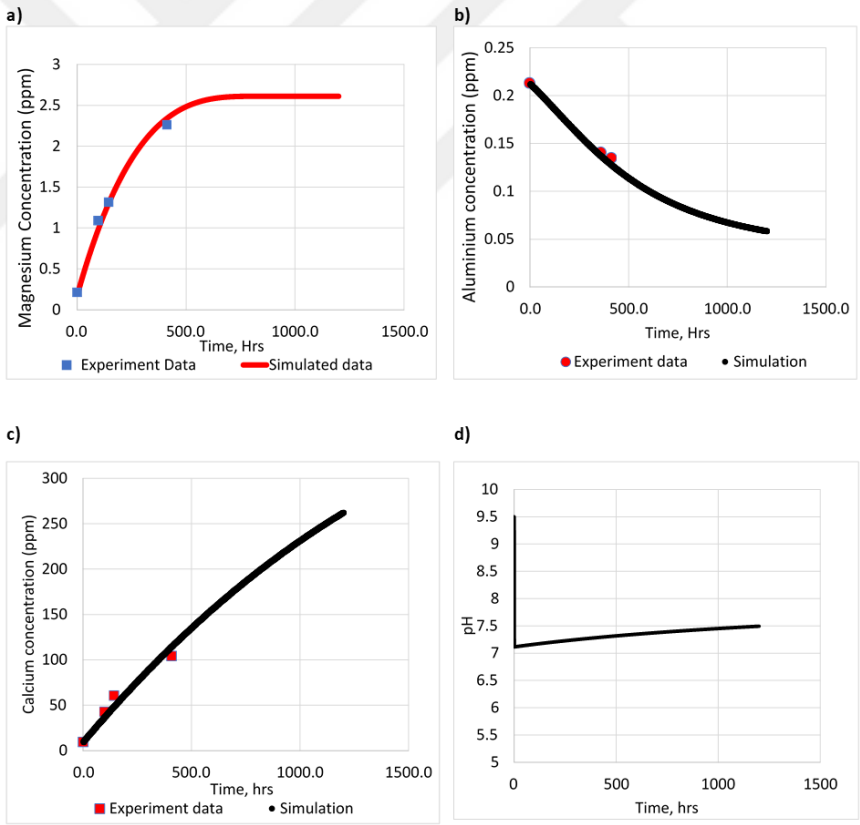

Figure 5.21 Experiment and simulation results for rock samples taken from 3000 m a) Magnesium b) Aluminum c) Calcium d) pH.

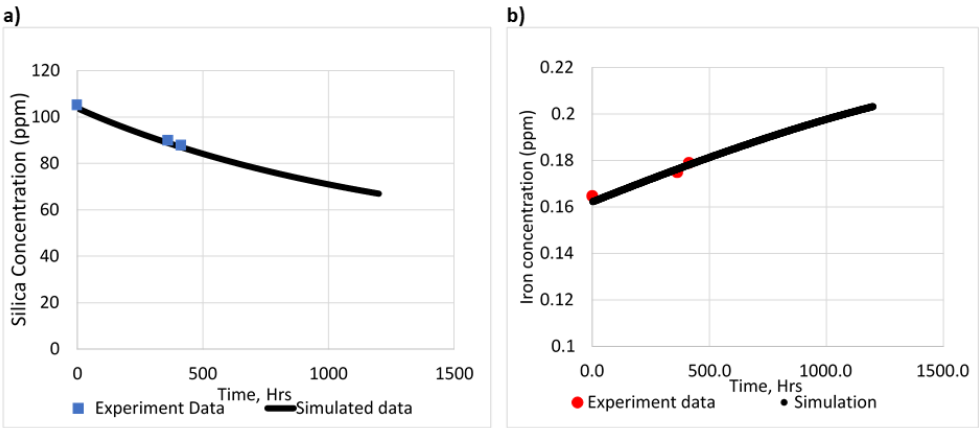

Figure 5.22 Experiment and simulation results for rock samples taken from 3000 m a) Silica b) Iron.

5.3 Water-Rock Interaction Core-flood Experiments

Reactive transport modeling is a powerful tool for estimating the rate of injected fluid flow in a reservoir. Reliable models are calibrated with experimental data. To realistically represent fluid-rock interaction, it is essential to use core samples of reservoir rock and geothermal fluid with similar geochemical compositions.

In this study, a core sample from the Kızıldere geothermal reservoir was exposed to continuous injection of CO2-dissolved fluid. The core sample was split into two pieces to produce a smooth single fracture. The single fracture core sample was subjected to confining pressure, which restricted fluid flow to the fracture. It was also assumed that the core sample had negligible primary porosity.

Before core-flood experiments, rock analyses were performed using chromatography, thin section, SEM and XRD measurements. Chromatographic measurements showed that the core contained a fracture filled with calcite mineral precipitation (Figure 5.24).

A thin section of the fracture surface was required for rock analysis. Since thin section analysis requires a rock slice, the analyses were performed after the core-flood experiments for both the backside and frontside of the fracture surface. The frontside of the fracture surface was exposed to water-rock interaction, while the backside of the fracture surface was not. A thin section of the fracture surface (frontside and backside) with a thickness of 1 cm is shown in Figure 5.23. The SEM measurements are shown in Figure 5.25 at varying magnifications. XRD results are shown in Figure 5.26. XRD results for the frontside of the fracture showed that the mineral composition in decreasing abundance by weight is: magnesite (34.9 %), quartzite (26.7 %), kaolinite (23.3 %), feldspar (12.1 %), siderite (2.7 %), dolomite (0.5 %), and hematite (0.2 %). The backside of the fracture surface showed the same mineral composition, but with different weights. This is not due to water-rock interaction, but to heterogeneity in the rock sample.

Core-flood experiments were performed under a confined pressure of 45.5 barg. The inlet and outlet pressures of the core holder was kept constant, and the variation of injection rate was monitored throughout the tests (Figure 5.27). The test was terminated after for 8.5 hours, due to the limited volume of brine available. The flow rate decreased from 8.8 ml/min to 1.5 ml/min, possibly due to plugging of the capillary tubing used in the experiments. When the tubing was disconnected, it was found that fine particles had plugged 1/8-inch capillary tubing, resulting in a decline in flowrate at constant pressure difference across the core holder.

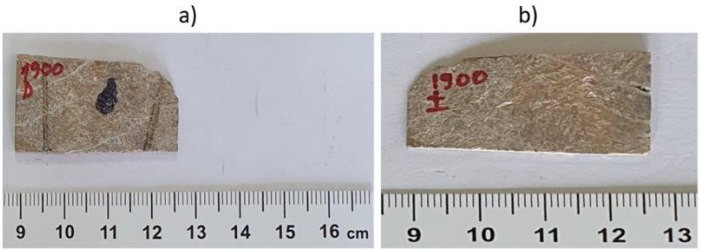

Figure 5.23 a) Front-side of fracture surface where water-rock interaction occurred b) backside of the fracture surface where no water-rock interaction occurred for core sample taken from 1900m depth.

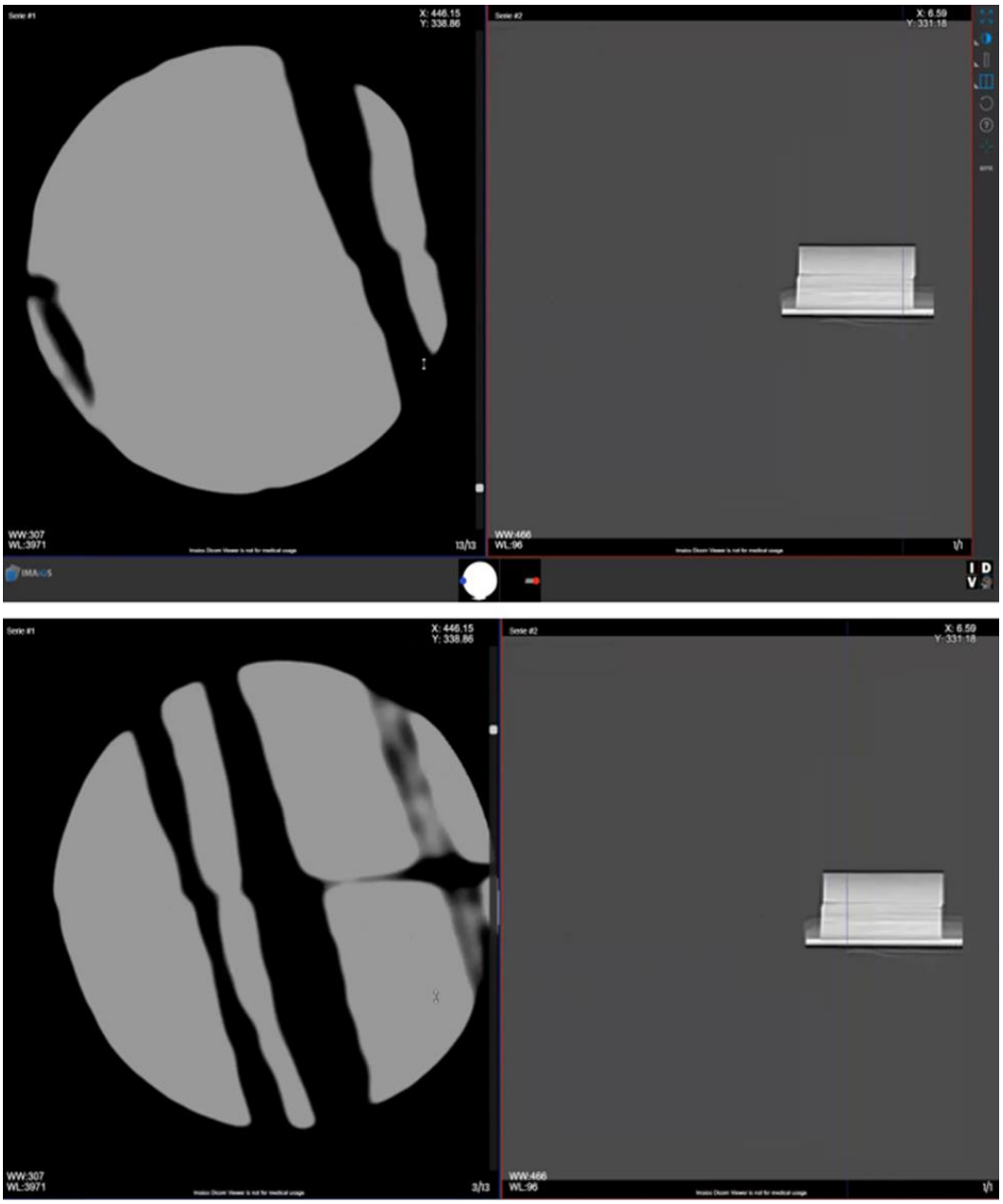

Figure 5.24 CT scan of the core sample (right hand image shows the slice location and lateral view of the core plug).

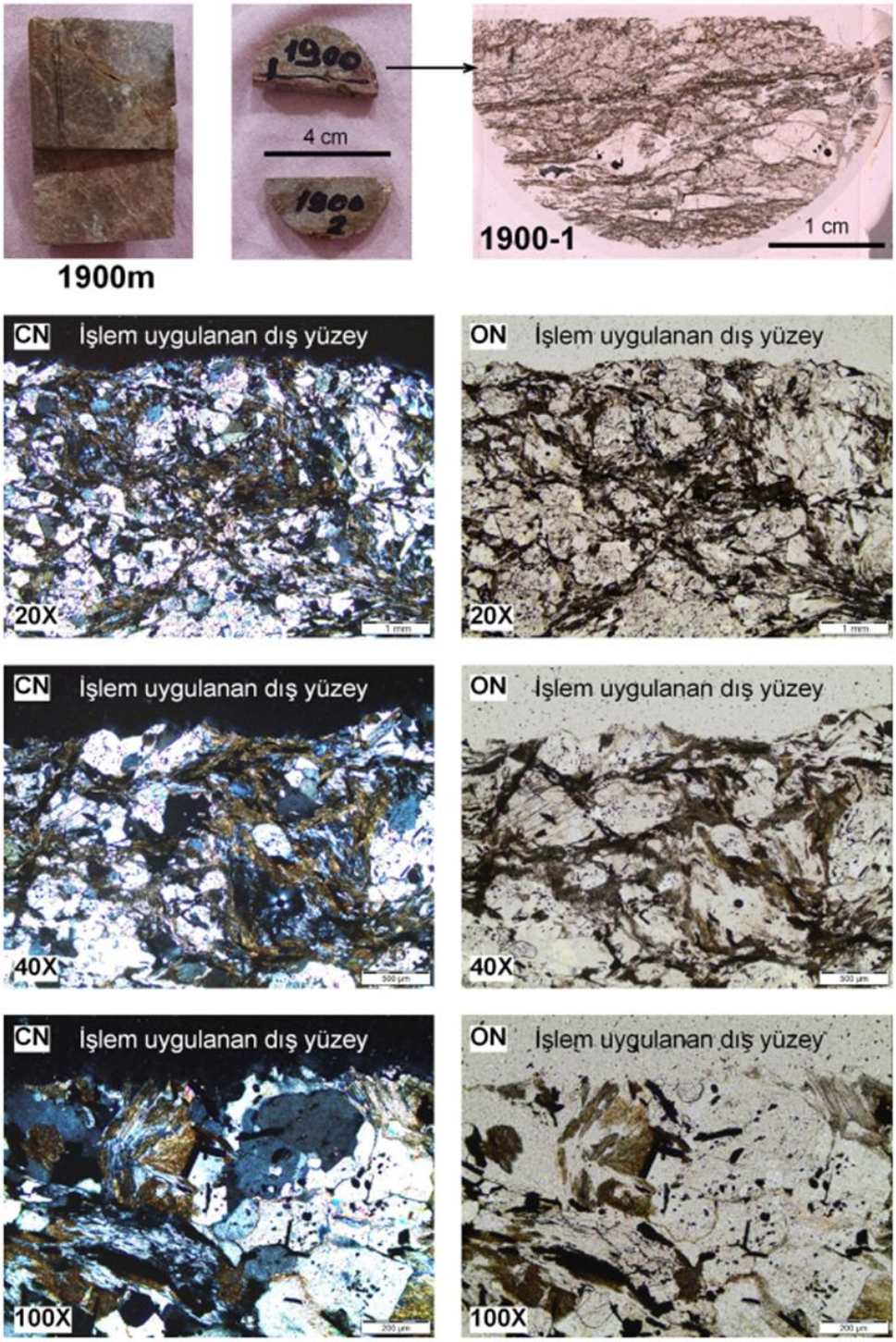

Figure 5.25 SEM analysis of fracture surface area at different magnification magnitudes for 1900m depth core sample.

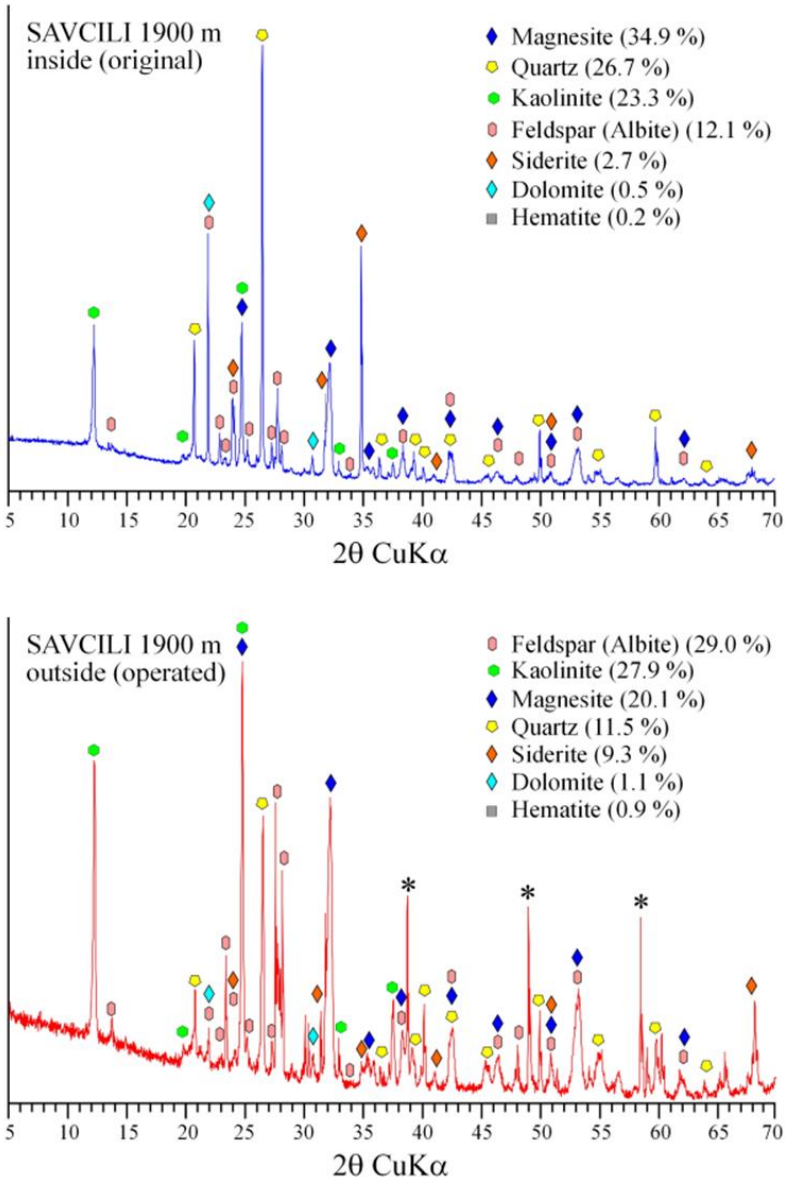

Figure 5.26 XRD analysis of the core sample with 1 cm thickness (analysis of two side of the sample).

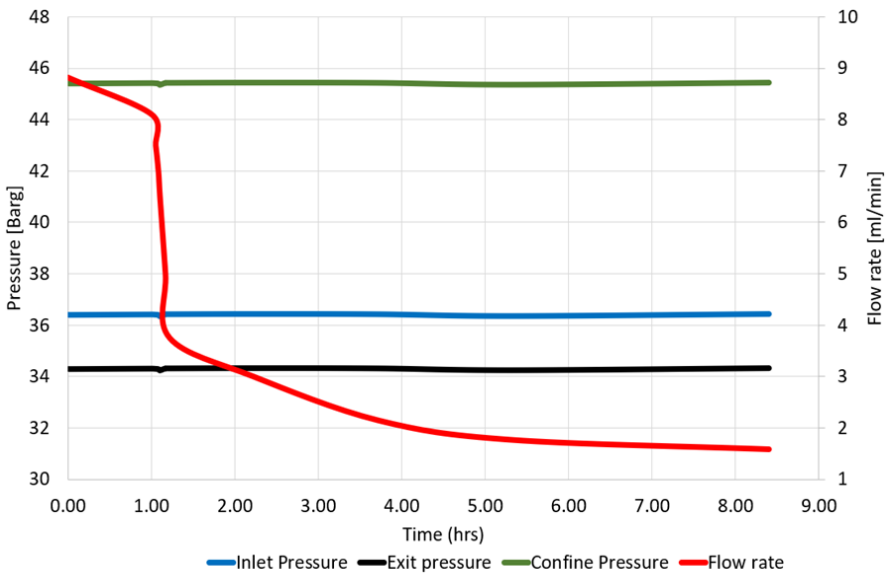

Figure 5.27 Pressure recordings and injection rate during core-flood experiment.

The decline in flow rate increased the duration of flow within the tubing, which resulted in a higher temperature decline of the brine. This temperature decline caused a decrease in silica concentration during the experiments (Figure 5.28). The fracture surface area was 14.7 cm^2 and the experiments lasted for 8.5 hours. Due to the limited mineral surface area and flow duration, it is not expected to observe significant changes in the fracture flow media due to water-rock interaction.

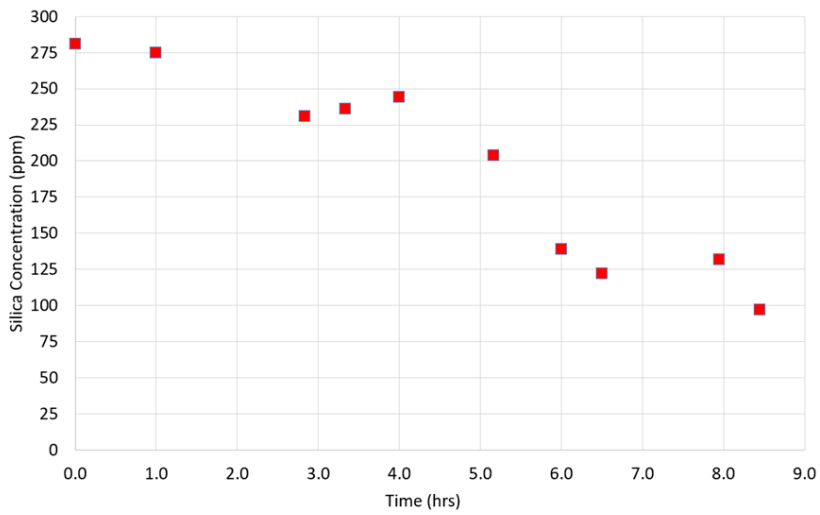

Figure 5.28 Silica concentration of brine during core flood experiment.

5.4 Results of 3D Numerical Reservoir Model for Heterogeneous System

Figure 5.29 and Figure 5.30 depict the pressure and temperature distribution in the studied area, respectively. There model reveals a temperature dome, which is consistent with field observations from existing wells.

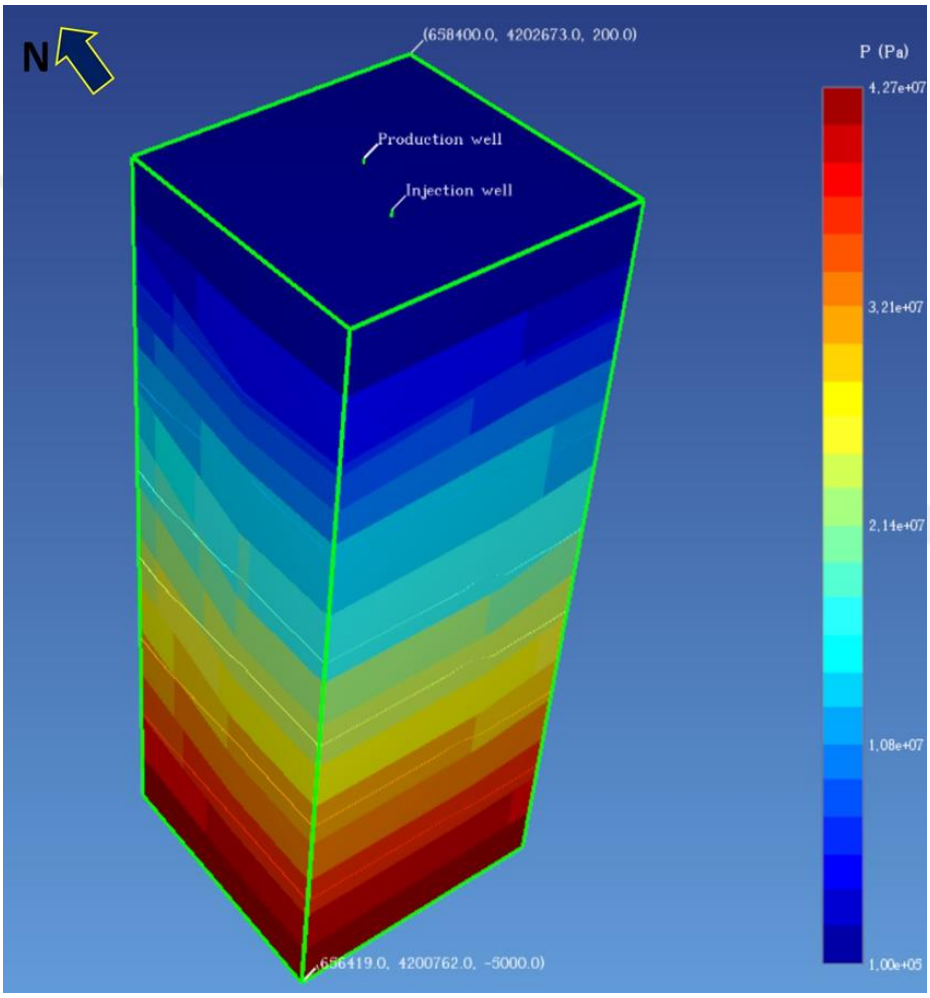

Figure 5.29 Pressure distribution of the studied field area.

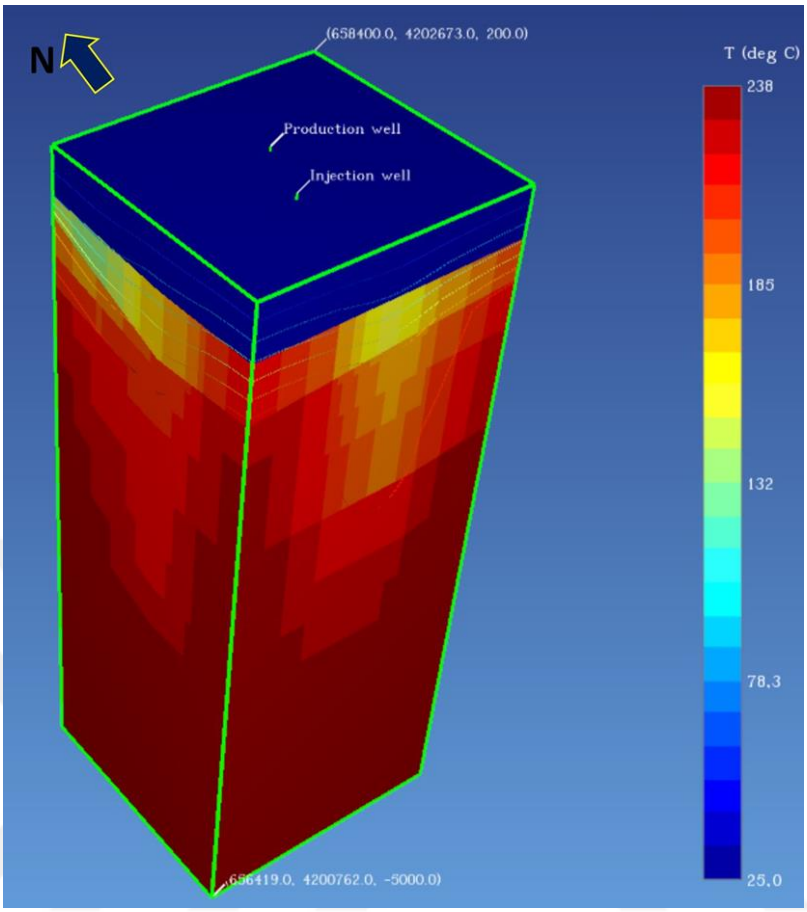

Figure 5.30 Temperature distribution of the studied field area.

Once the natural state of the model was established, the next step was to simulate production and reinjection. For the first two years of production, no reinjection was assumed. CO_2-free waste brine injection was then started at the end of second year of production. CO_2 injection started after 6 years of production (Figure 6.3). Figure 5.31 and Figure 5.32 depict the pressure and temperature changes in the reinjection well. During the first two years of production, the pressure declined by 50 barg. Reinjection increased the pressure by 35 barg, and the decline rate subsequently slowed. The reservoir temperature was initially around 220 ^{o}C, but it decreased to 105 ^{o}C with reinjection of waste brine. As the brine temperature decreased, its density also increased (Figure 5.33). A similar pressure behavior was observed in the production well (Figure 5.34 and Figure 5.35).

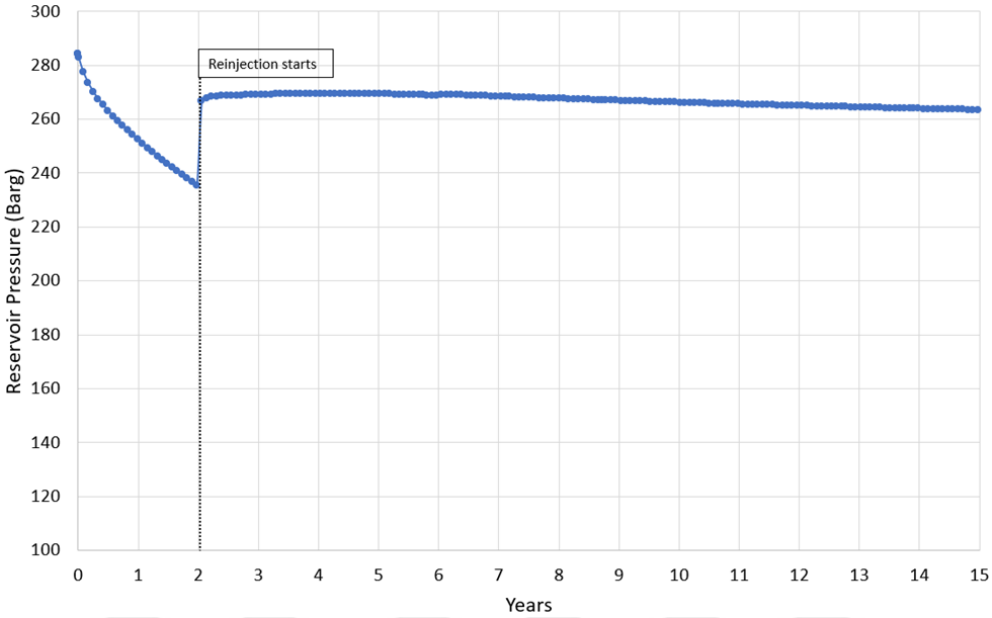

Figure 5.31 Pressure history of reinjection well.

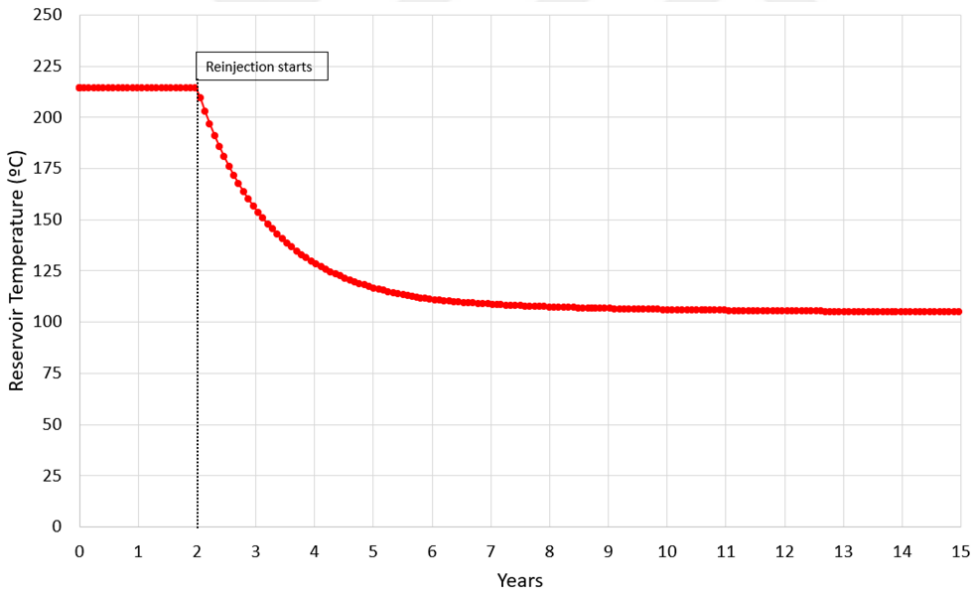

Figure 5.32 Temperature history of reinjection well.

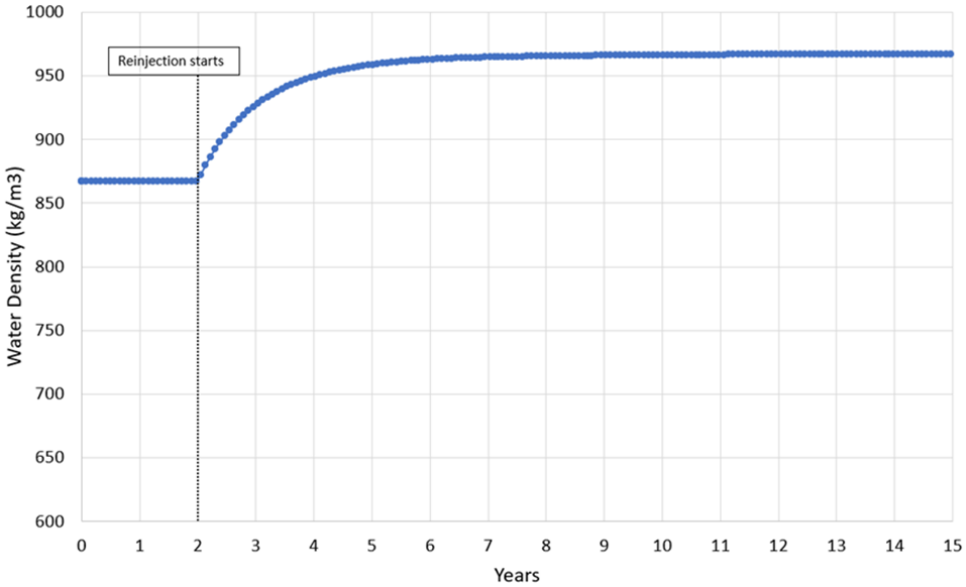

Figure 5.33 Density history of reinjection well.

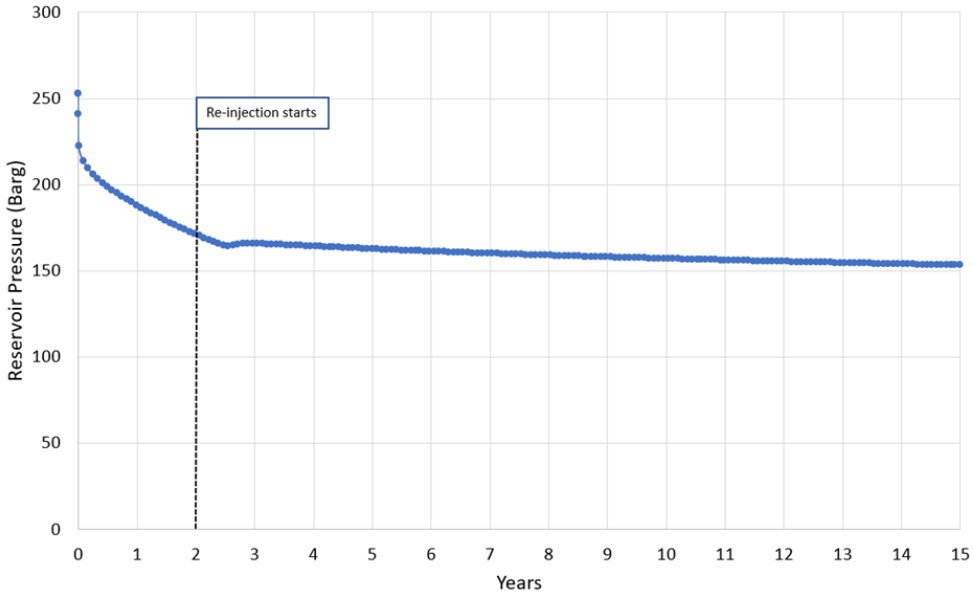

Figure 5.34 Reservoir pressure of production well.

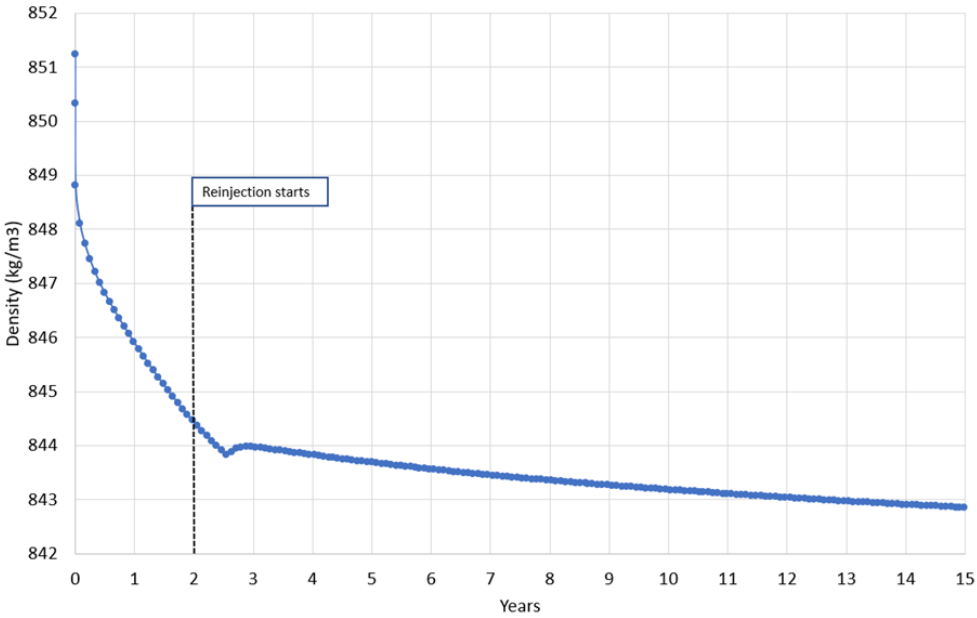

Figure 5.35 Water density of production well.

We investigated the effects of brine injection and dissolved CO_2 injection on the reservoir permeability and porosity using a 3D reactive-transport model. In Kızıldere field, reinjection brine is a mixture of shallow (Sazak formation) and deep reservoir (Menderes metamorphic) brines, with lower concentrations of major elements such as silica and calcium than the deep metamorphic brine. As a result, permeability and porosity of the formation at the reinjection well increase as CO_2-free brine injection begins at the end of the second year, due to mineral dissolution (Figure 5.36 and Figure 5.37). To assess the impact of mineral assemblage on the results, a sensitivity analysis was conducted by varying the mineral content in the model by +5% and -5%. As shown in Figure 5.38, the results are not significantly affected. Changes in secondary and primary minerals are shown in Figure 5.39 and Figure 5.40, respectively. Dolomite increased while magnesite decreased in secondary minerals. There were no significant changes in albite, kaolinite, and siderite. Calcite and quartzite decreased in primary minerals due to low pH, while muscovite remained unchanged. As the result of calcite dissolution, Ca^{2+} concentration increased (Figure

6.4). Mg^{2+} concentration was also increased as the result of magnesite dissolution (Figure 6.6). Decrease of Al^{3+} concentration (Figure 6.7) monitored as kaolinite precipitation. Silica concentration (Figure 6.7) was also in a decrease trend due to decreasing temperature near reinjection wellbore. Spatial distribution of elements are also drawn by using PETRASIM interface as shown in (Figure 6.8 through Figure 6.14). As shown in Figure 5.41, CO_2 injection compensate CO_2 decline of production wells.

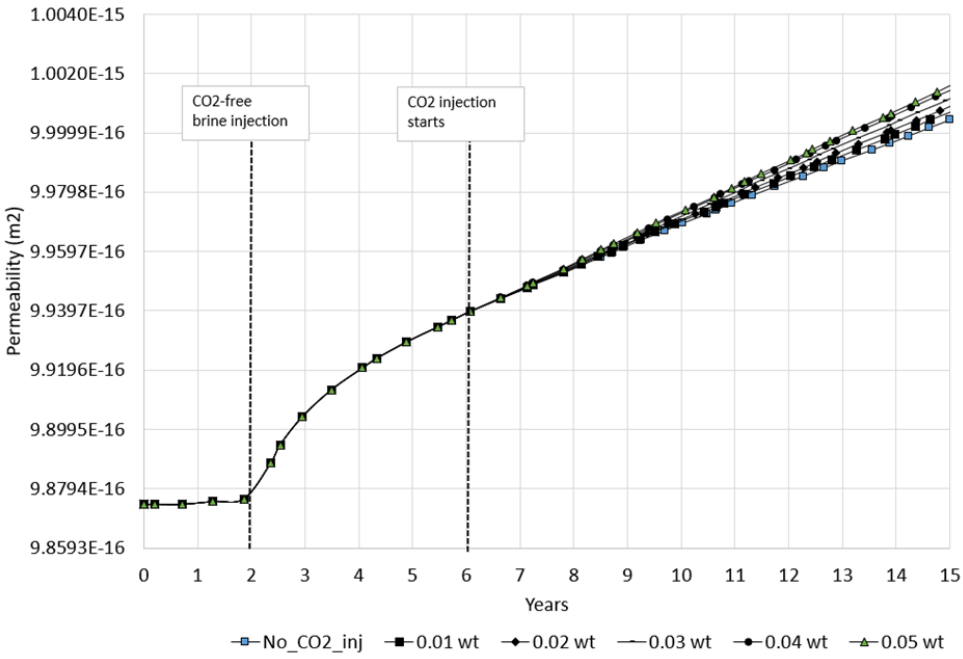

Figure 5.36 Permeability changes as the result of CO_2 injection in the reinjection well.

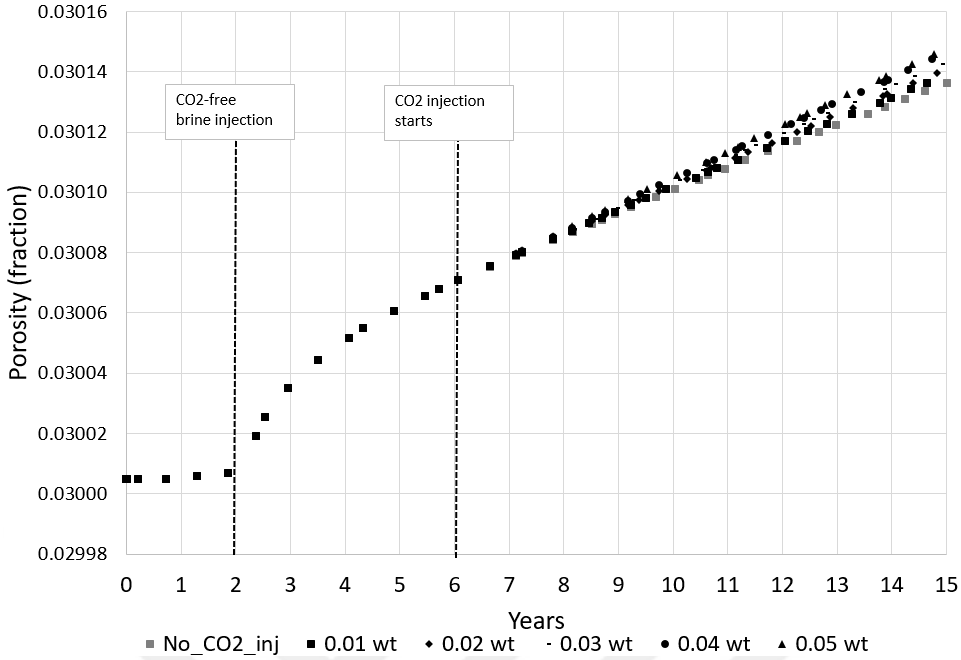

Figure 5.37 Porosity changes as the result of CO_2 injection in the reinjection well.

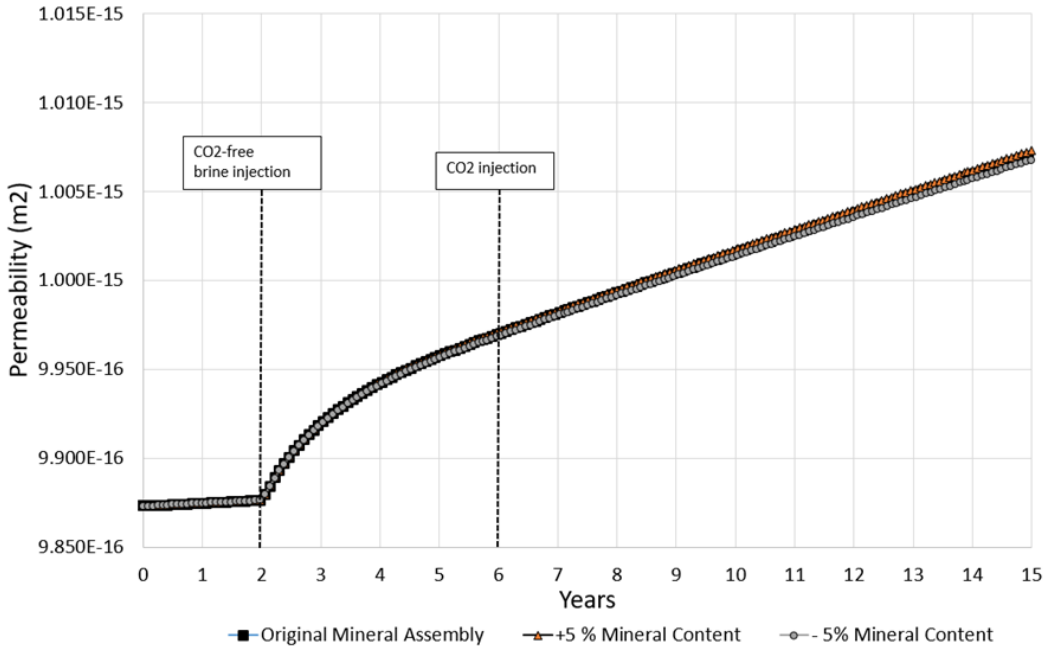

Figure 5.38 Sensitivity analysis for effects of mineral assembly on the permeability.

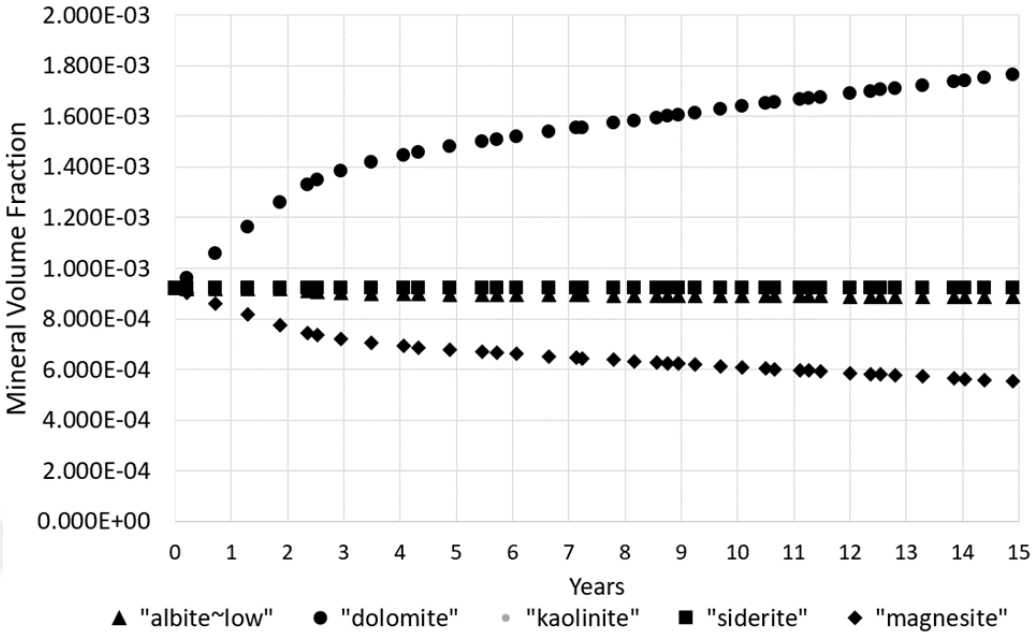

Figure 5.39 Changes in the secondary minerals during 0.03 wt CO_2 injection.

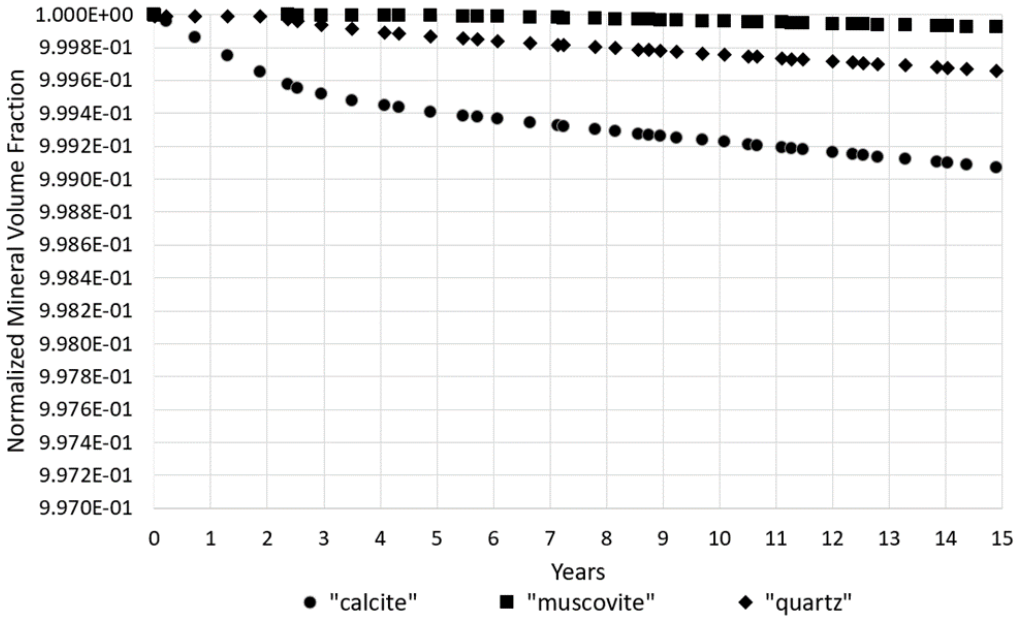

Figure 5.40 Changes in the primary minerals' volume fraction during 0.03 wt CO_2 injection (normalized values).

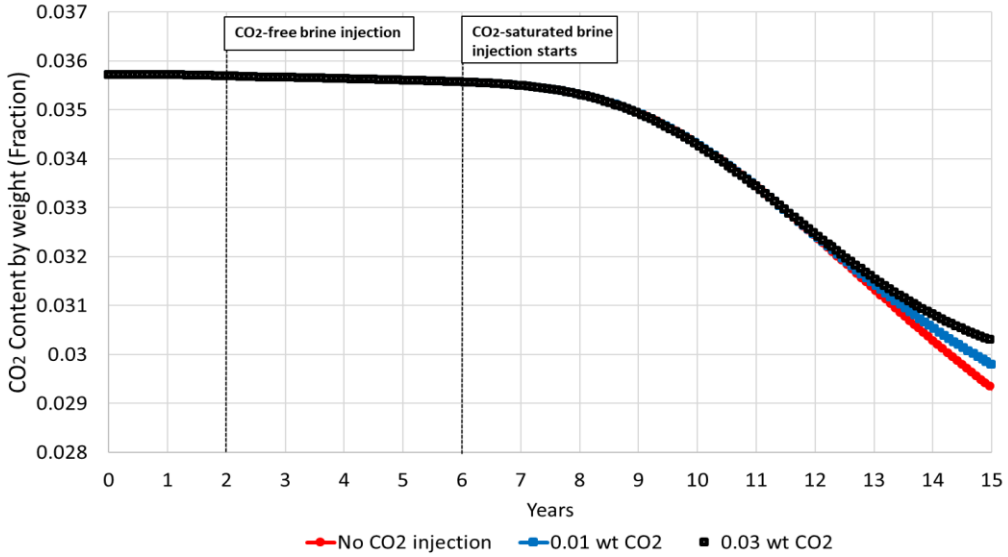

Figure 5.41 Changes in the CO_2 content of production well.

5.5 Results of 3D Numerical Reservoir Model for Homogeneous System

In the previous section, we investigated a heterogeneous system representing the Kızıldere geothermal field under reactive transport of CO_2-saturated geothermal brine in metamorphic rocks. In this section, we aim to perform simulations in a homogeneous system to simplify the model and better understand the long-term effects of CO_2 injection.

Figure 5.42 depicts the stratigraphic units of the Kızıldere field with a homogeneous distribution throughout the study area. The same gridding process as for the heterogeneous system was used.

A homogeneous pressure and temperature distributions (Figure 5.43) were obtained by assigning temperature and pressure gradients. Their spatial distribution do not change with east and north direction, but change with vertical direction only. Temperature variation along the grid cells between injection and production wells are shown in Figure 5.44 as line plot at 20th years of injection.

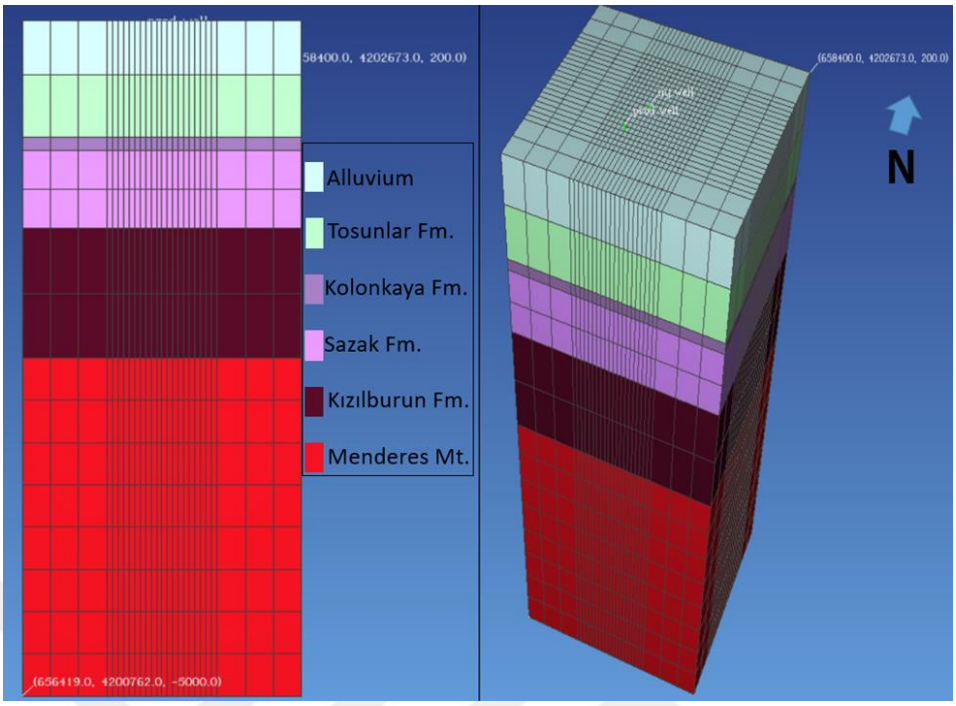

Figure 5.42 Gridding and stratigraphic units of homogeneous model.

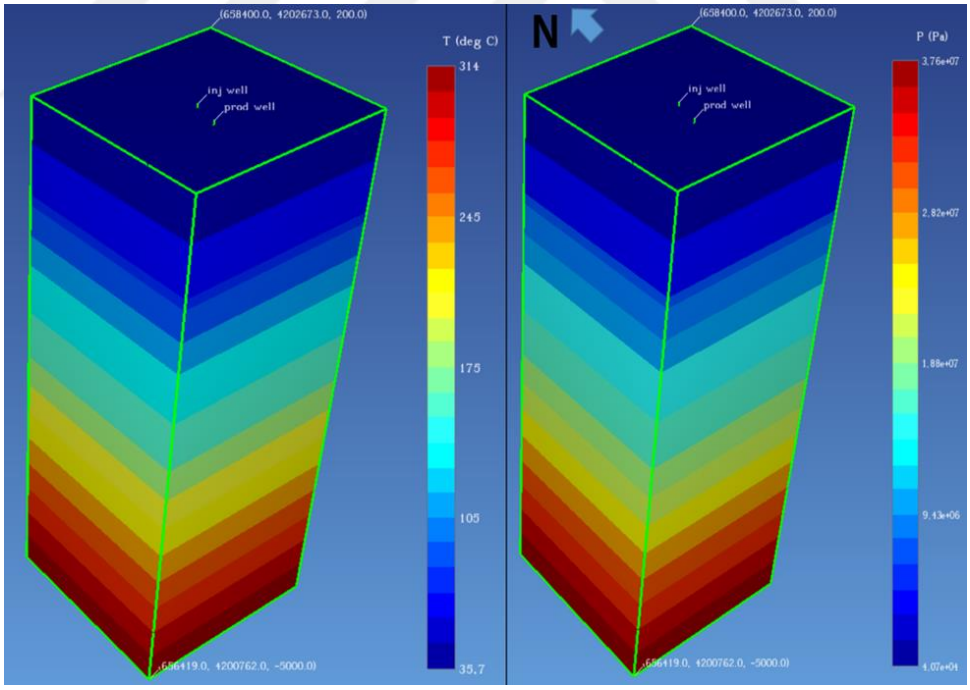

Figure 5.43 Initial temperature (left) and pressure (right) distribution of homogeneous model.

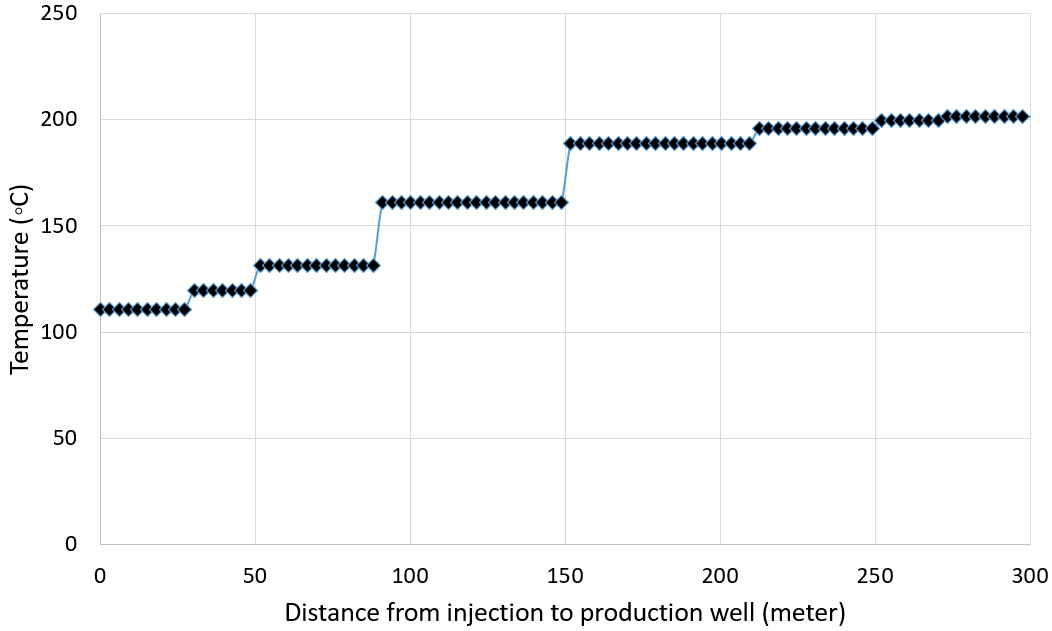

Figure 5.44 Temperature variation along the grid cells between injection and production wells.

Figure 5.45 depicts CO_2-free waste brine injection was then started at the end of second year of production. CO_2 concentration around the injection well was reduced to zero, and it increased towards the production well. This means that CO_2 decline can be used as a tracer to monitor communication between injection and production wells.

Figure 5.46 shows CO_2 distribution in the reservoir when injecting at 5% by weight. CO_2 concentration around the injection well increased to 5 % and there was no free gas in the simulation results. This probably due to that, the injected CO_2 dispersed and mixed in the reservoir brine and trapped as dissolved gas.

Figure 5.49 shows the CO_2 content variation along the grid cells between the injection and production wells in line plot.

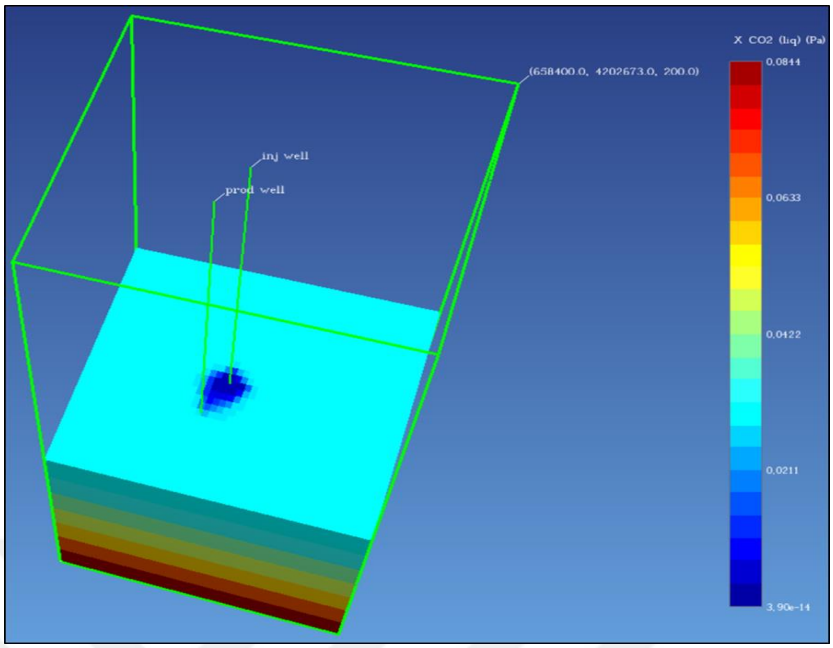

Figure 5.45 CO_2 distribution at gas-free brine injection.

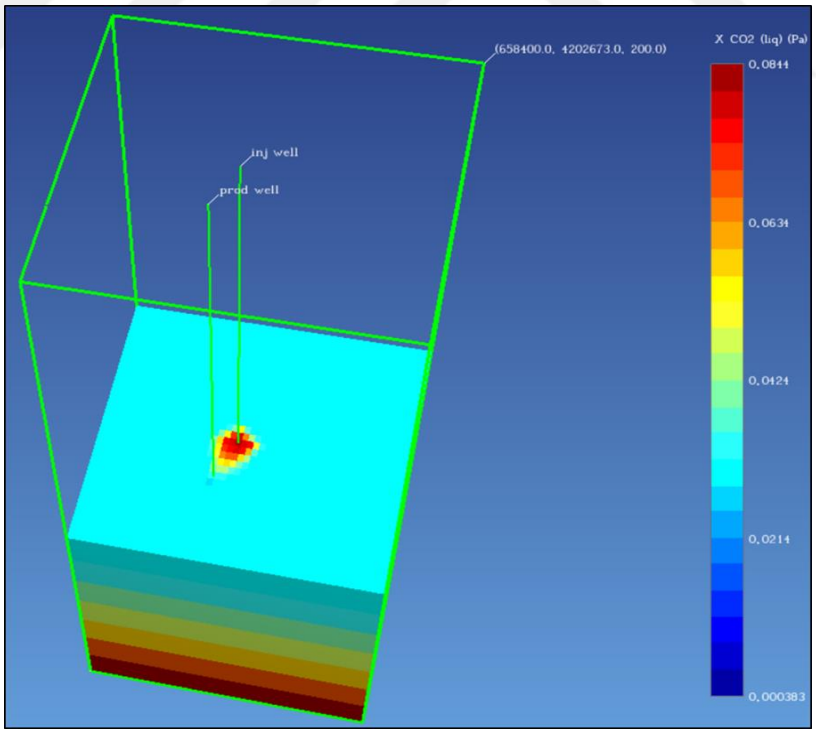

Figure 5.46 CO_2 distribution after gas injection at 5 % by weight.

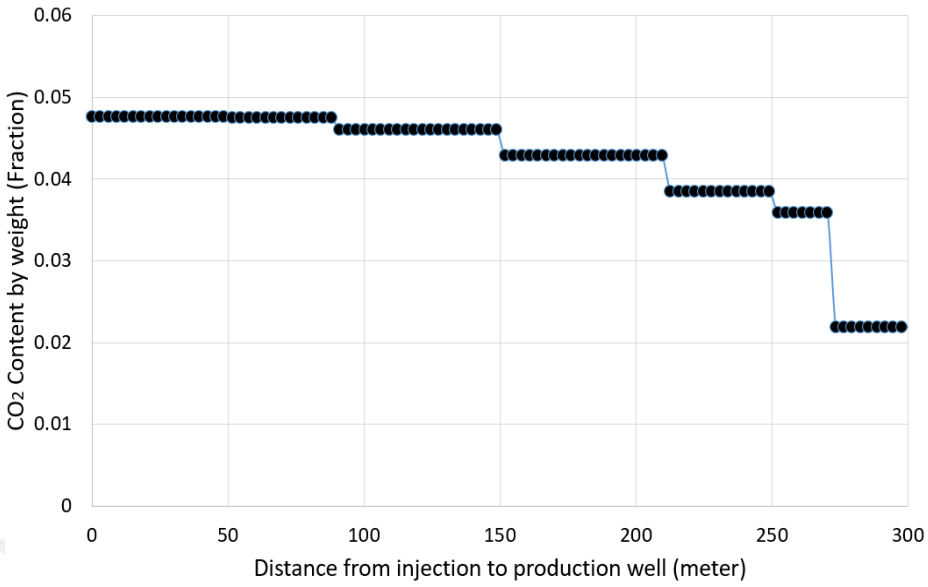

Figure 5.47 CO_2 variation along the grid cells between injection and production wells.

Figure 5.48 depicts the CO_2 history of production well in the homogeneous system. We found that CO_2 decline can be compensated with CO_2 stream from the injection well. Injecting CO_2 more than 4 %, increased CO_2 concentration of production well to a higher than its initial value. This increases production performance of the well.

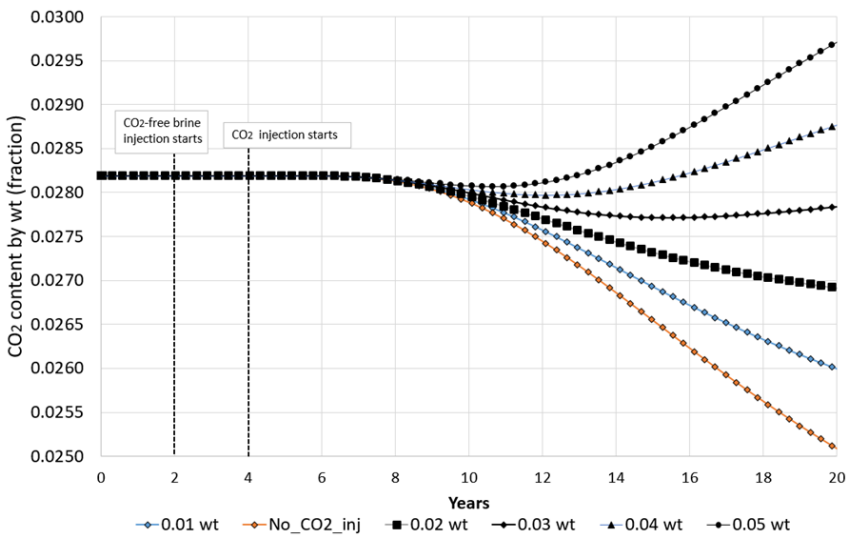

Figure 5.48 Changes in the CO_2 content of production well in homogeneous model.

TOUGHREACT uses equation (4.7) model the relationship between porosity and permeability. Changes in porosity due to mineral precipitation and dissolution affect permeability and thus modify fluid flow. Figure 5.49 and Figure 5.50 show the variation of permeability and porosity in the reinjection well. It is evident that a trend of mineral dissolution begins with the injection of brine. The dissolution rate increases with the injection of CO2. This is because the injection brine has a lower geochemical concentration than the initial reservoir brine, as shown in Table 4.3 and Table 4.4. As shown in Figure 5.51 and Figure 5.52, the volume fraction of reservoir minerals decreases, and porosity and permeability increase slightly. The dolomite fraction increases while the calcite fraction decreases, which is possibly due to "Mg^{2+}" and "Ca^{2+}" exchange. Other minerals are in a dissolution trend, which is favorable for injection capacity.

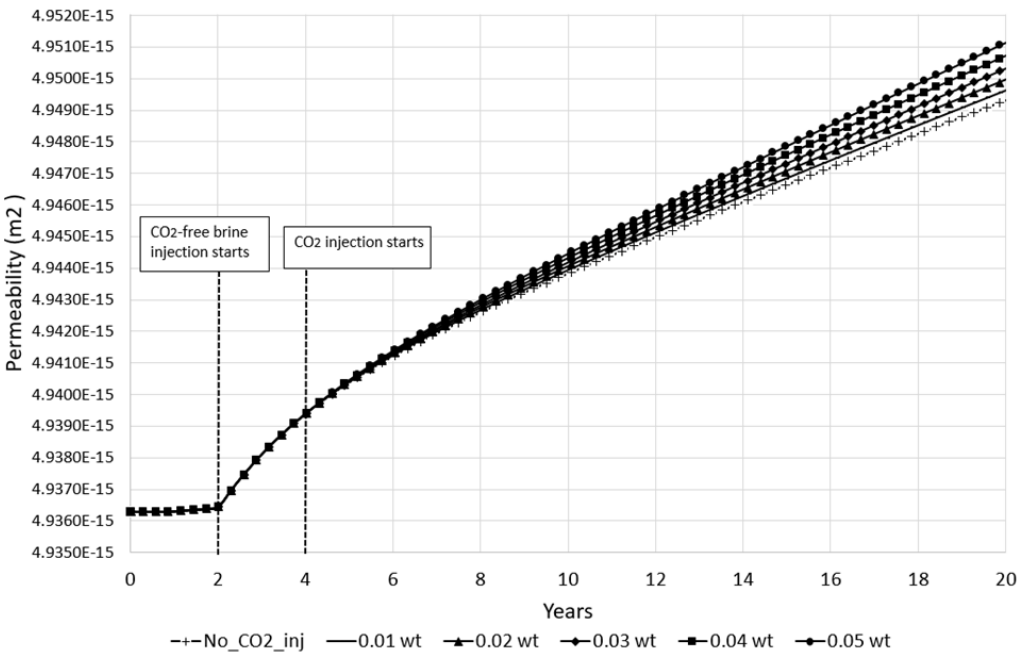

Figure 5.49 Changes in the permeability of reinjection well in homogeneous model.

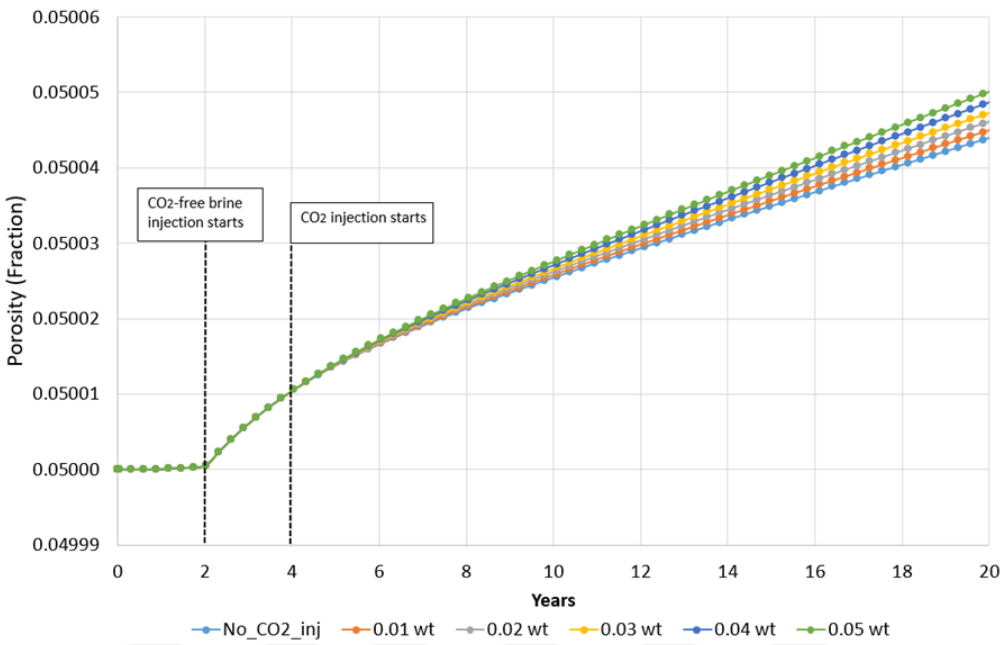

Figure 5.50 Changes in the porosity of reinjection well in homogeneous model.

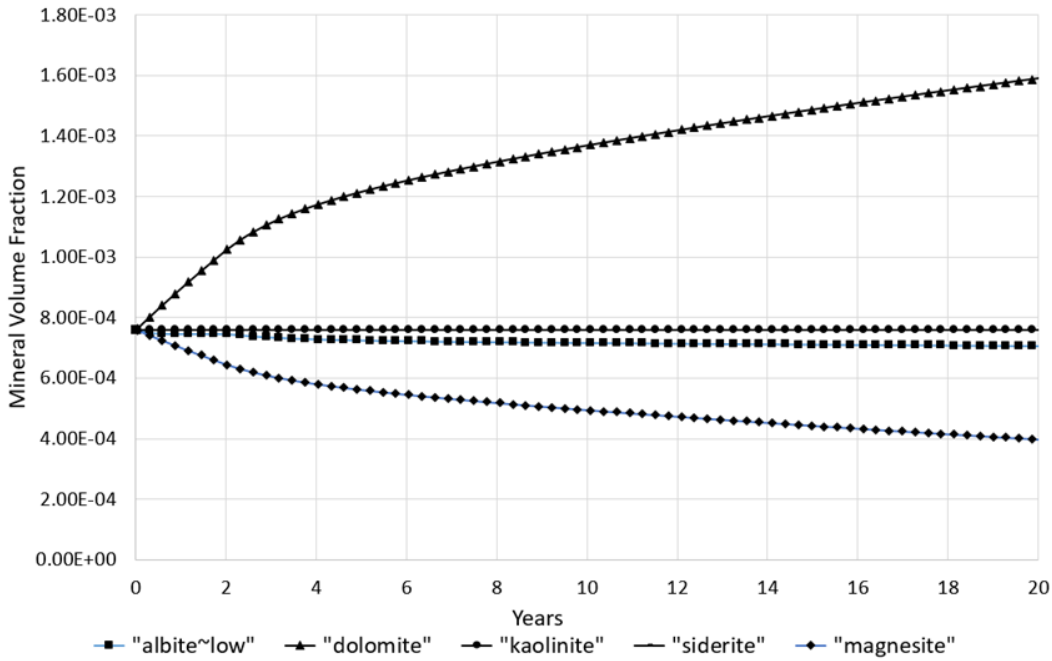

Figure 5.51 Changes in the secondary minerals' volume fraction during 0.05 wt CO_2 injection.

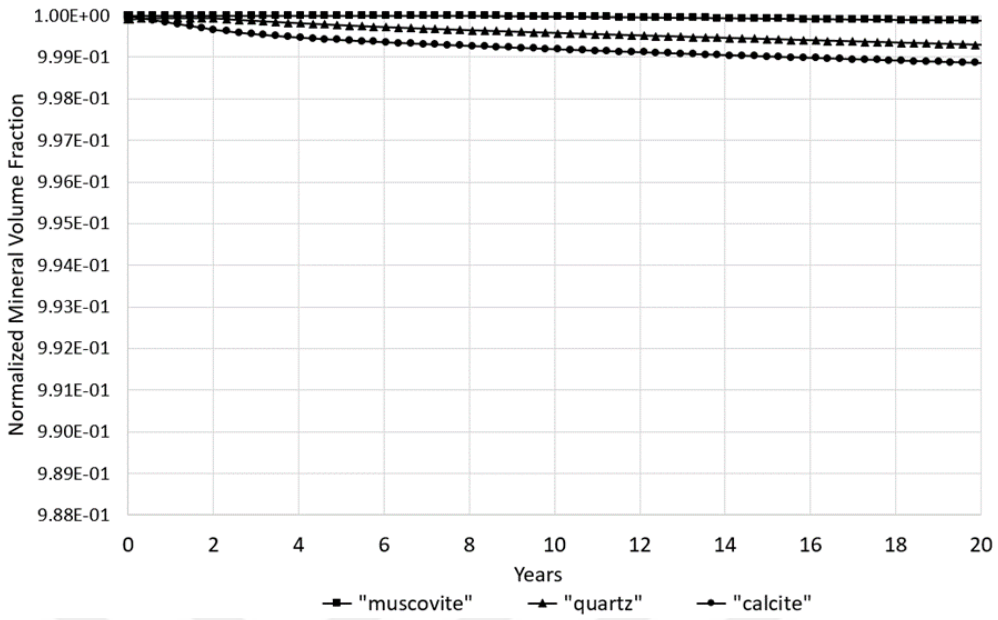

Figure 5.52 Changes in the primary minerals' volume fraction during 0.05 wt CO_2 injection (normalized values).

When the homogeneous model results were compared with the heterogeneous model. Similar trend of element concentrations was obtained with a clear effect of CO_2. It was difficult to differentiate the effects of CO_2 injection and temperature-pressure changes on the fluid flow behavior in heterogeneous model. The results of homogeneous model are presented in Figure 6.15, Figure 6.16, Figure 6.17, Figure 6.18, and Figure 6.19. The trend of element concentrations and mineral precipitation-dissolution were the same as of heterogeneous model.

The spatial distribution of brine geochemistry was obtained using the PETRASIM interface. Figure 5.53 shows that the initial brine bromide (Br^-) concentration was higher than that of the injection brine. Therefore, the Br^- concentration can be considered as a tracer. Bromide dilution is an indicator of injection effect.

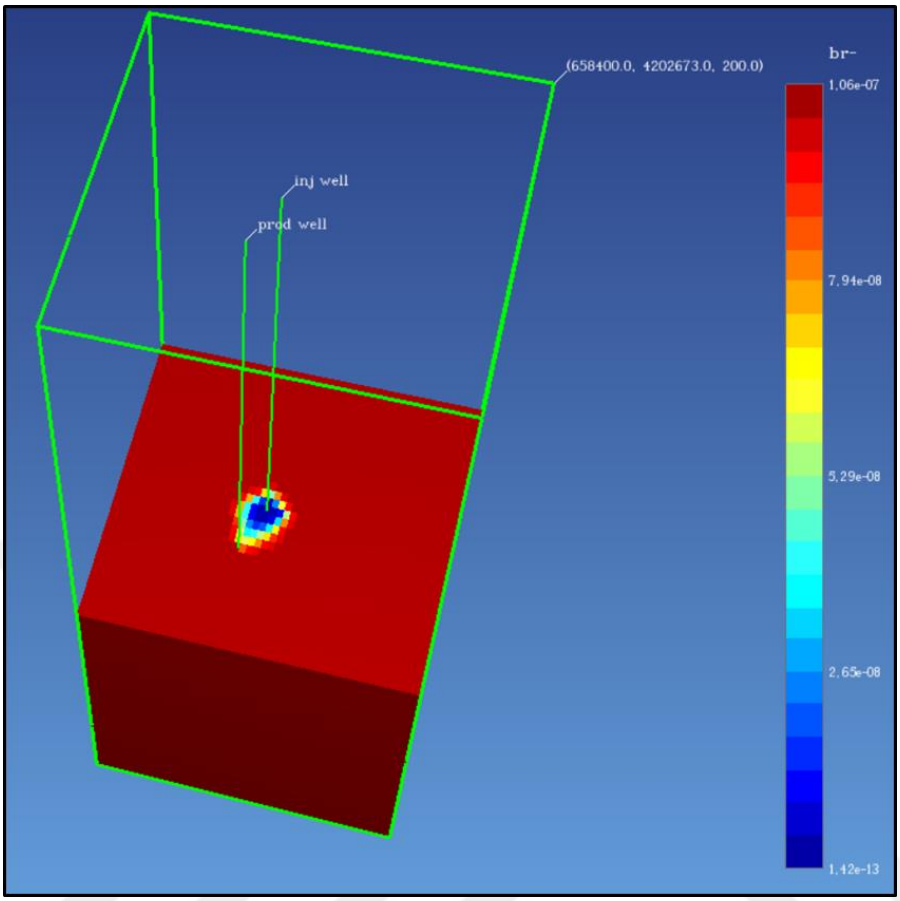

Figure 5.53 Bromide distribution after CO_2 injection.

Figure 5.54 depicts the aluminum dioxide (AlO_2^-) changes in the reservoir brine with injection. Source of AlO_2^- is kaolinite in this reservoir. Since injected brine has a lower AlO_2^- concentration than its initial reservoir brine, it enhanced kaolinite dissolution around the injection well.

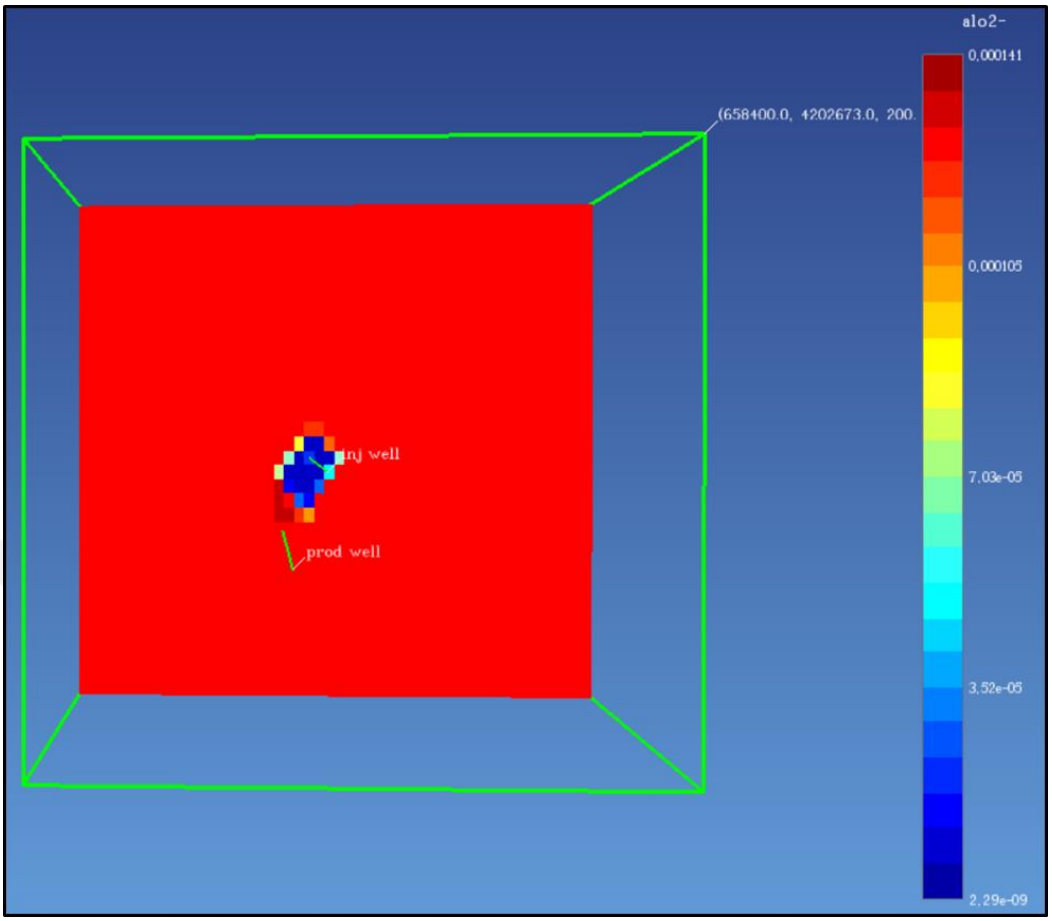

Figure 5.54 Aluminum distribution after CO_2 injection.

5.6 Effect of CO_2 on the Production Performance using Wellbore Simulation

CO_2 is generally found dissolved in geothermal brine at reservoir conditions in most geothermal fields in Turkey. In most fields, such as Alaşehir, Germencik, and Kızıldere, reservoir pressure is higher than the gas flashed out pressure. When the well is opened to flow, the geothermal fluid ascends in the wellbore and two-phase flow eventually occurs at the depth where the dynamic fluid pressure falls below the bubble point pressure. Wellbore flow simulation is a robust method for estimating flow performance and flashing depth at desired flow rates. Dynamic pressure-temperature (P-T) measurements in the wellbore at a constant flow rate are essential for calibrating wellbore flow simulations.

In this study, a wellbore simulation software, WELBOR, demonstrate the effects of CO_2 content on the production performance of geothermal wells. WELBOR is a two-phase flow simulator that was developed by Pitcher and Garg (1986). WELBOR assumes steady flow from the reservoir to the wellbore. The important user-defined parameters are well geometry (inner diameter, inclination, and depth), static temperature profile, productivity index, flow rate, CO_2 content, reservoir temperature, and pressure (Table 5.11).

The software subdivides the wellbore length into smaller interval lengths along the wellbore. As the single-phase geothermal fluid ascends in the wellbore, pressure and temperature reduction occurs. Pressure reduction occurs due to momentum loss. Temperature decline occurs because of phase dissociation from liquid to gas phase and heat loss towards the formations along the wellbore length. Wellbore simulation solves these processes from the feed point along the wellbore to the wellhead. WELBOR uses the modified Hughmark liquid holdup (Hughmark, 1962) and Dukler I friction (Dukler et al., 1964) correlations. The heat transfer coefficient approximated by Garg et al. (2004) was used to account for heat loss towards the formations during simulations. To delineate the influence of CO_2 on the production performance of geothermal wells, a calibrated wellbore simulation was constructed in WELBOR for a typical geothermal well in the Kızıldere geothermal field (Figure 5.55).

The calibrated model was run for different CO_2 contents, while all other parameters, such as reservoir pressure, temperature, and productivity index, were kept constant. Figure 5.56 shows that CO_2 content of the producing fluid has a significant impact on well performance. The main reason for the decline in CO_2 in the wells is the reinjection of gas-free geothermal brine. Therefore, injecting CO_2 will support performance of the production wells.

Table 5.11 Wellbore simulation parameters.

Parameters	
CO_2 Content	3
Productivity Index (ton/h/bar)	6
Reservoir Temperature (^oC)	244
Reservoir Pressure (Barg)	296
Flow rate (ton/h)	180

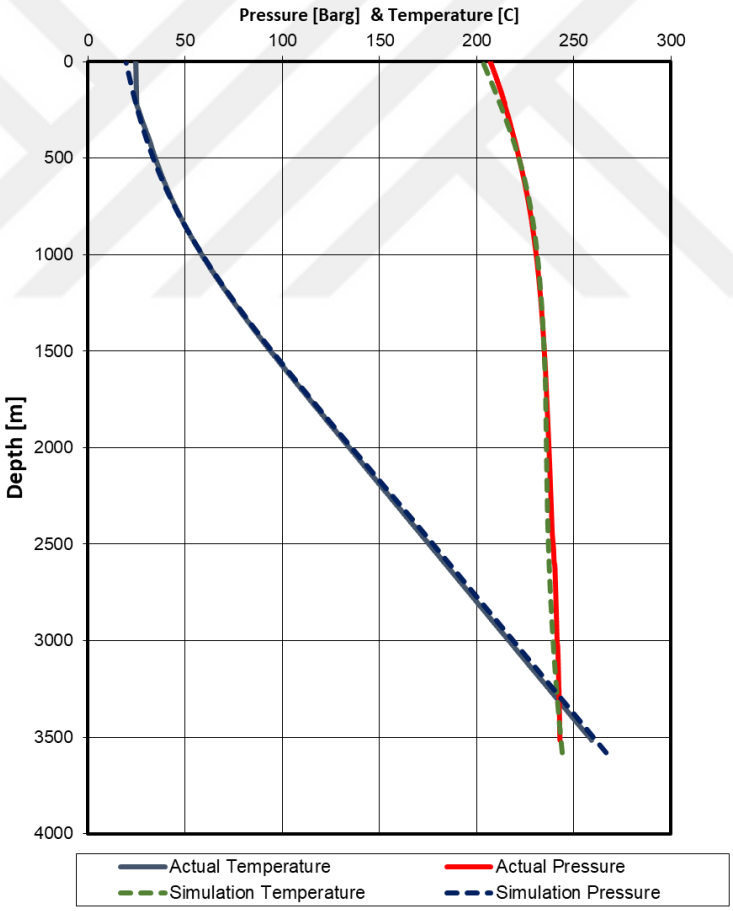

Figure 5.55 Calibrated wellbore simulation for a geothermal well in Kızıldere field.

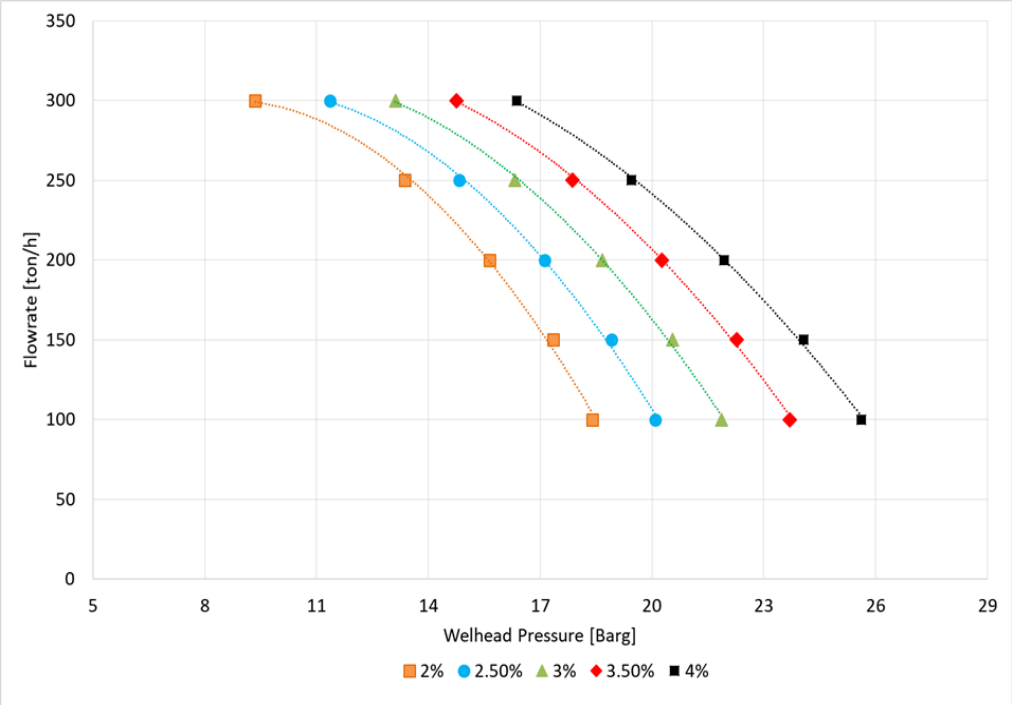

Figure 5.56 Effect of CO_2 on the performance of production well.

CHAPTER 6

CONCLUSION

This dissertation investigated CO_2 sequestration into Paleozoic-aged Menderes metamorphic rocks, which act as reservoir rocks for most of the geothermal fields in western Turkey. The study involves both experimental and simulation-based work.

First, CO_2 dissolution in geothermal brine was investigated using real field gas and brine collected from geothermal wells. The gas dissolution experiments were conducted in a batch reactor, and the results were matched with those of PHREEQC, a geochemical modeling software. The calibrated model was then used to estimate CO_2 dissolution at reservoir conditions. The effects of gas impurity, salting-out, and species distribution were also revealed with PHREEQC.

Next, water-rock interaction experiments were conducted using batch and flow-through experiments. The results of the batch experiments were then matched with a PHREEQC model to obtain the complexities, activation energy, and kinetic reaction rates. The data obtained from the batch experiments were then used in a 3D reactive transport model performed in TOUGHREACT.

1. The conclusion obtained from CO_2 dissolution experiments are:

- The experimental results were found to be in good agreement with the empirical formulations available in the literature. PHREEQC assumes the mixing of CO_2 with water at ideal conditions. That is why PHREEQC results were found to be somewhat larger than experimental ones, possibly due to the short duration of the tests and/or the limited mixing of CO_2 with the brine in the experiments. Increasing the test duration would improve the missing quality of gas and brine, thus increasing the experiments' accuracy.
- Most CO_2 was flashed out and measured as free gas during the measurements using a flowmeter connecting to the sampling separator (at atmospheric

pressure). The study also showed that most dissolved gas is found as bicarbonate in the liquid.

- The CO_2 dissolution kinetics showed an exponential decline with time for all studied gas/brine mixing ratios.
- It was found that gas dissolution kinetics is highly dependent on the contact surface area between geothermal brine and CO_2. At higher mixing ratios, the amount of time to reach maximum gas dissolution was found to be quite small. Therefore, it is critical to have enough mixing of CO_2 gas and brine to have dissolution. Otherwise, there will be free gas injection causing severe problems during injection in the wellbore.
- Gas impurity was found to reduce CO_2 solubility in geothermal brine.
- When the pH value of the brine was reduced from 9 to 5.5, most of the minerals shifted from precipitation to the dissolution state after CO_2 dissolution. However, amorphous silica shifted from a dissolution to a precipitation state.
- It is important to inject CO_2 above 30 bars to prevent amorphous silica for the given brine chemistry at 100 ^{o}C injecting temperature.

2. The conclusion obtained from core-flood experiments are:

- Chromatographic measurements showed that there is a fracture filled with calcite mineral precipitation in the core.
- XRD results of frontside and backside of 1 cm thick, thin section of the single fracture showed that the composition of minerals in decreasing abundance by weight is: magnesite (34.9 %), quartzite (26.7 %), kaolinite (23.3 %), feldspar (12.1 %), siderite (2.7 %), dolomite (0.5 %), and hematite (0.2 %). It was found from the backside of the fracture surface that mineral composition is the same with different weights. This is not because of water-rock interaction but heterogeneity of the rock sample.
- The core-flood experiment was lasted for 8.5 hours, due to the limitation of reserved brine volume. The fracture surface area was 14.7 cm^2. Therefore, it

is not expected to observe significant changes in the fracture flow media due to water-rock interaction due to limited mineral surface area and flow duration.

3. The conclusion obtained from batch experiments are:

- XRD results showed that rock samples involved certain minerals, such as siderite, magnesite, muscovite, kaolinite, dolomite, quartz, biotite, and feldspar (albite).
- In the studied batch experiments, the mineral assembly remained the same while abundancy of the minerals changed.
- The study showed that the existence of cations such as Ca^{2+}, AI^{3+} and Fe^{2+} promoted the precipitation of CO_2 as carbonates.
- In the batch experiment simulation, the activation energy and kinetic reaction rates of minerals were used as tuning parameters to match with experiment results. The tuned values were found to be in accord with USGS data for quartzite, muscovite, pyrite, dolomite, magnesite, siderite, and calcite minerals. Discrepancy was found between the model and USGS data for feldspar (Albite), and kaolinite minerals.
- Crushing rock sample into powder form increased mineral surface area significantly. Thus, 3 weeks of water-rock interaction was found to be sufficient to observe changes in the geochemical data of geothermal brine and mineral content.
- Both mineral assemblies are suitable for CO_2 injection, but the reservoir rock at 3000-m depth was found to be more favorable for CO_2 injection, because the injectivity of the wells will also be enhanced with CO_2-saturated brine and rock interaction.
- Kinetic reaction rates and activation energy obtained during tuning operation was found to be in accord with USGS data.

4. The conclusion obtained from 3D reactive-transport simulation:

- The calibrated 3D conceptual model revealed that a dome-shaped distribution of high temperatures at the center of the model, which is also observed in Kızıldere field.
- Reservoir temperature of reinjection wells decreased from 220 ^{o}C to 105 ^{o}C with reinjection. Temperature decline caused silica precipitation.
- Reinjected brine has a lower geochemical concentration comparing with initial reservoir brine. This resulted in mineral dissolution of minerals such as calcite, quartzite, muscovite, and magnesite.
- Mineral dissolution enhanced permeability and porosity of reinjection well slightly.
- Spatial distribution of bromide, chloride, and CO_2 was used for tracking injecting brine in the reservoir.
- Injecting CO_2 was found to compensate CO_2 decline of production well. This supported production performance of the well.
- The effects of CO_2 injection were found more clearly in the homogeneous model due to less variation of reservoir parameters.
- No-free gas was observed in the simulations even at injecting CO_2 with 5 % gas content by weight.
- During the numerical simulations, 12.6 kg/sec of CO_2 was injected along with 70 kg/sec of geothermal brine without encountering any difficulties.

REFERENCES

Akın, T., & Kargı, H. (2019). Modeling the geochemical evolution of fluids in geothermal wells and its implication for sustainable energy production. Geothermics, 77, 115-129.

Alt, J. C., Shanks III, W. C., Crispini, L., Gaggero, L., Schwarzenbach, E. M., Früh-Green, G. L., & Bernasconi, S. M. (2012). Uptake of carbon and sulfur during seafloor serpentinization and the effects of subduction metamorphism in Ligurian peridotites. Chemical Geology, *322*, 268-277.

Ampomah, W., Balch, R.S., Grigg, R.B., Dai, Z., Pan, F. 2015. Compositional Simulation of CO_2 Storage Capacity in Depleted Oil Reservoirs. CMTC-439476-MS.

Amponsah, N. Y., Troldborg, M., Kington, B., Aalders, I., & Hough, R. L. (2014). Greenhouse gas emissions from renewable energy sources: A review of lifecycle considerations. Renewable and Sustainable Energy Reviews, 39, 461-475.

André, L., Audigane, P., Azaroual, M., & Menjoz, A. (2007). Numerical modeling of fluid–rock chemical interactions at the supercritical CO_2–liquid interface during CO2 injection into a carbonate reservoir, the Dogger aquifer (Paris Basin, France). Energy conversion and management, 48(6), 1782-1797.

André, L., Azaroual, M., Bernstone, C., & Wittek, A. (2012). Modeling the geochemical impact of an injection of CO_2 and associated reactive impurities into a saline reservoir. In TOUGH Symposium (Vol. 2012).

Arnórsson, S. (1986). Chemistry of gases associated with geothermal activity and volcanism in Iceland: A review. Journal of Geophysical Research: Solid Earth, 91(B12), 12261-12268.

Assayag, N., Bickle, M., Kampman, N., Becker, J., 2009a. Carbon isotopic constraints on CO_2 degassing in cold-water Geysers, Green River, Utah. Energy Procedia 1 (1), 2361–2366.

Aydin, H., Akin, S., Senturk, E., & Energy, Z. (2020). Evaluation of production capacity of geothermal power plants in Turkey. GRC Transactions, 40, 163-174.

Aydin H. and Akin S., (2020): "Numerical Reservoir Simulation of Alaşehir Geothermal Field" 45th Workshop on Geothermal Reservoir Engineering Stanford University, at Stanford, California

Bachu, S., & Adams, J. J. (2003). Sequestration of CO_2 in geological media in response to climate change: capacity of deep saline aquifers to sequester CO_2 in solution. Energy Conversion and management, 44(20), 3151-3175.

Battistelli, A., Calore, C., & Pruess, K. (1997). The simulator TOUGH2/EWASG for modelling geothermal reservoirs with brines and non-condensible gas. Geothermics, *26*(4), 437-464.

Battles, D. A., & Barton, M. D. (1995). Arc-related sodic hydrothermal alteration in the western United States. *Geology*, *23*(10), 913-916.

Bayraktar, Y. Y. (2022). Sentetik rezervuar modeli ile Kızıldere jeotermal sahasında dikeydeki rezervuar bağlantılarının araştırılması (Master's thesis, Pamukkale Üniversitesi Fen Bilimleri Enstitüsü).

Bénézeth, P., Dandurand, J. L., & Harrichoury, J. C. (2009). Solubility product of siderite ($FeCO_3$) as a function of temperature (25–250 ^oC). Chemical Geology, 265(1-2), 3-12

Benson, S. M., & Cole, D. R. (2008). CO_2 sequestration in deep sedimentary formations. Elements, 4(5), 325-331.

BingLin, Z., LiQiang, Y., SuoYing, H., Yue, L., WenLong, L., RongXin, Z., ... & ShengGuang, L. (2014). Hydrothermal alteration in the Jiaojia gold deposit, Jiaodong, China. Acta Petrologica Sinica, 30(9), 2533-2545.

Bode, S., & Jung, M. (2006). Carbon dioxide capture and storage liability for non-permanence under the UNFCCC. International Environmental Agreements: Politics, Law and Economics, 6(2), 173-186.

Bray, A. W., Oelkers, E. H., Bonneville, S., Wolff-Boenisch, D., Potts, N. J., Fones, G., & Benning, L. G. (2015). The effect of pH, grain size, and organic ligands on biotite weathering rates. Geochimica et Cosmochimica Acta, 164, 127-145.

Brimhall, G. H., & Ghiorso, M. S. (1983). Origin and ore-forming consequences of the advanced argillic alteration process in hypogene environments by magmatic gas contamination of meteoric fluids. Economic Geology, 78(1), 73-90.

Bush, J. A., Vanneste, J., Gustafson, E. M., Waechter, C. A., Jassby, D., Turchi, C. S., & Cath, T. Y. (2018). Prevention and management of silica scaling in membrane distillation using pH adjustment. Journal of Membrane Science, 554, 366-377.

CarbFix project, 2018. https://en.amphos21.com/carbfix-project/. Accessed 16 July 2023.

Caumon, M. C., Sterpenich, J., Randi, A., & Pironon, J. (2016). Measuring mutual solubility in the H_2O–CO_2 system up to 200 bar and 100 C by in situ Raman spectroscopy. International Journal of Greenhouse Gas Control, 47, 63-70.

Chamwudhiprecha, N., Blunt, M.J. 2012. Carbon Dioxide Storage Potential in the North Sea. IPTC 14464.

Cramer S. D. (1982) The solubility of methane, carbon dioxide and oxygen in brines from 0 to 300°C. Report of Investigations 8706, U.S. Department of the Interior, Bureau of Mines.

Crovetto, R. (1991). Evaluation of solubility data of the system CO_2–H_2O from 273 K to the critical point of water. Journal of Physical and Chemical Reference Data, 20(3), 575-589.

Dalkhaa, C., & Okandan, E. (2013). 2-D numerical modeling of CO_2-water-caprock interactions at a potential CO_2 storage site in Turkey. Geochemical Journal, 47(5), 499-511.

Di Tommaso, I., & Rubinstein, N. (2007). Hydrothermal alteration mapping using ASTER data in the Infiernillo porphyry deposit, Argentina. Ore Geology Reviews, 32(1-2), 275-290.

DiPippo, R. (Ed.). (2016). Geothermal power generation: Developments and innovation. Woodhead Publishing.

Duan, G., Ram, R., Xing, Y., Etschmann, B., & Brugger, J. (2021). Kinetically driven successive sodic and potassic alteration of feldspar. Nature communications, 12(1), 1-8.

Duan, Z., Sun, R. 2003. An improved model calculating CO_2 solubility in pure water and aqueous NaCl solutions from 273 to 533 K and from 0 to 2000 bar. Chemical Geology 193 (2003) 257-271.

Duan, Z., Sun, R., Zhu, C., & Chou, I. M. (2006). An improved model for the calculation of CO_2 solubility in aqueous solutions containing Na^+, K^+, Ca^{2+}, Mg^{2+}, Cl^-, and SO_4^{2-}. Marine chemistry, 98(2-4), 131-139.

Dukler, A.E.., Wickes III, M., Cleveland, R.G. 1964. Frictional pressure drop in two phase flow. AIChE J. 10 (1), 44-51.

Dziejarski, B., Krzyżyńska, R., & Andersson, K. (2023). Current status of carbon capture, utilization, and storage technologies in the global economy: A survey of technical assessment. Fuel, 342, 127776.

Eiken, O. (2019). Twenty Years of Monitoring CO_2 Injection. Geophysics and geosequestration, 209.

Ellis, A.J., Golding, R.M., 1963. The solubility of carbon dioxide above 100 ^oC in water and in sodium chloride solutions. Am. J. Sci. 261, 47-60.

Emberley, S., Hutcheon, I., Shevalier, M., Durocher, K., Gunter, W. D., & Perkins, E. H. (2004). Geochemical monitoring of fluid-rock interaction and CO_2 storage at the Weyburn CO_2-injection enhanced oil recovery site, Saskatchewan, Canada. Energy, 29(9-10), 1393-1401.

Erol, S., Akın, T., Başer, A., Saraçoğlu, Ö., & Akın, S. (2022). Fluid-CO_2 injection impact in a geothermal reservoir: Evaluation with 3-D reactive transport modeling. Geothermic, 98, 102271.

Erten, A., Eroglu, M., Avci, İ., Karan, T., & Çoban, A. E. (2021). Prevention of the Antimony Compounds at the Geothermal Power Plants with HYDRODIS® GE Products. Bilge International Journal of Science and Technology Research, 5(2), 146-156.

Feng, X., Zhang, B., & Chery, L. (2008). Effects of low temperature on aluminum (III) hydrolysis: Theoretical and experimental studies. Journal of Environmental Sciences, 20(8), 907-914.

Fournier, R. O. (1989). Geochemistry and dynamics of the Yellowstone National Park hydrothermal system. Annual review of earth and planetary sciences, 17(1), 13-53.

Fridriksson, T., Mateos, A., Audinet, P., Orucu, Y. 2016. Greenhouse gases from geothermal power production.

Gallardo, R., Morata, D., Maza, S., & Cannatelli, C. 2018. Hydrothermal alteration in Nevados de Chillán Geothermal System: constrains regarding the chemical and thermal evolution of an active geothermal system. In AGU Fall Meeting Abstracts (Vol. 2018, pp. H33J-2221).

Gehrig, M., 1980. Phaseengleichgewichte und PVT-daten ternarer Mischurigen aus Wasser, Kohlendioxid und Natriumchlorid bis 3 kbar und 550 ^{o}C. PhD thesis, Univ. Karlsrushe, Freiburg.

Glazner, A.F. 1988. Stratigraphy, structure, and potassic alteration of Miocene volcanic rocks in the Sleeping Beauty area, central Mojave Desert, California. GSA Bulletin (1988) 100 (3): 424–435.

Grimekis, D., Giannoulidis, S., Manou, K., Panopoulos, K. D., & Karellas, S. 2019. Experimental investigation of CO_2 solubility and its absorption rate into promoted aqueous potassium carbonate solutions at elevated temperatures. International Journal of Greenhouse Gas Control, 81, 83-92.

Gunnarsson, I., Aradóttir, E. S., Oelkers, E. H., Clark, D. E., Arnarson, M. Þ., Sigfússon, B., ... & Gíslason, S. R. (2018). The rapid and cost-effective capture and subsurface mineral storage of carbon and sulfur at the CarbFix2 site. International Journal of Greenhouse Gas Control, 79, 117-126.

Haizlip, J.R., Stover, M., Garg, S., Haklidir, F. and Prin N., Origin and Impacts of High Concentrations of Carbon Dioxide in Geothermal Fluids of Western

Turkey, 41st Workshop on Geothermal Reservoir Engineering Stanford University, 2016.

Haklıdır, F. S. T., Şengün, R., & Aydın, H. (2021). Characterization and Comparison of geothermal fluids geochemistry within the Kızıldere Geothermal Field in Turkey: New findings with power capacity expanding studies. Geothermics, 94, 102110.

Han,W.S., Lu,M., McPherson, B.J., Keating, E.H., Moore, J., Park, E., Watson, Z.T., Jung, N.-H., 2013. Characteristics of CO_2-driven cold-water geyser, Crystal Geyser in Utah: experimental observation and mechanism analyses. Geofluids 13 (3), 283–297.

Hart, P. W., Colson, G. W., & Burris, J. (2013). Application of carbon dioxide to reduce water-side lime scale in heat exchangers. Pulp Pap. Canada, 114(1), 21-24.

Hellevang, H., Pham, V. T., & Aagaard, P. (2013). Kinetic modelling of CO_2–water–rock interactions. International Journal of Greenhouse Gas Control, 15, 3-15.

Hikov, A. (2004). Geochemistry of strontium in advanced argillic alteration systems–possible guide to exploration. Geology, 16-17.

Hou, Z., Rockhold, M. L., & Murray, C. J. (2012). Evaluating the impact of caprock and reservoir properties on potential risk of CO_2 leakage after injection. Environmental Earth Sciences, 66, 2403-2415.

Hughmark, G.A., 1962. Holdup in gas-lquid flow. Chem. Eng. Prog. 53 (4), 62-65.

İlhan, S., & Kabak, A. F. (2018). Alaşehir (Manisa) jeotermal alanında gelişen hidrothermal alterasyonların karakteristiği. Niğde Ömer Halisdemir Üniversitesi Mühendislik Bilimleri Dergisi, 7(3), 1078-1082.

Injection of carbon dioxide into depleted oil and gas reservoirs. https://www.sccs.org.uk/ . Accessed 16 July 2023.

Jin, M., Ribeiro, A., Mackay, E., Guimarães, L., & Bagudu, U. (2016). Geochemical modelling of formation damage risk during CO_2 injection in saline aquifers. Journal of Natural Gas Science and Engineering, 35, 703-719.

Kampman, N., Bickle, M., Wigley, M., & Dubacq, B. (2014). Fluid flow and CO_2–fluid–mineral interactions during CO_2-storage in sedimentary basins. Chemical Geology, 369, 22-50.

Karamanderesi, İ. H., & Helvaci, C. (2003). Geology and hydrothermal alteration of the Aydın-Salavatlı geothermal field, western Anatolia, Turkey. Turkish Journal of Earth Sciences, 12(2), 175-198.

Kelemen, P., Benson, S. M., Pilorgé, H., Psarras, P., & Wilcox, J. (2019). An overview of the status and challenges of CO_2 storage in minerals and geological formations. Frontiers in Climate, 1, 9.

Krauskopf, K. B. (1956). Dissolution and precipitation of silica at low temperatures. Geochimica et Cosmochimica Acta, 10(1-2), 1-26.

Krupp, R. E. (1988). Solubility of stibnite in hydrogen sulfide solutions, speciation, and equilibrium constants, from 25 to 350°C. Geochimica et Cosmochimica Acta, 52(12), 3005–3015.

Küçük, S. (2018). Simulation of geothermal reservoirs with high amount of carbon dioxide (master's thesis, Middle East Technical University).

Kumar, G. S., & Ghassemi, A. (2005). Numerical modeling of non-isothermal quartz dissolution/precipitation in a coupled fracture–matrix system. Geothermic, 34(4), 411-439.

Kumral, M., Abdelnasser, A., & Budakoglu, M. (2016). Geochemistry of hydrothermal alteration associated with Cenozoic intrusion-hosted Cu-Pb-Zn mineralization at Tavşanlı area, Kütahya, NW Turkey. Minerals, 6(1), 13.

Li, D., Zhang, H., Li, Y., Xu, W., & Jiang, X. (2018). Effects of N_2 and H_2S binary impurities on CO_2 geological storage in stratified formation–A sensitivity study. Applied energy, 229, 482-492.

Liang, Z. H., Rongwong, W., Liu, H., Fu, K., Gao, H., Cao, F., ... & Tontiwachwuthikul, P. P. (2015). Recent progress and new developments in post-combustion carbon-capture technology with amine-based solvents. International Journal of Greenhouse Gas Control, 40, 26-54.

Liu, B., Xu, J., Li, Z., Malekian, R., & Xu, Z. (2018). Modeling of CO_2 transport and pressure buildup in reservoirs during CO_2 storage in saline aquifers: a case in Dongying Depression in China. Environmental earth sciences, 77, 1-14.

Liu, D., Agarwal, R., Li, Y., & Yang, S. (2019). Reactive transport modeling of mineral carbonation in unaltered and altered basalts during CO_2 sequestration. International Journal of Greenhouse Gas Control, 85, 109-120.

Liu, F., Lu, P., Griffith, C., Hedges, S. W., Soong, Y., Hellevang, H., & Zhu, C. (2012). CO2–brine–caprock interaction: Reactivity experiments on Eau Claire shale and a review of relevant literature. International Journal of Greenhouse Gas Control, 7, 153-167.

Liu, Y., Hou, M., Yang, G., Han, B. (2011). Solubility of CO_2 in aqueous solutions of NaCl, KCl, $CaCl_2$ and their mixed salts at different temperatures and pressures. J. of Supercritical Fluids 56 (2011) 125-129

Mahmoodpour, S., Amooie, M. A., Rostami, B., & Bahrami, F. (2020). Effect of gas impurity on the convective dissolution of CO_2 in porous media. Energy, 199, 117397.

Mahmoodpour, S., Singh, M., Mahyapour, R., Omrani, S., & Sass, I. (2023). Numerical Simulation of Carbon Dioxide–Nitrogen Mixture Dissolution in

Water-Saturated Porous Media: Considering Cross-Diffusion Effects. Fluids, 8(1), 22.

Malinin, S.D., 1959. The system water – carbon dioxide at high temperatures and pressures. Geokhimiya (3), 292 – 306.

Malinin, S.D., Kurorskaya, N.A., 1975. Investigation of CO2 solubility in a solution of chlorides at elevated temperatures and pressures of CO2. Geokhimiya (4), 547 – 551.

Malmström, M., & Banwart, S. (1997). Biotite dissolution at 25 ^{o}C: The pH dependence of dissolution rate and stoichiometry. Geochimica et Cosmochimica Acta, 61(14), 2779-2799.

Maskell, A., Kampman, N., Chapman, H., Condon, D. J., & Bickle, M. (2015). Kinetics of CO_2–fluid–rock reactions in a basalt aquifer, Soda Springs, Idaho. Applied Geochemistry, 61, 272-283.

Mathieson, A., Midgely, J., Wright, I., Saoula, N., & Ringrose, P. (2011). In Salah CO_2 Storage JIP: CO_2 sequestration monitoring and verification technologies applied at Krechba, Algeria. Energy Procedia, 4, 3596-3603.

Matter, J. M., Broecker, W. S., Stute, M., Gislason, S. R., Oelkers, E. H., Stefánsson, A., ... & Björnsson, G. (2009). Permanent carbon dioxide storage into basalt: the CarbFix pilot project, Iceland. Energy Procedia, 1(1), 3641-3646.

Mazzotti, M., Pini, R., Storti, G. (2009). Enhanced coalbed methane recovery J. of Supercritical Fluids 47 (2009) 619–627.

Merey, S., & Sinayuc, C. (2016). Analysis of carbon dioxide sequestration in shale gas reservoirs by using experimental adsorption data and adsorption models. Journal of Natural Gas Science and Engineering, 36, 1087-1105.

Meunier, A., & Velde, B. (1976). Mineral reactions at grain contacts in early stages of granite weathering. Clay Minerals, 11(3), 235-240.

Morris, J.P., Hao, Y., Foxall, W. McNab, W. (2010). A Study of Injection-Induced Mechanical Deformation at the In Salah CO_2 Storage Project. ARMA 10-307.

Morrison, T.J., Billet, F. (1952). The salting-out of non-electrolytes:Part I. The effect of variation in non-eletrolyte. J. Chem. Soc., 3819-3822.

Moya, S. L., & Iglesias, E. R. (1992). Solubilidad del bióxido de carbono en agua en condiciones geotérmicas. Geofísica Internacional, 31(3), 305-313.

Musa, T. N., & Hamoshi, E. A. (2012). The effect of magnetic field on the solubility of NaCl and $CaCl_2$. $2H_2O$ at different temperature and pH values. Basrah Journal of Agricultural Sciences, 25(1), 19-26.

Nighswander, J.A., Kalogerakis, N., Mehrotra, A.K. (1989). Solubilities of carbon dioxide in water and 1 wt % NaCl solution at pressures up to 10 MPa and temperatures from 80 to 200 ^{o}C. J. Chem. Eng. Data 34, 355-360.

Nishiki, Y., Cama, J., Otake, T., Kikuchi, R., Shimbashi, M., & Sato, T. (2023). Formation of magnesium silicate hydrate (MSH) at pH 10 and 50° C in open-flow systems. Applied Geochemistry, 148, 105544.

Nuttal, B. C., Eble, C., Bustin, R. M., & Drahovzal, J. A. (2005). Analysis of Devonian black shales in Kentucky for potential carbon dioxide sequestration and enhanced natural gas production. In Greenhouse Gas Control Technologies 7 (pp. 2225-2228). Elsevier Science Ltd.

Olabi, A. G., Obaideen, K., Elsaid, K., Wilberforce, T., Sayed, E. T., Maghrabie, H. M., & Abdelkareem, M. A. (2022). Assessment of the pre-combustion carbon capture contribution into sustainable development goals SDGs using novel indicators. Renewable and Sustainable Energy Reviews, 153, 111710.

Olsen, N. J., Mountain, B. W., & Seward, T. M. (2012). Experimental study of stibnite solubility in aqueous sulfide solutions from 25 to 90°C. New Zealand Geothermal Workshop, 19(November).

Ors, O., & Sinayuc, C. (2014). An experimental study on the CO_2–CH_4 swap process between gaseous CO_2 and CH_4 hydrate in porous media. Journal of Petroleum Science and Engineering, 119, 156-162.

Özgür, N. (2010). Hydrogeological, Hydrogeochemical and Isotope Geochemical Modeling of the Thermal Waters in the Continental Rift Zones of the Menderes Massif, Western Anatolia. In Turkey. Proceedings World Geothermal Congress.

Palandri, J., Kharaka, Y.K. (2004). A compilation of rate parameters of water–mineral interaction kinetics for application to geochemical modeling. US Geological Survey Open File Report 2004-1068, 64pp

Pankaj, P., Mukisa, H., Solovyeva, I., Xue, H. (2018). Enhanced Oil Recovery in Eagle Ford: Opportunities Using Huff-n-Puff Technique in Unconventional Reservoirs. SPE 191780-MS. In: Presented at the SPE Liquids-Rich Basins Niorth Amercia Conference in Midland, Texas, USA. September 05-06, 2018.

Parkhurst DL, Appelo CAJ (2013). Description of input and examples for PHREEQC version 3 a computer program for speciation, batch-reaction, one-dimensional transport, and inverse geochemical calculations. U.S. Geological Survey Techniques and Methods. Amsterdam, Netherlands.

Parkhurst, D. L., & Appelo, C. A. J. (1999). User's guide to PHREEQC (Version 2): A computer program for speciation, batch-reaction, one-dimensional

transport, and inverse geochemical calculations. Water-resources investigations report, 99(4259), 312.

Parry, W. T., Jasumback, M., & Wilson, P. N. (2002). Clay mineralogy of phyllic and intermediate argillic alteration at Bingham, Utah. Economic Geology, 97(2), 221-239.

Pearce, K.J., Kirste, D.M.,Dawson, G.K.W., Farquhar, S.M., Biddle, D., Golding, S.D., Rudolph, V. (2015). SO_2 impurity impacts on experimental and simulated CO_2-water-reservoir rock reactions at carbon storage conditions. Chemical geology 399 (2015) 65-86.

Peng, D. Y., & Robinson, D. B. (1976). A new two-constant equation of state. Industrial & Engineering Chemistry Fundamentals, 15(1), 59-64.

Peterková, T., & Dolejš, D. (2019). Magmatic-hydrothermal transition of Mo-W-mineralized granite-pegmatite-greisen system recorded by trace elements in quartz: Krupka district, Eastern Krušné hory/Erzgebirge. Chemical Geology, 523, 179-202

Pfeiffer, A., Hepburn, C., Vogt-Schilb, A., & Caldecott, B. (2018). Committed emissions from existing and planned power plants and asset stranding required to meet the Paris Agreement. Environmental Research Letters, 13(5), 054019.

Phale, H. A., Zhu, T., White, M. D., & McGrail, B. P. (2006). Simulation study on injection of CO2-microemulsion for methane recovery from gas-hydrate reservoirs. In SPE Unconventional Resources Conference/Gas Technology Symposium (pp. SPE-100541). SPE.

Ramirez, A., Hagedoorn, S., Kramers, L., Wildenborg, T., Hendriks, C. (2010). Screening CO_2 storage optons in The Netherlands. Int. J. Greenh. Gas Control 4 (2), 367-380.

Rao, F., Ramirez-Acosta, F. J., Sanchez-Leija, R. J., Song, S., & Lopez-Valdivieso, A. (2011). Stability of kaolinite dispersions in the presence of sodium and aluminum ions. Applied clay science, 51(1-2), 38-42.

Ratouis TMP, Snæbjörnsdóttir SO, Sigfússon B, Gunnarsson I, Voigt MJ et al. (2021). Reactive transport model of CO_2 and H_2S mineral sequestration at the CarbFix2 reinjection site, Hellisheiði Geothermal Power Plant, SW-Iceland. In: World Geothermal Congress (WGC) October 24-27, Reykjavik, Iceland.

Ratouis TMP, Snæbjörnsdóttir SÓ, Voigt MJ, Sigfússon B, Gunnarsson G et al. (2022). Carbfix 2: A transport model of long-term CO_2 and H_2S injection into basaltic rocks at Hellisheidi, SW-Iceland. International Journal of Greenhouse Gas Control 114: 103586.

Raza, A., Rezaee, R., Gholami, R., Bing, C. H., Nagarajan, R., & Hamid, M. A. (2016). A screening criterion for selection of suitable CO_2 storage sites. Journal of Natural Gas Science and Engineering, 28, 317-327.

Ren, B., Zhang, L., Huang, H., Ren, S., Chen, G., & Zhang, H. (2015). Performance evaluation and mechanisms study of near-miscible CO_2 flooding in a tight oil reservoir of Jilin Oilfield China. Journal of Natural Gas Science and Engineering, 27, 1796-1805.

Richardson, J.C., Devinney, J. (2015). Optimizing hybrid noncondensable gas removal systems for flash steam geothermal power plants. Proceedings 37th New Zealand Geothermal Workshop 18-20 November 2015 Taupo, New Zealand.

Rubin, E. S., Mantripragada, H., Marks, A., Versteeg, P., & Kitchin, J. (2012). The outlook for improved carbon capture technology. Progress in energy and combustion science, 38(5), 630-671.

Rumpf, B., Nicolaisen, H., Ocal, C., Maurer, G. (1994). Solubility of carbon diozide in aqueous solutions of sodium chloride: experimental results and correlation. J. Solution Chem. 2 (3) 431-448.

Saeedi, A. (2012). Experimental study of multiphase flow in porous media during CO_2 Geo-Sequestration processes. Springer Science & Business Media.

Samadi, R., Torabi, G., Kawabata, H., & Miller, N. R. (2021). Biotite as a petrogenetic discriminator: chemical insights from igneous, meta-igneous and meta-sedimentary rocks in Iran. Lithos, 386, 106016.

Satman, A., Tureyen, O. I., Basel, E. D. K., Guney, A., Senturk, E., & Kindap, A. (2017). Effect of Carbon Dioxide Content on the Well and Reservoir Performances in the Kizildere Geothermal Field. In 42nd Workshop on Geothermal Reservoir Engineering.

Savary, V., Berger, G., Dubois, M., Lacharpagne, J. C., Pages, A., Thibeau, S., & Lescanne, M. (2012). The solubility of CO_2 + H_2S mixtures in water and 2 M NaCl at 120° C and pressures up to 35 MPa. International journal of greenhouse gas control, 10, 123-133.

Scottish Centre for Carbon Storage, (2023). Website: https://www.sccs.org.uk/ Accessed on 19.10.2023

Seki, Y. O. T. A. R. O. (1973). Metamorphic facies of propylitic alteration. J. Geol. Soc. Japan, 79, 771-780.

Sharifi, N., Kouhikamali, R., & Abadi, S. N. R. (2013). CFD simulation of supersonic jet behavior inside thermo-compressors at different converging angles. In IDA) World Congress (pp. 20-25).

Shevalier, M., Nightingale, M., Johnson, G., Mayer, B., Perkins, E., Hutcheon, I. 2009. Monitoring the reservoir geochemistry of the Pembina Cardium CO_2 Monitoring Project, Drayton Valley, Alberta. Energy Procedia 1 (2009) 2095–2102.

Shukla, R., Ranjith, P., Haque, A., Choi, X., 2010. A review of studies on CO_2 sequestration and caprock integrity. Fuel 89 (10), 2651–2664.

Silva, C. A., Liu, X., & Millero, F. J. (2002). Solubility of siderite (FeCO3) in NaCl solutions. Journal of solution chemistry, 31(2), 97-108.

Sınayuç, Ç., & Gümrah, F. (2009). Modeling of ECBM recovery from Amasra coalbed in Zonguldak Basin, Turkey. International Journal of Coal Geology, 77(1-2), 162-174.

Snæbjörnsdóttir, S. Ó., Gislason, S. R., Galeczka, I. M., & Oelkers, E. H. (2018). Reaction path modelling of in-situ mineralisation of CO_2 at the CarbFix site at Hellisheidi, SW-Iceland. Geochimica et Cosmochimica Acta, 220, 348-366.

Snæbjörnsdóttir, S. Ó., Sigfússon, B., Marieni, C., Goldberg, D., Gislason, S. R., & Oelkers, E. H. (2020). Carbon dioxide storage through mineral carbonation. Nature Reviews Earth & Environment, 1(2), 90-102.

Steel, L., Mackay, E., & Maroto-Valer, M. M. (2018). Experimental investigation of CO_2-brine-calcite interactions under reservoir conditions. Fuel Processing Technology, 169, 122-131.

Stemprok, M. 1987. Greisenization, a review. Geologische Rundschau 76/1 169-175.

Straub, F. G. (1932). Solubility of calcium sulfate and calcium carbonate at temperatures between 182 ^{o}C and 316 ^{o}C. Industrial & Engineering Chemistry, *24*(8), 914-917.

Sun, J., Zou, A., Sotelo, E., Schechter, D. 2016. Numerical simulation of CO_2 huff-n-puff in complex fracture networks of unconventional liquid reservoirs. Journal of Natural Gas Science and Engineering 31 (2016) 481-492.

Szymanek, K., Charmas, R., & Piasecki, W. (2021). Investigations of mechanism of Ca^{2+} adsorption on silica and alumina based on Ca-ISE monitoring, potentiometric titration, electrokinetic measurements, and surface complexation modeling. Adsorption, 27(1), 105-115.

Takenouchi, S. Kennedy, G.C. (1964). The binary system H_2O-CO_2 at high temperatures and pressures. Am. J. Sci. 262, 1055-1074.

Theo, W. L., Lim, J. S., Hashim, H., Mustaffa, A. A., & Ho, W. S. (2016). Review of pre-combustion capture and ionic liquid in carbon capture and storage. Applied energy, 183, 1633-1663.

Thomas, C., Lemaigre, L., Zalts, A., D'Onofrio, A., & De Wit, A. (2015). Experimental study of CO_2 convective dissolution: the effect of color indicators. International Journal of Greenhouse Gas Control, 42, 525-533.

Topcu, G., Koç, G. A., Baba, A., & Demir, M. M. (2019). The injection of CO_2 to hypersaline geothermal brine: A case study for Tuzla region. Geothermics, 80, 86-91.

Ueda, A., Ozawa, A., Unami, S., Kusakabe, M., Hirayama, N., Mogi, K., ... & Yonezu, K. (2022). Recovery of silica from saline geothermal brine at the Yamagawa Power Plant for inhibition of scale formation by batch-and circulation-tests using cationic flocculant and quicklime. Geothermics, 99, 102312.

Upton, S.P., Santoyo, E. 2003. A comprehensive evaluation of empirical correlations for computing the solubility of CO_2 in water. Twenty-Eighth Workshop on Geothermal Reservoir Engineering Stanford University, Stanford, California, January 27-29, 2003.

Utami, W. S., Herdianita, N. R., & Atmaja, R. W. (2014). The effect of temperature and pH on the formation of silica scaling of Dieng geothermal field, Central Java, Indonesia. In Proceedings, Thirty-Ninth Workshop on Geothermal Reservoir Engineering, Stanford University, California.

Vishal, V., Singh, T.N., Ranjith, P.G. (2012). Carbon capture and storage in Indian Coal Seams. CMTC 151614.

Waldmann, S., Busch, A., Van Ojik, K., & Gaupp, R. (2014). Importance of mineral surface areas in Rotliegend sandstones for modeling CO_2–water–rock interactions. Chemical Geology, 378, 89-109.

Wallace, C. J., & Maher, K. C. (2019). Phyllic alteration and the implications of fluid composition at the Copper Flat hydrothermal System, New Mexico, USA. Ore Geology Reviews, 104, 273-293.

Wang, K., Xu, T., Wang, F., & Tian, H. (2016). Experimental study of CO_2–brine–rock interaction during CO_2 sequestration in deep coal seams. International Journal of Coal Geology, 154, 265-274.

Watanabe, N., Abe, H., Okamoto, A., Nakamura, K., & Komai, T. (2021). Formation of amorphous silica nanoparticles and its impact on permeability of fractured granite in superhot geothermal environments. Scientific reports, 11(1), 1-11.

White, A. F., & Brantley, S. L. (2003). The effect of time on the weathering of silicate minerals: why do weathering rates differ in the laboratory and field? Chemical Geology, 202(3-4), 479-506

White, C. M., Smith, D. H., Jones, K. L., Goodman, A. L., Jikich, S. A., LaCount, R. B., ... & Schroeder, K. T. (2005). Sequestration of carbon dioxide in coal

with enhanced coalbed methane recovery a review. Energy & Fuels, 19(3), 659-724.

Wiebe, R., Gaddy, V.L. (1939). The solubility in water of carbon dioxide at 50°, 75°, and 100 °C at pressures to 700 atm. J. Am. Chem. Soc. 61, 315-318.

Witt, W. K. (1988). Evolution of high-temperature hydrothermal fluids associated with greisenization and feldspathic alteration of a tin-mineralized granite, northeast Queensland. Economic Geology, 83(2), 310-334.

Xu, T., Sonnenthal, E., Spycher, N., & Pruess, K. (2006). TOUGHREACT a simulation program for non-isothermal multiphase reactive geochemical transport in variably saturated geologic media: applications to geothermal injectivity and CO_2 geological sequestration. Computers & geosciences, 32(2), 145-165.

Yan, W., Huang, S., & Stenby, E. H. (2011). Measurement and modeling of CO_2 solubility in NaCl brine and CO_2–saturated NaCl brine density. International Journal of Greenhouse Gas Control, 5(6), 1460-1477.

Zhang, D., & Song, J. (2014). Mechanisms for geological carbon sequestration. Procedia IUTAm, 10, 319-327.

Zhang, K., Lau, H. C., & Chen, Z. (2022). Extension of CO_2 storage life in the Sleipner CCS project by reservoir pressure management. Journal of Natural Gas Science and Engineering, 108, 104814.

Zhang, W., Li, Y., Xu, T., Cheng, H., Zheng, Y., & Xiong, P. (2009). Long-term variations of CO_2 trapped in different mechanisms in deep saline formations: A case study of the Songliao Basin, China. International journal of greenhouse gas control, 3(2), 161-180.

Zhang, Y., Gao, J. F., Ma, D., & Pan, J. (2018). The role of hydrothermal alteration in tungsten mineralization at the Dahutang tungsten deposit, South China. Ore Geology Reviews, 95, 1008-1027.

APPENDICES

A. Water Rock Interaction Experiments

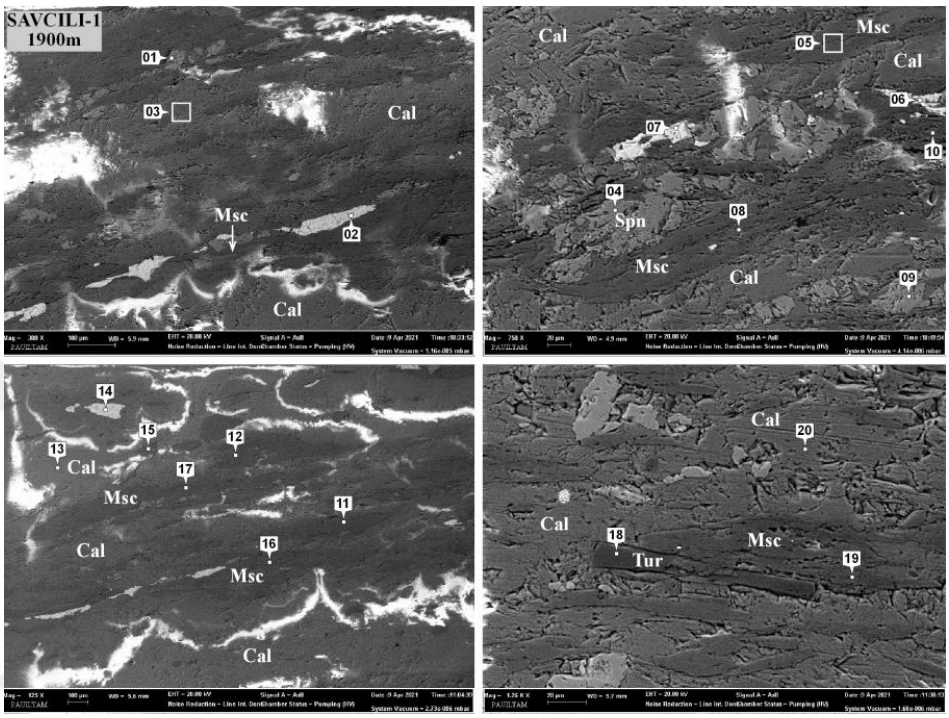

Figure 6.1 Images of EDX SEM analysis of rock samples from 1900 m depth.

Table 6.1 Chemistry of minerals found in EDX SEM of rock sample from 1900 m depth

1	Sphene (Titanite)	$CaTiSiO_5$
2	Chloritized biotite	$K_{0.6}(Si_{3.5}Al_{0.5})\ (AI_{2.5}Mg_{2.2}Fe_{0.1})\ O_{10}(OH)_8$
3	Calcite	$CaCO_3$
4	Sphene (Titanite)	$CaTiSiO_5$
5	Phengitic muscovite	$(K_{0.6}Na_{0.2}Ca_{0.1})\ (Si_{3.1}AI_{0.9})\ (AI_{1.5}Mg_{0.8})\ O_{10}(OH)_2$
6	Apatite	$Ca_{5.0}(PO_4)_3(OH)_{0.3}F_{0.3}CI_{0.3}$
7	Pyrite	FeS_2
8	Phengitic muscovite	$(K_{0.6}Na_{0.2}Ca_{0.1})\ (Si_{3.1}AI_{0.9})\ (AI_{1.5}Mg_{0.8})\ O_{10}(OH)_2$
9	Sphene (Titanite)	$CaTiSiO_5$

Table 6.1 (cont'd)

10	Phengitic muscovite	$(K_{0.6}Na_{0.2})$ $(Si_{3.1}AI_{1.0})$ $(AI_{1.5}Mg_{0.8})$ $O_{10}(OH)_2$
11	Phengitic muscovite	$(K_{0.6}Na_{0.1})$ $(Si_{3.1}AI_{0.9})$ $(AI_{1.5}Mg_{0.8})O_{10}(OH)_2$
12	Phengitic muscovite	$(K_{0.7})$ $(Si_{3.0}AI_{1.0})$ $(AI_{1.3}Mg_{1.3}Fe_{0.1})$ $O_{10}(OH)_2$
13	Calcite	$CaCO_3$
14	Pyrite	FeS_2
15	Quartz	SiO_2
16	Phlogopite	$(K_{0.7})$ $(Si_{3.0}AI_{1.0})$ $(AI_{1.0}Mg_{1.7}Fe_{0.1})$ O_{10} $(OH)_2$
17	Phlogopite	$(K_{0.6}Na_{0.2})$ $(Si_{3.0}AI_{1.0})$ $(AI_{1.1}$ $Mg_{1.4}Fe_{0.1})$ $O_{10}(OH)_2$
18	Tourmaline	$NaMg_{3.0}AI_{6.0}(BO_3)_3Si_6O_{18}(OH)_4$
19	Phengitic muscovite	$(K_{0.7})$ $(Si_{3.1}AI_{0.9})$ $(AI_{1.6}Mg_{0.7}Fe_{0.1})$ O_{10} $(OH)_2$
20	Calcite	$CaCO_3$

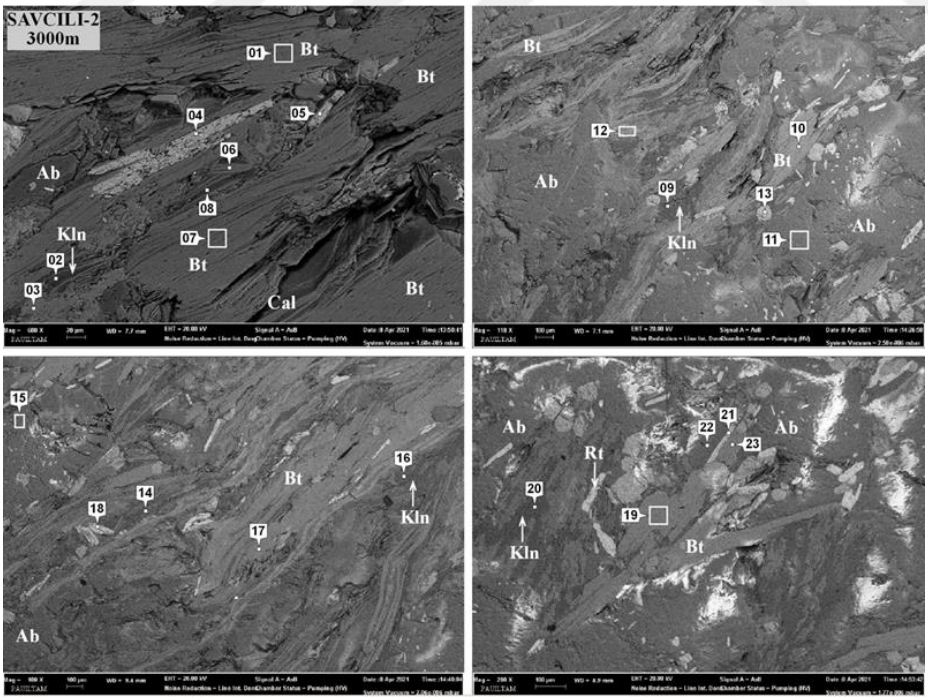

Figure 6.2 Images of EDX SEM analysis of rock samples from 3000 m depth.

Table 6.2 Chemistry of minerals found in EDX SEM of rock sample from 3000 m depth

1	Biotite	$(K_{0.9})\ (Si_{3.0}AI_{1.0})\ (Mg_{2.1}Fe_{0.8}AI_{0.2})\ O_{10}\ (OH)_2$
2	Kaolinite	$Si_2AI_2O_5\ (OH)_4$
3	Ferroan Magnesite	$((Mg, Fe)_2CO_3)$
4	IImenite	$(Fe^{2+}TiO_3)$
5	IImenite	$(Fe^{2+}TiO_3)$
6	Biotite	$(K_{0.7}\ Na_{0.1})\ (Si_{3.0}AI_{1.0})\ (Mg_{2.0}Fe_{0.6}AI_{0.3})\ O_{10}\ (OH)_2$
7	Biotite	$(K_{0.8})\ (Si_{3.0}AI_{1.0})\ (Mg_{2.1}Fe_{0.6}AI_{0.4})\ O_{10}\ (OH)_2$
8	Kaolinite	$Si_2AI_2O_5\ (OH)_4$
9	Kaolinite	$Si_2AI_2O_5\ (OH)_4$
10	Biotite	$(K_{0.7})\ (Si_{3.0}AI_{1.0})\ (Mg_{2.2}Fe_{0.3}AI_{0.5})\ O_{10}\ (OH)_2$
11	Feldspar	$Na_{1.0}AI_{1.0}Si_{3.0}O_8$
12	Calcian magnesian siderite	$(Ca,Mg,Fe)_2CO_3$
13	Apatite	$Ca_{5.0}(PO_4)_3(OH)_{0.3}F_{0.3}CI_{0.3}$
14	Kaolinite	$Si_2AI_2O_5(OH)_4$
15	Feldspar	$Na_{0.9}Ca_{1.0}\ AI_{1.1}Si_{2.9}O_8$
16	Kaolinite	$Si_2AI_2O_5(OH)_4$
17	Biotite	$(K_{0.9})\ (Si_{3.0}AI_{1.0})\ (Mg_{2.1}Fe_{0.8}AI_{0.2})\ O_{10}\ (OH)_2$
18	Rutile	TiO_2
19	Biotite	$(K_{0.7})\ (Si_{3.0}AI_{1.0})\ (Mg_{2.3}Fe_{0.2}AI_{0.5})\ O_{10}\ (OH)_2$
20	Kaolinite	$Si_2AI_2O_5(OH)_4$
21	IImenite	$Fe^{2+}TiO_3$
22	Feldspar	$Na_{1.0}AI_{1.0}Si_{3.0}O_8$
23	Biotite	$(K_{0.6}\ Na_{0.2})\ (Si_{3.0}AI_{1.0})\ (Mg_{2.2}Fe_{0.6}AI_{0.3})\ O_{10}\ (OH)_2$

B. 3D Reactive Transport Simulation

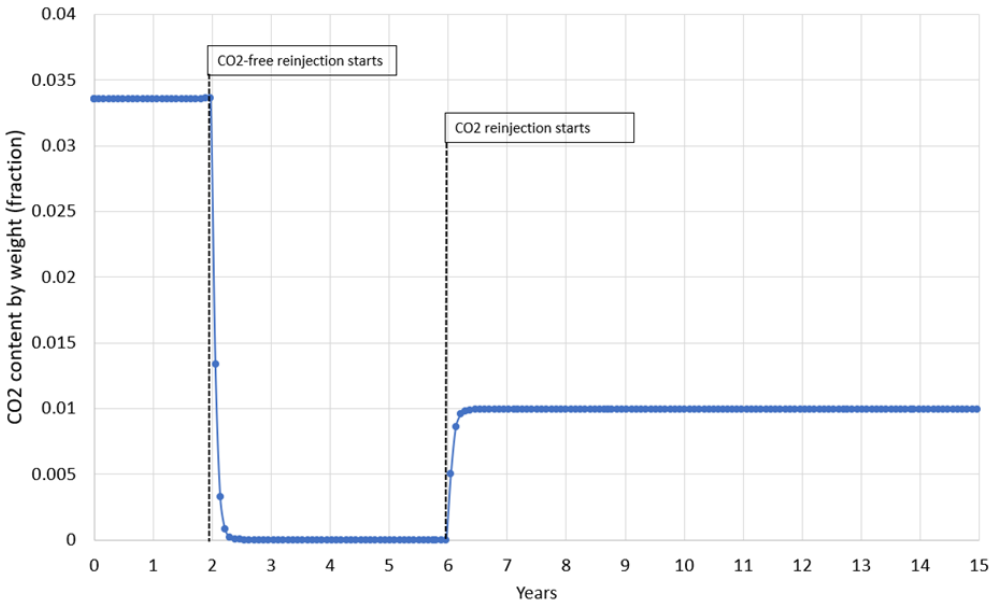

Figure 6.3 Dissolved CO_2 injection history in reinjection well.

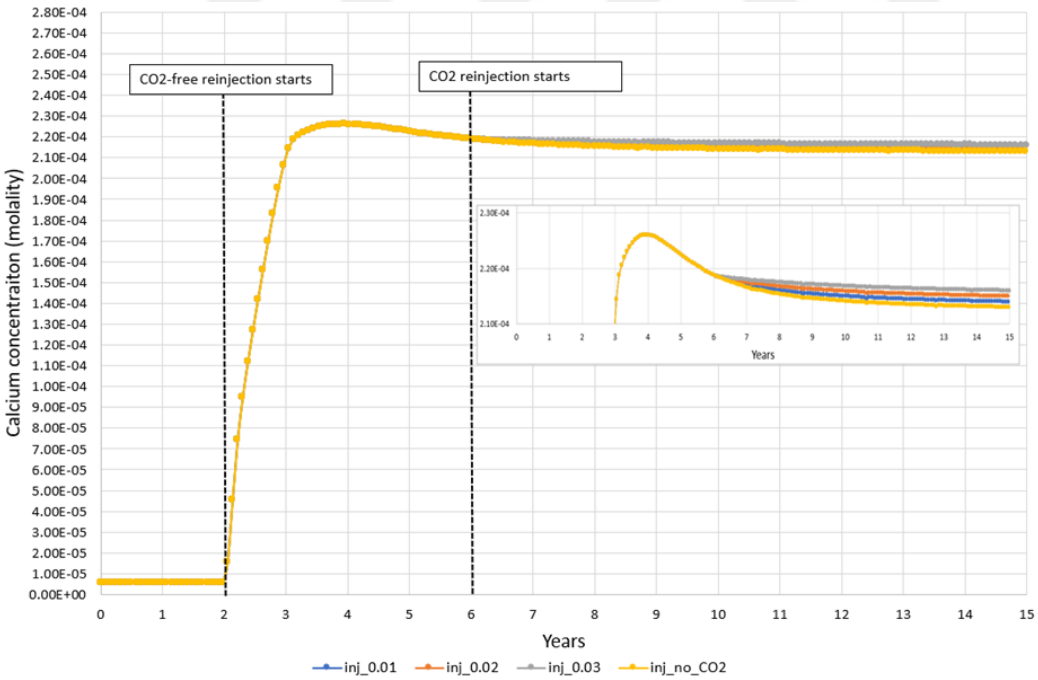

Figure 6.4 Changes in the calcium concentration of reinjection well in heterogeneous model.

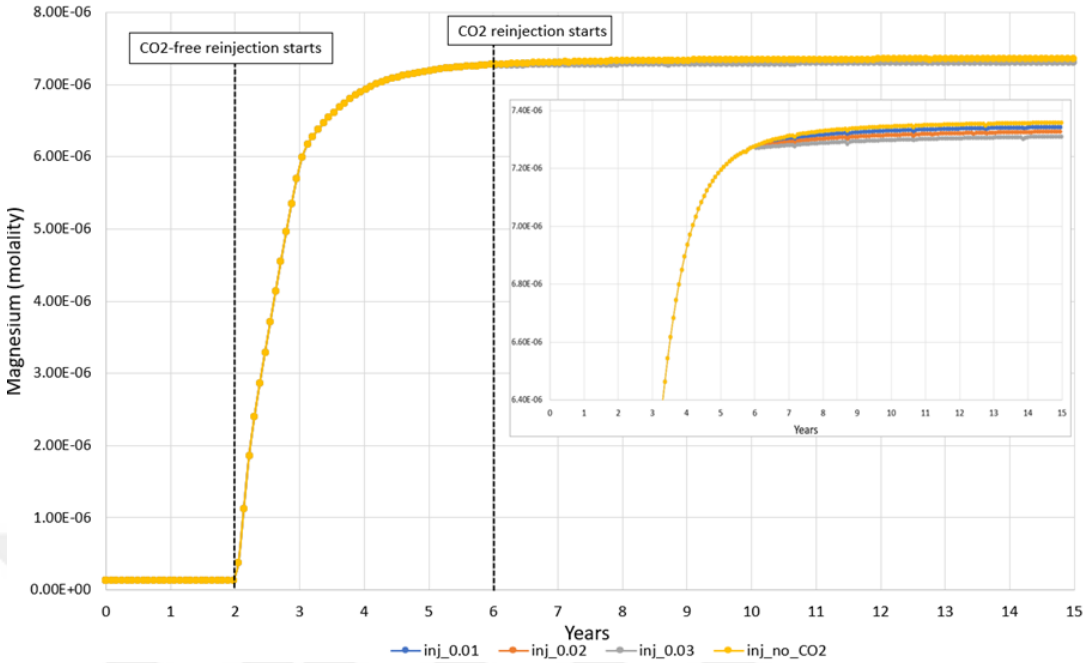

Figure 6.5 Changes in the magnesium concentration of reinjection well in heterogeneous model.

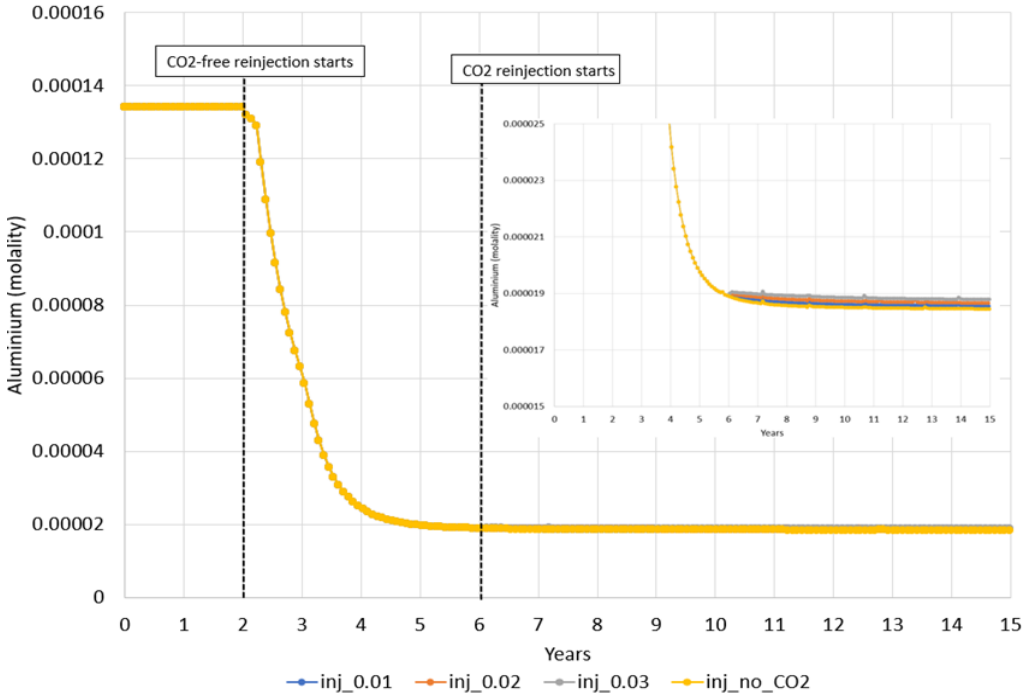

Figure 6.6 Changes in the aluminum concentration of reinjection well in heterogeneous model.

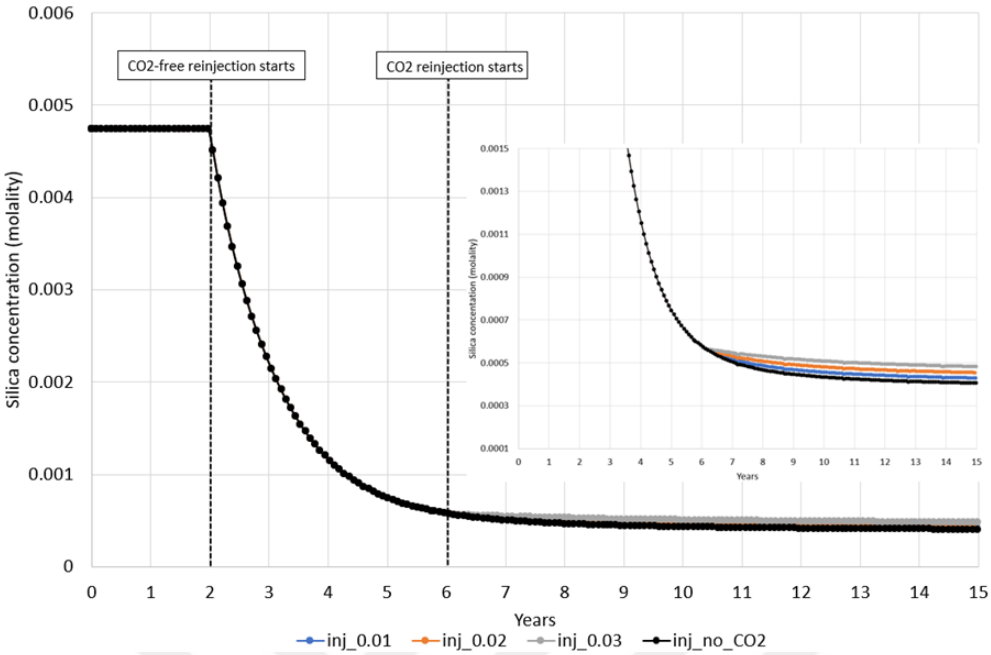

Figure 6.7 Changes in the silica concentration of reinjection well in heterogeneous model.

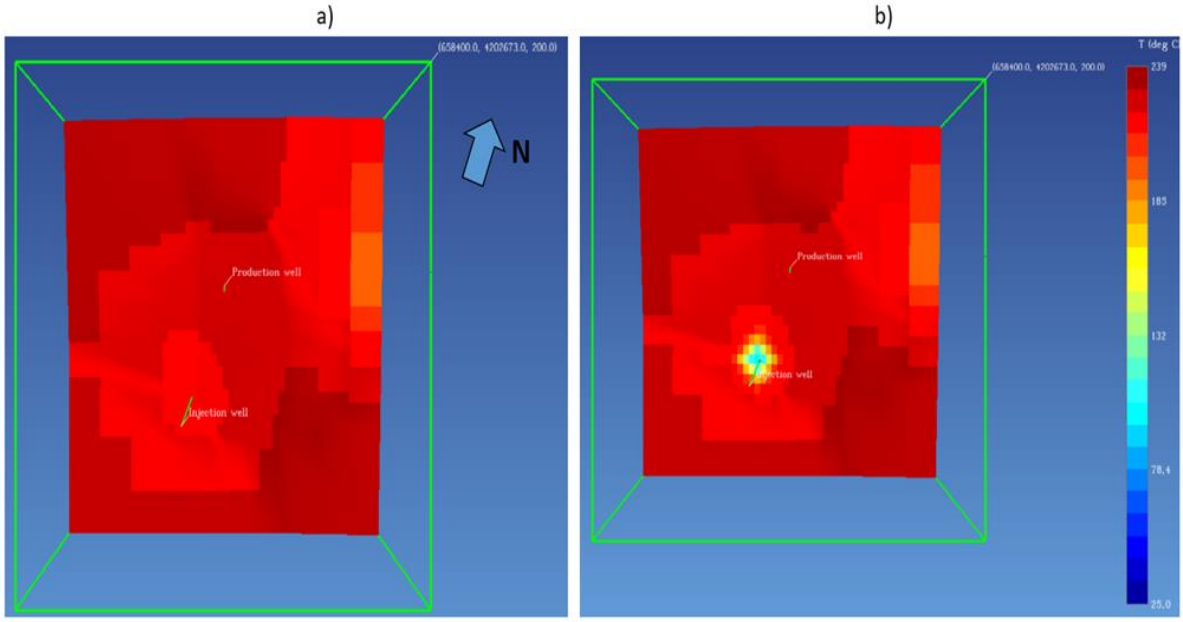

Figure 6.8 Spatial distribution of temperature before (a) and after reinjection (b) in heterogeneous model.

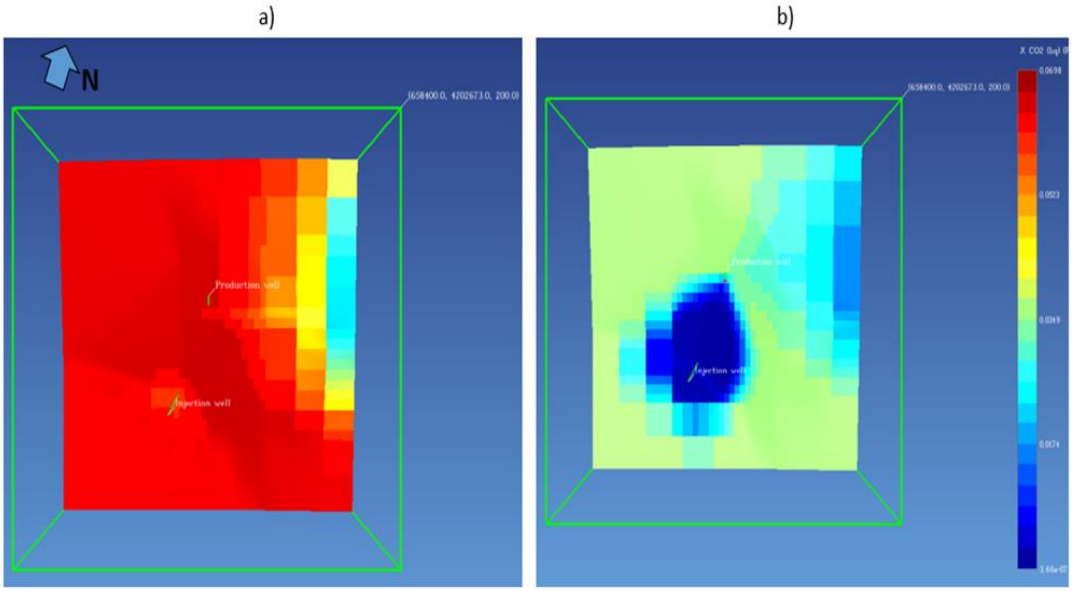

Figure 6.9 Spatial distribution of dissolved CO_2 before (a) and after reinjection (b) in heterogeneous model.

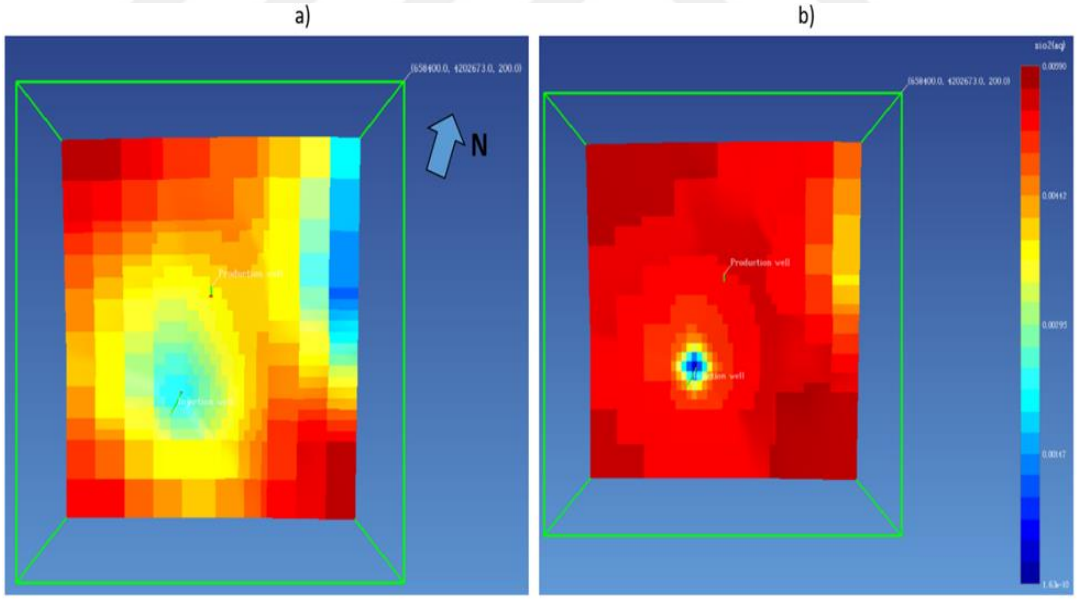

Figure 6.10 Spatial distribution of silica before (a) and after reinjection (b) in heterogeneous model.

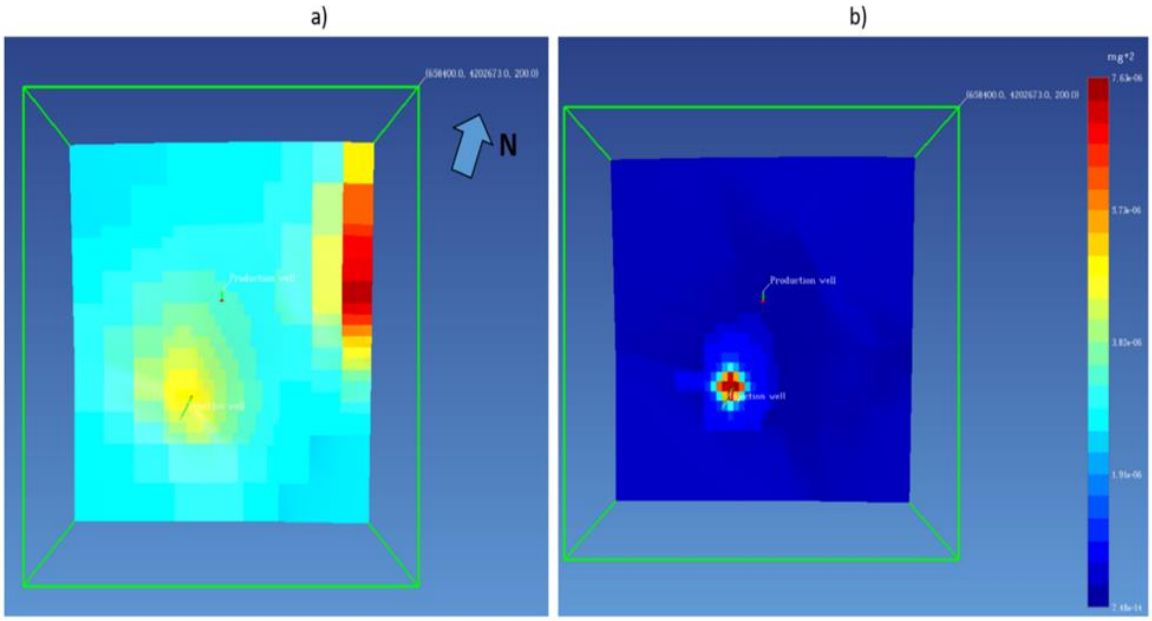

Figure 6.11 Spatial distribution of magnesium before (a) and after reinjection (b) in heterogeneous model.

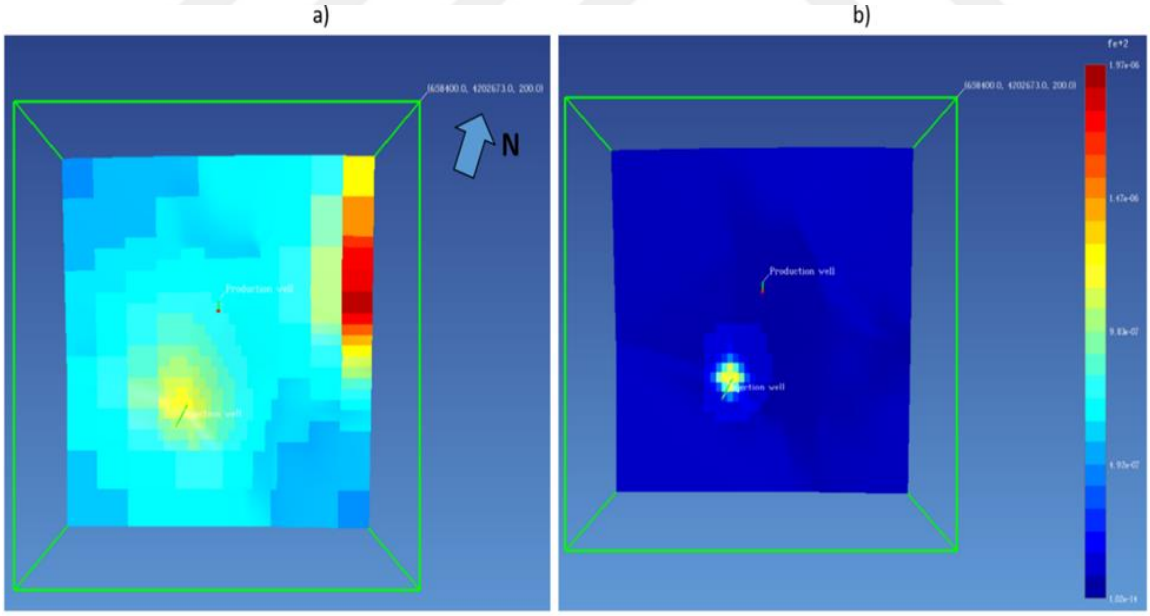

Figure 6.12 Spatial distribution of iron before (a) and after reinjection (b) in heterogeneous model.

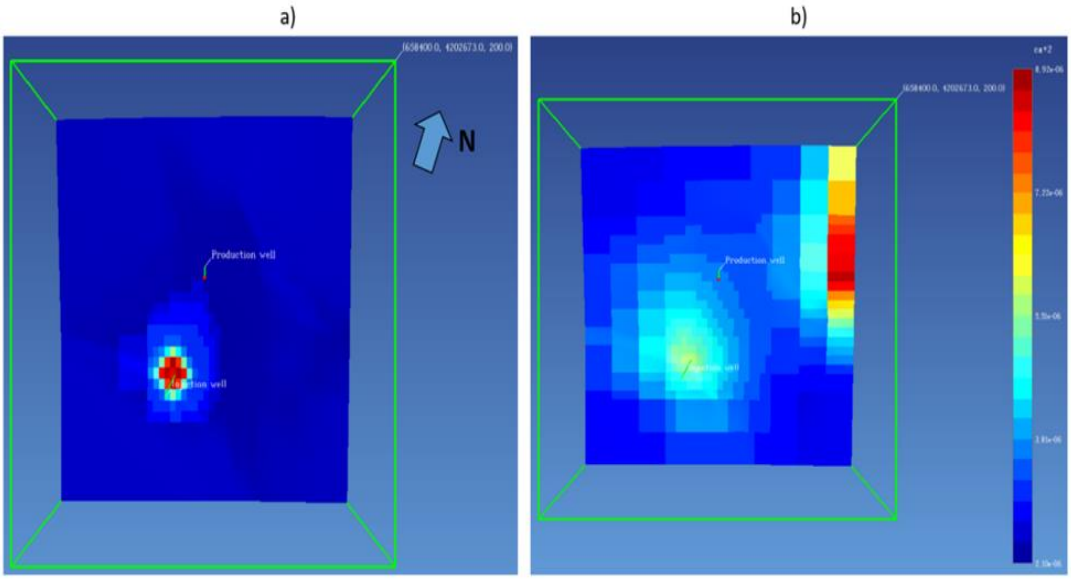

Figure 6.13 Spatial distribution of calcium before (a) and after reinjection (b) in heterogeneous model.

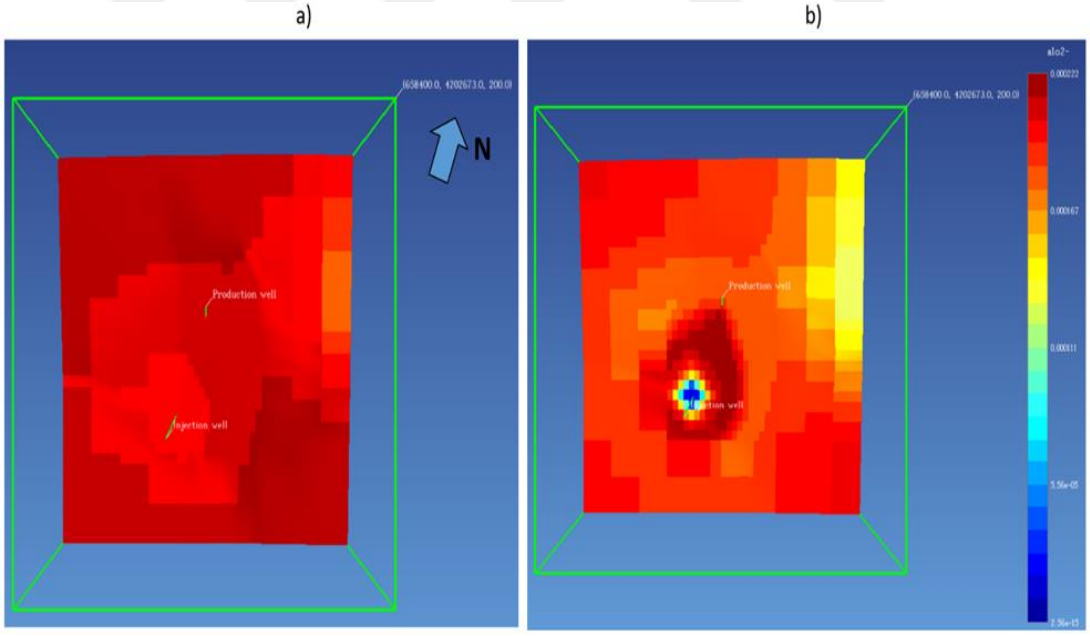

Figure 6.14 Spatial distribution of aluminum before (a) and after reinjection (b) in heterogeneous model.

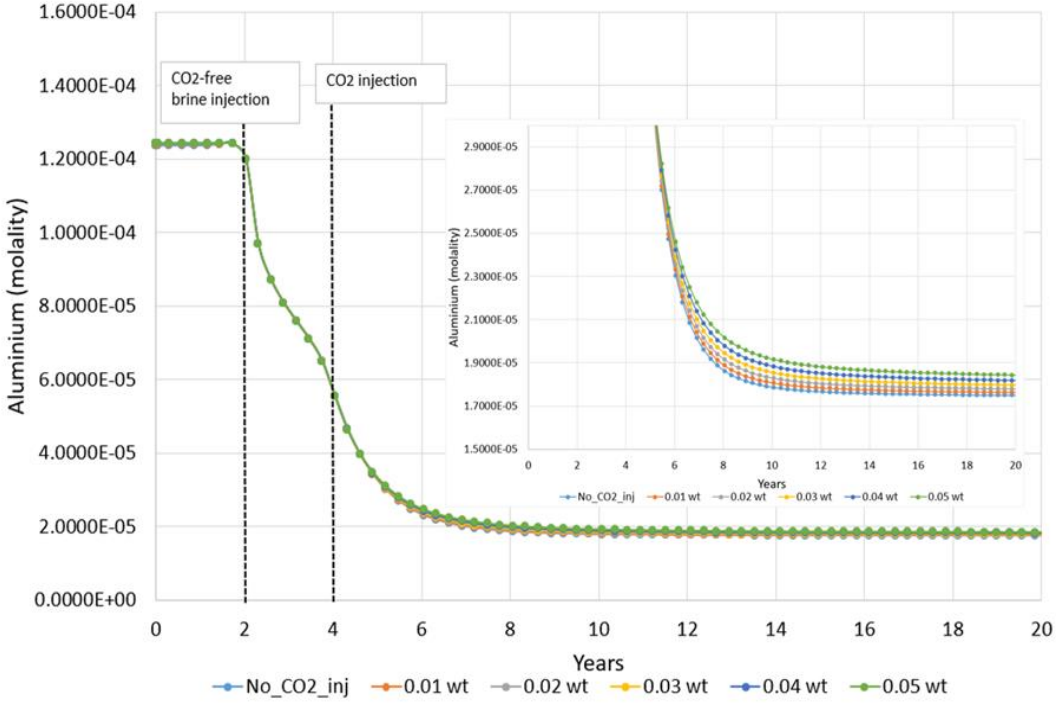

Figure 6.15 Changes in the aluminum concentration of reinjection well for homogenous model.

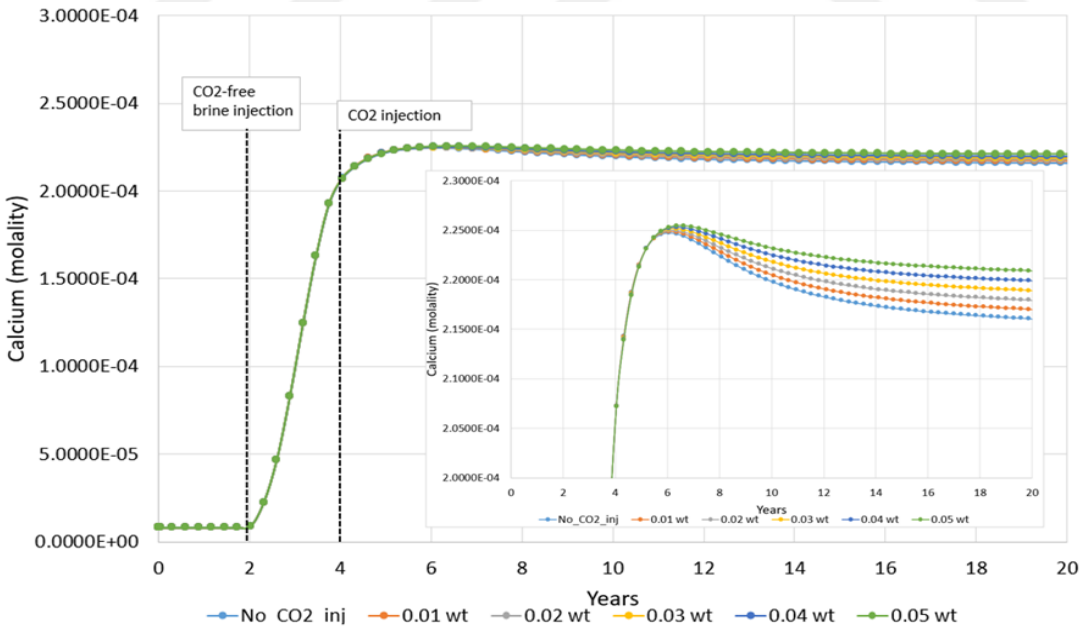

Figure 6.16 Changes in the calcium concentration of reinjection well for homogenous model.

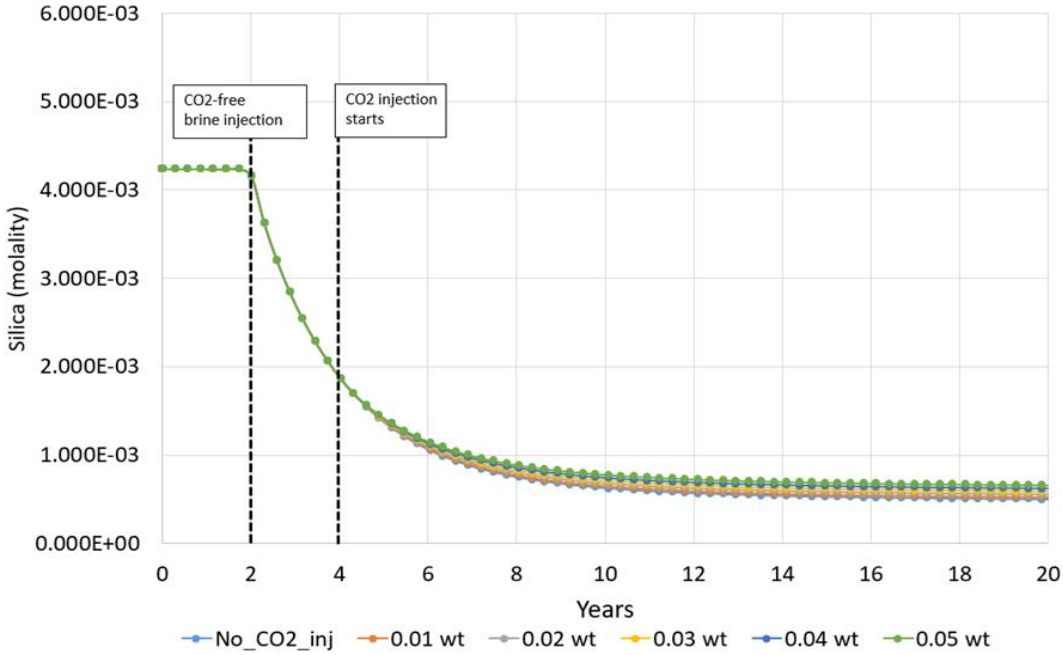

Figure 6.17 Changes in the silica concentration of reinjection well for homogenous model.

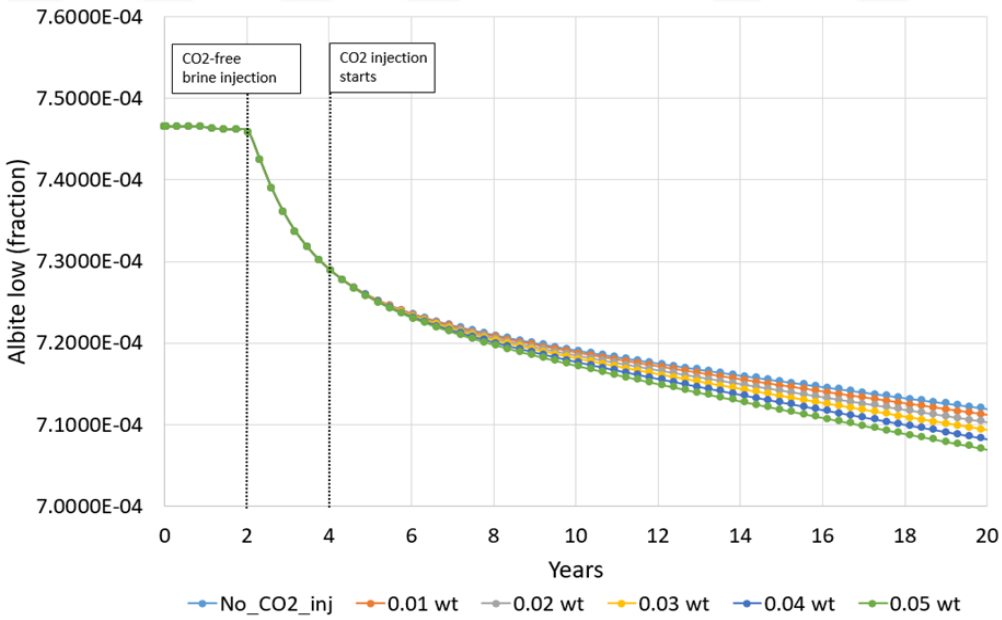

Figure 6.18 Changes in the Albite faction of reinjection well for homogenous model.

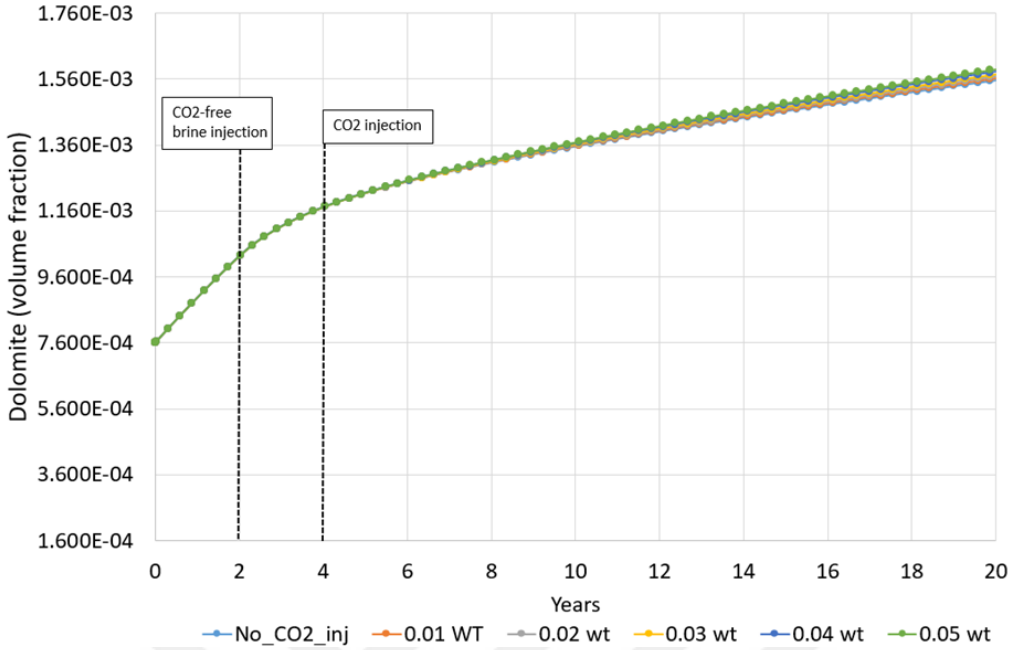

Figure 6.19 Changes in the Dolomite faction of reinjection well for homogenous model

CURRICULUM VITAE

Surname, Name: Aydın, Hakkı

EDUCATION

Degree	Institution	Year of Graduation
BSc.	METU Petroleum and Natural Gas Engineering	2015
MSc.	METU Petroleum and Natural Gas Engineering	2018
Ph.D.	METU Petroleum and Natural Gas Engineering	2023

FOREIGN LANGUAGES

Advanced English, Fluent Kurdish

EXPERIENCES

2016 –2022	Specialist, Geothermal Resource Management, Zorlu Energy
2022 – Present	Manager, Geothermal Resource Management, Zorlu Energy

PUBLICATIONS

Conference Papers:

1. **Aydin H**., Akin S., and Tezel S., (2018): "Practical Experiences About Reservoir Monitoring in Alasehir Geothermal Field", 43rd Workshop on

Geothermal Reservoir Engineering Stanford University, at Stanford, California

2. **Aydin H**., Akin S., and Salar M., (2018): "Application of Fluorescent Micro Particles as Geothermal Tracers", 43rd Workshop on Geothermal Reservoir Engineering Stanford University, at Stanford, California

3. **Aydin H**.(2018): "Discrete Fracture Network Modelling of Alaşehir Geothermal Field", MSc Thesis, Middle East Technical University

4. **Aydin, H**. (2018): "Negative Effects of Fast Production from Geothermal wells". IV. Geothermal and Natural Mineral Waters Symposium and Exhibition. Afyonkarahisar 21 Feb 2018.

5. **Aydin H**. and Akin S., (2019): "Discrete Fracture Network Modelling of Alaşehir Geothermal Field", 44th Workshop on Geothermal Reservoir Engineering Stanford University, at Stanford, California

6. **Aydin H**. and Akin S., (2019): "Parameter Study on Tracer Flow Test", 44th Workshop on Geothermal Reservoir Engineering Stanford University, at Stanford, California

7. **Aydin H**. and Akin S., (2020): "Numerical Reservoir Simulation of Alaşehir Geothermal Field" 45th Workshop on Geothermal Reservoir Engineering Stanford University, at Stanford, California

8. Senturk E., **Aydin H.** and Tuzen, M.K., (2020): "Injection Rehabilitation at Kızıldere Geothermal Field: Use of Flow Rate Weighted Average Production Wellhead Pressure for Reservoir Management". 45th Workshop on Geothermal Reservoir Engineering Stanford University, at Stanford, California

9. **Aydin, H**., Akin, S. (2020): "Analysis of a Comprehensive Tracer Test in Alaşehir Geothermal Field". Turkey IV. Scientific and Technical Petroleum Congress, Ankara Turkey.

10. **Aydin, H.**, Akin, S., Senturk, E. (2020): "Evaluation of Production Capacity of Geothermal Power Plants in Turkey". Geothermal Resource Council Annual Meeting. GRC Transactions, Vol. 44, pp. 163-174 (2020)

11. **Aydin, H**., Merey, Ş. (2021): "Changing Casing-Design of New Geothermal Wells in Western Anatolia for Adapting to the Changes in Reservoir Conditions". 46th Workshop on Geothermal Reservoir Engineering Stanford University, Stanford, California, February 15-17, 2021 SGP-TR-218.

12. **Aydin, H**., Akin, S., Tuzen, M.K., Senturk, E. (2021): "Artificial Lifting in Liquid Dominated High-Temperature Geothermal Fields in Turkey: Lessons Learned". 46th Workshop on Geothermal Reservoir Engineering Stanford University, Stanford, California, February 15-17, 2021 SGP-TR-218.

13. Temizel, C., Canbaz, C.H., **Aydin, H**., Wijaya, Z. (2021). A Deep Investigation of EOR/EGR and Stimulation Enhancement Methods in Unconventional Reservoirs. EAGE 2021, Conference Proceedings, IOR 2021, Apr 2021, Volume 2021, p.1 – 27.

14. Temizel, C., Canbaz, C.H., **Aydin, H**., Kudrashou, V., Haeri, F., Unal, Y., Nurlybayev, N. Huff'n Puff EOR Optimization by using Different Cyclic Gases in Unconventional Shales. EAGE 2021, Conference Proceedings, IOR 2021, Apr 2021, Volume 2021, p.1 – 32.

15. Temizel, C., Canbaz, C.H., Palabiyik, Y., **Aydin, H.**, Tran, M., Ozyurtkan, M.H., Yurukcu, M., Johnson, P. 2021. A Thorough Review of Machine Learning Applications in Oil and Gas Industry. SPE/IATMI Asia Pacific Oil & Gas Conference and Exhibition.

16. Temizel, C., Canbaz, C.H., **Aydin, H**., Hosgor, B.F., Kayhan, D.Y., Moreno, R. 2021. A Comprehensive Review of the Fourth Industrial Revolution IR 4.0 in Oil and Gas Industry. SPE/IATMI Asia Pacific Oil & Gas Conference and Exhibition.

17. Canbaz, C.H., **Aydin, H**., Canbaz, E., Akbarov, I., Akhasan, F., Hussain, A., Emadi, H., Temizel, C. 2021. A Comprehensive Review and Status of Renewable Resources and Oil and Gas. 82nd EAGE Annual Conference & Exhibition, Oct 2021, Volume 2021, p.1 – 77.

18. **Aydin, H**., Sengun, R., Haklidir, F.S.T. 2022. Potential Assessment of Lithium Extraction from Geothermal Reservoirs. 47th Workshop on Geothermal Reservoir Engineering Stanford University, Stanford, California, February 7-9, 2022.

19. **Aydin, H**. Temizel, C. 2022. Characterization of Geothermal Reservoirs 47th Workshop on Geothermal Reservoir Engineering Stanford University, Stanford, California, February 7-9, 2022.

20. Temizel, C., Yegin, C., Hosgor, F.B., **Aydin, H**., Kabir, S. 2022. Exploring Green Energy Applications in the Oil and Gas Industry. SPE Canadian Energy Technology Conference, Calgary, Alberta, Canada. SPE-208900-MS.

21. **Aydin, H**., Nagabandi, N., Jamal, D., & Temizel, C. (2022, April). A Comprehensive Review of Tracer Test Applications in Geothermal Reservoirs. In SPE Western Regional Meeting.

22. **Aydin, H**., Nagabandi, N., Temizel, C., & Jamal, D. (2022, April). Heavy Oil Reservoir Management-Latest Technologies and Workflows. In SPE Western Regional Meeting.

23. Temizel, C. T., Odi, U., Al-Sulaiman, N., Reddy, K., Putra, D., Yurukcu, M., **Aydin, H** & Yegin, C. (2022, April). Production Forecasting in

Conventional Oil Reservoirs Using Deep Learning. In SPE Western Regional Meeting.

24. **Aydin, H**., Yegin, C., Nagabandi, N., & Temizel, C. (2022, April). Latest Technologies and Methods for Carbon Capture and Underground Gas Storage. In SPE Western Regional Meeting.

25. **Aydin, H**., & Temizel, C. (2022, April). Renewables, Energy Transition, and the Future of Conventional and Unconventional Oil & Gas in California. In SPE Western Regional Meeting.

26. **Aydin, H**., Boppano, N., Yurukcu, M., Liu, S., Yegin, C., & Temizel, C. (2022, April). A Comprehensive Review of RTA/DCA Methods in Unconventional Reservoirs. In SPE Western Regional Meeting.

27. Haklidir, F.T., **Aydin, H.,** Ç.Ş., Raziye. 2023. Contribution of Artificial Intelligence Technology to Sustainability of Geothermal Energy Applications. 75th Geological Congress of Turkey.

Journal Article:

1. **Aydin H**., Akin S., and Senturk E. (2020). A proxy model for determining reservoir pressure and temperature for geothermal wells. Geothermics Vol. 88, November 2020, 101916 https://doi.org/10.1016/j.geothermics.2020.101916

2. Merey, S., **Aydin, H**., and Eren, T. (2020). Design of electrical submersible pumps in methane hydrate production wells: A case study in Nankai trough methane hydrates. Upstream Oil and Gas Technology, Volume 5, October 2020, 100023 https://doi.org/10.1016/j.upstre.2020.100023

3. **Aydin, H**., Merey, S. (2021). Potential of Geothermal Energy Production from Depleted Gas Fields: A Case Study of Dodan Field, Turkey. Renewable Energy 164 (2021) 1076-1088 https://doi.org/10.1016/j.renene.2020.10.057

4. **Aydin, H**., Akin, S. (2021) Estimation of upcoming problems in Alaşehir geothermal field using a numerical reservoir model. Arabian Journal of Geosciences volume 14, Article number: 562 (2021). https://doi.org/10.1007/s12517-021-06830-z

5. Haklidir F.T., Sengun, R., **Aydin, H**. 2021. Characterization and Comparison of geothermal fluids geochemistry within the Kızıldere Geothermal Field in Turkey: New findings with power capacity expanding studies. Geothermics Vol. 94. March 2021, 102110. https://doi.org/10.1016/j.geothermics.2021.102110

6. **Aydin, H**., Merey, Ş. 2021. Design of Electrical Submersible Pump system in geothermal wells: A case study from West Anatolia, Turkey. Energy, Volume 230, 1 September 2021, 120891. https://doi.org/10.1016/j.energy.2021.120891

7. **Aydin, H.**, Merey, Ş. 2021. The effect of gas production from deeper conventional gas reservoirs on shallower gas hydrate layer stability: A case study in the conditions of the Sakarya gas field, Western. Journal of Natural Gas Science and Engineering, Volume 93, 104103. https://doi.org/10.1016/j.jngse.2021.104103

8. **Aydin, H**., Özen Balaban, T., Bülbül, A., Merey, Ş., Tarcan, G. 2022. Determining the most representative reservoir model for the shallow depth salihli geothermal reservoir in Turkey using tracer test. Heat and MassTransfer volume 58, pages1105–1118 (2022). https://doi.org/10.1007/s00231-021-03166-y

9. Aslan, G., **Aydin, H**., Cakir, Z. 2022. Wide-area ground deformation monitoring in geothermal fields in western Turkey. Turkish J Earth Sci(2022) 31: 247-259. 10.55730/1300-0985.1771

10. Temizel, C., Odi, U., Balaji, K., **Aydin, H**., Santos, J.E. 2023. Classifying Facies in 3D Digital Rock Images Using Supervised and Unsupervised Approaches. Energies 2022, 15, 7660. https://doi.org/10.3390/en15207660

11. Temizel, C., **Aydin, H.,** Hosgor, F.B., Yegin, C., Kabir, C.S. 2023. Green Energy Sources Reduce Carbon Footprint of Oil & Gas Industry Processes: A Review. Journal of Energy and Power Technology 2023, Volume 5, Issue 1. 10.21926/jept.2301004

12. **Aydin, H**., Akin, S. CO_2 Dissolution in the reservoir brine: An experimental and simulation-based approach. Geothermics 113 (2023) 102774. https://doi.org/10.1016/j.geothermics.2023.102774

Book Chapter:

1. Aydin, H. 2020. 21. Yüzyılda Petrol ve Doğal Gaz Mühendisliği (in Turkish). Yenilenebilir Enerjiye Yönelim ve Saklı Kaynak Yer Altı Güneşi: Jeotermal Enerji. Chapter 11, pp. 315-332.
2.

Professional Activities

- Part Time Instructor at İzmir Katip Çelebi University Department of Petroleum and Natural Gas Engineering
- SPE Turkey President for 2022-2024
- Reviewer at the following Journals:

- Journal of Natural Gas Science and Engineering

- Petroleum Science and Technology